

ARMY RESEARCH LABORATORY



Materials Science Studies of High-Temperature Superconducting Ceramic Oxides

by G. C. Vezzoli, M. F. Chen,
F. Craver, and R. N. Katz

ARL-TR-1570

December 1997

19980126 033

DTIC QUALITY INSPECTED 2

Approved for public release; distribution is unlimited.

The findings in this report are not to be construed as an official Department of the Army position unless so designated by other authorized documents.

Citation of manufacturer's or trade names does not constitute an official endorsement or approval of the use thereof.

Destroy this report when it is no longer needed. Do not return it to the originator.

Army Research Laboratory

Aberdeen Proving Ground, MD 21005-5066

ARL-TR-1570**December 1997**

Materials Science Studies of High-Temperature Superconducting Ceramic Oxides

G. C. Vezzoli, M. F. Chen, F. Craver, and R. N. Katz
Weapons and Materials Research Directorate, ARL

Abstract

Herein is presented the results of a comprehensive program of research aimed at understanding the materials science and the mechanistic physics of high-temperature superconducting oxides. This comprehensive research program has identified the materials properties that are consistently associated with high- T_c superconductors and has shown that the mechanism that gives rise to the phenomenon of high- T_c superconductivity is associated with bound holes that are due to charge-transfer excitations at high frequency. The latter are a result of the high internal electric field present in high- T_c materials, owing to the asymmetry of the crystal structure. The interaction of bound holes with free electrons and the interaction of local spin fluctuations with the spin of free electrons generate a charge density wave and a spin density wave that cause Cooper pairing.

Acknowledgments

The authors wish to acknowledge the following persons for participating in valuable discussions and for experimental laboratory assistance: Ray Hinxman, Gary Wechsler, Ralph Harrison, Thomas Hynes, James Marzik, Lou Carreiro, Richard Desper, William Croft, William Spurgeon, Richard Benfer, Sing Shong Lin, Wai Chen, James Hrvonen, Diane van der Walker (U.S. Army Materials Technology Laboratory [USAMTL]); Terence Burke (U.S. Army Electronic Technology Devices Laboratory); William Stanley (Decision Software); A. J. Freeman (Northwestern University); Vladimir Kresin (Lawrence Berkeley Laboratory); Farrel Lytle (Boeing Aircraft Company); John Goodenough (University of Texas); Larry Rubin, Bruce Brandt, Don Heiman, August Witt, and Simon Foner (Massachusetts Institute of Technology); Josef Ashkenazi and Stewart Barnes (University of Miami); Carmine Vittorio and Alan Widom (Northeastern University); Carl Rau (Rice University); Munir Shoga (Hughes Corporation); B. M. Moon (Royal Swedish Institute); B. Lalevic, A. Safari, and B. Kear (Rutgers University); C. Gallo (3M Company); P. J. Walsh (Fairleigh Dickinson University); Stewart Kurtz and Rustum Roy (The Pennsylvania State University); Joseph Budnick (University of Connecticut); C. W. Paul Chu (University of Houston); Gene Venturini (Sandia National Laboratories [SNL]); Colonel Kenneth Grice (U.S. Military Academy at West Point); Robert Bonometti (U.S. Army); Stew Wolf, Warren Pickett, Barry Kline, and Donald Gubser (Naval Research Laboratory); Cliff Alexander (U.S. Air Force); Brent Mattes; John Ruvalds (University of Virginia); Rubin Braunstein (University of California Los Angeles [UCLA]); Ahmet Erbil (Georgia Institute of Technology); Monde Otooni, Frank Owens, Y. Carignon, C. DeFranco, T. Davidson, and P. Devens (U.S. Army Armament Research, Development, and Engineering Center [ARDEC], Picatinny Arsenal); David Tanner, Kathy Kamaras, and Jack Crow (University of Florida); Larry Bennet and L. Goldfarb (National Institute of Standards and Technology [NIST]); and Gerald Iafrate (Director of the U.S. Army Research Office). Finally, great appreciation is recollected in regard to fruitful discussions and many years of encouragement extended by the late Nobel Laureate John Bardeen.

In Memoriam: During the preparation of this manuscript, two outstanding scientists in the area of superconductivity passed from amidst us: John Bardeen of the University of Illinois and Steve Berko of Brandeis University. The authors wish to ask the readers to pause for a moment of prayer and gratitude on behalf of honor and respect to these splendid individuals.

Preface

This report presents and documents, in detail, the experimental and theoretical approaches, interpretation, and conclusions derived from the U.S. Army Materials Technology Laboratory (USAMTL) research program in high-critical-temperature (T_c) superconductivity, during the period 1 June 1987 to 30 September 1993. This program was aimed at the understanding of the mechanism, materials and ceramics science and engineering, and the processing criteria involved in bulk high- T_c materials, and, thereby, the improving of critical properties. The in-house work herein described was performed by Dr. G. C. Vezzoli as principal investigator, Ms. Michaeline F. Chen as synthesis chemist, and Dr. Frederick Craver as computer mathematician. The program was initiated and initially supervised by Dr. R. N. Katz. Additional branch and team supervisors of this work were Drs. James McCauley, Louis Carreiro, and James Marzik. In-house consulting discussions were conducted with Dr. Ralph Harrison.

Throughout this report, the format and syntax bring together the materials science, the solid-state physics, and the crystal or ceramics chemistry, such that the subject is addressed in an interdisciplinary fashion. It has been noted, that in an effort to quantitatively describe the density-of-states function and the coupling constant for high- T_c materials, the pure physics approaches have, unfortunately, frequently ignored pertinent considerations of crystal chemistry, such as the physical configurations leading to charge-transfer excitations, the importance of multivalence cations, as well as the notions of electronegativity and field strength. On the other hand, an approach purely through materials science and crystal chemistry cannot be expected to be sufficient to fully understand a newly discovered phenomenon, such as high- T_c superconductivity, from the fundamental standpoints of energy-band considerations and many-body interactions; hence, the approach through solid-state physics is equally important.

INTENTIONALLY LEFT BLANK.

Table of Contents

	<u>Page</u>
Acknowledgments	iii
Preface	v
List of Figures	xiii
List of Tables	xxi
1. Introduction to Superconductivity	1
1.1 Early Background	1
1.2 Fundamentals of the Microscopic Theory of Superconductivity Essential to Subsequent Materials Science Study of High- T_c Superconductivity	7
1.3 Hubbard Bands	10
1.4 The State of Perfect Diamagnetism	13
1.5 The Role of Temperature and T_c for Low-Temperature Conventional Superconductivity	16
1.6 Predictions of the BCS Theory of Superconductivity	19
1.7 The Critical Current Density J_c	20
2. Theoretical Basis for Research Into High-T_c Superconducting Materials	23
2.1 Metallic Hydrogen and Excitons	23
2.2 Other Nonphonon-Based Mechanisms	26
2.2.1 <i>Plasmons</i>	26
2.2.2 <i>Polarons and Bipolarons</i>	27
2.2.3 <i>Resonant Valence Bond (RVB)</i>	29
2.2.4 <i>The Spin Fluctuation Mechanism</i>	30
2.2.5 <i>The Charge-Transfer Excitation and Valence Fluctuations [68-70]</i>	30
2.3 Band Structure	30
2.4 Fundamental Properties of Matter	31
3. Experimental Basis for High-T_c Superconductivity	32
3.1 Early Work in the CuCl System and CdS Polymorphs	32
3.2 More Recent Work on CuCl	37
3.3 The Discoveries of 1986 and 1987 in the LaCuO System [91-93]	42
3.4 The Discovery of Superconductivity in the YBaCuO System [120]	45
3.4.1 <i>Crystal Structure of $Y_1Ba_2Cu_3O_{7-\delta}$</i>	45
3.4.2 <i>Role of Each Ion</i>	49

3.4.2.1	<i>Yttrium</i>	49
3.4.2.2	<i>Barium</i>	49
3.4.2.3	<i>Cu²⁺</i>	50
3.4.2.4	<i>Cu³⁺</i>	51
3.4.2.5	<i>Oxygen</i>	51
3.4.3	<i>Ionic Charge and Stability Considerations</i>	51
3.4.4	<i>Radius Ratio and Coordination Number Considerations</i>	55
3.4.5	<i>Isotope and Charge Concentration Considerations</i>	58
3.5	The Thallium-Based and Bismuth-Based High-T _c Superconductors	59
3.5.1	<i>Structure and Composition</i>	59
3.5.2	<i>Size and Radius Ratio Criteria for High-T_c Superconductors</i>	62
3.6	Major Experimental Findings of Others That Are Related to the USAMTL	
	Approach and Interpretations	63
3.6.1	<i>Excitons</i>	63
3.6.2	<i>Antiferromagnetism</i>	64
3.6.3	<i>Hall Effect</i>	64
3.6.4	<i>Fermi Surface</i>	65
3.6.5	<i>Valence of Copper</i>	66
3.6.6	<i>Superconducting Gap</i>	67
3.6.7	<i>Ferroelectric Behavior</i>	67
3.6.8	<i>Hole Excitation Spectra and Charge-Transfer Excitations</i>	68
4.	Overview of the USAMTL Program	69
4.1	Statement of the Problem	69
4.2	Objectives of the Research Program	69
4.3	Relevance of High-T _c Superconducting Materials to the U.S. Army's	
	Material Requirements and Future Needs	70
4.4	Short Summary of Conclusions and Breakthroughs That Derived From the	
	USAMTL Program on High-T _c Superconducting Ceramics	71
5.	Experimental Procedure, Synthesis, and Characterization	73
5.1	The Y ₁ Ba ₂ Cu ₃ O _{7-δ} Material	73
5.1.1	<i>Chemistry of Materials Synthesizing</i>	74
5.1.2	<i>Purchasing Source</i>	74
5.1.3	<i>Laboratory Equipment</i>	74
5.1.4	<i>Preparation Procedure</i>	75
5.2	Bi ₁₁₁₂ (Bi ₁ Ca ₁ Sr ₁ Cu ₂ O ₆), Bi ₂₁₂₂ (Bi ₂ Ca ₁ Sr ₂ Cu ₂ O ₈), and Bi ₂₂₂₃	
	(Bi ₂ Ca ₂ Sr ₂ Cu ₃ O ₁₀) General Procedure of Preparation and	
	Characterization	77
5.2.1	<i>Starting Chemicals</i>	81
5.2.2	<i>Laboratory Equipment</i>	81
5.2.3	<i>Preparation Procedure</i>	82

	<u>Page</u>
5.2.4 <i>Test and Characterization Procedure</i>	82
6. Experimental and Theoretical Results From the USAMTL Research Program	89
6.1 The Hall Effect in $Y_1Ba_2Cu_3O_{7-\delta}$	89
6.2 Antiferromagnetism in the YBaCuO System	97
6.3 The Role of RE Substituted for Yttrium in High- T_c $Y_1Ba_2Cu_3O_{7-\delta}$	101
6.3.1 <i>Experimental Data on RE Substitution</i>	101
6.3.2 <i>Details of the Calculations of the Paramagnetic Central Ion Capacity to Decouple Cooper Pairs and the Indirect Exchange Polarization</i> ...	107
6.3.3 <i>Frequency and Time Considerations of Interaction Between the Cooper Pair and the Paramagnetic Ion</i>	112
6.3.4 <i>Polarization of Cu^{2+} Spin Fluctuations by the Paramagnetic Central Ion</i> .	113
6.3.5 <i>Calculations of Approximate Energy and Torque for Polarization</i>	117
6.3.6 <i>Ferrimagnetic Correlations</i>	117
6.3.7 <i>Quantized Flux Trapped in a High-T_c Superconductor When $H > H_{cl}$: Vortice Lines of Quantized Flux</i>	119
6.3.8 <i>Calculation of Cooper-Pair Concentration</i>	120
6.4 Magnetically Related Properties of the Bismuth-, Gallium-, Antimony-, and Gadolinium-Containing High- T_c Superconductors	122
6.4.1 <i>The Effect of the Applied Magnetic Field on Resistance vs. Temperature Behavior in the Normal, Preonset, Transitional, Foot, and Zero-Resistance Regions</i>	122
6.4.2 <i>The Zero-Resistance Time Dependence of Flux Readmission</i>	130
6.4.3 <i>The Cation Diamagnetism</i>	131
6.4.4 <i>The Anion Atomic or Zero-Valence Paramagnetism</i>	134
6.4.5 <i>The Effect of Magnetic Field on Low-Frequency Small Oscillations in Resistance vs. Time at Constant Temperature Below the Preonset Temperature</i>	135
6.5 The Exciton Analysis and the Fundamentals of the Interaction of the Hole Constituent of the Bound of Virtual Exciton With Candidate Conduction Electrons for Cooper Pairing	135
6.6 Critical Current in $Y_1Ba_2Cu_3O_{7-\delta}$ vs. Temperature Dependence: The Recovery Regime	139
6.7 Quantitative Treatment of Cooper-Pairing, Based on Bound Holes or Virtual Excitons as Mediators in $Y_1Ba_2Cu_3O_{7-\delta}$	150
6.7.1 <i>Polar Analogues in Magnetostatics</i>	150
6.7.2 <i>The Coulombic Interactions</i>	152
6.7.3 <i>Initial Conditions and Perturbations</i>	155
6.7.4 <i>Displacement of Positive Charge and Work Done by e_2 Conduction Electron</i>	157

6.7.5	<i>Potential Function for $e_1 - e_2$ Interaction Derived From Conservation of Momentum and Conservation of Energy</i>	157
6.7.6	<i>Calculation for Net Attraction Between Two Conduction Electrons as Mediated by Displaced Positive Charge Contribution of Virtual Exciton</i>	159
6.7.7	<i>Calculation Temperature for Adequate Hole Lifetime ($\tau_{Lh} = \Delta t_e$) Using Coulombic-Interaction Model</i>	163
6.8	The Properties of High-T_c Superconducting Materials That Relate to Characteristics of Marginal Ferroelectrics	165
6.8.1	<i>Overview</i>	165
6.8.2	<i>Introduction to Ferroelectric Properties as Related to High-T_c</i>	166
6.8.3	<i>General Theory of Ferroelectric Materials</i>	169
6.8.4	<i>Persistent Polarization in Ferroelectric Materials and Perfect Diamagnetism in Superconductors</i>	173
6.8.4.1	<i>Peaking Dielectric Constant</i>	174
6.8.4.2	<i>The Polarization vs. Temperature Curve</i>	177
6.8.5	<i>The Internal Electric Perturbation Field Calculation in $Y_1Ba_2Cu_3O_{7-\delta}$</i> ...	178
6.8.5.1	<i>The Computational Model</i>	178
6.8.5.2	<i>Computation of Internal Electric Field of $Y_1Ba_2Cu_3O_{7-\delta}$</i>	182
6.8.5.3	<i>The Electric Field Using Single-Point Idealized Ionic Sources for Each Ion, According to the Composition ($Y_1^{3+}Cu^{3+}$), ($Ba_2^{2+}Cu_2^{2+}$), $O_{8-\delta}^{2-}$</i>	183
6.8.5.4	<i>Employing the Refinement of an Electron Distribution</i>	184
6.8.5.5	<i>Conductivity Within the Base Plane of the Pyramids (CuO_2 Planar Region) in $Y_1Ba_2Cu_3O_{7-\delta}$</i>	185
6.8.5.6	<i>Charge Substitutions</i>	186
6.8.5.7	<i>Random Substitutions</i>	190
6.8.5.8	<i>Vector Fields in and Near the Chain Region</i>	191
6.8.5.9	<i>Modifications Due to Molecular Orbital Considerations</i>	193
6.8.5.10	<i>Tests for Convergence</i>	194
6.8.6	<i>Implications of the Internal Field Study Regarding High-T_c Superconductivity and Crystal Chemistry in $Y_1Ba_2Cu_3O_{7-\delta}$</i>	195
6.8.6.1	<i>The Valence of Copper</i>	195
6.8.6.2	<i>The Polyhedral Building Blocks</i>	197
7.	The Empirical Scaling of Low-T_c and High-T_c Materials With Basic Parameters	198
7.1	<i>Low-T_c Scaling</i>	198
7.2	<i>High-T_c Scaling</i>	201
8.	Conclusions and Interpretations Regarding Materials Science and Mechanism of High-T_c Superconductivity	205

	<u>Page</u>
8.1 The Materials Science and Materials Engineering	205
8.2 The Mechanism of High- T_c Superconductivity	207
9. References	211
Distribution List	225
Report Documentation Page	227

INTENTIONALLY LEFT BLANK.

List of Figures

<u>Figure</u>	<u>Page</u>
1. Conventional Low- T_c Elemental Superconductors vs. Density	2
2. Magnetic Field (H) vs. Temperature (T)	3
3. Superconductivity and Z_v , where Z_v = No. Valence Electrons/Atom	4
4. Magnetic Induction B vs. Applied Field H_a for (a) Normal Metal Conductor, (b) Perfect Idealized Conductor, and (c) Superconductor (With Axis of Long Individual Superconductor Parallel to H_a)	5
5. Flux Characteristics Related to Superconductors in External Magnetic Field	6
6. Applied Field H_a for (a) Type-1 and (b) Type-2 Superconductors	6
7. Exchange of Virtual Phonon	8
8. Diagrams Indicating the Qualitative Temperature Dependence of Magnetic Susceptibility for (a) Simple Paramagnetism, (b) Ferromagnetism, (c) Antiferromagnetism	12
9. $\beta \geq U$ Overlap	12
10. Resonating Moments in a Highly Correlated Electron Gas	13
11. T-x-Phase Diagram of $\text{NiS}_{2-x}\text{Se}$	13
12. Applied Magnetic Field	21
13. Illustration of (a) Normal-State Electrons and (b) Superconducting Pairs	23
14. Size of the Polaron	28
15. Phases of CuCl , CuCl_2 , and Cu^0 Attached to a Glass Fiber for X-ray Diffraction Analysis	33
16. Wave-Function Overlap, Excitons, and Polytypic-Stacking Variants in Zincblende Configurations	34

17.	The Sort of Situation Envisaged as Possible in Disproportionate CuCl for an Electron From a Small Region of Segregating Copper Creating a Virtual Exciton Across the Boundary to the Charge-Ordered State	35
18.	Anomalies of Resistance, Diamagnetism, and Phase Angle	35
19.	Meissner Exclusion Effect at ~100 K and 5 kbar	36
20.	(a) CuCl and (b) CdS as Viewed Through Diamond Cell (White Transmitted Light)	37
21.	Optical Transmission of CuCl at 50 kbar vs. Time at Room Temperature	38
22.	Valence Charge for CuCl and Si [1, 2]	39
23.	CuCl/CaF ₂ Deep Quantum Well Structure	40
24.	Time-Dependent Photoluminescence for (a) CuCl Single-Crystal at 1.8 K and (b) 150 Å CuCl Quantum Well at 1.8 K	40
25.	Relative Resistance vs. Temperature for BiSb in Vacuum Showing Increasing Resistance Anomaly Upon Cooling and Reversible Minimum-Resistance Turning Point	41
26.	The Partially Filled 3-D Wave Functions of the Cu ³⁺ /Cu ²⁺ Mixed-Valence States	43
27.	Temperature Dependence of Resistivity in Ba _x La _{5-x} Cu ₅ O _{5(3-y)} for Samples With x = 1 (Upper Curves, Left Scale) and x = 0.75 (Lower Curve, Right Scale) (x Nominal)	44
28.	Structure of La ₂ CuO ₄	44
29.	The Structure of Y ₁ Ba ₂ Cu ₃ O _{7-δ} [124] Showing Lattice Parameters: a = 3.8231 Å, b = 3.8864 Å, c = 11.680 Å, Space Group P _{mmm} , Orthorhombic Bravais Lattice ..	46
30.	A ₂ BX ₄ Structure of Antiferromagnetic K ₂ NiF ₄	47
31.	Single Structural Building Block and Polyhedron of Coordination (Chains and Pyramids)	54
32.	Ratios of Cu ²⁺ /Cu ³⁺ to T _c	56

	<u>Page</u>
33. Increase in T_c	60
34. T_c vs. Carrier Concentration for High- T_c Materials	61
35. Dependency of Carrier Density N for the BCS Phonon-Electron Coupling	61
36. Crystal Structures of (a) $Tl_2Ba_2CuO_6$ and (b) $Tl_2CaBa_2Cu_2O_8$	62
37. Crystal Structures of (a) $Y_1Ba_2Cu_3O_{7-\delta}$, (b) $Tl_1Ca_1Ba_2Cu_2O_7$, and (c) K_2NiF_4	63
38. Hall Constant in $La_{1.85}Sr_{0.15}CuO_4$ vs. Temperature	65
39. Fermi Surfaces Analyzed From Brillouin Zone	66
40. Meservey [161] Results Showing the Presence of a BCS Gap	67
41. Superconducting State Transition From a Poled State of a Relaxor Ferroelectric Material	68
42. 2% Antimony Substitution in the Y_{1-2-3} Compound	78
43. 0.5% Gallium Substitution in the Y_{1-2-3} Compound	78
44. X-ray Diffraction Patterns for (a) $Y_1Ba_2Cu_3O_{7-\delta}$ at 20° for CuK_α , (b) $Y_1Ba_2(Cu_1O_xGa_x)_3O_{7-\delta}$, and (c) $Ba_2YCu_3O_{9-\delta}$	79
45. 0.5% Indium Substitution in the Y_{1-2-3} Compound	80
46. SEM Micrographs of $SbBiCaSrCuO$ After Sintering Process	83
47. Valence, Charge Transfer, and Carrier Type	84
48. X-ray Scans for Samples 2-4	84
49. As the Concentration of Calcium Substitution Increases, the Crystal Size Increases	87
50. Structure of the Superconductor $Y_1Ba_2Cu_3O_{7-\delta}$	90
51. The Hall Data on $La_{1-x}Sr_xCuO_4$ [150]: Hall Constant in $La_{1.85}Sr_{0.15}CuO_4$ vs. Temperature	90
52. Hall Effect Experiments at 6.8 and 5.0 T	91

	<u>Page</u>
53. Hall Effect at 5 T vs. Resistance Study of $Y_1Ba_2Cu_3O_{7-\delta}$ Superconductor	92
54. Hall Effect vs. Temperature for Yttrium Barium Cuprate [183]	93
55. Single-Crystal Hall Data	95
56. Weighted Two-Carrier Normalized Hall Number vs. Temperature Showing Second-Order Slope Change	96
57. Variation of Hall Coefficient (R_H) With Temperature (TK) to Be So	97
58. Experimental Phase Diagrams for (a) $YBa_2Cu_3O_{7-x}$ and (b) $La_{2-x}(Ba, Sr)_2CuO_{4-y}$.	98
59. MIT SQUID Results	99
60. Transition Temperatures vs. Element (R) in $R_1Ba_2Cu_3O_{7-\delta}$ [196]	102
61. Graph of the Preonset and Zero-Resistance Temperatures for RE $Ba_2Cu_3O_{7-\delta}$	103
62. $Ln_{0.2}$ (RE) Substituted Into $La_{1.6}Sr_{0.2}Ln_{0.2}CuO_4$	103
63. Spin and Effective Magnetic Moment vs. RE Series	104
64. Curie Point and Domain Transition	104
65. Spin-Fluctuation Contributing Mechanism for High- T_c Superconductivity	106
66. Oscillations in Electrical Resistance During Transition at $B = 0$ to Superconductivity as a Function of Time at Constant Temperature for $Y_1Ba_2Cu_3O_{7-\delta}$	108
67. Oscillations in Electrical Resistance During Transition at $B = 0$ to Superconductivity as a Function of Time at Constant Temperature for $Y_1Ba_2Cu_3O_{7-\delta}$ (Small Oscillation Data Observed at Temperature Data Points Shown With Vertical Bars)	108
68. The Structure of $Y_1Ba_2Cu_3O_{7-\delta}$ [111, 112] Showing Lattice Parameters: $a = 3.8231 \text{ \AA}$, $b = 3.8864 \text{ \AA}$, $c = 11.680 \text{ \AA}$, Space Group P_{mmm} , Orthorhombic Bravais Lattice	116
69. Electrical Resistance vs. B-field at Constant Temperature in the Intermediate State for BiSrCaCuO High- T_c Superconductor	123

	<u>Page</u>
70. Electrical Resistance vs. Reciprocal Temperature for $\text{Bi}_y\text{Ca}_z\text{Sr}_w\text{Cu}_t\text{O}_x$ as a Function of Applied Magnetic Field During Transition to Superconducting State	123
71. Resistance vs. $1,000/T$ for BiSrCaCuO as a Function of Magnetic Field	124
72. Hall Effect vs. Temperature K at $B = 4$ T for BiSrCaCuO (Heating Cycle ~ 0.1 K/min)	125
73. Hall Effect vs. Temperature for BiSrCaPbCuO , Suggesting Singularity and Showing Abrupt Drop to Zero	126
74. Resistance vs. B-field for Several Values of Temperatures in $\text{Y}_1\text{Ba}_2\text{Cu}_3\text{O}_7$	126
75. Hall Voltage vs. Temperature in Kelvin for $\text{Bi}_y\text{Ca}_z\text{Sr}_w\text{Cu}_t\text{O}_x$ Sample No. 1 at $B = +5$ T	127
76. Change in Resistance vs. B-field at Temperatures From Normal State to Zero-Resistance State: Up-Field Sweep 20 T in 60 s, ΔR in div at $20 \mu\text{v/div}$ Using 50 ma	128
77. Resistance vs. Temperature of $\text{Y}_{0.5}\text{Gd}_{0.5}\text{Ba}_2\text{Cu}_3\text{O}_{7-x}$	129
78. Potential ($\mu\text{v}/50\text{ma}$) vs. $1,000/T$ in Inverse $^\circ\text{K}$	130
79. Resistance vs. Temperature Data for $\text{Y}_1\text{Ba}_2\text{Cu}_{3-x}\text{Ga}_x\text{O}_{7-\delta}$	131
80. Resistance vs. Temperature for $\text{Y}_1\text{Ba}_2\text{Cu}_{3-x}\text{Ga}_x\text{O}_{7-\delta}$ at Zero Magnetic Field (Fifth Cycle)	132
81. $\text{Y}_1\text{Ba}_2\text{Cu}_{3-x}\text{Ga}_x\text{O}_{7-\delta}$ Recovery of Electrical Resistance as B-Field Is Raised From 2 to 18 at Different Sweep Rates	133
82. Reduced Data of Recovering Resistance of Superconducting $\text{Y}_1\text{Ba}_2\text{Cu}_{3-x}\text{Ga}_x\text{O}_{7-\delta}$ as a Function of Magnetic-Field Sweep Rate	133
83. Raw Data for Small Oscillations in BiSrCaCuO High- T_c Superconductor	135
84. BiSrCaCuO High- T_c Superconductor (Sample No. 2) Amplitude of Small Oscillation vs. Applied Magnetic Field	136
85. Raw Data for Recovery of $\text{Y}_1\text{Ba}_2\text{Cu}_3\text{O}_{7-\delta}$ Superconductor	140

	<u>Page</u>
86. J_c Circuit Schematic	141
87. Magnitude of Superimposed Pulse vs. Temperature for $Y_1Ba_2Cu_3O_{7-\delta}$ Superconductors	142
88. Applied Current Pulse and Recovery of Resistance With Increasing Temperature	144
89. Recovery-of-Resistance Slope vs. Temperature for $Y_1Ba_2Cu_3O_{7-\delta}$ Superconductor	145
90. Oscilligrams For Transition Into and Recovery From the Superconducting State	146
91. Recovery From the Superconducting State	147
92. Voltage Response to Short Pulse in the Superconducting State	149
93. Bar Magnet Analogue to Cooper Pairing	151
94. Coulombic Pyramidal Structure Model for Cooper-Pairing Calculation	153
95. Net Force Between Free Electron e_1 and e_2 After Displacement of Bound Holes ..	160
96. Graph of Turn-Around Conditions From Repulsive to Net-Attractive Electron-Electron Interaction, Based on Interaction With Positive Hole Cores of Bound Excitons on Four-Pyramid Cluster Having Common Base Plane	161
97. Theoretical Plot of Coherence Length vs. Temperature	164
98. Computer Screen Array of Lattice Sites in $Y_1Ba_2Cu_3O_{7-\delta}$ Structure	167
99. Display of Calculated Internal Electric Field Magnitude and Direction at (a) Cu^{2+} , (b) O_2 , (c) O_3 , and (d) O_4 Sites	167
100. Computer Calculation for Internal Field Lines at Center Unit Cell of 75-Cell Array of $Y_1Ba_2Cu_3O_{7-\delta}$ Using One-Quarter Pyramid	168
101. Internal Electric Field Lines for $Y_1Ba_2Cu_3O_{7-\delta}$ Single-Cell Probe Points in x-Direction Through Neighborhood of Cu^{2+} : Edge Effects	169
102. Comparison of Field Paths for $Y_1Ba_2Cu_3O_{7-\delta}$ With $Pr_1Ba_2Cu_3O_{7-\delta}$	170

	<u>Page</u>
103. Calculated Graph of $T^* - T_0$ vs. E_N in esu for $T_0 = 400$ K and Temperature Varying From 40 to 300 K	175
104. T^* vs. Frequency for $Y_1Ba_2Cu_3O_{7-\delta}$ [235, 236]	176
105. Dielectric Loss ϵ' vs. Temperature Reproduced From Kurtz, Bhalla, and Cross [235, 236]	177
106. Plot of Log P vs. T for Idealized Ferroelectric High- T_c Superconductor and Comparison With Experimental (Inset) Using $Gd_1Ba_2Cu_3O_{7-\delta}$	178
107. Polyhedral Building Block Units of $Y_1Ba_2Cu_3O_{7-\delta}$	179
108. Internal Electric Field Vectors in Probing Planes Perpendicular to c-Axis of Unit Cell of $Y_1Ba_2Cu_3O_{7-\delta}$ Starting With Plane Containing Upper Cu(1)-O(1)-Cu(1)-O(1) Chain and Ending With Plane Between O(4) and Base Plane of Pyramid ...	187
109. Vector Directions Near Chain Region in $Y_1Ba_2Cu_3O_{7-\delta}$	192
110. T_c (K) vs. Atomic Weight of Constituents in Nb_3 "A" Structure	200
111. T_c (K) vs. Atomic Weight of Total Constituents in V_3 "B" Structure	200
112. H_0 vs. Number of Missing Electrons to Form Stable Shell in Low- T_c Elemental Superconductor	201
113. T_c for High- T_c Materials vs. Mass of Formula Unit	202
114. T_c for High- T_c Materials vs. Number of Multi- or Single-Valence Ions	203
115. Transition Temperature for High- T_c Materials vs. Number of Holes, Due to Internal Field-Induced Neutralization of Multivalence Metal Atom	203

INTENTIONALLY LEFT BLANK.

List of Tables

<u>Table</u>	<u>Page</u>
1. Electron-Phonon Interaction Constant λ and Coulomb Interaction Pseudopotential μ^* for Some Older and Newer Superconductors	18
2. Calculations of Oxygen, Cu^{2+} , and Cu^{3+} Stoichiometries	52
3. Ionic Charge in $\text{Y}_1\text{Ba}_2\text{Cu}_3\text{O}_{7-\delta}$	55
4. Radius Ratio $[\text{R}(\text{CAT})/\text{R}(\text{AN})]$ and Coordination No.	57
5. Radius Ratio $[\text{R}(\text{CAT})/\text{R}(\text{AN})]$ and Coordination No., Including Multivalence Ions Diamagnetic in the Zero-Valence State	59
6. Substitutional Chemistry	86
7. Interaction of Electron e_2 at O (2 A) Site in Base Plane of Pyramid With Bound Hole Cores of Bound or Virtual Excitons	158
8. Summary of Theoretically Derived Properties of High- T_c Superconductivity in $\text{Y}_1\text{Ba}_2\text{Cu}_3\text{O}_{7-\delta}$	162
9. Perturbation Field at Ion Sites	170
10. Specifications of Charge Array Approximation for $\text{Y}_1\text{Ba}_2\text{Cu}_3\text{O}_{7-\delta}$	185
11. Field Moments From a Refined Charge Array Distribution at O(2) for $\text{Y}_1\text{Ba}_2\text{Cu}_3\text{O}_{7-\delta}$	186
12. Perturbation Fields Under Charge Substitution	189
13. Internal Perturbation Electric Field Calculated Using Modified Charge Magnitudes of Center Unit Cell in $7 \times 7 \times 5$ Array	194

INTENTIONALLY LEFT BLANK.

1. Introduction to Superconductivity

1.1 Early Background. The phenomenon of superconductivity refers to a state of matter that is characterized by resistancelessness to the flow of electrical charge and perfect diamagnetism or exclusion of an externally applied magnetic field. This latter characteristic of superconducting materials is referred to as Meissner Exclusion. The phenomenon of superconductivity at low temperature is among those phenomena in nature that were not predicted by theorists. Superconductivity was quite surprisingly observed experimentally for the first documented time by Onnes [1, 2] in 1911 when studying mercury under conditions of the then new technology of the liquification of He (at 4.15 K). Thus, the field of superconductivity physics was born and related in a fairly close manner to the already-developing field of superfluidity. Two years later, superconductivity was observed in lead at 7.2 K. Subsequent studies showed that many of the metallic elements were superconducting, and, in 1940, the then-record-high critical temperature (T_c) of superconductivity was observed in niobium at 9.2 K. In addition to simple elements, metallic compounds and alloys, such as A15 structures, were found to show the phenomenon of superconductivity. Also, the maximum transition temperature to the superconducting state (T_c), prior to the new oxides of the late 1980s, was observed in Nb_3Ge at 18 K. Figure 1 gives the values of T_c vs. density for the elements (designated by atomic number) and also gives the valence shell configurations. These elements are referred to as the low- T_c superconducting elements. In Figure 1, the elements that are diamagnetic at room temperature are circled in the left-hand portion of the figure. It is interesting to note the peaked behavior as a function of density. This will be discussed and explained mathematically in section 7.1, referring to the new class of superconductors with T_c greater than ~40 K and constituting the essential subject matter of this report.

The macroscopic theories of London [3] and Ginzburg and Landau [4] subsequently gave explanation, respectively, to the Meissner Exclusion effect, predicting a penetration depth λ of the applied magnetic field, and explained superconductivity in terms of an order parameter that provided a derivation of the London equations (to be treated subsequently). In the same time frame as the Ginzburg-Landau theory (1950), the effect of isotopic mass on decreasing the transition

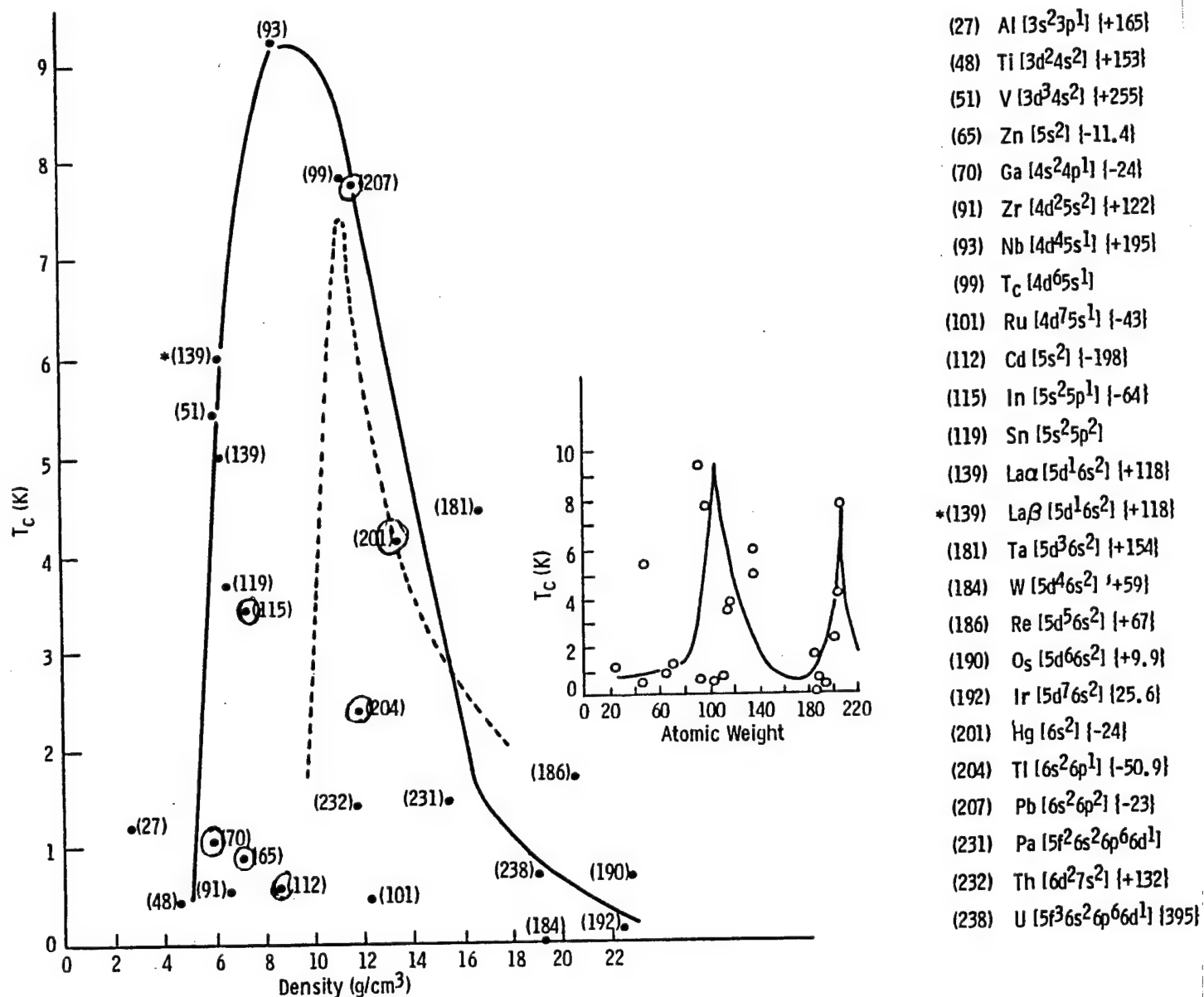


Figure 1. Conventional Low- T_c Elemental Superconductors vs. Density. (Weight Is in Parentheses; Circled Are Diamagnetic.)

temperature was predicted by Frohlich [5] and experimentally observed by Maxwell [6]. The "isotope effect" was a strong support of a mechanism of superconductivity, which intrinsically involved the lattice motion that would be affected by changes in the mass or weight of the vibrating entity, and hence involving quasi-particle phonons interacting with real-particle electrons. From this correlation, the microscopic theory of superconductivity was developed by Bardeen, Cooper, and

Schreiffer [7], which will be treated briefly in the next section and for which they were awarded the Nobel Prize in Physics. This theory (known as the BCS theory) embraces the formation of bound electron pairs (Cooper pairs) that carry the supercurrent and an energy gap needed to stabilize the superconducting state. The supporting mathematics is generally referred to as BCS formalism and appropriately explains both the earlier London and Landau-Ginzburg treatments in a convincing fashion.

At temperatures less than the transition temperature (T_c) the superconductivity of a material can be quenched (stabilized as a thermodynamic state), but the normal conductivity can be restored by the application of an external magnetic field of sufficient intensity (the critical or threshold magnetic field that is designated H_c). The effect of the critical magnetic field is shown in Figure 2 in the form of an H_c vs. T -phase diagram or, more precisely, the H - T cross section of an appropriate free-energy diagram (the H - T projection on the Gibbs surface). As deduced from the figure, H_c can be represented by

$$H_c = H_0 (1 - (T/T_c)^2), \quad (1)$$

where $H_0 = H_c$ at $T = 0$ K.

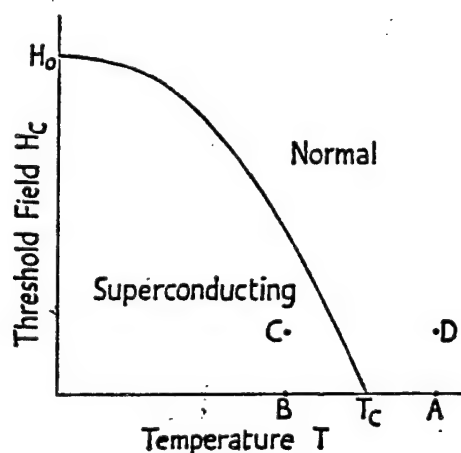


Figure 2. Magnetic Field (H) vs. Temperature (T).

Empirically, four observations have been made for low- T_c superconductors in an effort to understand the materials engineering of these substances, and, interestingly, these have some correlation or contrast with the new high- T_c superconductors (a correlation or contrast that will be described later).

These empirical observations are as follows.

- Superconductivity is observed in metallic elements for which the number of valence electrons (Z_v) is between 2 and 8 (shown schematically in Figure 3).
- In all cases involving transition metals, the T_c vs. Z_v shows sharp maxima at $Z_v = 3, 5, 7$ (also shown in Figure 3).
- Certain crystal structures for a given value of Z_v seem more favorable than others for superconductivity.
- T_c increases with a high power of atomic volume, but varies inversely with atomic mass.

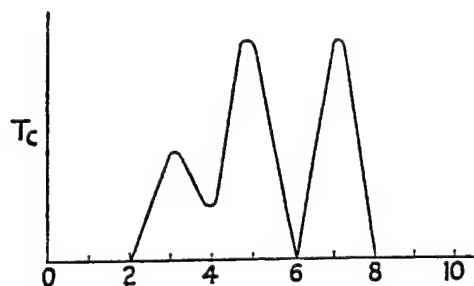
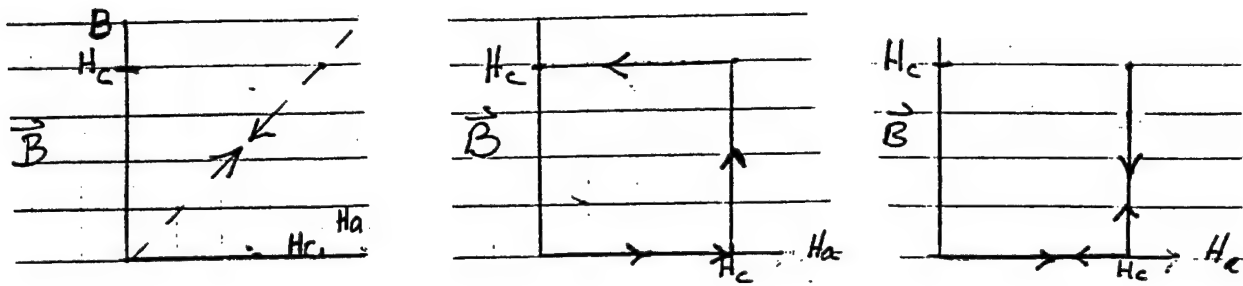


Figure 3. Superconductivity and Z_v , where Z_v = No. Valence Electrons/Atom.

A distinction should be presented here between a normal metal conductor, a perfect conductor, and a superconductor. This distinction can best be understood by examining the schematic of Figure 4. In the normal metal (Figure 4a), the magnetic induction varies directly and reversibly with the applied field. In the perfect conductor (Figure 4b), where $m dv/dt = eE$ (m = mass of carrier, v =



(a) Normal Metal Conductor. (b) Perfect Idealized Conductor. (c) Superconductor.

Figure 4. Magnetic Induction B vs. Applied Field H_a for (a) Normal Metal Conductor, (b) Perfect Idealized Conductor, and (c) Superconductor (With Axis of Long Individual Superconductor Parallel to H_a).

velocity of carrier, e = charge of carrier, and E = electric field) with no retarding term, $B = 0$ until $H_{\text{applied}} = H_c$ when it becomes normal, and $B = H_{\text{applied}}$. However, when H_{applied} then decreases, the magnetic induction within the perfect conductor is maintained at the threshold level $B = H_c$ by surface currents, and, even in zero-applied field, the material retains a magnetic current. The superconductor (Figure 4c) expels the magnetic flux, as long as H_{applied} is less than H_c , returns to its initial state with $B = 0$, and has no retained moment. If a superconductor or perfect conductor at $T < T_c$ is placed in an external magnetic field, it will prevent the magnetic flux from entering, except in a shallow surface region (Figure 5a). However, if the external magnetic field is applied prior to the reducing of temperature to below T_c , then the magnetic flux will be locked into the perfect conductor, due to induced persistent currents, even after the external field is reduced to zero (Figure 5b).

With regard to H_c , there are two major types of behavior. These differing forms of behavior are related to consequences of an applied magnetic field and identify the type-1 and type-2 superconductors, respectively. These are illustrated in Figure 6a (type 1) and b (type 2). In the type-2 superconductors (to which category the new high- T_c superconductors belong), there are actually two values of the critical magnetic field. These are designated as H_{c1} and H_{c2} . As the externally applied magnetic field (H_{applied}) increases, the magnetic flux begins to penetrate the

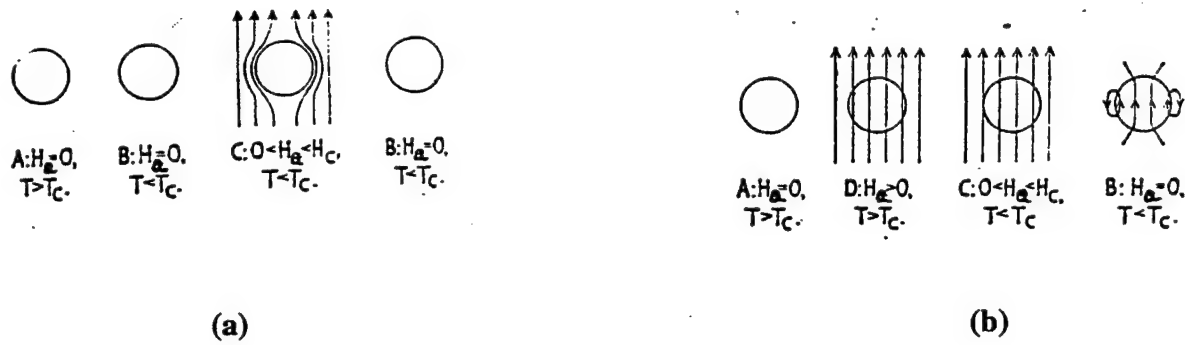


Figure 5. Flux Characteristics Related to Superconductors in External Magnetic Field.

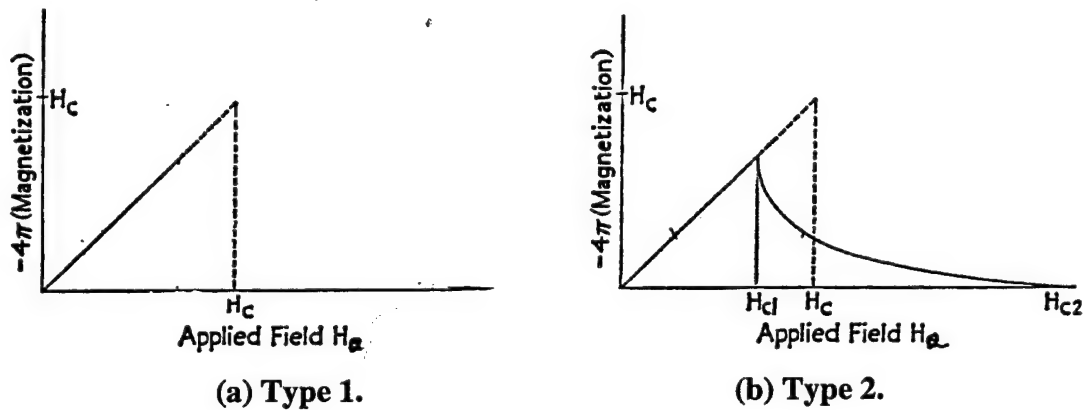


Figure 6. Applied Field H_a for (a) Type-1 and (b) Type-2 Superconductors.

material when the field reaches a value that is designated as $H_{\text{applied}} = H_c$. The field fully penetrates at a much higher field that is designated as $H_{\text{applied}} = H_{c2}$ —this full penetration then removes of all form of diamagnetism (negative magnetic susceptibility) and, thus causes the quantity $-4\pi M$ to become zero. The flux penetrates by means of quantized vortex lines about which electrons circulate to give rise to an internal B-field. These vortices favor defect sites for their positional location and can be pinned (stabilized positionally) at these sites or undergo flow or motion at high enough currents or magnetic fields. It is the motion of these vortices that is associated with the re-establishment of resistance at critical field and current conditions (critical current is discussed shortly). For the type-2 superconductor, the magnetization vanishes completely at $H_{\text{applied}} = (2)^{1/2} K H_c$, where K is the established Ginzburg-Landau constant defined through $K^2 \equiv 2e^2 H_0^2 \lambda_0^4 / \hbar^2 C^2$, where λ_0 is the empirical penetration depth in what is called the weak-field limit.

1.2 Fundamentals of the Microscopic Theory of Superconductivity Essential to Subsequent Materials Science Study of High- T_c Superconductivity. The macroscopic theory of superconductivity described the zero-resistance perfectly diamagnetic state through a second-order-phase transition. The microscopic BCS showed that this second-order-phase transition arises from the pairing of electrons (as related to a gap ΔE_g) in the ground state (to create a supercurrent) and requires a condensate wave function. The supercurrent is described by a quantum system's effective wave function having an amplitude and phase. Since the superconducting state and the normal state differ only minutely in energy ($H_0^2/8\pi$ differing only by 10–8ev/atom as compared to a typical Fermi energy of 10–20 ev), and since the superconducting state must be highly correlated (because of the absence of statistical fluctuations) involving a large system of electrons—these two statements being seemingly contradictory—the theory is necessarily fraught with demanding requirements for consistency. At higher values of T_c , corresponding to the new class of high- T_c superconductors, the welding together of these two observations into a theory is even more difficult.

The BCS theory [7] showed that the only fundamental interaction that could lead to zero electrical resistance involving phonons (as established by the isotopic effect), and thereby must involve a perturbed vibrational redistribution of an ionic or electrovalent charge density, would be an interaction of a pair of free electrons by means of the emission and absorption of a short-lived phonon. This phonon is referred to as a virtual phonon because its very short lifetime renders it an exception to the Conservation of Energy Law, due to the Heisenberg Uncertainty Principle. This exchange of a virtual phonon can be best illustrated through the schematic of Figure 7a.

In basic description, the phenomenon of superconductivity is cast in terms of a consequence of the distortion of the materials' crystalline lattice by a moving electron; this distortion is best described statistically by the emission of a quasi-particle phonon. The distortion causes a fluctuation in the lattice-charge distribution. This fluctuation propagates through the lattice. At some distance away, a second electron is perturbed by the propagating fluctuation. This perturbation is described physically by a phonon being absorbed. In Figure 7a (following the treatment of BCS [7] and Lynton [8]), a free electron of wave vector k emits a virtual phonon q , which then becomes absorbed by an electron k' . The net-scattering will result in k being decreased by q , and k' being increased

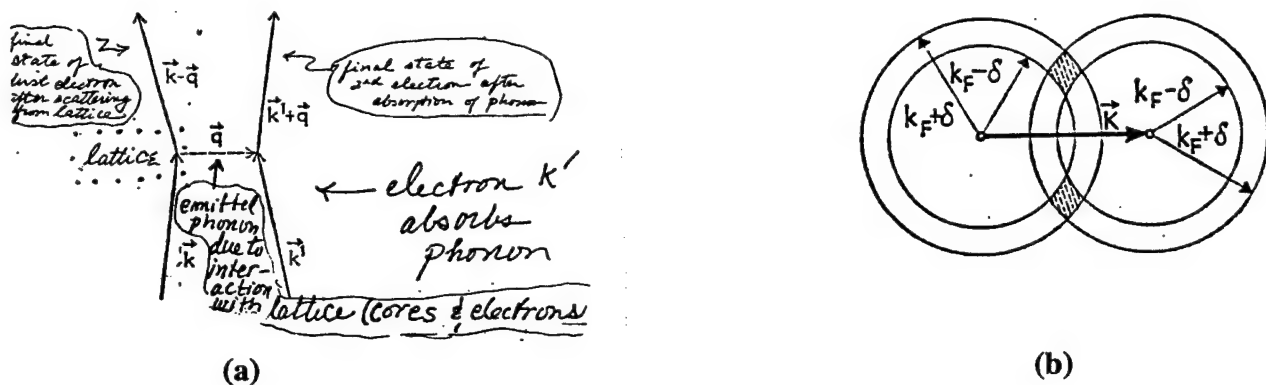


Figure 7. Exchange of Virtual Phonon.

by q . This electron-electron interaction is dependent upon the relative magnitudes of the electronic energy change $\Delta(E_e)$ and the phonon energy $(h/2\pi)\omega_q$. Then if $(h/2\pi)\omega_q - \Delta(E_e) > 0$, the interaction is attractive. From a coulombic point of view, the charge fluctuation of the lattice effectively causes one of the free electrons to be surrounded by a positive-screening charge greater than the electronic charge, so that the second electron experiences and is attracted to a new positive charge (or a region of "enhanced" positive charge). Thus, the fundamental postulate of the theory of superconductivity is that the transition to zero electrical resistance occurs when an attractive interaction between two electrons, by means of mediating-particle exchange (phonons for low- T_c superconductors), overcomes the usual or normal-screened coulomb interaction. For the new high- T_c superconductors, one would tend to hypothesize that any difference in mechanism might first be explored by studying a different mediating-particle exchange that could quantitatively lead to higher values of T_c and perhaps avoid the limitations set by the low- T_c approach, which, through the BCS theory, is unalterably linked with the Debye temperature (Θ_D).

The Debye temperature is a quantity that has the dimension of temperature; it plays a role of a characteristic temperature as related to lattice vibrations, but is actually independent of temperature, except for a slight temperature variation introduced by the variation of the volume of the crystalline unit cell and the variation of the phase velocity of the vibration with temperature. Thus, it serves a purpose mathematically similar to the Einstein temperature that relates to specific heat in crystals. Nonetheless, a dependence of T_c in any way strongly connected to Θ_D creates a limitation in the

maximum of T_c , provided that one does not break the assumptions and approximations of the formalism.

If there is a net attraction between a pair of electrons just above the Fermi surface, albeit even a very weak attraction, the two electrons can form a bound state. (The Fermi surface is a surface in momentum k -space of constant energy that encloses a volume of k -space in which the electron lies. If the temperature is at zero absolute, the electronic energy states will be occupied in accord with the Pauli exclusion principle, up to a specific Fermi energy, E_F .) The electrons that are attractively interacting in a bound state exist in a thin shell of breadth $\approx (h/2\pi)\omega_q$ for a conventional superconductor, where $(h/2\pi)\omega_q$ is of the order of the average phonon energy of the metal. (For the new high- T_c superconductors, the electron distribution should also be within a narrow shell of width $\approx (h/2\pi)\omega_q$, where ω_q is the angular frequency related to the group velocity at which work is done by the mediating particle.) The lowest energy associated with possible interactions that transform a pair of electrons from any two k values in this shell to any two other k values, restricting oneself to matrix elements of a single sign, is attained by allowing for the maximum number of possible transitions (each represented by a matrix element all of the same sign). Thus, all possible k values are associated in pairs k_1 and k_2 , and from any one set of values (k_1, k_2) , transitions are allowed into all other pairs (k'_1, k'_2) . Momentum must be conserved so that $k_1 + k_2 = k'_1 + k'_2 = K$. All bound pairs must have the same momentum K [9]. To obtain the values of k_1 and k_2 , which satisfy the previous equation and lie in a narrow shell that straddles the Fermi surface k_F , one can envision concentric circles of radii $k_F + \delta$ and $k_F - \delta$ as shown in Figure 7b. All conceivable values of k_1 and k_2 that satisfy the conservation-of-momentum equation lie in the two shaded regions of Figure 7. As K decreases, the volume of phase space available for the bound pairs under attractive interaction (Cooper pairs) increases and becomes a maximum for $K = 0$. Thus, for the most probable condition (topologically in k space), $k'_1 + k'_2 = 0$, or $k'_1 = -k'_2$, and similarly $k_1 = -k_2$. This realization gives rise to the requirement of equal and opposite linear momenta for the paired electrons. In addition, the exchange term in the wave equation analysis of this phenomenon tends to reduce the interaction energy for pairs of parallel spin. Thus, it is energetically most favorable to confine the bound pairs to those of antiparallel spin (opposite spin). Thus, at 0 K, the superconducting materials' ground state is highly correlated, and, in momentum space, the normal

electron states (in a thin shell straddling the Fermi surface) are, to the maximum possible extent, occupied by pairs of electrons of opposite magnetic spin and opposite linear momentum. Flux quantization measurements (described later) are the most direct measurement to verify the existence of these Cooper pairs.

The energy of the superconducting state is lower than the normal material by what is referred to as the condensation energy, which equals, at zero absolute, $H_0^2/8\pi$ per unit volume. Thus, a finite amount of energy is required to excite even a single normal unpaired electron when temperature is less than T_c . Thus, in terms of the single-electron spectrum, the theory of superconductivity correctly predicts a superconducting gap that influences the variation of the specific heat, thermal conductivity, absorption of high-frequency electromagnetic (EM) radiation, existence of perfect diamagnetism, and perfect conductivity in the low-frequency limit [7, 8, 9, 10].

1.3 Hubbard Bands. For a system of one-electron centers within a cubic structure, a material is normally a metal or an antiferromagnetic insulator (or ferromagnetic insulator). As shown by Slater [11, 12], an antiferromagnetic correlation (equal but opposite spin associated with each ion, typified by copper d^9 states) can cause the splitting of the conduction band, thereby creating a full and empty band and insulating general behavior. The resulting bands are known as Hubbard Bands [13]. The insulating behavior itself does not depend on the antiferromagnetic order and persists above the Neel temperature (the temperature at which antiferromagnetism breaks down). The Hubbard model is extensively utilized in theoretical studies of superconductivity to calculate density of states, coupling criteria, and general behavior. Because this model strongly relates to materials science properties and mechanistic physics, its fundamentals are treated within this introductory section.

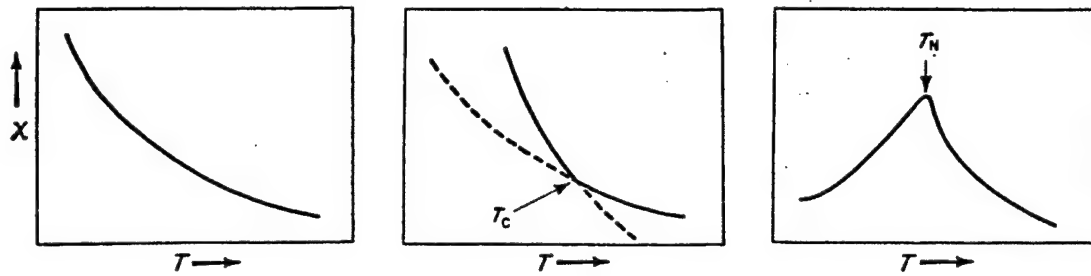
A crystalline array of one-electron centers at a distance "a" from each other, each being described by an atomic wave function $\phi(r)$, which behaves according to the form $\exp(-r/a_H)$ for large r , will admit to a tight-binding approximation for sufficiently large a . When the number of electrons per atom differs from an integral value, the Hubbard model should always predict metallic behavior, but

for an integral number of electrons per atom (including unity), the behavior will be insulating. The Hubbard intra-atomic energy U is defined by Hubbard [14]

$$U = \iint (e^2/\kappa r_{12}) |\phi(r_1)|^2 |\phi(r_2)|^2 d^3x_1 d^3x_2 \quad (2)$$

When κ is the background dielectric constant for hydrogen-like wave functions, $U = 5e^2/8\kappa a_H$. If the functions ϕ are not changed by the addition of an electron, and if " ι " is the ionization potential of each atom, and " ξ " is the electron affinity of each atom, then $U = \delta - \xi$. There are four major properties of such a system that relate to either low- T_c or high- T_c superconductors.

- (1) For large " a " (small overlap energy integral I), the system is antiferromagnetic with an energy below that of the ferromagnetic state equal to $-2zI^2/U = -\beta^2/2zU$, where β = bandwidth without distortion. The Neel temperature, above which antiferromagnetism disappears (see Figure 8), is of the aforementioned order.
- (2) An additional electron placed on one of the atoms is permitted to move with a κ vector just as in a simple normal band and has an energy in the upper Hubbard band. This electron will polarize the spins on surrounding atoms antiparallel to itself, provided the atomic orbitals are nondegenerate, or parallel to itself if the atomic orbitals are degenerate, thus forming a spin polaron. The bandwidth of this electron is $\sim\beta$ when the latter is calculated without correlation.
- (3) The hole that is formed by extracting an electron from one atom has similar characteristics, being permitted motion with wave vector κ and having a range of energies similar to β . The electrons in these singly occupied states are considered to be in a lower Hubbard band; however, it is more convenient to visualize a band of holes.
- (4) The two bands will overlap when " a " is sufficiently small, and β is large enough, such that $\beta \geq U$. Under this condition, an insulator \rightarrow metal transition occurs, often referred to as a Mott or Mott-Anderson transition from an antiferromagnetic insulator to an



(a) Simple Paramagnetism. (b) Ferromagnetism. (c) Antiferromagnetism.

Figure 8. Diagrams Indicating the Qualitative Temperature Dependence of Magnetic Susceptibility for (a) Simple Paramagnetism, (b) Ferromagnetism, and (c) Antiferromagnetism.

antiferromagnetic metal. As the overlap increases, and the number of free carriers (n) increases, the moments on the atoms and the Neel temperature will decrease and eventually vanish when $n = (1/2)z$. This is illustrated in Figure 9 and Anderson [15] and Mott [16, 17].

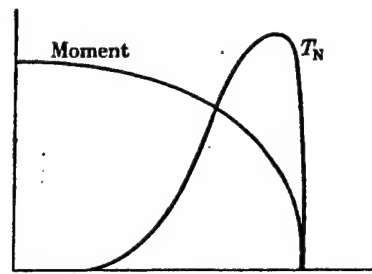


Figure 9. $\beta \geq U$ Overlap.

Property (4), previously discussed, indicates that there may be two transitions associated with the Mott transition; however, the range of the antiferromagnetic metal may be absent. When the conditions are such that the magnetic moments vanish, the electron gas has become highly correlated [18, 19]. Thus, only a small proportion of states (or sites) is doubly occupied or unoccupied at any one instant. The electron spins on the remaining sites are then no longer oriented antiferromagnetically, but rather quantum-mechanically resonate between their two positions, as shown in Figure 10. The band is no longer split into two Hubbard bands, and there is a large enhancement of effective mass that gives rise to large values of Pauli susceptibility and electronic specific heat. An example of a system in which the properties differ dramatically, depending upon the precise electron and hole configuration, is observed in the T - x -phase diagram of $\text{NiS}_{2-x}\text{Se}$ and reproduced in Figure 11.

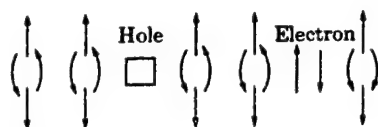


Figure 10. Resonating Moments in a Highly Correlated Electron Gas.

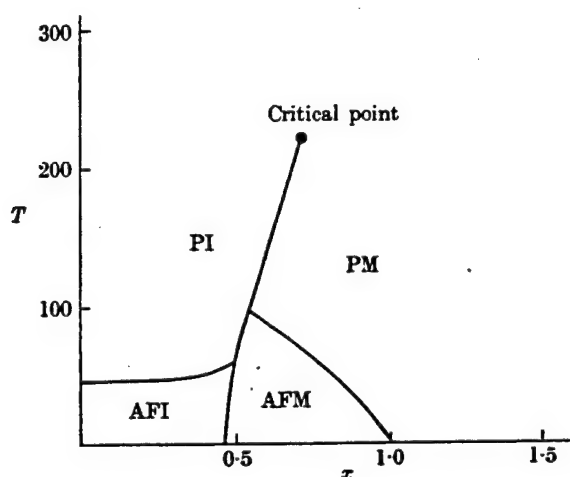


Figure 11. T-x-Phase Diagram of $\text{NiS}_{2-x}\text{Se}$.

1.4 The State of Perfect Diamagnetism. Perfect diamagnetism in a substance that refers to a diamagnetic state (negative susceptibility), which completely and entirely expels magnetic lines of force from the substance. In the past, it has been unclear as to whether perfect conductivity or perfect diamagnetism was the fundamental property of a superconducting material, and if one of these properties necessarily gave rise to the other. Because the new class of superconductors (the high- T_c oxides) has a strong relationship to diamagnetism in its crystal physics behavior, it is important to describe the perfect diamagnetism of conventional low- T_c superconductors in some detail. It is necessary in this manuscript to furnish background that has led to an understanding of the magnetic properties of cation constituents of the high- T_c materials, and has thereby led to materials engineering of new high- T_c substances.

The attributing of the diamagnetism in superconductors to electron currents, rather than spins for example, is demonstrated by a superconductor's gyromagnetic ratio (ratio of magnetic moment to angular momentum), which is observed to have the value $g = -e/2 mc$. Thus, the vanishing of the

magnetic induction (B) in the interior of a superconductor must be related to induced surface currents. In the presence of an externally imposed magnetic field, the intensity and distribution of this surface current creates an opposing interior field (or a shielding field as inferred from Lenz's Law) that cancels out the applied field. The changing magnetic field, ranging from zero to its final value, then induces a current in a closed circulating-loop electron path that gives rise to the magnetic moment that opposes the external field. In a normal nonsuperconducting state, the induced current is soon damped out by the resistance or scattering suffered in the circulating loop. However, in the absence of electrical resistance, the induced and opposing moment persists as long as the magnetic field remains unchanged. Since the electrons move in an unimpeded manner in an atom (viewing the atom as a microscopic conductor whose isolated electrical resistance is zero), and, since in a superconductor, the sea of free electrons bathing individual atoms (and relating them to each other) does not suffer electrical resistance, the degree of diamagnetism in the superconductor would be expected to be, and indeed is, complete and total. Thus, the states in the Hubbard model that, after overlap of the bands, are neither unoccupied or doubly occupied and are resonating, will become aligned opposite to the external field, provided they are resistanceless.

This description effectively treats the superconductor in the presence of an external magnetic field as a magnetic body with an interior field and magnetization, such that, (1) in the interior,

$$B_i = 0, \quad (3a)$$

H_i and M_i are different from 0; (2) at the surface (s)

$$J_s \quad (3b)$$

is different from 0; and (3) outside,

$$B_a = H_a + H_s, \quad (3c)$$

where H_s is the field that is due to the magnetization of the sample, and the letter "a" refers to "applied."

Since $B = H + 4\pi M$, this treatment becomes equivalent to attributing to the superconductor a magnetization per unit volume $M_i = -(1/4\pi)H_i$, which indicates that the superconductor has the ideal diamagnetic susceptibility $-1/4\pi$.

Polarization of a more or less permanent persistence can be established in ferroelectric materials by several processing techniques, including by melting then solidifying in a strong electric field, thereby forming what are called electrets. (The permanent dipoles become oriented in the molten state, and the orientation is retained or "frozen" upon solidification.)

Permanently polarized entities, such as electrets or regions of internal charge separation due to high internal electric fields (to be treated in the next section), experience forces and torques that can be calculated from $E = \int_{\tau} E' \rho_p d\tau$, where $\rho_p = -\nabla \cdot p$, and E' is the electric field at $d\tau$ that is obtained by neglecting or ignoring the field of the electric dipole (p) itself. The electric field produced by a permanently polarized entity is the vector sum of the fields provided by all of the individual dipoles of the dielectric.

In a nonuniform electric field, there is a net force on the internal dipoles (created by the internal electric field and charge-transfer excitations) given by $F = \nabla (E \cdot p)$ where p = dipole moment of the separated charges, and E = an electric field in the domain of which the dipole exists. Since p is constant, then the net force is proportional to the gradient of that component of E that is parallel to the positive direction of p . In the $Y_1Ba_2Cu_3O_{7-\delta}$ superconductor, that direction is z . The resulting force then points in the direction in which this component of E increases most rapidly.

Thus, the net result in highly nonuniform fields can be rapidly circling electrons, such as individual circulating loops, insulating with respect to each other, but not with respect to themselves.

Interestingly, the negative magnetic polarizations of diamagnetic materials (such as the perfect diamagnetism of superconductors) can be understood if one envisions a loop of material with the same zero electrical resistance and attempts to establish a magnetic field therein. From Lenz's Law, the current that is induced in such a loop would be in a direction to prevent the establishment of that magnetic field. The resulting current loop would represent a magnetic dipole acting in the direction opposite to the applied B-field. An array of such loops then represents a diamagnetic material. This reasoning suggests the coexistence of superconductivity (resistancelessness) and diamagnetism (negative magnetic polarization). The orbital electrons in completely filled atomic shells behave very similar to nonresistive circulating current loops. The application of a B-field perturbs their orbits to some degree, such as to oppose the applied field (the new orbital motion remaining until B changes again). However, in the absence of the applied magnetic field, the orbital electrons have no net magnetic moment. The resulting (negative) diamagnetic susceptibility is not significantly temperature-dependent.

Thus, polar electret-like behavior in ferroelectrics and perfect diamagnetism in largely ionically bonded superconductors (such as high- T_c oxides) have some degree of commonality. The associated large dielectric constants of ferroelectric materials may provide a means or channel for an enhanced electron-pairing interaction. This correlation then seems to be another link between microscopic ferroelectricity and high- T_c superconductivity. It is shown in this document that, when all the links between high- T_c superconductivity and ferroelectric materials are woven together, a strong argument can be cast for high- T_c materials being a form of relaxor ferroelectrics.

1.5 The Role of Temperature and T_c for Low-Temperature Conventional Superconductivity. Since the number of collisions between charge carriers and the lattice (including the lattice irregularities, these collisions being the limiting factor regarding the current dq/dt) is proportional to the temperature, it is understood that the conductivity " σ " varies at T^{-1} , which is true in rough approximation for most materials above Θ_D , the Debye temperature, $((h/2\pi)\omega_{\max}/\kappa)$. As temperature becomes lowered, the crystal vibrations dampen out rapidly, and, in this temperature range, σ increases with decreasing T more strongly than T^{-1} . However, the temperature variation in this range may be influenced by crystal irregularities that are consequences

of causes other than thermal transport [20, 21]. The magnitude and frequency of crystal vibrations have a strong effect on the delicately balanced condition at which the phonon-induced cloud of positive charge surrounding one of the to-be-paired electrons has a larger magnitude attractive interaction with the other to-be-paired electron, as compared to the two electrons' mutual-screened repulsion. Since the structural and material properties of the crystal intimately affect the vibration level, it is not surprising that different materials have fairly widely differing values of T_c .

An expression for T_c must necessarily relate to the electron-electron net attractive potential $V(\omega)$, such that $V(\omega) = V$ for electron energies within the range $\epsilon_F \pm E_D$ of the Fermi energy E_F (where E_D is a limiting energy, which, for phonon-electron coupling, is equal to the Debye energy $\kappa_B \Theta_D$ characteristic of the lattice vibration). Outside of the range (or shell) $E_F \pm E_D$, the potential V is taken as zero [22].

To obtain the expressions for T and the superconducting energy gap, a transcendental integral equation must be solved. The solutions yield

$$T_c = 1.134 \Theta_D [\exp(-1/\lambda)], \quad (4a)$$

and

$$E_g = 4 E_D [\exp(-1/\lambda)], \quad (4b)$$

where $\lambda = V[N(E_F)]$ is the electron-electron interaction referred to as the electron-phonon-coupling constant (dimensionless), and $N(E_F)$ = density of states at the Fermi level. These two criteria, λ and $N(E_F)$, from the physics standpoint, specify the state of superconductivity for a given Θ_D . Table 1 gives values of λ for both the low- T_c and the new high- T_c compounds and shows that λ tends to increase as T_c increases. The universal dimensionless ratio that typifies low- T_c superconductors is written as $E_g/\kappa_B T_c = 3.528$ and is obtained by dividing equation (4b) into equation (4a).

Table 1. Electron-Phonon Interaction Constant λ and Coulomb Interaction Pseudopotential μ^* for Some Older and Newer Superconductors

Material	T_c (K)	λ	μ^*
Ru	0.49	0.47	0.15
Zr	0.61	0.22	0.17
Os	0.66	0.44	0.12
Mo	0.92	0.35	0.09
Re	1.7	0.37	0.1
V ₃ Ge	6.1	0.7	—
Pb	7.2	1.55	0.6
Pb-Bi Alloy	9	2.13	—
Nb	9.3	0.85	—
NbC	11.1	0.61	—
TaC	11.4	0.62	—
Ba(Pb, Bi)O ₃	12	1.3	—
V ₃ Si	17.1	1.12	—
Nb ₃ Sn	18.1	1.67	—
Nb ₃ Ge	23.2	1.80	—
LaSr*	18	1.2.2.4	0.12
LaSr(0.1)	27	1-2	—
LaBaCuO	30-40	2.5	0.1
LaBa (0.05 ≤ x ≤ 0.15)	30-40	≥2	—
LaSr (0.05 ≤ x ≤ 0.15)	30-40	≥2	—
LaSr*	35	~2.0	0.2
YBa*	—	≤0.3	—

When the repulsive screened coulomb potential V_c is considered via pseudopotential calculations, the expression for T_c becomes

$$T_c = 1.14 \Theta_D \exp[-1/(\lambda - \mu^*)], \quad (5a)$$

where μ^* is the Coulomb interaction pseudopotential given as

$$\mu^* = \mu/[1 + \mu \ln(E_F/E_D)], \quad (5b)$$

and μ = Coulomb constant = $\langle V_c \rangle N(E_F)$, where $\langle V_c \rangle$ = expectation value. The values of μ^* are also listed in Table 1.

A further sophistication that involves the electron-phonon coupling of strength $\alpha(\omega)$ relates to averaging over the phonon density of states $D(\omega)$ to yield the Eliashberg expression [23, 24, 25],

$$\lambda = 2 \int_0^\infty \alpha^2(\omega) D(\omega) / \omega d\omega. \quad (6a)$$

The semi-empirical formula was then given for T_c by McMillan [26],

$$T_c = \Theta_D \exp[-1.04(1 + \lambda)/(\lambda - \mu^*(1 + 0.62\lambda))]. \quad (6b)$$

1.6 Predictions of the BCS Theory of Superconductivity. From the previous sections, the following predictions of the BCS theory can be extracted.

- If the superconductor has an energy gap, then that gap is related to the critical-transition temperature via the expression $E_G = k_B T_c = 3.528$.
- The state of perfect diamagnetism exists at $T < T_c$ with $\chi = -1/4\pi$.
- T_c is related to the Debye Temperature, Θ_D , the electron-phonon coupling constant λ , and the density of states at the Fermi surface $N(E_F)$.

- Magnetic flux that penetrates the superconductor at $H > H_c$ is quantized with the value $\phi = hc/2e$. This is a consequence of the London equations.
- For a phonon-electron coupling, the transition temperature is affected by the average isotopic mass according to $T_c \propto M^{-\alpha}$, where $\alpha = 1/2$ for a simple phonon-electron model.
- The electronic contribution to the specific heat suffers a discontinuity at T_c given by $(C_s - C_n)/C_n = 1.43$, where s = superconducting, n = normal, and $C_n = \gamma T_c$.

These predictions of the BCS theory formalism are listed not only for the purpose of summarizing the essential elements of what the theory means in terms of measurables, but also to determine later on whether the properties of the new high- T_c materials subscribe to these predictions, and, if not, then what deviations or modifications of the theory are necessary to describe the new compounds from the standpoints of superconductivity physics and materials science.

1.7 The Critical Current Density J_c . The critical current density (J_c) refers to that current density, $(dq/dt)/A$, where q = charge, t = time, and A = area, above which the superconductor is no longer resistanceless and will thus support a real (nontrivial) electric field. The critical current is actually a measure of the kinetic energy (KE) that will break the Cooper-pair bond, and destroy the bound paired state. The value of J_c can be measured by determining the circuit current that will lead to a small voltage drop (typically 1 μ V) induced across a sample using a four-probe resistivity measurement (in which no charge flows through the sample region d between the voltage probes). Alternatively, J_c can be measured by use of a magnetization vs. magnetic field hysteresis loop via the expression $J_c = 30\Delta M/d$, where ΔM = hysteresis of M/vol in emu/cm^3 . This expression shows that J_c is a consequence of H_c and will be influenced by the applied magnetic field (see Figure 12) [27, 28]. Since the resistivity of superconducting states is effectively about $10^{-23} \Omega - \text{cm}$, critical currents in bulk materials can be upward of $10^5 \text{ A}/\text{cm}^2$. Because the critical current can arise from the motion of magnetic flux (magnetic lines of force) through a superconductor, it is thus favorable to prevent this fluxoid motion in the material by introducing defects that will pin or immobilize this flux motion at structural centers.

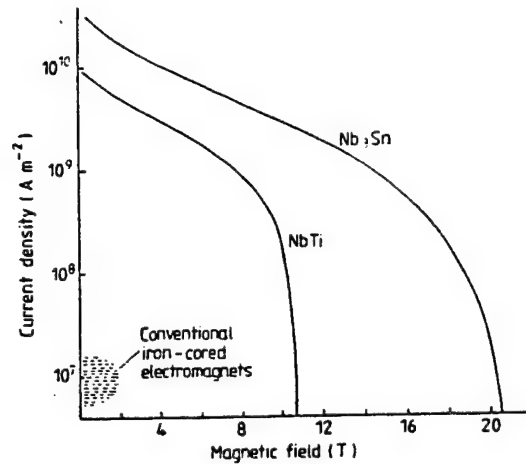


Figure 12. Applied Magnetic Field.

The mechanism giving rise to critical current density in a superconductor must necessarily involve the KE of the Cooper-paired electrons. For small values of the momenta of a Cooper pair, the current density is proportional to the momenta (P). In general, the current density (J_c) is proportional to the rate at which the free energy changes as a function of the momenta of a Cooper pair [29]. As the free energy of the superconducting state approaches that of the normal state, the current density, as a function of momenta, falls to zero, and the transition to the normal state occurs. Conceptually, when the KE associated with a Cooper pair exceeds the Cooper-pairing energy, J_c is achieved, and the transition to the normal state must occur. In low- T_c superconductors, this energy is the gap. The coherence length is then the distance over which electrons are Cooper-paired prior to undergoing pair scission for any reason whatsoever. This is a relatively high number in low- T_c materials ($\sim 2,000$ Å) and suggests local atomic behavior. The meaning of J_c can be more easily seen quantitatively by relating to crystal momentum, entropy, and T_c as follows [30].

$$J_c(t) = \alpha' dG/dp, \quad (7)$$

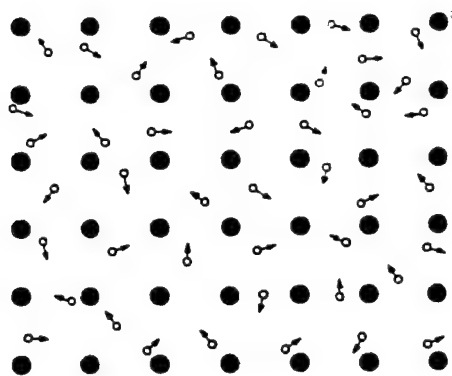
where J_c = critical current density, G = Gibbs free energy, p = crystal momentum of Cooper-pair, α' = constant, $G = U - TS + PV$, $\Delta G = \Delta U - T\Delta S + P\Delta V$, $E = J/\sigma$ (U = lattice energy, T = temperature, P = pressure, V = volume, S = entropy, $v/d = E$ = electric field, and $\sigma =$

conductivity), v = voltage, and d = interelectrode spacing. The voltage accepted by the superconductor upon rewarming from 77 K at a given T is

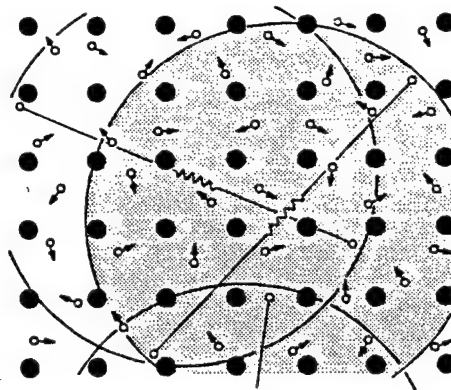
$$\begin{aligned} V(T) &= (d/\sigma(T))(J_{v,T} - \alpha' dG/dp) = (d/\sigma(T))(J_{v,T} - \alpha' \Delta G/\Delta p) \\ &= (d) \rho_{(T)} (J_{v,T} - \alpha' (\Delta u - T\Delta S)/\Delta p). \end{aligned} \quad (8)$$

From this relationship, it can be proven that the lower the change in entropy relative to the wave vector, k , the higher J_c at a given temperature. It can also be proven that the higher the group velocity of the pilot waves that represent the carrier particle, the greater J_c at a given temperature. Realizing that at $T = T_c$, $J_c = 0$, leads to $T_c \approx (dp/dS)v_g$, where v_g is the group velocity or the velocity at which carriers can do work.

The entropy relationship helps conceptualize the notion of a finite intraelectron distance over which the pair can exist as a bound state. Critical magnetic fields and critical currents will cause increased entropy and attack the pair (via magnetic moments and KE, respectively). Statistical fluctuations will also cause pair scission, but if $H < H_{c1}$, and $J < J_c$, then other pairs will form to replace the statistically dissipated pairs, thus yielding the notion of a Cooper-pair transient lifetime (which is about 10^{-12} s). Thus, the highest values of T_c should occur for a material whose crystal momentum undergoes the most increase for the least change in entropy and whose group velocity of the carrier wave envelope is maximum so that the electron-phonon interaction is enhanced. Figure 13 gives an illustration of superconducting Cooper pairs [31, 32] and of normal-state electrons, and helps to visualize how a slight difference in entropy (disorder) can lead to a major difference in correlation and linear momenta. Figure 13 also shows how pairs can interpenetrate each other and undergo statistically dependent scission and formation.



(a) Normal-State Electrons.



(b) Superconducting Pairs.

Figure 13. Illustration of (a) Normal-State Electrons and (b) Superconducting Pairs.

2. Theoretical Basis for Research Into High- T_c Superconducting Materials.

2.1 Metallic Hydrogen and Excitons. The discipline of high-pressure physics has, for many decades, studied insulator \rightarrow metal-phase transformations in solids. The effect of high compression to reduce interatomic spacing and to increase time-independent perturbations can cause an overlap in energy bands, and thereby create a metallic state from an insulating or semiconducting gap state. In the case of hydrogen, the state-of-the-art theory suggests a pressure-induced transition to a metallic solid phase at between 2 and 4 Mbar (2–4 million atmospheres). Furthermore, sophisticated theoretical studies suggest that this metallic-atomic phase should be a superconductor at very low temperature.

Under the regime of electron-phonon interactions as the superconducting mechanism, a metallic state of atomic hydrogen (H, not H_2) would constitute with its one proton and one electron, ideally, the simplest of all superconducting systems. The polarization or distortion of the solid-state array of hydrogen atoms, single-valence electron and single-proton core would create a change in total charge distribution as in the BCS theory and would be influenced simply by the mass of the proton and an analogy to the Θ_D . As shown earlier, $T_c \propto M^{-\alpha}$, one might envision elevating T_c by making analogy to the condensed hydrogen lattice with an alternate sublattice or quasi-lattice, which was

similar in every way excepting substituting a particle of lower mass (lower M , hence, higher $1/M$) for the comparatively heavy proton particle.

A detailed Soviet literature [33–38], appearing mostly in the 1960s, treated an underlying belief that high- T_c superconductivity could exist if a transition occurred to a new excitonic phase, which itself was characterized by a spontaneous current. At about the same time period, the work of Little [39] at Stanford in the United States developed a description of an excitonic mechanism for one-dimensional (1-D) superconductors.

These mechanistic themes suggested that at a large difference in mass (m) between electrons and holes, a special-ordered excitonic phase or excitonic system could be created. The exciton (unrecombined electron-hole pair, moving through the lattice, or bound, as an entity) would then be very similar to the hydrogen atom, provided the spectra of electrons and holes is isotropic. The condensed excitonic phase would develop somewhat akin to solid-state phases of hydrogen: molecular liquid \rightarrow molecular crystal \rightarrow metallic crystal. In an excitonic phase, the mass of the hole, instead of the much heavier mass of the proton, will be the governing phenomena when calculating any mass-influenced property. Then the vibration frequencies for the exciton sublattice will be larger than the hydrogen lattice by the factor $(m_H/m_h)^{1/2}$, which is approximately 10 (where H = hydrogen atom, and h = hole).

In hydrogen, the transition H^2 (molecular) \rightarrow $2H$ (metallic) requires several megabars of pressure. However, in the exciton subsystem, the role of pressure is fulfilled by the altering of the valence and conduction band configurations (and altering the energy gap between the bands) through the spontaneous formation of excitons (the structure of which shows a hydrogenic orbit of the excited electron relative to its "wake" hole). The exciton is normally created by the incidence of light, such as infrared (IR) radiation. However, excitons can also be created by charge-transfer excitations in compounds, which are composed of constituent ions, which admit to more than a single-valence state (such as the copper ion, which can take on the charge states $+1$, $+2$, or, in some cases, $+3$). Thus, the theory suggested researching materials for which, as the temperature is lowered, the energy gap E_G between valence and conduction bands (which is a function of the five thermodynamic variables

of temperature, pressure, electric field, magnetic field, and composition) undergoes, via some localized overlap phenomenon, a collapse to zero magnitude. The initial theory suggested that excitons would be produced when the forbidden gap is reduced to $E_G \approx m_e e^4 / 2\epsilon_0^2$ (where m_e = mass of the electron, and e = charge of the electron), but that the concentration of excitons does not change substantially until overlap conditions occur at $e^2/\epsilon_0 v_e = e^2 m_e/\epsilon_0 p_0 \leq 1$, where p_0 is the limiting Fermi momentum given by $p_0 = (2m_e (E_V - E_C))^{1/2}$, where E_V and E_C are the valence- and conduction-band energies. Then, the Fermi velocity becomes $v_f = [2(E_C - E_V)/m_e]^{1/2}$. Relative to superconductivity, the upshot of this early line of reasoning is that the most effective electron interaction mechanism is the exchange of exciton-lattice vibration quanta. From the BCS theory, T_c can be written as $T_c \sim \omega(2p_0) \exp(-1/\lambda)$, where $\lambda \sim (e^2/m_e)/\epsilon_0 p_0 \leq 1$ in the metallic region. With increasing overlap, the valence band moves into the conduction band ($E_{V_{max}} > E_{C_{min}}$), and then λ increases because of decrease in p_0 and increase in the reduced effective mass m_e^* . For minimal overlap conditions, the maximum attainable critical temperature, implied by the previous approach, is attained at $\lambda \sim 1$. Thus, $T_c(\text{max}) \sim m_e e^4 (m_e/m_h)^{1/2}/\epsilon_0^2$. Assuming a typical $m_e \approx 0.2 m_0$, where m_0 = rest mass of the electron, with a value of ϵ_0 from 1 to 3; then $m_e/m_h \approx 0.01$, and $T_c(\text{max})$ is predicted to be about 200 K (using the excitonic-coupled mechanism).

The exciton theory has more recently been reformulated to accommodate some potential pitfalls [40] and can be supported as a possible operative mechanism by the Eliashberg theory referred to earlier [22–25, 41, 42]. If the phonon excitation energy E_D in equation (5a) is replaced by the larger electronic excitation energy E_e , then T_c should increase significantly. Physically, the exciton viewpoint was initially invoked by Little [39] to treat polymeric materials in which a conduction electron associated with charge transport along a main chain (or spine) within a structure will induce a perturbation of charge associated with a side chain. This perturbation of charge in the side chain, leaving a region of deficient negative charge, could then be attractive to a second conduction electron in the local vicinity a short time later. The credibility of an excitonic-based mechanism in a given superconducting material depends to a great measure upon the observation of a sharp absorption peak in the mid-IR through the ultraviolet (UV) spectral regions (0.1–3.5 eV). The spectral response will be discussed in the upcoming experimental sections of this report, where such mid-IR absorption will be documented. The exciton can be of the short-range Frenkel-type or of the long-range

Wannier-type. The electron constituent can also oscillate at such a high frequency that the exciton can be so short-lived as to violate conservation of energy and thus be a virtual particle.

2.2 Other Nonphonon-Based Mechanisms.

2.2.1. Plasmons. The plasmon is a quantum of plasma oscillation that has properties akin to a charged gas when condensing to a charged liquid. As such, it can participate in strong coupling with the phonon system and thus be a candidate for a high- T_c bosonic mechanism [43–51]. "Boson" refers to a particle whose velocity may be the same as other particles of the same kind (contrasting a Fermi-ion) and one that also obeys Bose-Einstein statistics. There indeed exists IR evidence for plasmons [52]. The plasmon is a collective excitation that is supported by the itinerant-electron system. For low-momentum conditions, the plasma frequency that is associated with its energy is $\nu_p = (4\pi ne^2/m)^{1/2}$, where n is the average electron density. The plasmon is a temporal oscillation (not a spacial oscillation) in the density of the fluid of itinerant electrons. The origin of the plasmon is rooted in itinerant electrons of high mobility, compared to that of an ion, and in the long range of the coulomb interaction between them. (The electron responds by a factor of 1×10^2 faster than the ion.) The interaction, which could lead to superconductivity at temperatures much higher than the T_c of conventional compounds, can arise between copper 3d and oxygen 2p bands. As temperature increases, the subsequent breaking of Cooper pairs is a consequence of inelastic electron-phonon and electron-electron scattering processes. These lead to a suppression of T_c relative to the energy gap and give rise to values of E_g/kT_c larger than the BCS value of 3.5. The itinerant electrons in a metallic regime tend to act in a manner to maintain charge neutrality. A longitudinal phonon can cause a concentration disturbance in the otherwise uniform distribution of positive charge by the process of displacing ions. The electron cloud will then quickly enter the positively charged region in order to restore charge balance locally. This is a type of screening effect because the electrons will move (oscillate) in phase with the ions and, hence, screen any local variations in charge density. The range within a metallic state at which the local force attracting the screening electrons overcomes the thermal energy of the electrons is the Debye length. The electrons that rush into the region of excess positive charge acquire KE in the process and, thereby, because of the velocity term, overshoot the target, are attracted back, then again, overshoot, etc. The entire sea of itinerant

electrons oscillates back and forth, but out of phase with ions. A system that includes localized magnetic moments can also undergo collective excitations, which will be described later in treating spin density waves. However, systems that contain localized electrical moments (permanent dipoles) do not support collective excitations thereof. Hence, the effect of the local dipoles must be in terms of an internal electric field (also to be treated later) in which there exists at most microscopic ferroelectricity rather than macroscopic ferroelectricity. In summary, the emission of a plasmon and the subsequent absorption of a plasmon are perturbations that can cause superconductive Cooper pairing [53].

2.2.2. Polarons and Bipolarons. The concept of polarons (Figure 14) can be traced to early work by Landau [54] who introduced the idea of the self-trapped electron in an effort to explain F-centers in crystals. The notion was that an electron, through its coulomb interaction with the ions of an ionically bonded crystal, produces a polarization that constitutes a potential "hole" surrounding the electron. The hole then becomes trapped or bound in the net potential. The effect may be described by comparing the field energy of an electron (considered as a rigid-charge distribution) in a dielectric medium ($\epsilon > 1$) with that in vacuo ($\epsilon = 1$). The binding energy of the electron in the dielectric medium is

$$\epsilon(\epsilon \neq 1) - \epsilon(\epsilon = 1) = \int [(D^2/8\pi)(1/\epsilon - 1)] \delta\tau < 0 \quad (9)$$

because $\epsilon > 1$, where D = displacement current. The model then predicts a binding effect; if a rigid charge is considered to move through a lattice and carry its potential with it, then, when neglecting optical resonances (which are of low magnitude and in the absence of magnetic and radiation effects), the polarization caused by the moving electron is

$$P = (1/4\pi)(1/\epsilon_\infty - 1/\epsilon)D \equiv (1/4\pi E)D, \quad (10)$$

where ϵ = static dielectric constant, and ϵ_∞ = high-frequency dielectric constant. The size of the polaron actually refers to the extent of the coulombic potential (as shown in Figure 14). The

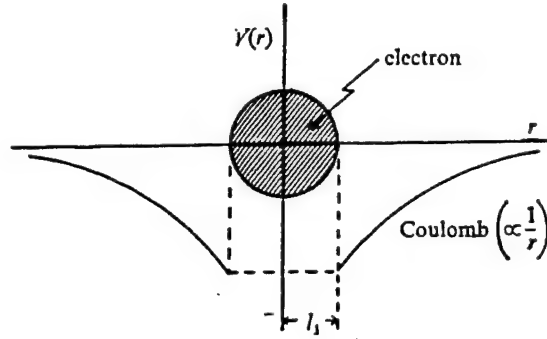


Figure 14. Size of the Polaron.

potential is approximately the coulomb energy of a total charge "e" distributed over a sphere of radius l_1 and is of the order $-e^2/\epsilon' l_1$, where ϵ' refers to an averaged value over the distribution. The KE is $(\hbar k/2\pi)^2/2m$, where k is the wavenumber of a system that is confined to a region whose spatial domain is of order l_1 . Then, calculating the total energy and differentiating to find the value of l_1 for minimum energy U , yields $l_1 = 4\pi^2(\hbar/2\pi)^2\epsilon'/me^2 = \text{size of the polaron}$, and $U \sim -me^4/8\pi^2(\hbar/2\pi)^2\epsilon'^2$. Interestingly, the polaron theory was further developed by Froilich [55] to apply field theoretic concepts as a preliminary investigation of the mechanism of superconductivity through the notion of the field of lattice displacements (polarization field). This line of thinking at that time (as early as 1937) led to the phonon-coupling theory of superconductivity. However, a polaron-based theory can be developed by realizing that retardation effects on the longitudinal optical phonon exchange between two polarons are attractive.

A bipolaron is an exciton-like system where the two particles are of the same sign (both being polarons). In the limit of a static lattice, yielding a sufficiently strong electron lattice interaction, the binding between the two electrons (that produce the two polarons) can occur. Each electron can interact both with its own well and with that produced by the other electrons (the wells overlap). The motion of the two electrons must be well correlated, and the KE of the lattice is a very important factor because the binding criteria of the bipolaron are so sensitive [56]. Large bipolarons can only be produced in multidimensional ionic materials with highly displaceable ions ($\epsilon_j/\epsilon_\infty \gg 2$), such as ferroelectric-like materials with long-range electron-lattice interaction (such as oxides), and less than three-dimensional (3-D) electronic dimensionality, such as layered materials [57]. Superconductivity

associated with bipolarons demands a fluid ground state and a sufficiently large concentration of bipolarons. Aleksandrov, Grebenev, and Mazur [58–63] cite papers on bipolaron-based interpretations of superconductivity. However, the mechanism of the coupling with conduction electrons is similar to phonon coupling, except with a longitudinal optical frequency of 2×10^{14} Hz (because displacement of heavy ions is replaced by charge displacement, and the heavy ions will not return to their equilibrium position during a half period of the electrons motion in the trapping potential). It follows clearly that if the polaron or bipolaron is excited by a conduction electron, then that polaron system will cause the propagation of a new charge redistribution, such that a second electron will be perturbed by this repropagation. The spin polaron is a special polaron case that involves the motion of holes on an anion sublattice and induces spin deviations at cation sites that would normally be associated with antiferromagnetic correlations. These spin deviations can cause superconductive coupling with conduction electrons.

2.2.3 Resonant Valence Bond (RVB). The RVB approach has been developed by Anderson and Pauling [64–67] and relates to a magnetic mechanism associated with peculiar magnetic properties. The RVB state is related to a fractional quantum-Hall effect and a Bose condensate of Cooper pairs associated with a wave that preserves its shape, even through (after) interactions (a solution). This condensate is interpreted as a quantum-spin liquid or an interacting-spin gas with short-range correlations. Physically, each atom is bonded to a single neighboring atom by a single electron pair, and the ground state is a linear coherent superposition of all the states that can be formed by such a dimerization of the lattice. Excitations of the RVB state require local and nonlocal operators involving the entire background liquid (collective effect). The peculiar magnetic properties of such a state involve what is referred to as frustration, which is the inability to achieve complete nearest-neighbor antiferromagnetic pairing. The resonant valence stems from an ion that can assume several different and stable charged states, such as copper, which can undergo the resonance $2\text{Cu}^{2+} \rightarrow \text{Cu}^+ + \text{Cu}^{3+}$. The coupling to achieve a superconducting state is thus a spin excitation, which is a neutral soliton or spin 1/2 and charge-zero particle. The physical basis for the RVB model is very abstract and is best described as a Luttinger liquid state (non-Fermi liquid) involving a Fermi surface that is largely associated with spin rather than charge. The RVB model predicts the absence of superconducting gaps for the creation of neutral solitons (spinons and holons).

2.2.4 The Spin Fluctuation Mechanism. When local fluctuations in magnetic states cause a deviation from normally compensated antiferromagnetism, the net unpaired-valence spin (or spin fluctuation from antiferromagnetism) on a cationic site (such as copper) can be strongly coupled to spins in the free-electron system, establishing a superconducting gap. This model for superconductivity requires a delicately "tuneable" force or parameter to establish the condition for the spin fluctuation from antiferromagnetism. Such variable parameters include varying stoichiometry of cation or anion in an ionic crystal of the A_2BX_4 or ABX_3 type, where antiferromagnetism can exist under idealized and fragile conditions.

2.2.5 The Charge-Transfer Excitation and Valence Fluctuations [68–70]. Compounds that contain multivalence cations bonded to oxygens can undergo charge transfer from the cation, such as copper to oxygen and vice versa. The charge transfer will cause the valence to fluctuate or oscillate from the maximum value to zero. This charge transfer is an excitation that is promoted by unbalanced local electrical forces in the crystal. These unbalanced forces are due to structural bonding and symmetry considerations and produce a bonafide internal electric perturbation field. The charge-transfer excitation actually takes place to relieve this field. The relieved field state is only temporary because the KE of the transferring electrons, and the bound holes created by the charge transfer set up an unstable condition from an energy standpoint. The transferring electron undergoes such high-frequency resonance ($\nu \approx 10^{13} - 10^{14}$ Hz) that its relationship to an associated hole is more virtual than real, and, hence, the resulting electron-hole entity localized to a cation, such as copper, or to oxygen is referred to as a virtual exciton. This particle does not have to obey conservation of energy because of its ultrashort lifetime and the implications of the Uncertainty Principle. The virtual exciton does, however, have to subscribe to conservation of momenta. The superconductivity mechanism then involves the coupling or mediating by the virtual excitons (or their hole constituents) in relationship to conducting electrons, thus not really requiring a phonon coupling.

2.3 Band Structure. Band structure calculations using main-frame computers and all-electron calculations employing the full linear augmented plane wave (FLAPW) technique have allowed for the precise calculation of band structure (energy vs. wave vector or vs. position) for semiconductors,

metals, and superconductors, as well as at interfaces thereof. These band-structure calculations are then compared with experimental work on high-resolution angle-resolved photoemission under ideal vacuum and purity conditions to verify their credibility. In recent years, these calculations have been borne out by experiment with amazing exactness because of the accuracy of theory, the capability of large digital machines, such as the Cray, and the preciseness of experimental techniques. In this manner, the density of states (DOS) for superconductors has been calculated very accurately. Although the band structure of superconductors can be overwhelmingly complex with respect to many levels crossing each other, in the region of the Fermi level, the band structure of some materials, such as the new high- T_c superconductors that are the subject of this report, is relatively simple, with only two or three bands crossing the Fermi level. The subject of band structure will again be treated in a subsequent section of this report.

2.4 Fundamental Properties of Matter. It has been through studies of the fundamental properties of matter that the new high-temperature superconductors have been discovered. One such property involves the understanding of the basic molecular or polyhedral building block schemes of materials. In the case of condensed matter, the building blocks of solids refer to the symmetry and bonding of basic units that repeat themselves to constitute the unit cell. These units include both coulombically or ionically bonded polyhedra, such as octahedral, tetrahedral, and pyramidal groups, as well as covalently hybridized groups, such as chains. Complex materials containing mixed bonding (anisodesmic materials), such as coulombic and covalent or covalent and metallic, can be further complicated if they contain multivalence ions that can undergo charge-transfer excitations. In such cases (such as copper oxides), the charge-transfer excitation is promoted by the high internal inhomogeneous electric perturbation field (or field gradient, ∇E) that arises from interfaces between polyhedra of vastly differing symmetry, such as octahedra (O_h space group symmetry) and tetrahedra (T_d space group symmetry), or between pyramids and chains. This building block view of matter, where both polyhedral symmetry and chemical bonding are considered, assists the crystal chemist and/or materials scientist to tailor-engineer materials having certain desired properties, such as, different electrical conductivity or different heat transport, depending upon the direction in the crystal. The realization that the "engineering" into a material of more than a single building block with differing symmetry and different bonding would lead to inhomogeneous internal electric fields,

combined with the belief that ferroelectric-type materials would enhance polar and polarization effects, and also combined with the belief that oxides had the proper range of electronegativities, all of these scientific notions led to the research that paved the way to high- T_c materials [71–76].

3. Experimental Basis for High- T_c Superconductivity

3.1 Early Work in the CuCl System and CdS Polymorphs. Two compounds that were predicted by inferences from the Soviet theory to be excitonic candidates at high pressure for superconducting states at temperatures far in excess of conventional values for T_c were CuCl and BiSb. These materials were selected because of their calculated band structure (which involved a valence band maximum proximity to a conduction band minimum), the expectations for band overlap at high pressure, and their known exciton formation under the influence of light. It was well known that under proper illumination CuO_2 would show a line spectra that was interpreted as being due to excitons [23]. Excitons are properties of the host crystal and are not properties of the impurities; however, both excitons and impurities induce energy levels within the "forbidden" energy gap. Other materials that tend to create excitons under appropriate illumination are CdS, HgI_2 , PbI_2 , CdI_2 , and Ge.

In the late 1970s, Russakov [36] of the Soviet Union came to the United States, bringing with him the high- T_c notions of Abrikosov [35, 37] and other Soviet theorists [34–38]. Russakov pursued research into these ideas in collaboration with Chu [74], who was conducting high- T_c research at Cleveland State University. Chu was following channels of thought that had been embraced by his mentor Matthias during Ph.D. studies at the University of California at La Jolla. The results of Chu and Russakov, using high-pressure diamond-cell anvil apparatus, as well as independent work of Lefkowitz [75] on Meissner Exclusion, and Vezzoli and Bera [76] using a Bridgman anvil system, showed, albeit not reproducibly, that in some samples of starting material, CuCl at high-pressure (5–45 kbar) an insulator \rightarrow metal transition occurred [76] in the temperature range of 77–125 K that was associated with a transition to a diamagnetic state [74, 75] and a major change in phase angle from highly capacitive to highly inductive [76]. Although the CuCl work was highly controversial,

not duplicated at some of the major research laboratories in the United States and abroad, and also occurred only in selective samples, it still served as a positive force and an embryo of encouragement in the minds of some researchers. It was realized by Vezzoli and Bera [76–78] and also by Piermarini and Block [79] that the experimental system that produced the collapse in resistance that was thought to be suggestive of possible superconductivity was not simply CuCl, but was, in reality, a disproportionated system that contained Cu^+Cl^- , $\text{Cu}^{2+}\text{Cl}_2^-$, and free copper (Cu^0) via the pressure-induced disproportionation $2\text{CuCl} \rightarrow \text{CuCl}_2 + \text{Cu}^0$. Examination of the recovered products from the high-pressure low-temperature experiments clearly showed the presence of three phases: CuCl (cloudy white), CuCl_2 (green in the presence of water or water vapor), and Cu^0 (gold-bronze in color). Figure 15 shows these phases attached to a glass fiber for x-ray diffraction analysis. Because the superconducting-like effects in the CuCl could be observed in situ at pressures less than 40 kbar [58–67], it became apparent that the zincblende-to-tetragonal-phase transition at about 40 kbar was not necessary in order to observe the phenomenon.



Figure 15. Phases of CuCl, CuCl_2 , and Cu^0 Attached to a Glass Fiber for X-ray Diffraction Analysis.

In an effort to explain the work of Chu and Russakov from an excitonic standpoint, and in what turned out to be a very prophetic paper, Wilson [80] discussed wave-function overlap, excitons, and polytypic-stacking variants in zincblende configurations associated with disproportionate superconductivity and pointed out the pressure-induced trend from zincblende through various polytypic phases, to layer structures that involve edge-sharing tetrahedra and, finally, to a fully

octahedral coordination. This suggested the extremely strained internal conditions that could exist at the interfaces of these configurations, and how this strain could substitute for photons in producing excitons. These notions of Wilson [80] are illustrated in Figures 16 and 17 and further lead to the ideas of materials-engineering substances containing building blocks of differing symmetry and differing bonding that share common ions. The work also suggested the existence of high internal electric field gradients in the boundary regions between the building block structural polyhedra.

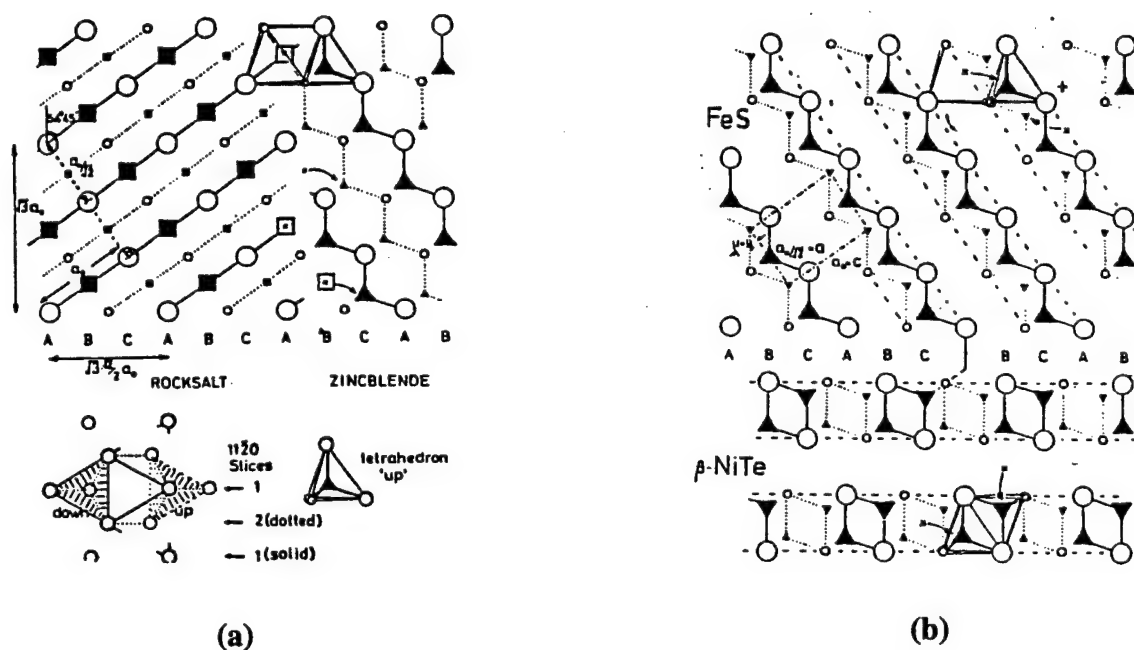


Figure 16. Wave-Function Overlap, Excitons, and Polytypic-Stacking Variants in Zincblende Configurations.

In addition to the anomalies of resistance, diamagnetism, and phase angle (Figure 18) that suggested possible superconductivity-like states, the work of Brandt et al. [81] showed, in CuCl, a significant Meissner Exclusion effect at ~ 100 K and 5 kbar (reproduced in Figure 19).

The interface between the opaque phase of disproportionate Cu^0 (as observed in situ along the diamond cell axis) of CuCl/CuCl₂ is shown in Figure 20 (lower), where the phase boundaries (at 50 kbar) can be observed, due to the pressure gradient across the anvils as a consequence of the nonhydrostatic conditions when a pressure-transmitting fluid is not utilized [82]. Extremely high

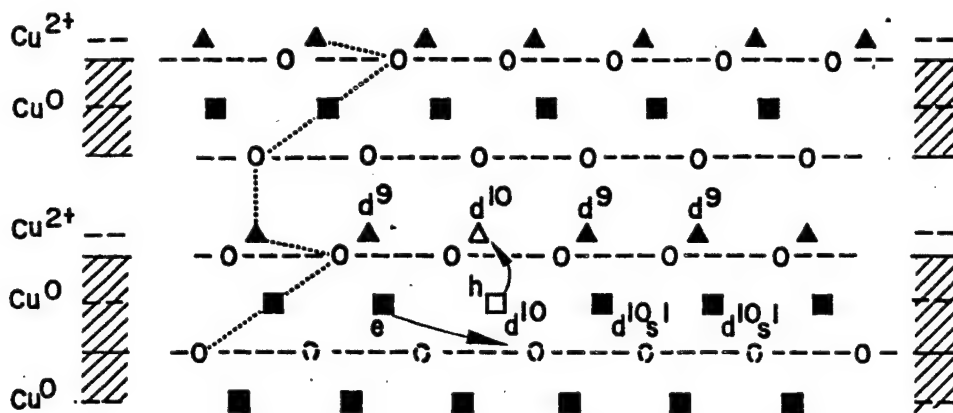


Figure 17. The Sort of Situation Envisaged as Possible in Disproportionate CuCl for an Electron from a Small Region of Segregating Copper Creating a Virtual Exciton Across the Boundary to the Charge-Ordered State. The Exciton Serves as a Boson, Mediating the Possible Superconductive Interaction and Constitutes a Local Reversal of the Disproportionation Reaction. (○, Cl; ▲ Tetrahedral Cu^{2+} ; □ Octahedral Cu^0 ; ◻, Cl Displaced; (□, Δ) Exciton.)

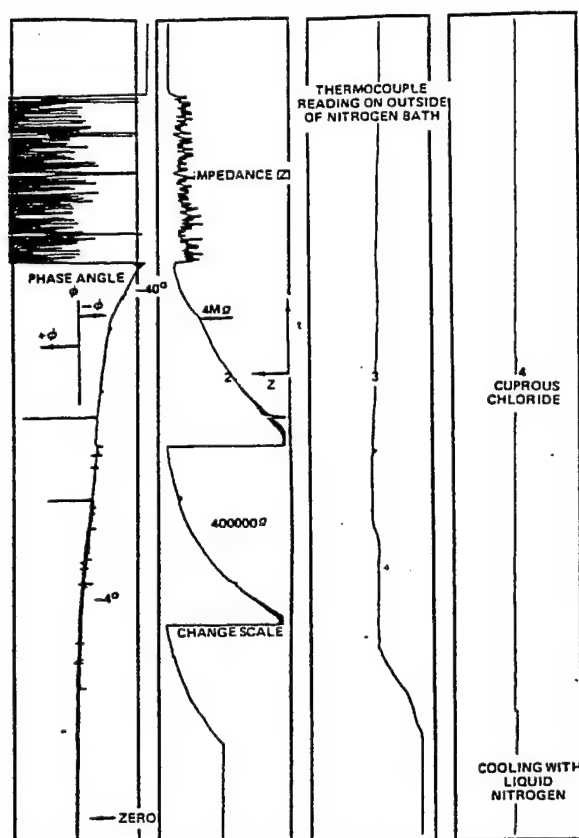


Figure 18. Anomalies of Resistance, Diamagnetism, and Phase Angle.

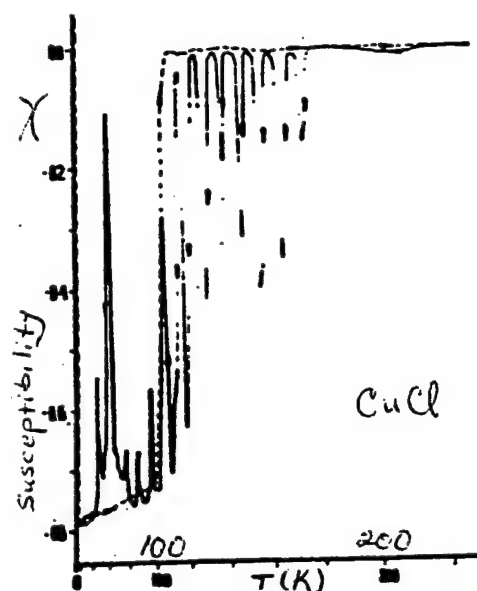
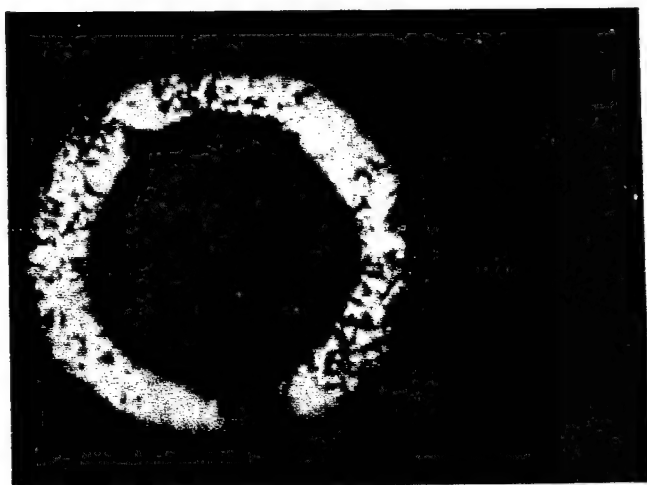


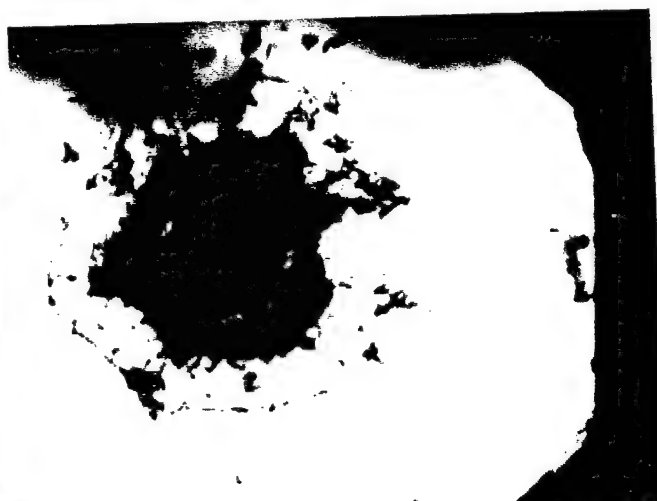
Figure 19. Meissner Exclusion Effect at ~100 K and 5 kbar.

electrovalent strain would be expected to exist at such a boundary, which could establish charge-transfer excitations and virtual excitons, due to the perturbation local internal electric field (which is discussed in detail later in this document).

Three phases of CdS under high pressure (pressure gradient again present) to include the rocksalt, sphalerite, and wurzite phases, and the interfaces thereof [82] are shown in situ in Figure 20a. In this system, an octahedral phase (rocksalt) is in boundary interface with a tetrahedral phase (sphalerite or wurzite) similar to what was conceptualized by Wilson [80]. This high-pressure study was conducted to verify previous work by Homan, Kendal, and MacCrone [83] and Brown, Homan, and MacCrone [84], which claimed that after quick removal of pressure (pressure-quenching) from about 40 kbar (this pressure representing the zincblende-to-rocksalt phase transformation region at 300 K in the pressure-temperature phase diagram), the recovered product showed a Meissner Exclusion effect at liquid-nitrogen conditions that persisted for about a day. Being an excitonic material, these results further reinforced the ideas of a new form of superconductivity, based on exciton-induced mediation. Interestingly, the superconducting-like effect in CdS only occurred in starting material that was chlorinated (containing about 1% chlorine). This is believed to occur because only in the



(a) CdS Showing Three Phases Present Due to Pressure Gradient (Yellow, Black, and Red With Increasing Pressure).



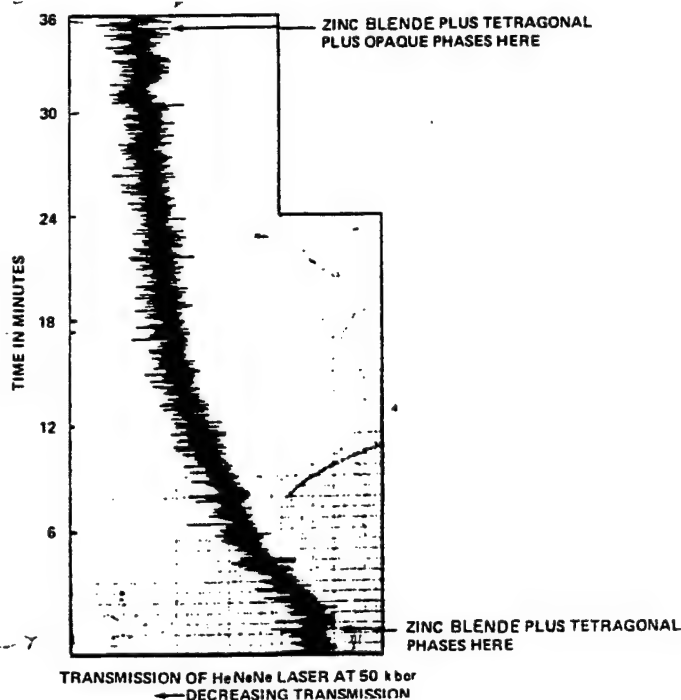
(b) CuCl Showing Opaque Phase Developing With Time From Tetragonal Phase. Outer Ring Is Zincblende Phase.

Figure 20. (a) CuCl and (b) CdS as Viewed Through Diamond Cell (White Transmitted Light).

presence of the chlorine ion could the rocksalt structure be quenched and retained metastably at 1 atm [84, 85]. This observation supplied further credence to the importance of compounds having more than a single-structural building block.

The disproportionation in CuCl, as well as the phase transformation in CdS, is a kinetically dependent phenomenon, and, for CuCl, this is shown in the laser transmission vs. time data of Figure 21 [82, 86].

3.2 More Recent Work on CuCl. In an effort to determine whether in the high-pressure CuCl work the effect of strain due to internal electric fields could have accomplished the equivalent of the effect of light in the production of excitons, Mattes and Foiles [87] succeeded in depositing CuCl on single-crystal silicon and studied whether the strain caused by the mismatch of lattice parameters at the CuCl-Si interface could produce properties similar to those detected by Chu and Russakov at liquid-nitrogen conditions. Their experiments were indeed successful and indicated that the origin



(a)

PHOTOGRAPH OF CuCl
AFTER 4 DAYS AT 50 k bar



(b)

Figure 21. Optical Transmission of CuCl at 50 kbar vs. Time at Room Temperature. (a) Data from Diamond-Anvil (No Gasket) Apparatus Giving Optical Transmission of the Development of the Opaque Disproportionated Phase from Approximate Time of the Beginning of Zincblende to Tetragonal Transition at 45–50 kbar; (b) Photograph Through Diamond Anvils (No Gasket) of Opaque Phase After 4 Days at ~50 kbar Pressure.

of the excitons could be due to an internal spontaneous effect that was governed by local fields and lattice mismatches at interfaces. In order to examine this structural heterotype quantitatively, Yu [88] and Freeman, Yu, and Fu [89] under the funding supplied by G. C. Vezzoli utilized FLAPW calculations to show that metallic states were established at the interface between CuCl and Si and that superconductivity, as related to the resulting band structure, did not conform to phonon-coupling predictions. The valence-charge mappings of isoenergetic contours for this configuration are given in Figure 22. This result suggested that if the metallic states were due to phonon coupling, these states would not occur at temperatures as high as those employed by Mattes.

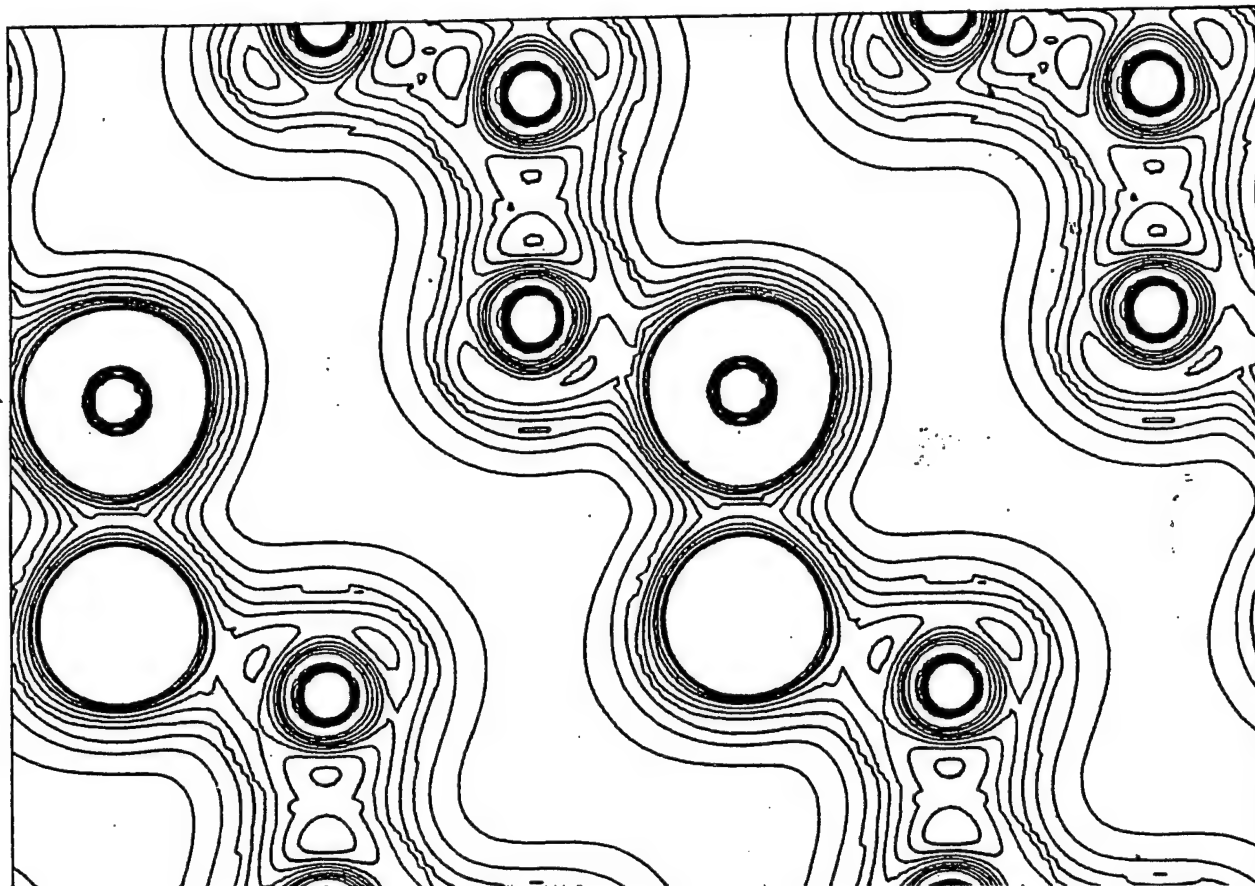


Figure 22. Valence Charge for CuCl and Si [1, 2].

In a similar time frame, Williams and Zink [90] deposited a deep quantum well structure of CuCl and CaF_2 (as shown in Figure 23) for the purpose of studying exciton spectroscopy and dynamics. They measured time-dependent luminescence in this structure at 1.8 K, and their results are reproduced in Figures 24a and b.

Finally, in an effort to determine whether any low-temperature anomalies existed in BiSb, as suggested in the work of Abrikosov [37], a series of experiments was conducted by Vezzoli [86], which revealed the anomalous resistance vs. temperature behavior (shown in Figure 25). These results lent some more credence to the implications of the CuCl and CdS work.

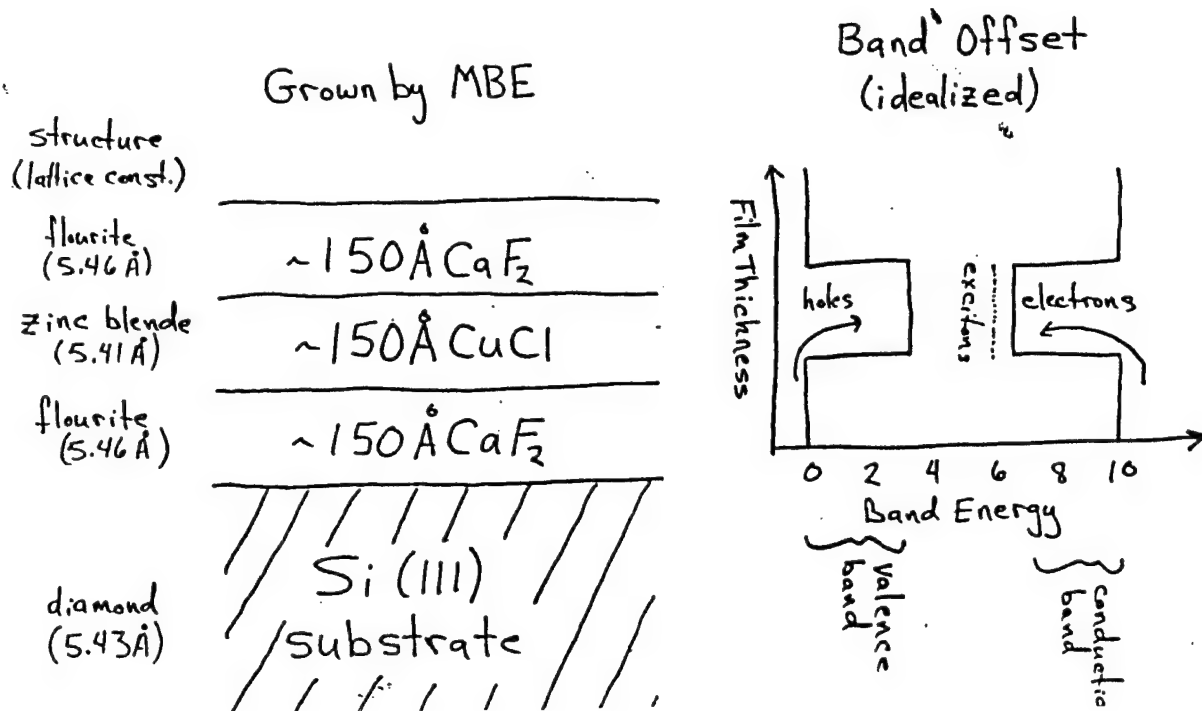
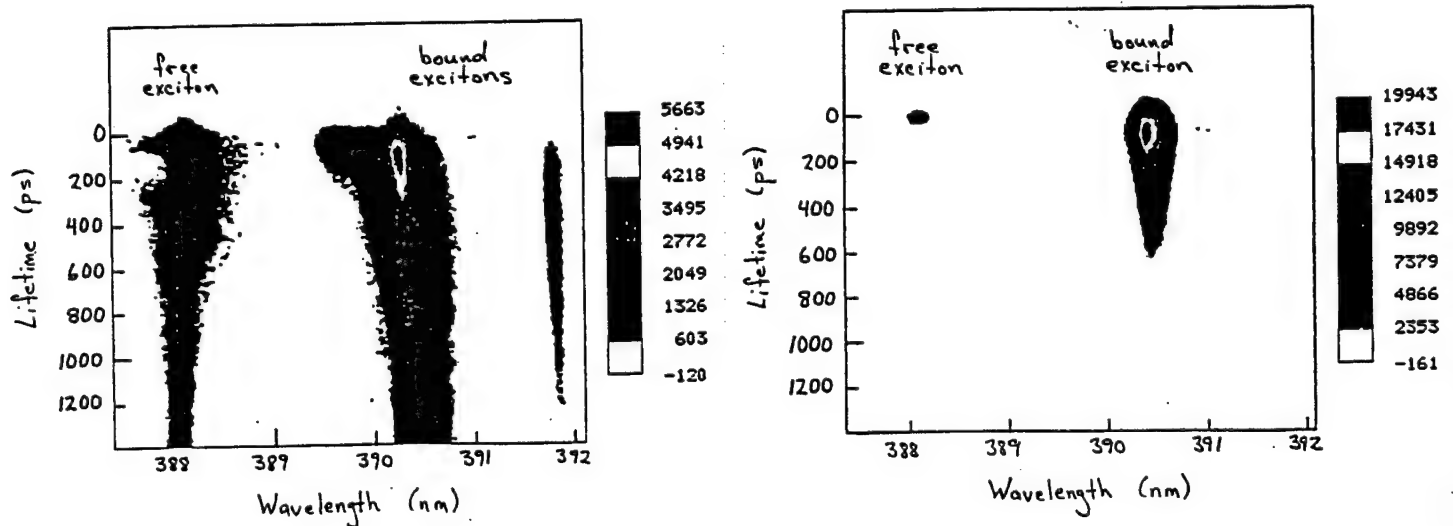


Figure 23. CuCl/CaF₂ Deep Quantum Well Structure.



(a) CuCl Single-Crystal at 1.8 K.

(b) 150 Å CuCl Quantum Well at 1.8 K.

Figure 24. Time-Dependent Photoluminescence for (a) CuCl Single-Crystal at 1.8 K and (b) 150 Å CuCl Quantum Well at 1.8 K.

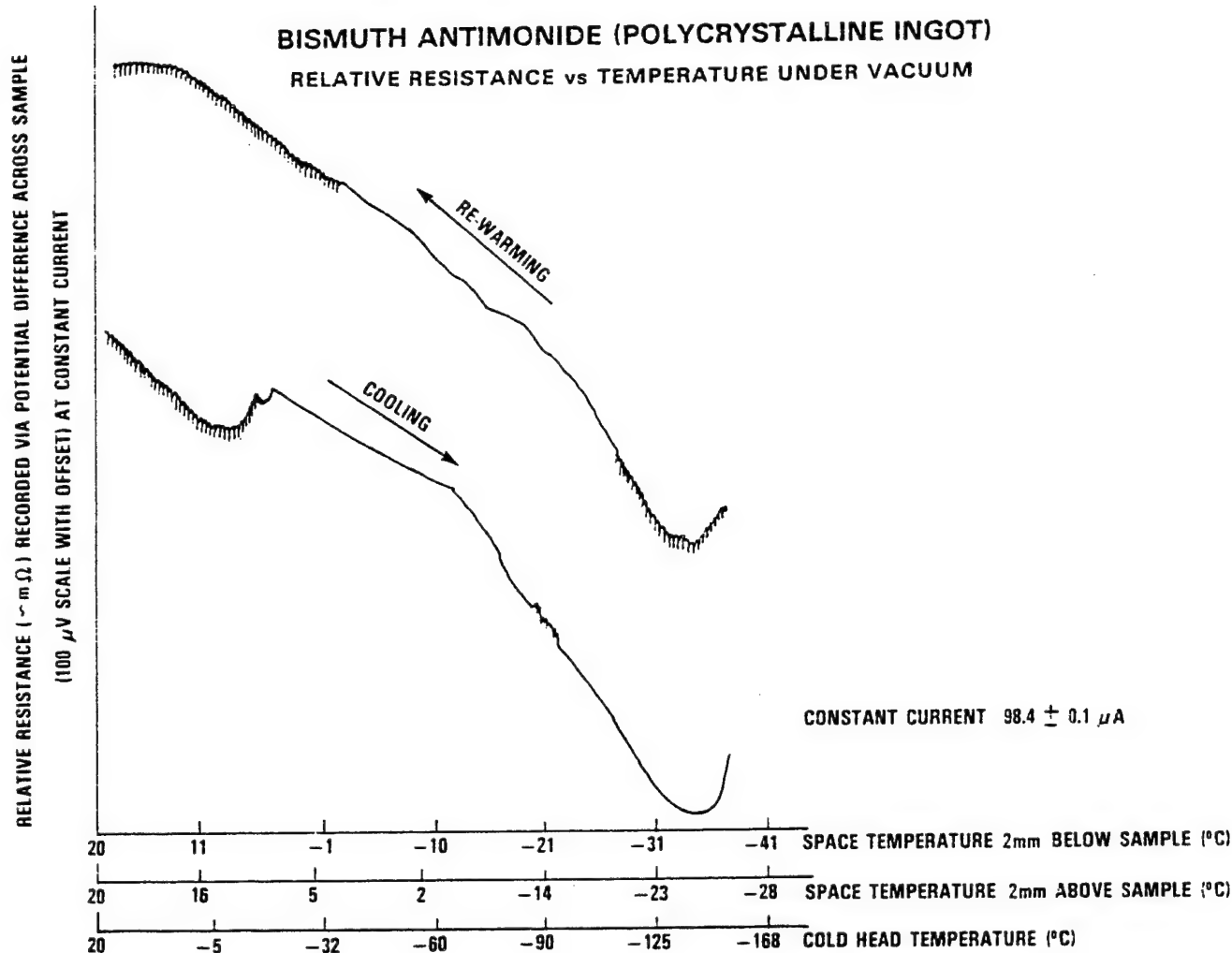


Figure 25. Relative Resistance vs. Temperature for BiSb in Vacuum Showing Increasing Resistance Anomaly Upon Cooling and Reversible Minimum-Resistance Turning Point. Note Regions of Noise Oscillations Preceding Anomaly and Accompanying Reversal of Minimum-Resistance Turning Point.

In summing up the work on CuCl, CdS, and BiSb, it was concluded that the possibility of a form of superconductivity that was associated with phases thereof and high-pressure effects could not be definitely ruled out, but that processing and materials criteria, such as pressurization and depressurization rates, cooling and rewarming rates, impurities, and nonhydrostatic shearing phenomena caused an irreproducibility of results that indicated far more materials, and engineering was necessary to synthesize a stable and irrefutable high- T_c superconductor. However, the path was nonetheless incipiently chartered experimentally toward a materials science that would involve the

types of structural and excitonic effects observed at high-pressure in CuCl and CdS and would be expected to involve multivalence cations, such as copper and bismuth.

3.3 The Discoveries of 1986 and 1987 in the LaCuO System [91–93]. The first of the superconducting metallic oxides was SrTiO₃ with a T_c of 0.3 K, which could be increased to 0.7 K by niobium-doping (having a carrier concentration of only $2 \times 10^{20} \text{ cm}^{-3}$). Subsequent research led to observing superconductivity in a spinel phase of the LiTiO system with T_c as high as 13.7 K [94, 95] and in the mixed-valence Perovskite compound BaPb_{1-x}Bi_xO₃ [96]. In the latter, the highest T_c in homogeneous oxygen-deficient mixed crotals occurs at 13 K with a comparatively low-carrier concentration of 2×10^{21} to $4 \times 10^{21} \text{ cm}^{-3}$. According to the BCS theory, the small-carrier concentrations implied very strong electron-phonon coupling. The polaron formation and mixed-valence states of oxides can be associated with strong electron-phonon interactions, as well as proposed within the notion of a superconducting-to-bipolaronic-insulator transition [97–99]. One mechanism that can lead to polaron formation is the Jahn-Teller distortion; heavy polaronic masses can be produced if the Jahn-Teller stabilization energy becomes comparable to the bandwidth of degenerate orbitals. Strong Jahn-Teller effects are associated with Cu²⁺, Fe⁴⁺, and Ni³⁺ in an octahedral oxygen environment because their incompletely occupied e_g orbitals point toward the negatively charged ligands (see Figure 26). From studies of SrFe⁴⁺O, LaNiO₃, and LaCuO₃, it was decided by Bednorz and Mueller [91, 92] that materials research should be further pursued to investigate and engineer nickel- and copper-containing oxides with reduced bandwidth ($\sim b_{II}$, where b_{II} also equals the transfer energy of the e_g electrons). This was a natural extension of the superconductivity research of Bednorz and Mueller and the two decades of research at their institution in Ruschlikon on insulating oxides that undergo structural and ferroelectric transitions [100–104].

In the summer of 1985, Bednorz and Mueller [91, 92] concentrated their work on copper-containing compounds such as LaCuO₃ because Cu³⁺ has two electrons in the e_g subshell (e_g being half-filled), and the ground state is not degenerate. The concept was then to prepare and study an oxide with mixed valence, such as Cu²⁺/Cu³⁺ or Cu³⁺/Cu⁴⁺. Bednorz and Mueller became aware of the work of Michelle, Er-Rakho, and Raveau [105], which was part of a project for the French

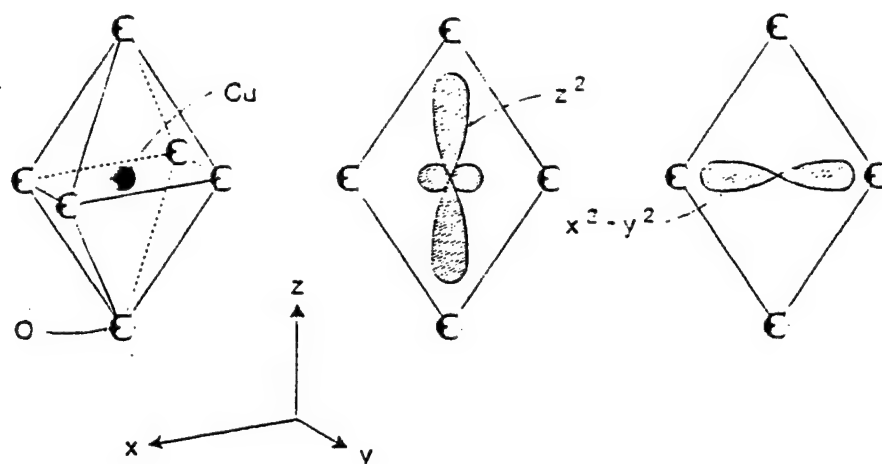


Figure 26. The Partially Filled 3-D Wave Functions of the $\text{Cu}^{3+}/\text{Cu}^{2+}$ Mixed-Valence States. Positions of Copper and Oxygen Atoms Are Shown at Left.

government aimed at synthesizing materials that showed very differing thermal conductivity, depending upon direction. This work reported the properties of the mixed Perovskite $\text{BaLa}_4\text{Cu}_5\text{O}_{13.4}$, which turned out to exactly satisfy the mixed-valency requirement in the Bednorz and Mueller work. For this reason, the latter researchers studied the $\text{Ba}_x\text{La}_{5-x}\text{Cu}_5\text{O}_{5(3-y)}$ system, varying the x stoichiometry.

In the aforementioned system, superconductivity was observed at temperatures as high as 35 K, and it was determined that the system actually consisted of three phases CuO ; $\text{Ba}_x\text{Cu}_{5-x}\text{O}_{5(3-y)}$, which was originally intended; and a K_2NiF_4 phase containing Perovskite layering [106]. The K_2NiF_4 was La_2CuO_4 and was indeed the superconducting species. The initial resistivity vs. temperature data from these historic experiments are given in Figure 27 [107], and the structure of La_2CuO_4 is illustrated in Figure 28 [108].

The work of Bednorz and Mueller [91, 92] was shortly afterward confirmed by Uchida et al. [109, 110] in Tokyo; by Chu et al. [111, 112] at the University of Houston; by Cava et al. [113] Murphy et al. [114], Moddenbaugh et al. [115], Franck, Jung, and Mohamed [116] at Bell Laboratories (who succeeded in strontium substitution for some of the lanthanum to sharpen the transition); and by Tarascon et al. [117] at Bellcore.

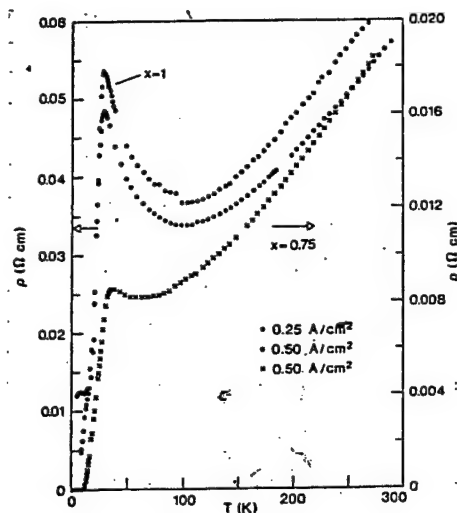


Figure 27. Temperature Dependence of Resistivity in $\text{Ba}_x\text{La}_{5-x}\text{CuO}_{5(3-y)}$ for Samples With $x = 1$ (Upper Curves, Left Scale) and $x = 0.75$ (Lower Curve, Right Scale) (x Nominal). The First Two Cases Also Show the Influence of Current Density.

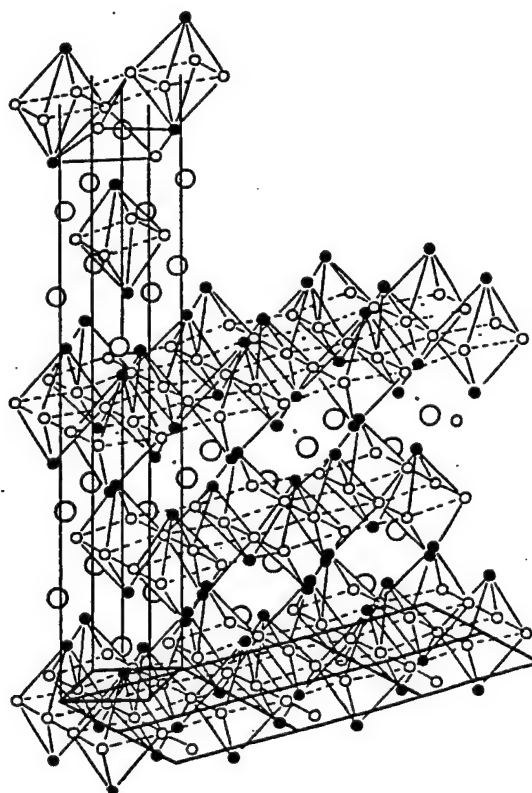


Figure 28. Structure of La_2CuO_4 .

Chu et al. [111, 112] utilized high hydrostatic pressures to elevate the T_c in La_2CuO_4 to 52 K, and researchers at the Academy of Science in China optimized the barium and strontium substitution for some of the lanthanum, and achieved T_c of 48 K at 1 atm. All of this had been accomplished by the end of the year 1986. The known crystalline structure of La_2CuO_4 permitted Mattheiss to conduct electronic structure calculations for the tetragonal lattice of La_2CuO_4 and show a half-filled $\text{Cu}(3d) - \text{O}(2p)$ band of $3d(x^2 - y^2)$ and a two-dimensional (2-D) character with a nearly square Fermi Surface [118, 119]. This early calculation of a Fermi surface relative to the electronic structure was helpful in formulating initial thinking on the underlying mechanism of high- T_c superconductivity. The fact that lanthanum could assume valences of 1+ and 3+ suggested that the use of copper, with its mixed valency as well, would foster a superconductivity in oxides at higher-than-ever-before temperatures.

3.4 The Discovery of Superconductivity in the YBaCuO System [120]. The research group of Chu et al. [111, 112] and the group at the Academy of Science in China, as well as a group at the University of Alabama led by Wu [120], after considering the success of high-pressure in elevating T_c in the LaSrCuO system and realizing that high pressure can cause electron-cloud compaction, decided to substitute the smaller Y^{3+} (radius 0.893 Å) for La^{3+} (radius 1.016 Å). Furthermore, barium was substituted for strontium, perhaps because barium could exist in +1, as well as the common +2 state, and because barium can coordinate a large number of anions. The results of these substitutions generated the YBaCuO system of high- T_c superconductors and showed $T_c \sim 90$ K in the $\text{Y}_1\text{Ba}_2\text{Cu}_3\text{O}_{7-\delta}$ defect stoichiometry compound [120, 121]. The structure of this material (known as the 1-2-3 compound) was studied by Hazen [122] by x-ray diffraction and by Jorgenson et al. [123] by neutron diffraction. The structure of the orthorhombic crystal lattice of $\text{Y}_1\text{Ba}_2\text{Cu}_3\text{O}_{7-\delta}$ is given in Figure 29 and compared to the K_2NiF_4 (or Li_2NiO_4 or K_2MnO_4) structure in Figure 30.

3.4.1 Crystal Structure of $\text{Y}_1\text{Ba}_2\text{Cu}_3\text{O}_{7-\delta}$. We now more fully compare the structure given in Figure 29 with the much earlier work of Birgeneau et al. [124] giving the A_2BX_4 structure of antiferromagnetic K_2NiF_4 (Figure 30), also derived from neutron diffraction data. If, in the K_2NiF_4 structure of Figure 30, we make the following substitutions: Cu^{3+} for the corner Ni^{2+} , Cu^{2+} for the edge K^+ , Ba^{2+} for the upper and lower interior K^+ , Y^{3+} for the central Ni^{2+} ; remove the 100-direction

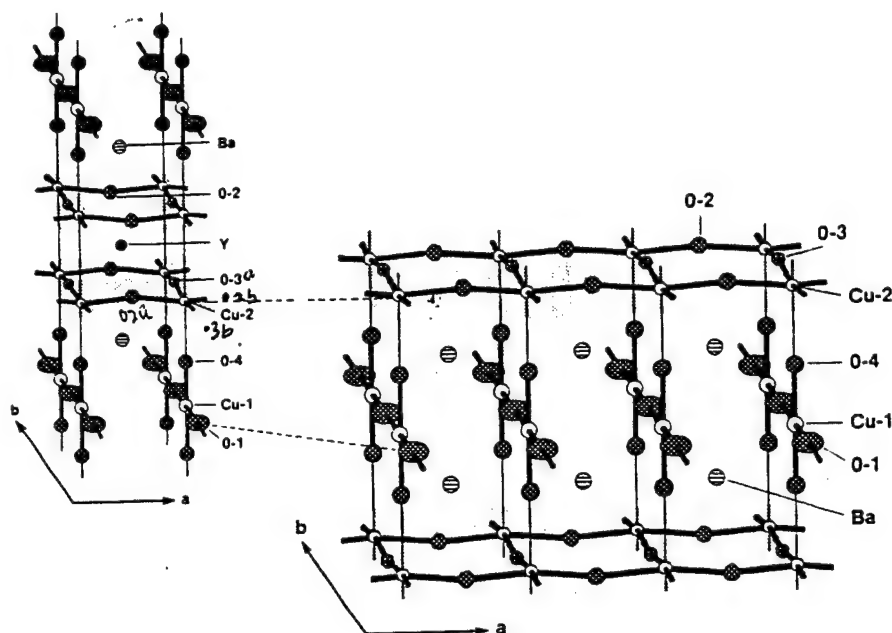


Figure 29. The Structure of $\text{Y}_1\text{Ba}_2\text{Cu}_3\text{O}_{7-\delta}$ [124] Showing Lattice Parameters: $a = 3.8231 \text{ \AA}$, $b = 3.8864 \text{ \AA}$, $c = 11.680 \text{ \AA}$, Space Group P_{mmm} , Orthorhombic Bravais Lattice. Chains in the b - c Planes Are CuO_3 . Layers in the a - b Planes Are CuO_2 . Bond Lengths Are

$\text{Cu}(1) \text{ Cu}^{+3} - \text{O}^{-2}(1) \text{ (in Plane)} = 1.943 \text{ \AA}$

$\text{Cu}(1) \text{ Cu}^{+3} - \text{O}(4) \text{ (Below Plane)} = 1.850 \text{ \AA}$

$\text{Cu}(2) \text{ Cu}^{+2} - \text{O}(2) \text{ (in } a\text{-Direction of Puckered Plane)} = 1.928 \text{ \AA}$

$\text{Cu}(2) \text{ Cu}^{+2} - \text{O}(3) \text{ (in } b\text{-Direction of Puckered Plane)} = 1.962 \text{ \AA}$

$\text{Cu}(2) \text{ Cu}^{+2} - \text{O}(4) \text{ (in } c\text{-Direction)} = 2.303 \text{ \AA}$

The Numbers 1, 2, 3, and 4 Refer to the Identified Oxygen Ion. These Lattice Parameters Suggest Jahn-Teller Distortion in d^9 (Cu^{+2}) With Elongation in d_{z^2} , Hence Favoring the e_g State to Be in the Configuration $(d_{z^2})^2 (d_{x^2-y^2})^1$.

basal plane anions; remove the fluorine anions octahedrally coordinated by the central Ni^{2+} ; substitute O^{2-} for the remaining F^- anions; and, finally, introduce two puckered and two nonpuckered O^{2-} ions in the plane that now includes the edge Cu^{2+} , we then establish a hypothetical YBaCu_3O_8 (which is not a superconductor). For it to become superconducting, a processing must occur that creates an oxygen deficiency from O_8 to $\text{O}_{7-\delta}$. We have divided the three copper ions into two Cu^{2+} and one Cu^{3+} to achieve charge balance with the O_7^{2-} , to introduce two valence states of copper for charge transfer, and to associate with inhomogeneous internal electric perturbation fields. The ionic radii criteria are

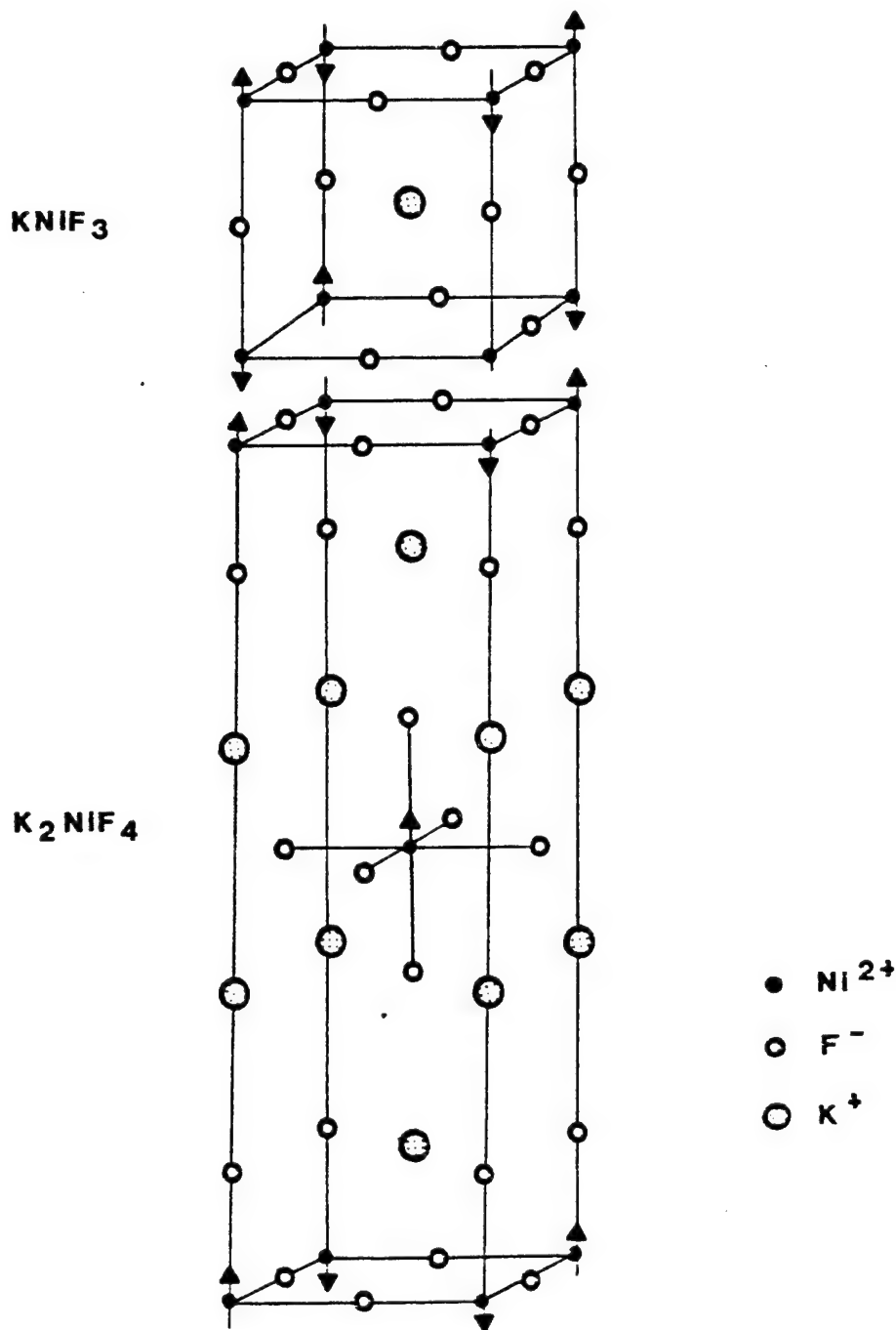


Figure 30. A₂BX₄ Structure of Antiferromagnetic K₂NiF₄.

$$\text{Ba}^{2+} = 1.34 \text{ \AA}, \text{Y}^{3+} = 0.893 \text{ \AA}; \text{Cu}^{2+} = 0.72 \text{ \AA}; \text{Cu}^{3+} = 0.62 \text{ \AA}.$$

The radius ratio for Cu²⁺ to O²⁻ is 0.55, which is greater than for tetrahedral or square planar coordination and somewhat less than for typical octahedral coordination, thus in accord with the observed five-fold coordination (not to be confused with five-fold symmetry outlawed in general

space group theory). The Cu^{2+} is referred to as Cu(2) in the 1-2-3 structure and is coordinated in a pyramidal fashion with four oxygens almost in the plane of the copper (these are designated as two O(2) and two O(3) ions) and with one apical oxygen (designated O(4)). The resulting pyramid is a polyhedral building block of the unit cell and the crystalline structure and is, within itself, largely coulombically bonded.

Although the trivalent positive ionic state of copper is uncommon, it clearly exists in such compounds as K_3CuF_6 and KCuO_2 , and in these two materials exists respectively in a four-coordinated square or a six-coordinated octahedral structure having a d^8 orbital configuration. The $\text{M}_2^{\text{I}}\text{CuX}_4$ compounds (where M^{I} refers to a univalent cation, and $\text{X} = \text{Cl}^-$ or Br^-) contain planar (CuX_4) ions. Squashed tetrahedra of CuX_4 can also exist as in Cs_2CuCl_4 [125–129].

At anion stoichiometry ≤ 6.44 , the phenomenon of high- T_c superconductivity clearly disappears in $\text{Y}_1\text{Ba}_2\text{Cu}_3\text{O}_{7-\delta}$. Charge-balance requirements for chemical reduction from 7 to $7-\delta$ stoichiometry (or from the favorable $\text{O}_{6.5}$ to the near-borderline 6.5 stoichiometry) suggest the composition $(\text{Ba}_2^{2+}\text{Cu}_2^{2+})(\text{Y}_1^{3+}\text{Cu}_1^{2+})\text{O}_{6.5}$. In such a compound, the chain-copper ions (Cu(1)) have gained an electron to become $2+$ (instead of $3+$ at O_7). The observation that stoichiometry of $\sim\text{O}_{6.5}$ is associated with the elimination of superconductivity and with all the copper ions being in the $2+$ state gives further suggestion that cationic mixed-valence states seem to be a necessary materials ingredient of high- T_c superconductors. The absence of some of the molar concentration of the oxygen (for $\text{O}_{<7.0}$) can reflect an ordered or disordered arrangement.

We address the $\text{O}_{6.9}$ condition and make note that any disorder that is created in the pyramidal or in the chain regions affects the collective phenomena, and write $(\text{Ba}_2^{2+}\text{Cu}(2)_2^{2+})_1(\text{Y}_1\text{Cu}(2)_x^{2+}\text{Cu}^{3+})_1\text{O}_{6.9}$, where $x = 0.2$, and $y = 0.8$. This missing oxygen due to reduction from O_7 to $\text{O}_{7-\delta}$ can be either ordered or disordered. The replacement of 20% of the $\text{Cu}(1)^{3+}$ sites by $\text{Cu}(1)^{2+}$ ions, accomplished in order to achieve charge balance, is likely to cause an upset or deviation from the delicately balanced (or compensated) antiferromagnetism existing at the Cu(2) d^9 sites for the idealized O_7 and $\text{O}_{6.5}$ stoichiometries (for which, in the idealized case, no upset occurs because the chain ions are either all d^9 or all d^8).

3.4.2 Role of Each Ion.

3.4.2.1 Yttrium. By itself, yttrium, under the previously discussed argument, is not essential or critical to superconductivity in the 1-2-3 compound because substitutions using Sc^{3+} and the other rare earths (REs) do not cause the loss of superconductivity or reduced stability. However, a trivalent RE cation at most of the yttrium centrosymmetric sites is required to retain charge balance and superconductivity (substitution of Pr^{4+} can only be accomplished within a limited range without terminating superconductivity by destroying the condition of proper copper multivalency). The yttrium ion is basically a stereochemical spacer ion to maintain the proper separation between the CuO_2 planes (the base planes of the pyramids). The radius ratio of Y^{3+} to O^{2-} is 0.668. Although, for eight-coordination, a radius ratio of 0.732 to 1.000 is normally required, it is probable that the puckered anionic geometry allows more available ligand space and may compensate for a lower-than-ideal radius ratio. In a later section, we show, in detail, the effects on the resistance vs. temperature curve and the zero-resistance temperature, due to substituting the RE series for yttrium in the 1-2-3 compound, and interpret these findings, based on the presence of magnetic interactions as a contribution to the mechanism that governs the transition to the superconductive state.

3.4.2.2 Barium. Because of its large size and, therefore, its ability to coordinate a high number of anions, Ba^{2+} is an essential-ion type. In $\text{Y}_1\text{Ba}_2\text{Cu}_3\text{O}_{7-\delta}$, the barium must coordinate 12 oxygens. The radius ratio with oxygen gives a value of 1.02, which is at the lower limit of 12-coordination. The large field strength of barium influences the basal plane ions ($\text{Cu}(1)$ and $\text{O}(1)$), as well as the ions in the base plane of the pyramid. The field strength of barium can also influence any electrons trapped in the oxygen vacancies. This 12-coordination ability is precisely why Ba^{2+} is the ideal alkaline earth metal to accomplish the adequate separation between chain regions (basal plane) and the base planes of the pyramids in the $\text{Y}_1\text{Ba}_2\text{Cu}_3\text{O}_{7-\delta}$. Neither Sr^{2+} nor Ca^{2+} are as suitable, except as minor concentration substitutes because they cannot coordinate enough anions. The radius ratio for calcium with oxygen is 0.75, which is borderline for just eight-fold coordination. Ca^{2+} prefers six-fold coordination as in the calcite and aragonite structures. The radius ratio for Sr^{2+} is about 0.85, which normally suggests eight-coordination cubic CsCl structure and is less than borderline for the coordination of 12 oxygens, SrTiO_3 being an exception.

3.4.2.3 Cu^{2+} . The planar or edge copper ions in Figure 29 (believed to be $\text{Cu}^{2+} d^9$) are important a five-fold Jahn-Teller ion [125, 130, 131]. The Jahn-Teller connection has been described in quantum-mechanical treatments of high- T_c by Johnson et al. [132], showing oxygen p π states at the Fermi energy suggesting a "tubular" polarized Ψ^+ and Ψ^- propagation. Calculations for T_c using a Jahn-Teller approach are seemingly compatible with T_c data and suggest a maximum T_c near 240 K, at which temperature fluctuations in conductivity have been reported. The tubes set up by d_{xy} orbitals transfer charge in the z-direction, which accentuates the bridging role of the apical O_4 ion.

Specifically, the Jahn-Teller theorem states that if a subshell (t_{2g} or e_g) is neither filled, half-filled, nor empty, a distortion will occur to remove any possible degeneracy. This removal of degeneracy is due to the split of orbital energies. In the $\text{Cu}^{2+} d^9$ case, the three electrons in e_g could be arranged in either $(d_{z^2})^2 (d_{x^2-y^2})^1$ or $(d_{z^2})^1 (d_{x^2-y^2})^2$. In the former state, there would exist more repulsion between the Cu^{2+} and the ligand (O) electrons along d_{z^2} than along $d_{x^2-y^2}$ simply because of the additional electron. The net result would be a lengthening of the two bonds along d_{z^2} relative to the bonds in the $d_{x^2-y^2}$ -directions. The reverse situation would lead to a lengthening of the bonds in the $d_{x^2-y^2}$ -direction, this being very rare in nature, but observed in crystals of the CuF_4^{2-} and CuF_3^{1-} complexes. In the Cu^{2+} ions in the 1-2-3 structure, the condition is somewhat different because the coordination is five-fold rather than six- or four-fold. In oxygen stoichiometries between O_7 and $\text{O}_{6.5}$, when charge balance causes a Cu^{2+} to exist at one or more of the Cu(1) sites per x unit cells, then the situation is still unique because the symmetry in the environment of that particular set of Cu^{2+} ions is not truly octahedral, due to the missing oxygens, and is not tetrahedral because the four oxygens surrounding the site are almost square planar instead. The x-ray diffraction data support the conjecture of a Jahn-Teller distortion existing in the 1-2-3 structure because the Cu(2)-O(4) bond is lengthened relative to the Cu(2)-O(2) and Cu(2)-O(3) almost-in-plane bonds, as well as relative to the O(4)-Cu(1) bond. Hence, the d-state configuration must be $(d_{z^2})^2 (d_{x^2-y^2})^1$.

The Cu^{2+} ions are the major contributor to the 2-D charge density of the central planes (the base planes of the pyramids). Because these copper ions are so much smaller than the barium ions, it is very unlikely that they would substitute for barium.

3.4.2.4 Cu^{3+} . The Cu(l) ions, believed from electron spectroscopy chemical analysis (ESCA) to be $Cu^{3+} d^8$ (under idealized charge balance in the O_7 stoichiometry) are believed to display partial covalent, as well as partial metallic bonding, in addition to their ionicity. The covalent and metallic bonding relates to bonding to the O(l) ions, thus forming a chain substructure or polyhedral building block [126–135]. Hence, the chain copper is only truly trivalent in its extreme ionic condition, but not so on the statistical average. Thus, the Cu(l) exists in a highly mixed-bonded condition. The fact that the apical O(4) ion is coordinated in the +z- and -z-directions by two differently charged copper ions creates a gradient in the internal electric field in the neighborhood of the O(4). This gradient then facilitates the transfer of charge between the oxygens and coppers, as well as between the two types of copper ions, in the neighborhood of that field gradient. Thus, physical grounds for the charge-transfer excitation reaction $Cu^{3+} \rightarrow Cu^{2+}$ are established. This leads to the total charge-transfer relationships between the coppers and oxygens, which can be specified through every cycle of the resonance as: $Cu^{3+} + O^{2-} + O^{2-} \rightarrow Cu^0 + O^0 + O^{1-} + 3 \text{ holes}$, or $Cu^{2+} + O^{2-} \rightarrow Cu^0 + O^0 + 2 \text{ holes}$.

3.4.2.5 Oxygen. The significance of oxygen is associated with a host matrix to which the holes or virtual excitons are bound. In this role, the O(4) is perhaps the most important of the oxygen ions because it bridges the pyramidal and chain polyhedral building blocks [126]. It is important to note that other group IV cations, such as sulfur, selenium, and tellurium, cannot be substituted for oxygen except in very small weight-percents without the loss of superconductivity in the 1-2-3 structure. This may be due to crystal radii criteria relative to the integrity of the pyramidal structure; but may also in some way involve oxygen's paramagnetism as contrasted to the diamagnetism of sulfur, selenium, and tellurium; or may be related to considerations involving electronegativity. The absence of O(4) mirror symmetry causes lattice dynamics anharmonicity [126, 133], which gives rise to internal local electric fields.

Table 2 gives some of the crystal chemistry criteria identified in the previous sections.

3.4.3 Ionic Charge and Stability Considerations. The $Y_1Ba_2Cu_3O_{7-\delta}$ structure shows reproducible superconductivity in the neighborhood of 82–90 K, compared to the inconsistent data on the precursor materials CuCl and CdS. Factors that decrease the stability of the oxide

Table 2. Calculation of Oxygen, Cu²⁺, and Cu³⁺ Stoichiometries

Oxygen			
Plane and Oxygen Designation	No. of O ²⁻ Ions	Contribution of Each to Unit Cell	Total in Plane
1. Top Cu ³⁺ Plane (O1)	2	1/4	1/2
2. Ba ²⁺ Plane (O4)	4	1/4	1
3. Cu ²⁺ Edge Plane (O3 in b-Axis)	4	1/2	2
4. Y ³⁺ Plane	0	0	0
5. Cu ²⁺ Edge Plane	4	1/2	2
6. Ba ²⁺ Plane (O4)	4	1/4	1
7. Bottom Cu ³⁺ Plane (O1)	2	1/4	1/2
			Total = 7
Cu ²⁺			
Coordination No. Plane	No. of Ions	Contribution of Each to Unit Cell	Total
1	0	—	0
2	0	—	0
3	4	1/4	1
4	0	—	0
5	4	1/4	1
6	0	—	0
7	0	—	0
			Total = 2
Cu ³⁺			
Coordination No. Plane	No.	Contribution	No. Ions
1	4	1/8	1/2
2	0	—	—
3	0	—	—

Table 2. Calculation of Oxygen, Cu²⁺, and Cu³⁺ Stoichiometries (continued)

Cu ³⁺			
Coordination No. Plane	No.	Contribution	No. Ions
4	0	—	—
5	0	—	—
6	0	—	—
7	4	1/8	1/2
			Total = 1

superconductors are those that involve water vapor and hostile environments. Thin film depositions as from rapidly solidified melts give some indication of assisting in improved stability [131]. Stability of the superconducting oxides against radiation and charged-particle fields is an additional consideration because of radiation effects on the ratio of states of different valence of the same atom and the production of vacancies.

Two very important considerations can be derived from inspection and scrutiny of the Y₁Ba₂Cu₃O_{7-δ} and K₂NiF₄ structures of Figures 29 and 30. The first is the relationship to antiferromagnetism or near-antiferromagnetic correlations. The second is the presence of more than a single structural building block or polyhedron of coordination, namely chains and pyramids as shown in Figure 31. In this figure, it is also shown that if the Cu(I) ion is considered as being coordinated not only to the two O(1) chain ions, but also to the two O(4) bridging apical ions of the pyramid, as well as to the two vacancy sites, then corner-sharing of an inverted pyramid with a defect octahedron can be visualized. The region between these two different-symmetry polyhedral building blocks must inescapably be subjected to highly inhomogeneous local internal perturbation electric fields.

The ionic charge description given in the previous sections corresponds to perfect ionic or electrovalent (coulombic) bonding in the absence of cation-anion wave function overlap

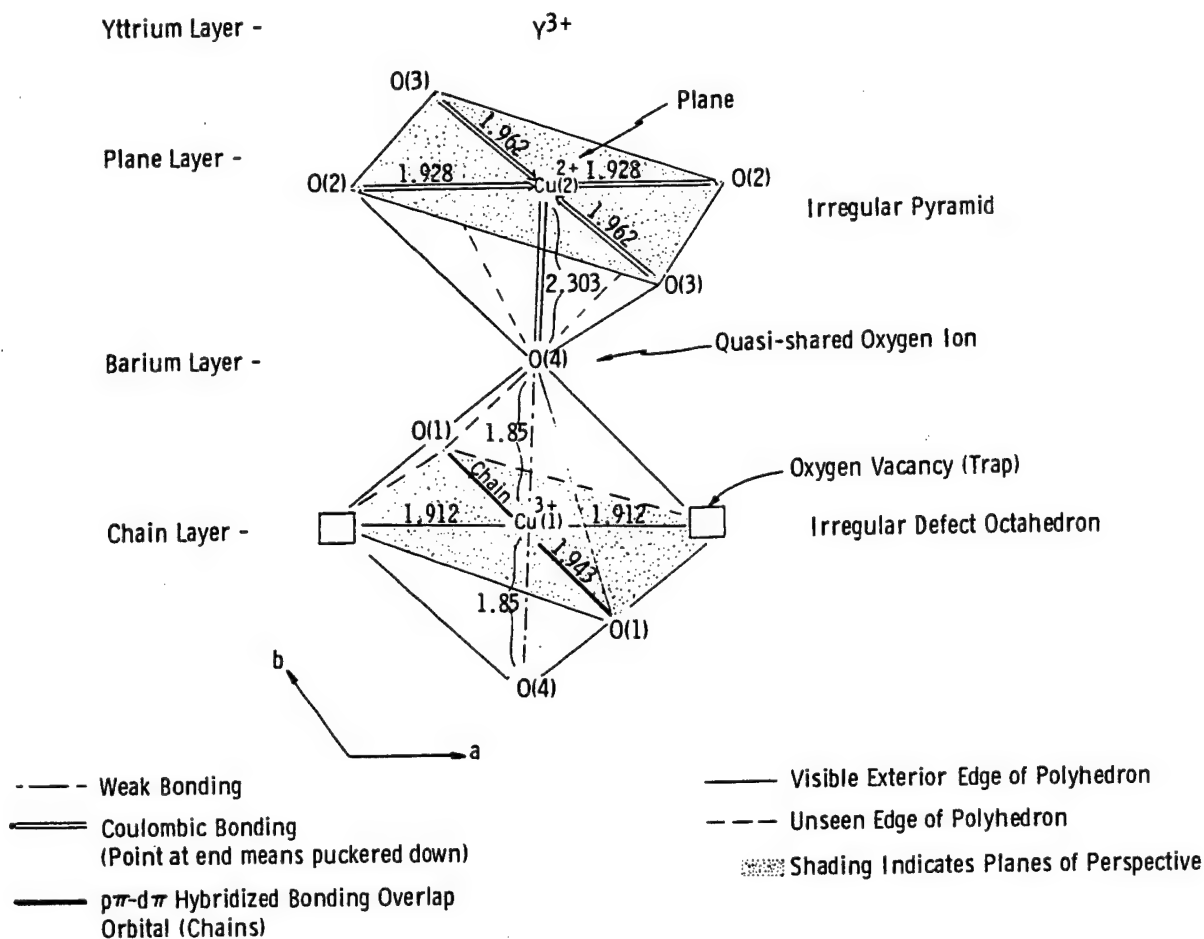


Figure 31. Single Structural Building Block and Polyhedron of Coordination (Chains and Pyramids).

hybridization. In $Y_1Ba_2Cu_3O_{7-\delta}$, such hybridization occurs especially in the chain region $Cu(1)O(1)Cu(1)O(1)Cu(1)$ in the form of d-p π bonding overlap formed by $Cu(1) 3d_{xy}$ and $O(1) 2p_y$ orbitals. In addition the $Cu(2)^{2+}$, which coordinates the pyramid of oxygens, also admits to bonding hybridization (albeit to a lesser degree) with the ligand oxygens. This hybridization alters the average charge on the ions to a modified value shown in Table 3. It is noted that in this averaged value, it is possible for charge not to balance because the averaged value is not a steady-state equilibrium configuration, but instead an expectation value [132].

Table 3. Ionic Charge in $Y_1Ba_2Cu_3O_{7-\delta}$

	Idealized Charge	Modified Charge Due to Hybridization
Cu(2)	2+	1.60+
O(2)	2-	1.98-
O(3)	2-	1.94-
O(4)	2-	1.54-
O(1)	2-	1.85-
Cu(1)	3+	1.16+
Y	3+	3+
Ba	2+	2+

It has also been found that T_c is critically related to the deviation δ from O_7 stoichiometry as shown in Figure 32. In the data of Figure 32, the oxygen content x can be converted into a ratio of Cu^{2+} to Cu^{3+} by solving simple charge-balance equations. For example, for $x = 0.93$, such that stoichiometry is $O_{6.93}$. This stoichiometry corresponds to a maximum T_c . The compound can be written as $y^{3+}Cu_y^{3+}Ba_2^{2+}Cu_{3-y}^{2+}$, which, after simple solution of crystal chemical equation yields $y = 0.86$ or $0.86 Cu(1)^{3+}$ and $2.14 Cu(2)^{2+}$. This gives a Cu^{2+}/Cu^{3+} ratio of ~ 2.5 for a maximum T_c . If the mixed-valence condition is indeed necessary (as interpreted herein), then this implies that at exactly $x = 6.5$, there should not be a superconductive state if all of the coppers are in the $2+$ valence state, as suggested by simple charge balance for the $O_{6.5}$ stoichiometry. Deviation from the all- Cu^{2+} condition, however, may be in the form of the occurrence of Cu^{1+} and Cu^{3+} states. For $x > 6.5$, Figure 32 (using the upper abscissa) gives the ratios of Cu^{2+}/Cu^{3+} corresponding to a specific x and corresponding experimentally to the dependent T_c . The figure shows that superconductivity terminates at $x = 0.44$ instead of, as predicted, $x = 0.50$. This discrepancy is probably due to the factors that relate to states of matter near a phase boundary, particularly metastable configurations.

3.4.4 Radius Ratio and Coordination Number Considerations. Table 4 gives a listing of the multivalent ions that are diamagnetic in their zero-valence state and have been successfully utilized

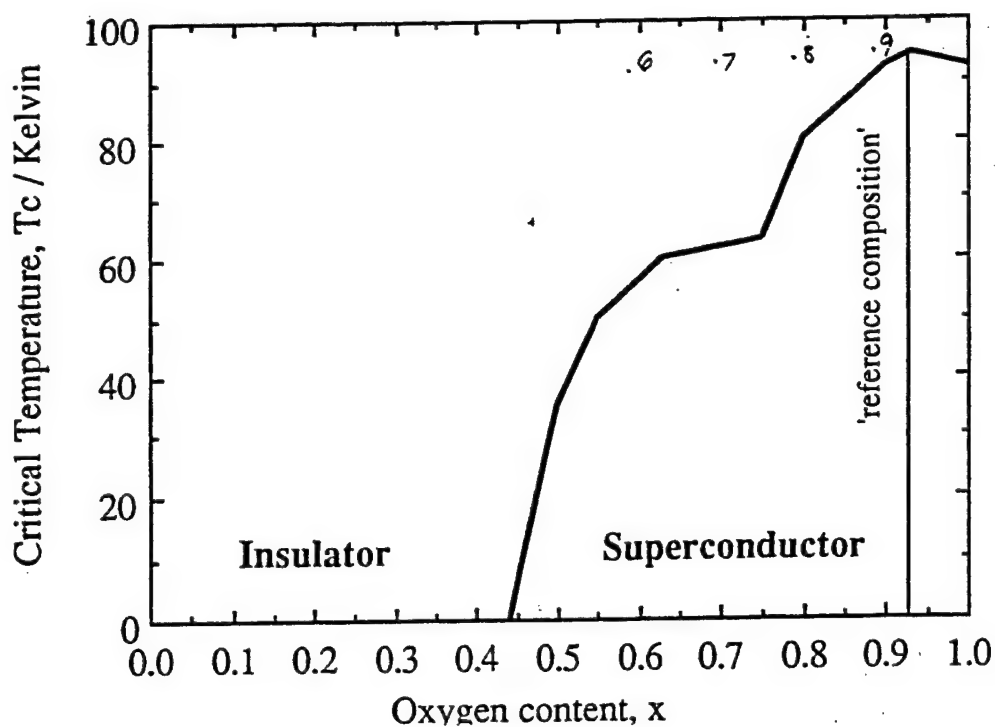


Figure 32. Ratios of $\text{Cu}^{2+}/\text{Cu}^{3+}$ to T_c .

as constituents of high- T_c materials. The columns include ion charge, ionic radius, the ratio of charge to radius (Z/r), the radius ratio (RR), and consequent expected coordination number (CN) with respect to the anion O^{2-} and with respect to related anions S^{2-} , Se^{2-} , Te^{2-} , F^{1-} , and Cl^{1-} . This table shows, from a stereochemical standpoint, why oxygen is an appropriate anion, in that it coordinates in a five-fold or six-fold manner in the great majority of cases. Such coordination produces the quasi-pyramids and the octahedra for polyhedral building blocks of high- T_c materials. With respect to Cu^{3+} , oxygen can still coordinate five-fold or six-fold (to form the defect octahedron described earlier). The reason why the Cu(1) does not, however, coordinate six oxygens is because the two O(4) oxygens are elements of the coulombic pyramids (with shortened Cu(1)-O(4) bonds because of Jahn-Teller distortion) and in that sense are not strongly bonded to the Cu(1), and the two oxygens in the base plane at the $1/2, 0, 0$ sites are missing in order to produce proper charge-balanced stoichiometry. Thus, from a bonding standpoint, two-fold chain coordination for Cu(1) is readily explicable. The table also shows why only a very small molar weight of Ga^{3+} and Sb^{5+} can be substituted into the YBaCuO-based superconductor and the bismuth-based superconductor (to be discussed subsequently), respectively. This is because the radius ratios for these ions are just

Table 4. Radius Ratio [R(CAT)/R(AN)] and Coordination No.

Ion Charge	r (Å)	Z/r	RR/CN					
			O ²⁻	S ²⁻	Se ²⁻	Te ²⁻	F ⁻	Cl ⁻
Bi ⁺	0.98	1.02	0.74/6, 8	0.53/5, 6	0.51/5, 6	0.46/5, 6	0.74	0.54/5, 6
Bi ³⁺	0.96	3.13	0.73/5, 6	0.52/5, 6	0.50/5, 6	0.45/5, 6	0.72	0.53/5, 6
Bi ⁵⁺	0.74	6.76	0.56/5, 6	0.40/4	0.39/4	0.35/4	0.56	0.41/4, 5
Cu ⁺	0.96	1.04	0.73/5, 6	0.52/5, 6	0.50/5, 6	0.45/4	0.72	0.53/5, 6
Cu ²⁺	0.72	2.78	0.55/5, 6	0.39/4	0.38/4	0.34/4	0.54	0.40/4, 5
Cu ³⁺	0.68	4.41	0.52/5, 6	0.37/4	0.36/4	0.32/4	0.51	0.38/4
Tl ²⁺	1.47	0.68	1.12/1, 2	0.80/8	0.77/8	0.70/5, 6	1.11	0.81/8
Tl ³⁺	0.95	3.16	0.72/5, 6	0.52/5, 6	0.50/5, 6	0.45/5, 6	0.71	0.52/5, 6
Pb ²⁺	1.2	1.67	0.11375	0.65/5, 6	0.63/5, 6	0.57/5, 6	0.9	0.66/5, 6
Pb ⁴⁺	0.84	4.76	0.64/5, 6	0.46/5, 6	0.44/5, 6	0.40/4, 5	0.63	0.46/5, 6
Ga ⁺	0.81	1.23	0.61/5, 6	0.44/5, 6	0.42/5, 6	0.38/4	0.61	0.45/5, 6
Ga ³⁺	0.62	4.84	0.47/5, 6	0.34/4	0.322/4	0.29/4	0.47	0.34/4
Sb ³⁺	0.76	3.95	0.58/5, 6	0.44/5	0.40/4	0.36/4	0.57	0.42/4, 5
Sb ⁵⁺	0.62	8.06	0.47/5, 6	0.36/4	0.32/4	0.0725	0.47	0.34/4
Ag ⁺	1.26	0.8	0.90/8	0.68/5, 6	0.66/5, 6	0.60/5, 6	0.95	0.70/5, 6
Ag ²⁺	0.89	1.12	0.68/5, 6	0.48/5, 6	0.47/5, 6	0.42/5, 5	0.67	0.49/5, 6
Sn ²⁺	0.93	1.09	0.70/5, 6	0.51/5, 6	0.49/5, 6	0.44/5, 6	0.7	0.51/5, 6
Sn ⁴⁺	0.71	5.64	0.54/5, 6	0.39/4	0.37/5, 6	0.34/4	0.53	0.39/4
Zn ⁺	0.88	1.04	0.67/5, 6	0.48/5, 6	0.46/5, 6	0.42/4	0.66	0.49/5, 6
Zn ²⁺	0.74	1.35	0.56/5, 6	0.40/4	0.39/4, 5	0.35/4	0.56	0.41/4, 5

NOTES: CN - Coordination No.
 RR - Radius Ratio
 Z/r - Ratio of Charge to Radius

above the minimal value for five- and six-fold coordination (almost borderline), and, hence, these ions can only substitute in very small concentrations (agreeing perfectly with our experiments, showing only a fraction of a percent substitution allowable).

Table 4 also indicates that the S^{2-} , Se^{2-} , Te^{2-} , and Cl^{1-} are not suitable anions for the $Y_1Ba_2Cu_3O_{7-\delta}$ structure because the radius ratio with respect to Cu^{2+} does not fall within the limit for five-fold quasi-pyramidal or six-fold octahedral coordination. This is also true for Br^{1-} and I^{1-} , but not for F^{1-} . The ionic radius of F^{1-} is so close to that for O^{2-} that from a size standpoint, they are interchangeable. Hence, the limitations of any possible fluorine substitution for oxygen in the high- T_c materials would be due to charge and electron affinity criteria.

The Z/r criteria (field strength) will be treated in general terms in the next section.

Table 5 analogues Table 4, but includes multivalence ions that are diamagnetic in the zero-valence state (and hence are feasible candidates for high- T_c from those standpoints), but have not been satisfactorily substituted into high- T_c superconductors. The reason for the inappropriateness of substitution stems from radius ratios that do not fit five- and six-fold coordination, excessive charge of ions that could otherwise suite two-coordinated chain species, or inappropriate Z/r values. Ge^{2+} and Ge^{4+} may be exceptions to this viewpoint and may eventually be capable of substitution into high- T_c materials similar to the way that lead has been successfully substituted.

3.4.5 Isotope and Charge Concentration Considerations. The enormous increase in T_c due to the materials science research in the 1986–1987 time frame is well illustrated in Figure 33. These unusually high temperatures and the absence of sufficiently large isotope effects in the new oxide superconductors argued against a purely electron-phonon coupling BCS conventional-type of mechanism for superconductivity in the new oxides.

Further indication that the new materials did not subscribe to a phonon-based mechanism is derived from the work of Gallo, Whitney, and Walsh [134] and Beasley and Geballe [135]. The latter work showed critical temperature vs. carrier concentration for the new high- T_c materials

Table 5. Radius Ratio [R(CAT)/R(AN)] and Coordination No., Including Multivalence Ions Diamagnetic in the Zero-Valence State

Ion Charge	r (Å)	Z/r	RR/CN					
			O ²⁻	S ²⁻	Se ²⁻	Te ²⁻	F ⁻	Cl ⁻
Be ⁺	0.44	2.27	0.33/4	0.24/3, 4	0.23/3, 4	0.21/3	0.33	0.24/4
Be ²⁺	0.35	5.71	0.27/4	0.19/2	0.18/3	0.17/3	0.26	0.19/3
B ⁺	0.35	2.27	0.27/4	0.19/2	0.18/3	0.17/3	0.26	0.19/3
B ³⁺	0.23	4.34	0.17/4, 3	0.13/2	0.12/2	0.11/2	0.17	0.13/2
Ge ²⁺	0.73	2.75	0.56/5, 6	0.40/4	0.38/4	0.35/4	0.55	0.40/4, 5
Ge ⁴⁺	0.53	7.55	0.40/4	0.29/4	0.28/4	0.25/3, 4	0.4	0.29/4
Hg ⁺	1.27	0.79	0.96/8	0.69/5, 6	0.66/5, 6	0.60/5, 6	0.95	0.70/5, 6
Hg ²⁺	1.1	1.82	0.83/8	0.60/5, 6	0.58/5, 6	0.52/5, 6	0.83	0.61/5, 6
P ³⁺	0.44	6.8	0.33/4	0.24/4	0.23/3, 4	0.21/3, 4	0.33	0.24/4
P ⁵⁺	0.35	14.3	0.27/4	0.19/3	0.18/3	0.17/3	0.26	0.19/3
As ⁵⁺	0.46	10.8	0.35/4	0.25/3, 4	0.24/3, 4	0.22/3, 4	0.35/4	0.25/4
As ³⁺	0.58	5.2	0.44/5, 6	0.32/4	0.30/4	0.27/4	0.44/4	0.32/4

NOTES: CN - Coordination No.
RR - Radius Ratio
Z/r - Ratio of Charge to Radius

(reproduced in Figure 34), which did not fit the expected dependence of T_c on the carrier density N for the BCS phonon-electron coupling, but are in accord with what would be expected from an exciton coupling theory [93–95] as shown in Figure 35.

3.5 The Thallium-Based and Bismuth-Based High- T_c Superconductors.

3.5.1 Structure and Composition. A series of thallium-based and bismuth-based high- T_c superconductors having layered structures to include $Tl_2Ba_2CuO_6$, $Tl_2CaBa_2Cu_2O_8$,

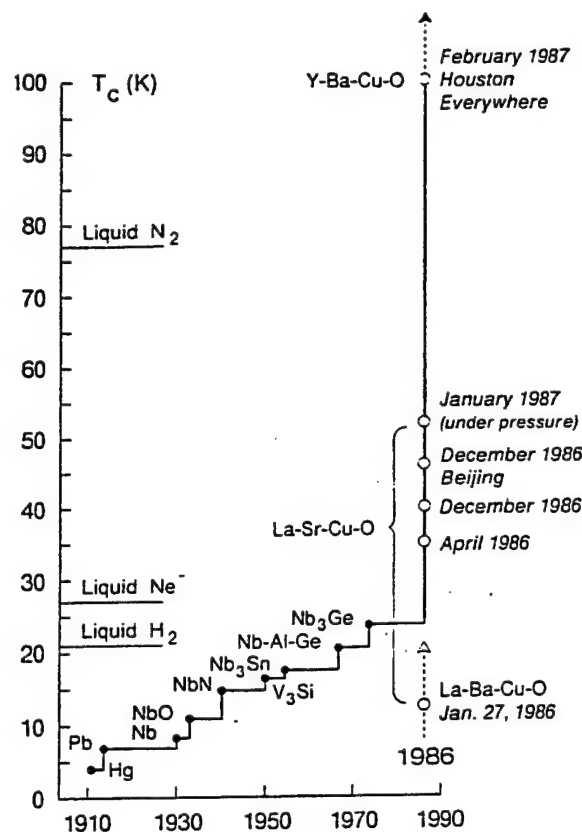


Figure 33. Increase in T_c .

$Tl_1Ca_1Ba_2Cu_2O_7$, $Tl_2Ca_2Ba_2Cu_3O_{10}$, $Bi_2Ca_2Sr_2Cu_3O_{10}$, $Bi_2Ca_1Sr_2Cu_2O_8$, and related materials was synthesized by a number of researchers [136–143]. The crystal structures of the thallium-based materials are given in Figures 36 and 37a and shown to contain more than a single building block polyhedron of coordination, such as octahedra and sheets (planes), or pyramids, octahedra, and sheets. In Figure 37, the structure of $TlCaBa_2Cu_2O_7$ is compared to $YBa_2Cu_3O_{7-\delta}$ and to K_2MnF_4 . In $TlCaBa_2Cu_2O_7$, charge-balance criteria (again for idealized ionic bonding) demand that one-half of the copper ions coordinating the polyhedra are in the +2 state, and one half are in the +3 valence, again indicating the presence of multivalence. The fact that bismuth and thallium can both exist in a monovalent and trivalent state, that barium and strontium are favorable stereochemical ions to control interplanar spacing, and that calcium is a favorable producer of mobile holes renders these compounds subject to similar physics and materials science research approaches as $YBa_2Cu_3O_{7-\delta}$. The properties of some of these compounds are given later along with interpretations of the commonality of mechanistic criteria.

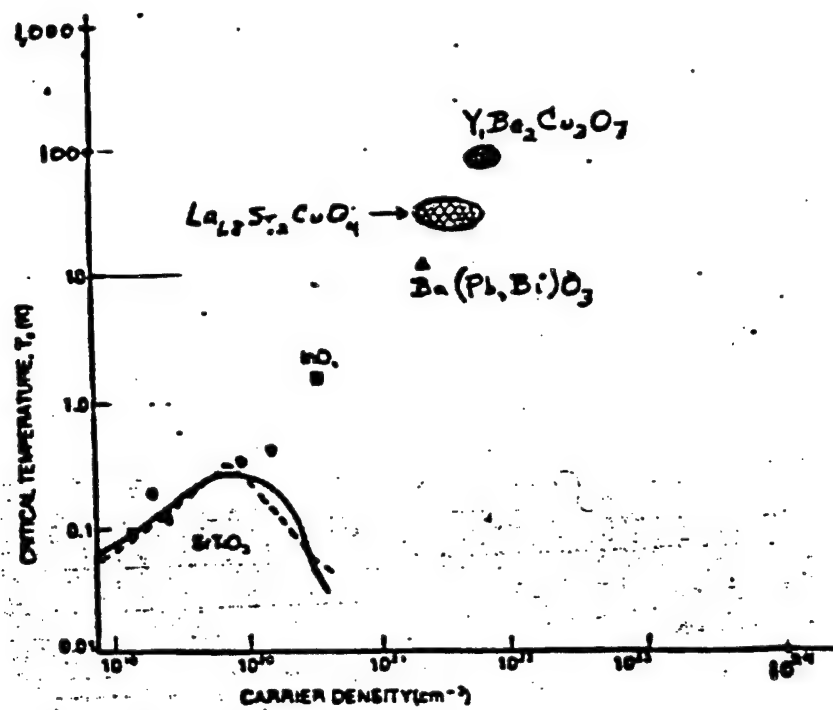


Figure 34. T_c vs. Carrier Concentration for High- T_c Materials.

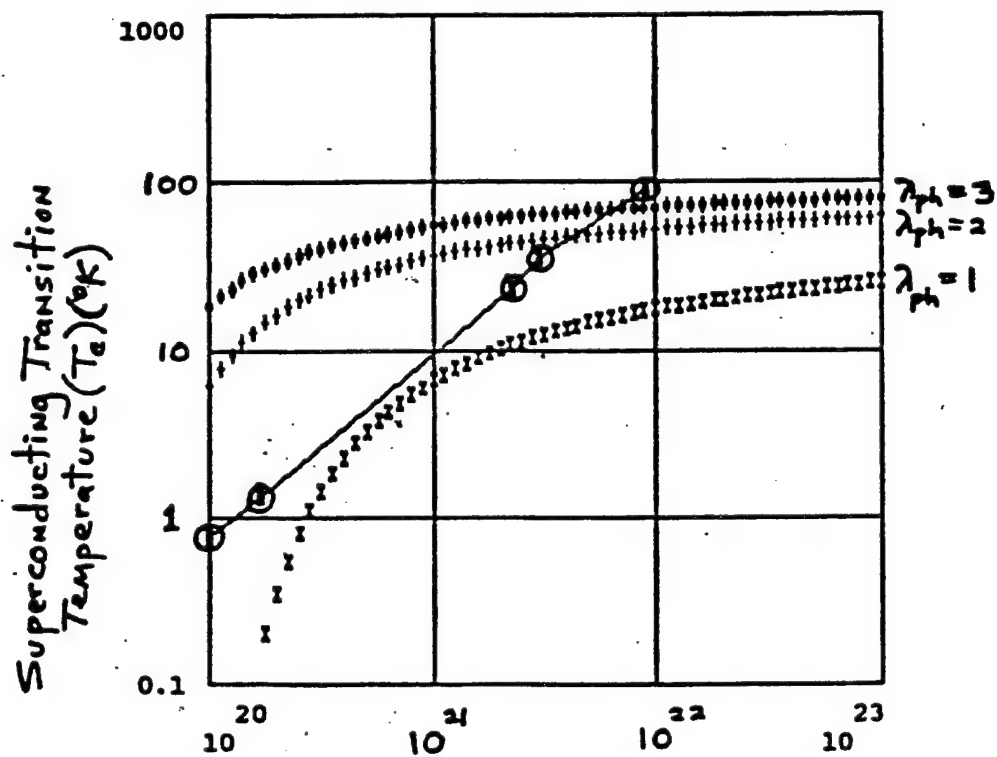


Figure 35. Dependency of Carrier Density N for the BCS Phonon-Electron Coupling.

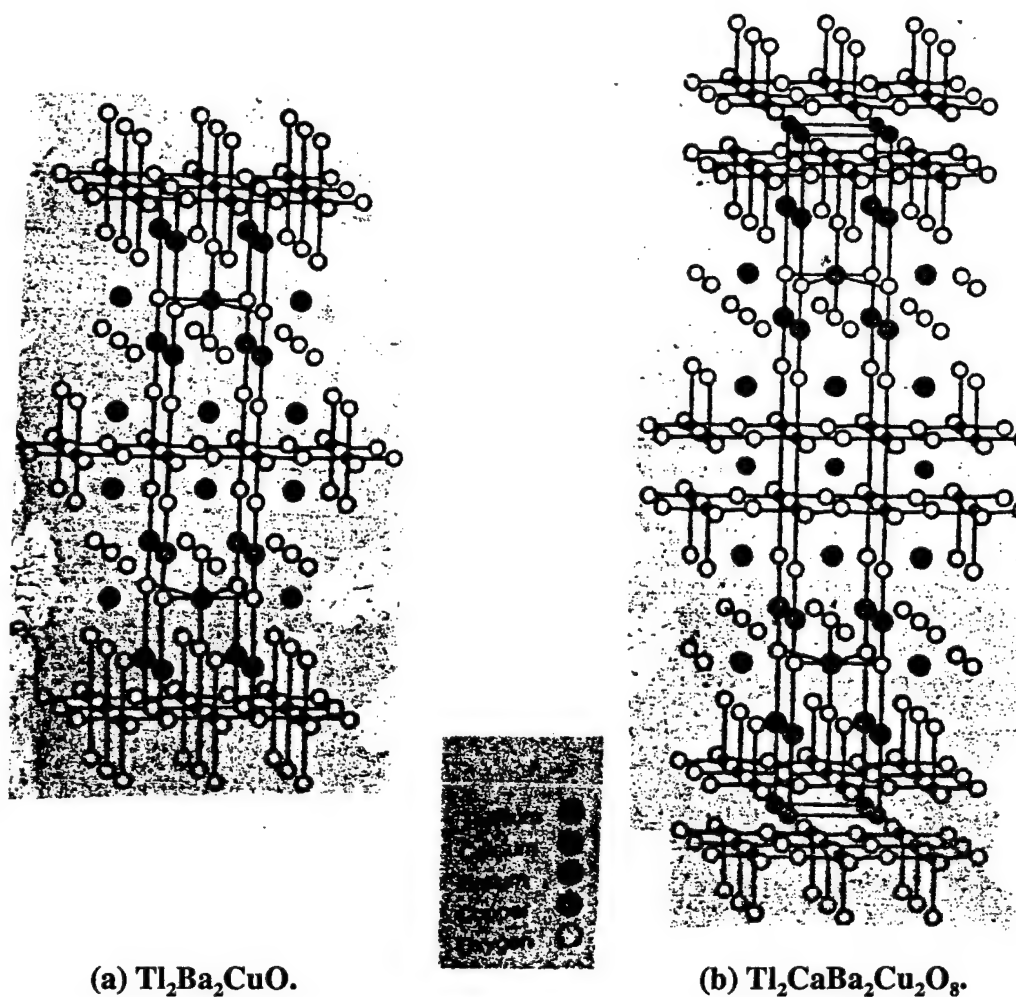


Figure 36. Crystal Structures of (a) $\text{Tl}_2\text{Ba}_2\text{CuO}_6$ and (b) $\text{Tl}_2\text{CaBa}_2\text{Cu}_2\text{O}_8$.

3.5.2 Size and Radius Ratio Criteria for High- T_c Superconductors. The reader is again asked to refer to Tables 4 and 5. It is notable in Table 4, from a coordination-number standpoint with respect to oxygen, that the Tl^{1+} state and possibly the Pb^{2+} state may indeed not participate in the charge-transfer excitations associated with principal multivalence cations. However, in high- T_c compounds that contain thallium and lead, the bismuth and copper ions may take on the full responsibilities for the charge-transfer excitations. However, the very high frequency of the charge-transfer excitation (its virtual nature) may loosen steric requirements and permit otherwise forbidden states. The range of Z/r in Tables 4 and 5 is dictated by field-strength criteria that relate to charge-
The high Z/r ions ($>\sim 3$) are favored for the electrolattice dynamics of high- T_c materials; however, transfer excitations (or virtual excitons), which are discussed in detail subsequently in this report.

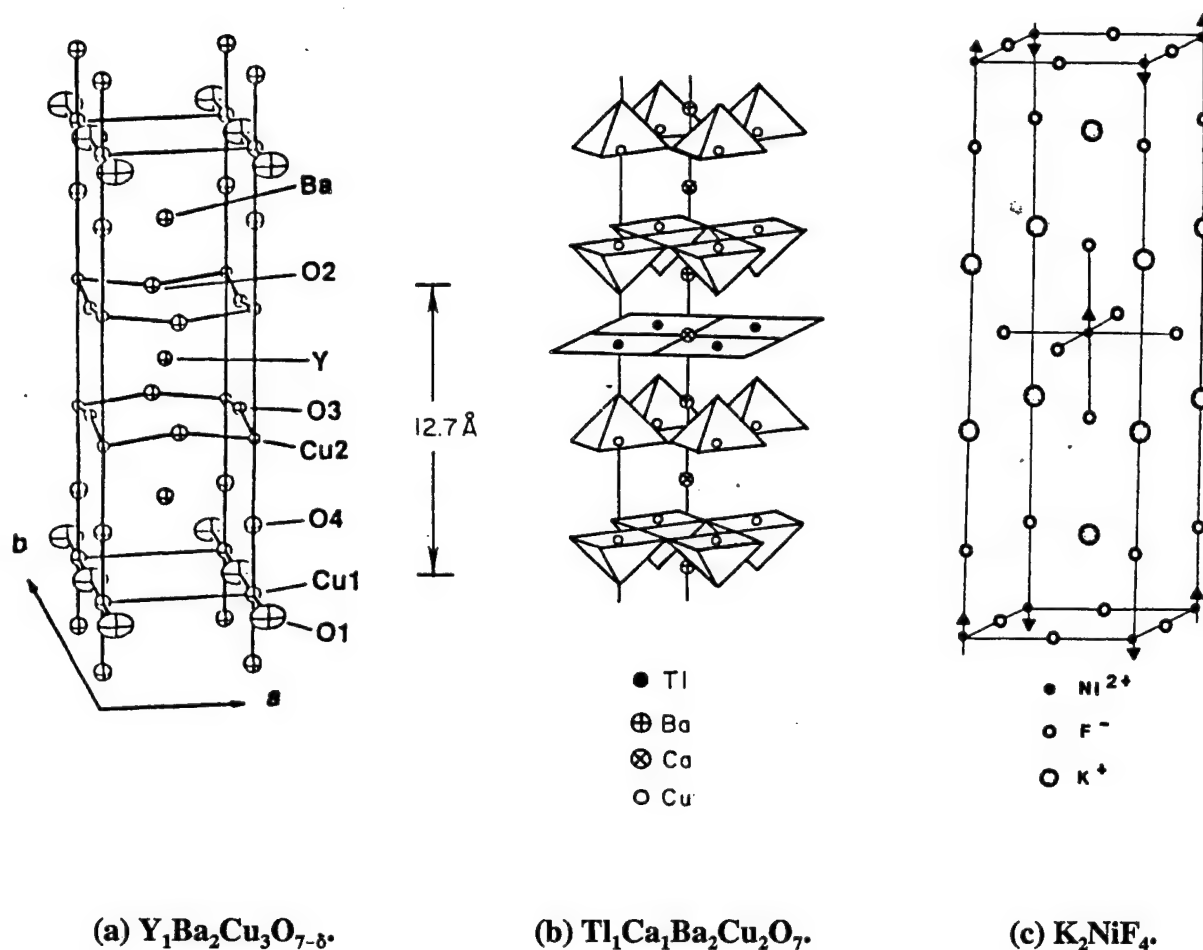


Figure 37. Crystal Structures of (a) $\text{Y}_1\text{Ba}_2\text{Cu}_3\text{O}_{7-\delta}$, (b) $\text{Tl}_1\text{Ca}_1\text{Ba}_2\text{Cu}_2\text{O}_7$, and (c) K_2NiF_4 .

the full effects of field-strength criteria and chemical potential have not yet been established in high- T_c superconductors.

3.6 Major Experimental Findings of Others That Are Related to the USAMTL Approach and Interpretations. The following sections are summaries of research findings of others that have been very valuable to our understanding of high- T_c materials during the course of our own study. (They are listed by topic.)

3.6.1 Excitons. Superconducting samples of $\text{YBa}_2\text{Cu}_3\text{O}_{7-y}$ that were studied at the University of Florida ($y = 0.1$) showed two strong electronic transitions at $3,000 \text{ cm}^{-1}$ (0.37 eV) and at

20,000 cm^{-1} (2.5 eV), which correspond to exciton absorption peaks. Nonsuperconducting samples ($y \approx 0.8$) did not show these features [136]. A strong polarization-sensitive resonant enhancement of selected Raman lines is observed in single-crystal $\text{La}_2\text{CuO}_{4+y}$ near a 2 eV electronic transition at room temperature [144]. The resonance phenomena are observed only for light polarized parallel to the CuO layers and are generally quenched with addition of excess oxygen. These results are consistent with a 2-D charge-transfer excitation from a copper ion to the four neighboring oxygen ions (a symmetric charge excitation or virtual exciton) [136].

3.6.2 Antiferromagnetism. Neutron diffraction measurements at Brookhaven and Exxon on $\text{YBa}_2\text{Cu}_3\text{O}_{6+x}$ (nonsuperconducting with $x = 0.0$ and ≈ 0.15) show the existence of long-range, 3-D, antiferromagnetic order of the copper spins with a Neel Temperature of 400 ± 10 K for $x = 0.15 \pm 0.05$ and ≥ 500 K for $x = 0.0$ [145, 146]. Antiferromagnetism was also discovered in $\text{La}_2\text{CuO}_{4-y}$. The antiferromagnetism in $\text{La}_{2-x}\text{Sr}_x\text{CuO}_4$ is in a half-filled $\sigma_{x^2-y^2}$ band and the material undergoes the charge-transfer equilibrium $\text{Cu}^{3+} + \text{O}^{2-} = \text{Cu}^{2+} + \text{O}^{1-}$ [147]. Antiferromagnetism has also been observed at the RE sites in $\text{RE}_1\text{Ba}_2\text{Cu}_3\text{O}_{7-\delta}$, with a Neel Temperature of 0.3 K for $\text{Gd}_1\text{Ba}_2\text{Cu}_3\text{O}_{7-\delta}$ [148]. Thus, when substituted for yttrium, the RE ions retain their local moments and can be readily magnetized by an applied magnetic field. This can occur even in the superconductive state at temperatures well below T_c . Therefore, independent superconductivity and paramagnetism can exist in these RE derivatives, such as in $\text{Ho}_1\text{Ba}_2\text{Cu}_3\text{O}_z$ [148]. The antiferromagnetism in nonsuperconducting compounds of $\text{Y}_1\text{Ba}_2\text{Cu}_3\text{O}_{7-\delta}$ implies the absence of spin fluctuations, which, according to the earlier description of mechanisms in section 1.2 would be in consonance with a system that is not superconducting at high- T_c .

3.6.3 Hall Effect. The Hall effect studies of ceramic and single-crystal high- T_c superconductors, excepting the Ce-Nd system, show domination by holes in the charge transport properties [149]. In the ceramic polycrystalline material $\text{La}_{1.85}\text{Sr}_{0.15}\text{CuO}_4$, work conducted at the University of California, Berkeley, reported that the Hall coefficient shows a narrow delta-function-like peak as reproduced in Figure 38 [150]. This finding was very much a keynote in motivating our own very detailed Hall effect studies conducted at the Francis Bitter National Magnet Laboratory. The structure of Figure 38 seemed in consonance to Vizzoli with a long-favored viewpoint of an exciton-induced

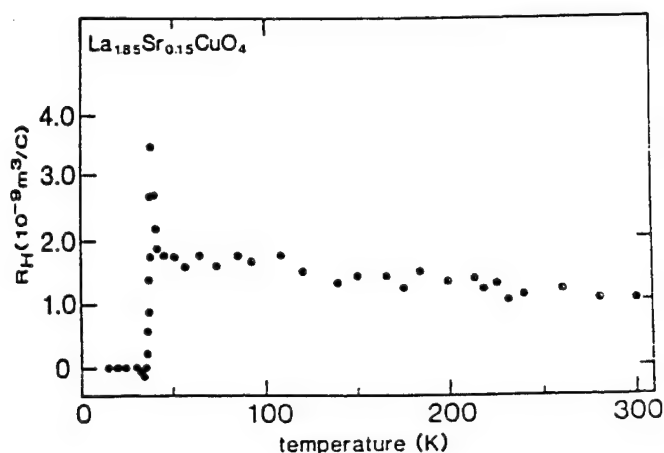


Figure 38. Hall Constant in $\text{La}_{1.85}\text{Sr}_{0.15}\text{CuO}_4$ vs. Temperature.

mechanism for high- T_c superconductivity. Even in single-crystal Hall effect studies, anomalous behavior in the Hall coefficient was observed near T_c and near the temperature where the electrical resistance became zero. The latter region in Figure 38 shows a change of sign, suggesting that negative carrier concentration may overtake the positive carrier concentration or that other anomalies are occurring. An observation suggesting the decrease in hole concentration and the increase in electron concentration (the downward trend in the Hall coefficient subsequent to the peak as temperature is lowered beneath T_c) also seemed to be in accord with an exciton viewpoint. Specifically, the relationship to excitons involved the extraction of holes from the charge-transport system in favor of the formation of excitons as the temperature was lowered to the vicinity of T_c (the positive Hall coefficient would then rise), and secondly the ionization of these weakly bonded excitons when Cooper-pair-forming forces competed with the exciton binding force, thus releasing electrons and holes, which would be free to participate in charge transport until they suffered recombination or become trapped or bound. A more detailed analysis of the Hall experiments will be given in the experimental results and interpretations sections of this report.

3.6.4 Fermi Surface. Positron annihilation experiments conducted at Brandeis University, as well as in Geneva and at Argonne National Laboratory, indicated a true Fermi surface for $\text{YBa}_2\text{Cu}_3\text{O}_{7-\delta}$ [151]. This suggested a Fermi-liquid-type material, which had been predicted by Freeman and Yu [152] at Northwestern University and by Pickett [153] at the Naval Research

Laboratory, and was later corroborated in photoemission studies by Arko [154] at Los Alamos National Laboratories. (In January of 1992, the cover feature of the highly respected learned periodical *Science* presented more recent work by Pickett et al., which fully delineated the Fermi surface for $\text{YBa}_2\text{Cu}_3\text{O}_{7-\delta}$ [155] and indicated that only the exciton, electron-phonon, and spin fluctuation theoretical mechanisms were compatible with the Fermi surface data in a reasonable manner.) All of these findings in their conventional meaning were thus not in accord with those theoretical viewpoints that believed that the high- T_c superconductors were non-Fermi-liquid materials. However, special-case conditions, which might involve a spin rather than charge description of a Fermi surface, were (are) thought by some to still remain feasible. Also, in order to explain some of the fine structure in the photoemission and NMR spectra, which are not normally associated with a Fermi liquid, the term of "marginal Fermi liquid" has been invoked [156]. Examples of Fermi surfaces analyzed from Brillouin zone theoretical studies are given in Figure 39 [157].

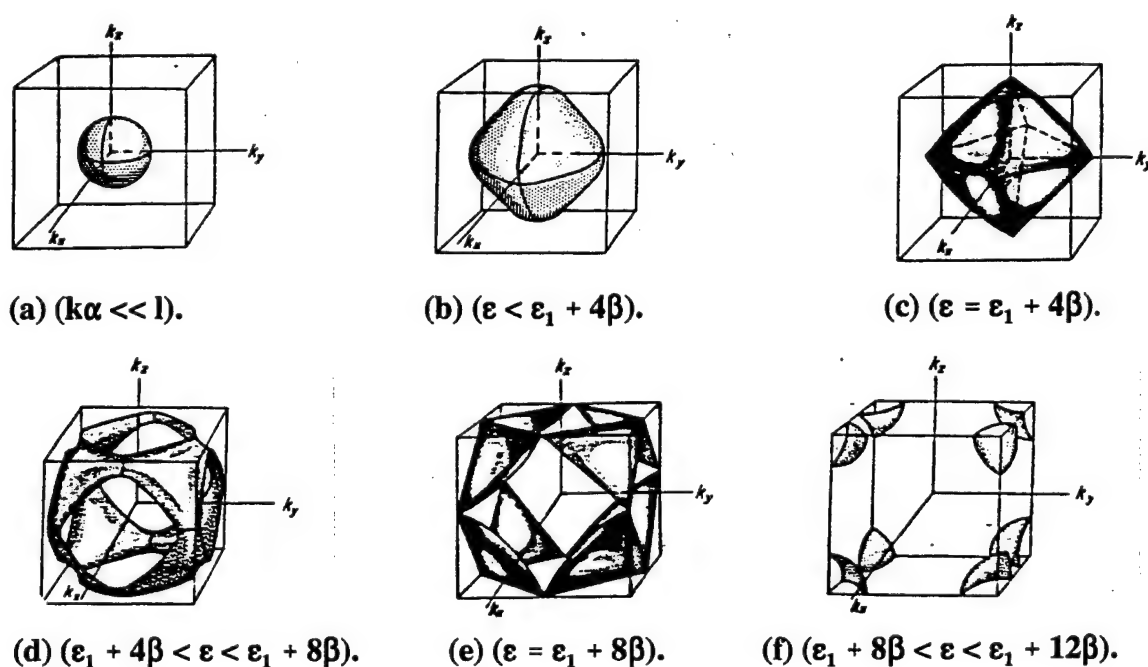


Figure 39. Fermi Surfaces Analyzed From Brillouin Zone.

3.6.5 Valence of Copper. Use of x-ray absorption fine structure spectroscopy (EXAFS), conducted at the Boeing Aircraft Company by Lytle [158], and ESCA conducted at Bell Telephone

Laboratories by Cava [159], showed that at least a portion of the copper ions in the compound $\text{YBa}_2\text{Cu}_3\text{O}_{7-\delta}$ were in a valence state greater than 2+. These ions were believed to be in the chain region of the unit cell. This was in accord with our own crystal chemical viewpoint expressed much earlier in Vezzoli, Benfer, and Spurgeon [123]. Photoelectron spectroscopy studies at the Max Planck - Fritz Haber Institute conducted on $\text{Y}_1\text{Ba}_2\text{Cu}_3\text{O}_{7-\delta}$ (and compared to a molecular Cu III complex) indicated from the Cu 2p core-level spectra that the minority copper ions are in formal valency 3+ and undergo strongly covalent interaction with oxygens [160].

3.6.6 Superconducting Gap. The presence or absence of a true energy gap in superconducting compounds has been a controversial matter. In the work of some researchers, no gap was observed, and, in others, indication was found for interpreting two gaps to exist. A superconductor can possess only one gap in the normal meaning of the notion of a gap in a zero-resistance material, namely the energy of Cooper pairing (rather than the energy between insulating and conduction states). The results of Meservey [161] are given in Figure 40 and show the presence of a gap of typically BCS magnitude, namely $2E_g = 3.53 \text{ kT}$.

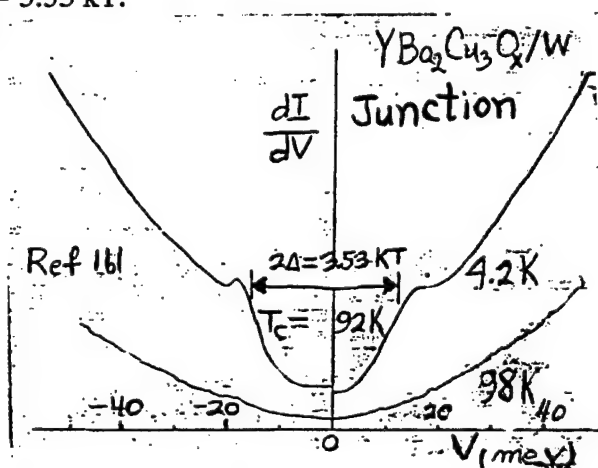


Figure 40. Meservey [161] Results Showing the Presence of a BCS Gap.

3.6.7 Ferroelectric Behavior. The work of Kurtz et al. [162] at The Pennsylvania State University showed for the first time that the transition to the superconducting state was from a poled state of a relaxor ferroelectric material as shown in Figure 41. This experimental finding was in accord with the theme of thought that motivated much of the early research into high- T_c materials and was in consonance with our own expectations of high internal electric fields creating

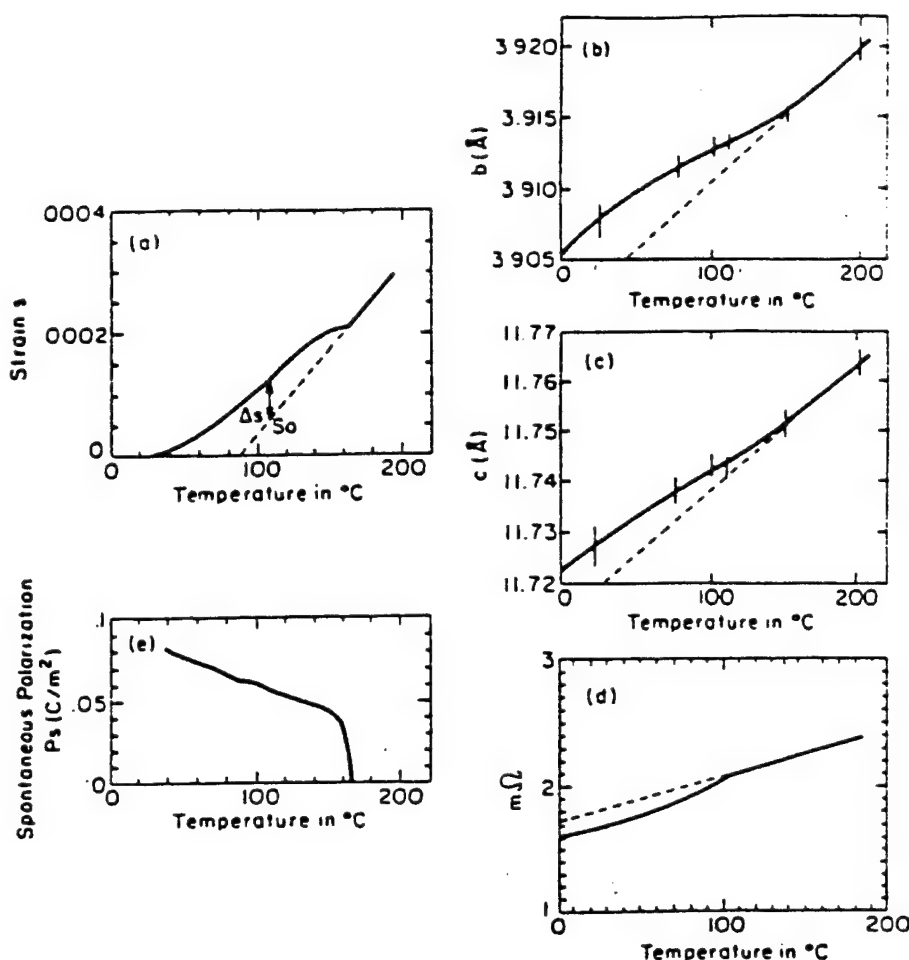


Figure 41. Superconducting State Transition From a Poled State of a Relaxor Ferroelectric Material.

microscopic ferroelectricity in charge-separation domains, as well as our prediction that at some temperature above T_c , the dielectric constant of high- T_c materials should experience a maxim (as a function of temperature). Our mathematical analysis showing the existence of microscopic ferroelectricity and very high internal electric perturbation fields in high- T_c materials is given in a later section.

3.6.8 Hole Excitation Spectra and Charge-Transfer Excitations. The work of Schuttler [163]; Zhong and Schuttler [164]; Chen and Schuttler [165]; Schuttler, Zhong, and Fedro [166]; Fedro and Schuttler [167]; Schuttler and Fedro [168]; and Chen, Schuttler, and Fedro [169] showed that for a single dopant-introduced hole carrier in the strong-coupling limit single-orbital and three-orbital Hubbard model lattice, there existed a close quantitative correspondence in the ground state and low-

lying excited state properties of high- T_c superconductors. Direct evidence was found that for the three-orbital model, there existed a singlet-triplet excitation gap associated with the CuO spin-hole singlet state. These results indicate that there exists a well-defined robust energy gap between the low-energy and high-energy states. The work of Yu and Freeman [152] showed from energy dispersion and Fermi surface analysis that charge-transfer excitations (excitons) of occupied Cu(l) - O d-p π bonding orbitals into their empty Cu(l) - O d-p σ antibonding orbital partners result in poorly screened $\text{Cu}^{n+} \rightarrow \text{Cu}^{(n+1)+}$ charge fluctuations, which (akin to the transfer that causes $\text{Cu}^{3+} \rightarrow \text{Cu}^{4+}$) induce attractive interactions ($-U$ centers) both in the chains and to the 2-D (Cu(2)) bands. High- T_c is then interpreted to be due to the exchange of these excitons. From the materials scientist point of interest, this finding motivates studies of multivalent systems that involve d-p π bonding orbitals and d-p σ antibonding orbitals.

4. Overview of the USAMTL Program

4.1 Statement of the Problem. The problem addressed in this study, simply stated, is to research the phenomenon of high- T_c superconductivity in regard to mechanism, physical and chemical properties, materials science, materials engineering, and potential usefulness of the optimized superconductive materials for applications needed by the Army.

4.2 Objectives of the Research Program.

- To develop an understanding of the general and specific physical and chemical mechanisms governing the phenomenon of high- T_c superconductivity.
- To study the materials science properties and the processing technologies of existing high- T_c materials and to understand the nature of the properties and processing as related to the materials engineering of new and improved materials. These materials science properties include structure, point and space group symmetry, valence states, stoichiometry, impurities, grain boundaries, grain and particle size, density and porosity, and chemical substitutions.

- To conduct research into new synthesis and processing techniques, which will be instrumental in elevating T_c , J_c , and H_{c1} , as well as increasing stability, especially in hostile environment conditions.
- To measure electrical, magnetic, and thermal properties of high- T_c materials in order to better understand mechanism and applications.
- To material-engineer and -design, based on all of the aforementioned objectives, ceramic high- T_c superconductors with enhanced stability and improved properties and usefulness to meet Army requirements in relevant applications.

4.3 Relevance of High- T_c Superconducting Materials to the U.S. Army's Materiel Requirements and Future Needs. The areas of Army requirements where high- T_c materials are most likely to lead to improved performance are as follows.

- Josephson junction devices for IR detection and general bolometry. (Although these devices are of thin-film configuration, many of the synthesis techniques of thin films involve very high-quality bulk ceramics for materials growth, and it is the understanding and the optimizing of these bulk materials that are the subjects of our research.
- Switching and logic devices for ultrafast digital computer operations. (These materials are also of thin film configuration, but require very high-quality starting ceramic materials for target materials in sputtering or for parent materials in deposition and epitaxy techniques.)
- Nuclear magnetic resonance imagery for medical diagnostics.
- Superconductor windings for homopolar motors to generate electromagnetic propulsion for rail gun applications, and superconductive windings for high magnetic field apparatus for research purposes.

- Frictionless bearings for tank turrets, and wheeled and tracked vehicles, as well as for rotary mechanical devices, such as helicopter blade shafts.
- Superconducting quantum-interference devices for magnetometry, possibly mine detection.
- Superconducting coatings for microwave antennae and superconducting devices in microwave systems. This application is expected to show improved sensitivity over existing microwave antennae.
- Superconducting materials, such as inductive devices and pulsers for directed energy weapons.
- Superconducting wire for low-loss power transmission.
- Superconducting applications to electro-optics and photoelectron devices related to superconducting components of intruder detection and motion-sensing fiber-optic hybrid circuits.

4.4 Short Summary of Conclusions and Breakthroughs Derived From the USAMTL Program on High- T_c Superconducting Ceramics.

- The phenomenon of high- T_c superconductivity in ceramic materials is a consequence of an electronic mechanism that couples bound holes as mediators (or virtual excitons) to conduction electrons generating Cooper pairs. The mechanism is influenced by high internal local electric perturbation fields and charge-transfer excitations.
- Key chemical ingredients in high- T_c superconducting materials are a polarizeable anion, such as oxygen, that can be crystal-chemically coordinated five- or six-fold by copper, bismuth, or a similar cation that is multivalent and diamagnetic in its atomic state, as well as large appropriate spacer ions, such as barium or strontium. The multivalence cation and

the polarizeable anion must have appropriate ionic radii to allow for polyhedral building block considerations, such as quasi-pyramidal substructures, octahedra, as well as planes and chains.

- Key structural factors in high- T_c materials are the presence of more than a single polyhedron of coordination, such as pyramids and chains, pyramids and planes, or pyramids, octahedra, and planes, as well as proper stereochemical considerations.
- Magnetic interactions related to spin fluctuations from antiferromagnetism exist in these materials and play a role in producing the superconducting Cooper-paired state.
- The maximum T_c that continued research should be able to achieve is at least -220 K, based on materials engineering and synthesis that develops a compound having high-valence-state multivalence cations that are diamagnetic in their atomic states and are in the proper radius relationship with the polarizeable anion such that very high internal electric perturbation fields exist that will furnish an optimal bound-hole concentration.
- Processing techniques that involve extremely slow cooling rates, as well as high-pressure oxygen, can enhance the stability and usefulness of properties of high- T_c materials. Processing by rapid solidification of the melt in some high- T_c materials gives rise to optimal density and optimal critical current density.
- The general category or archetype material that leads to high- T_c superconductivity is a material that shows marginal microscopic ferroelectricity of the relaxor type. These materials show high local internal electric perturbation fields that arise from polarization effects in the regions of internal electric field gradients.

5. Experimental Procedure, Synthesis, and Characterization

In this study, we concentrated on solid-state synthesizing [170–172] and processing methods of two families of ceramic copper oxide systems: $Y_1Ba_2Cu_3O_{7-\delta}$ and $BiSrCaCuO$. These syntheses included experiments aimed at substituting multivalence ions for copper in $Y_1Ba_2Cu_3O_{7-\delta}$, Gd^{3+} for Y^{3+} in the same compound and multivalence cations for bismuth and copper in the $BiCaSrCuO$ system of three different stoichiometries with nominal cation composition in the molar ratio of 1:1:1:2, 2:2:1:2, and 2:2:2:3. Substitutions were intended to test the validity of the developing theory for the mechanism of high- T_c superconductivity and to enhance the properties of the high- T_c superconductor itself. Substitutions included Ga, In, Cd, Mn, Ca, Nb, Re, and Gd in $Y_1Ba_2Cu_3O_{7-\delta}$, and Sb, V, Pb, Mn, Nb, and Re in the $BiCaSrCuO$ system. Throughout the experimental syntheses, we tested the effect of the various processing parameters of firing, sintering, and cooling temperature-time profiles. The 1-2-3 material required a lengthy period of annealing in flowing oxygen to produce the superconductivity structure; the bismuth-based or -containing materials, on the other hand, did not require oxygen annealing, but slow cooling is essential and critical $\sim 1^\circ C/5 \text{ min}$.

5.1 The $Y_1Ba_2Cu_3O_{7-\delta}$ Material. The general procedure of $Y_1Ba_2Cu_3O_{7-\delta}$ preparation and characterization is described in sections 5.1.1 through 5.1.4.

The oxide superconductors were prepared by solid-state reaction. Starting materials were high purity technical-grade powder of Y_2O_3 , $BaCO_3$, CuO , Ga_2O_3 , with required proportion for each nominal composition under study. These powders were thoroughly mixed and placed in the alumina crucible for heat treatment. Pulverizing, mixing, and calcining (heating is usually about 20 hr at $950^\circ C$) were repeated several times until high homogeneity of the resulting material was ensured. After heat treatment, the mixture was then pressed into pellets for final sintering in flowing oxygen for 12 hr at temperature $\sim 950^\circ C$. The preparations were conducted as described in sections 5.1.1 through 5.1.4.

5.1.1 Chemistry of Materials Synthesizing.

- HNO_3 conc.: 2 ml.
- Urea ($\text{CO}(\text{NH}_2)_2$): 2 μg approx.
- Acetone: 30 ml.
- Yttrium Oxide: 0.6052 g.
- Barium Carbonate: 2.1156 g.
- Cupric Oxide: 1.2792 g.

5.1.2 Purchasing Source.

AESAR Chemical
892 Lafayette Road, P.O. Box 1087
Seabrook, NH 03874-1087
Tel: 800-343-1990

5.1.3 Laboratory Equipment.

- Alumina crucible, alumina boat, and alumina plate.
- Agate mortar and pestle.
- Utility tongs.
- Heat-proof gloves and heat-proof pad.

- Regular high-temperature furnace.
- Pellet press: same as for KBR pellets for IR studies.
- Quartz tube: equipped with tight connection, made at one end for attachment to an oil-filled bubbler (tube should extend about 20 cm from either end of the furnace).
- Tank of oxygen with regulator and tygon tubing to connect to quartz tube.
- An Sm-Co magnet.
- Plastic tweezers or a pair of chopsticks.
- Furnaces: two small box furnaces with Barber Colman controller.
- A Lindberg high-temperature crucible furnace with LFE programmable controller.
- A Lindberg high-temperature 3-zone tube furnace with programmable temperature and time controller.

5.1.4 Preparation Procedure. In the mortar and pestle, the yttrium oxide, cupric oxide, and barium carbonate were ground together with enough acetone to dissolve the organic impurities. The acetone was allowed to evaporate completely in air under the hood. The well-mixed powder was transferred into a porcelain crucible. Concentrate nitric oxide was added (for better homogenous mixing), as were a few grains of urea to make a thick slurry. (Although the urea does not actually react in the process, it slows the formation of the precipitate and allows control of the size of the particles that are formed [173].) The reaction proceeded in hood, evaporating some of the acid vapor; the mixed ceramic oxide compound was transferred into a muffle furnace to dry overnight at 120° C.

The dried light-greenish-blue powder of the copper complex ion mixture was transferred into mortar and pestle for more fine grinding. This finely ground powder was then transferred into an alumina crucible. The alumina crucible containing the greenish-blue powder sample was inserted into a high-temperature furnace for thermal treatment. Firing was conducted at 950° C in 4 hr, the temperature was held constant for 24 hr, then cooling was accomplished in a furnace to room temperature at 5° C/min. When cool, the black powder was reground, and the thermal treatment was repeated at 950° C for 12 hr. The black powder was again ground in the mortar and pestle. The thermal treatment was applied for the third time for 6 hr. The sample was again ground and formed into two 1/2-in diameter pellets using the pellet presser at about 50,000 lb/in².

The pellets were placed in an alumina boat, placed in the quartz tube furnace, and heated at 950° C for 6 hr in order to sinter the pellets (to increase strength, density, and promote intergranular bonding). The tube furnace was allowed to cool to 600° C, and pure oxygen gas was passed through the quartz tube and over the pellets at a rate of about 10 ml/min for 5 hr (or 3 bubbles/s). The furnace was allowed to cool to room temperature. The sample was then tested for the Meissner Effect of levitation at liquid-nitrogen temperature by using a small magnet.

Substitutions for copper in the 1-2-3 material may be expected to yield information about the mechanism of superconductivity, believed to be a common mechanism that is operative in all high-T_c oxides. In the 1-2-3 structure [174], however, there are two distinct copper sites in this structure, the Cu(1) "chain" and Cu(2) "plane" sites. Therefore, substitutions must be engineered by size, charge, and polarizability to substitute preferentially on a particular site, or, on the other hand, be randomly distributed. Substitutions into the chain site may have a significant influence on the ordering and amount of oxygen in the chain layer [175].

Characterization of these compounds was conducted by means of x-ray diffraction, chemical analysis, morphology by SEM, density, Hall effect, transition temperature, zero-resistance temperature, and magnetoresistance. In addition, microstructure, surface chemistry, and susceptibility were studied. Specifically the following was accomplished.

- SEM morphology micrograph of 2% Sb substitution for copper in the 1-2-3 compound is shown in Figure 42, using the JOEL SEM with Kevac Energy dispersion x-ray diffractometer. The crystal structures are not homogeneous in size or shape. The sample failed to pass the levitation test at liquid-nitrogen temperature by means of the Meissner Effect.
- SEM morphology of substitution for copper with 0.5% gallium in $Y_1Ba_2(Cu_{1-x}Ga_x)_3O_{7-\delta}$ is shown in Figure 43, using the same instrument as mentioned previously. The crystals are well packed with moderate porosity. The sample was superconducting. The x-ray diffraction pattern of $Y_1Ba_2(Cu_{1-x}Ga_x)_3O_{7-\delta}$ is compared to the x-ray pattern of the published 1-2-3 pattern is shown in Figure 44, using Phillip model 1820 x-ray diffractometer.
- SEM morphology of 2% Indium substitution for copper in the 1-2-3 compound is shown in Figure 45. This material was not superconducting. Substitution of low percentages of antimony, nickel, manganese, and indium for yttrium or copper failed passing the levitation by means of Meissner's Effect at liquid-nitrogen temperature.

5.2 $Bi_{1112}(Bi_1Ca_1Sr_1Cu_2O_6)$, $Bi_{2122}(Bi_2Ca_1Sr_2Cu_2O_8)$, $Bi_{2223}(Bi_2Ca_2Sr_2Cu_3O_{10})$ General Procedure of Preparation and Characterization. We have successfully prepared many bismuth-based or bismuth-containing high- T_c compounds and investigated the relationship between superconductivity and processing parameters, finding it to be an important deciding factor regarding the state of the material. Among these processing parameters are (1) the firing profile, (2) the optimum sintering conditions, and (3) the cooling schedules.

The general procedure of solid-state synthesis and processing of bismuth-containing [176] superconducting materials is described in sections 5.2.1 through 5.2.4.



Figure 42. 2% Antimony Substitution in the $Y_{1-2,3}$ Compound.

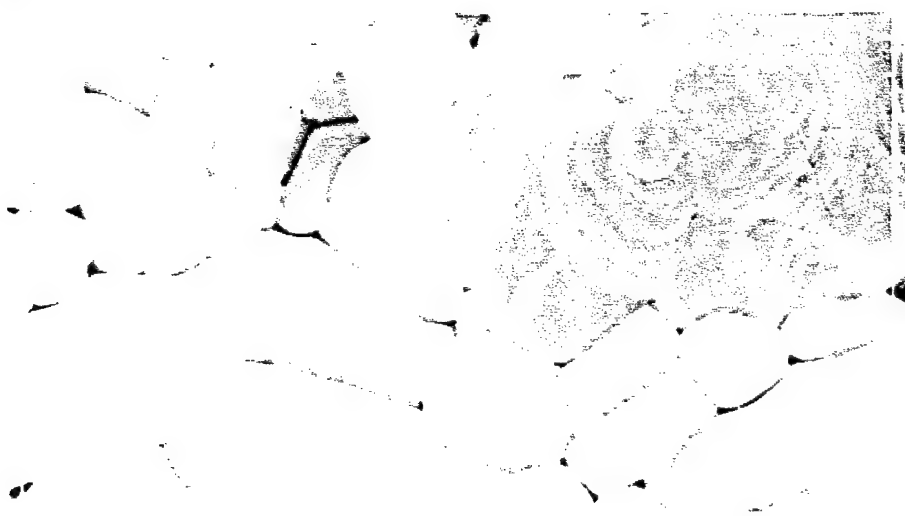
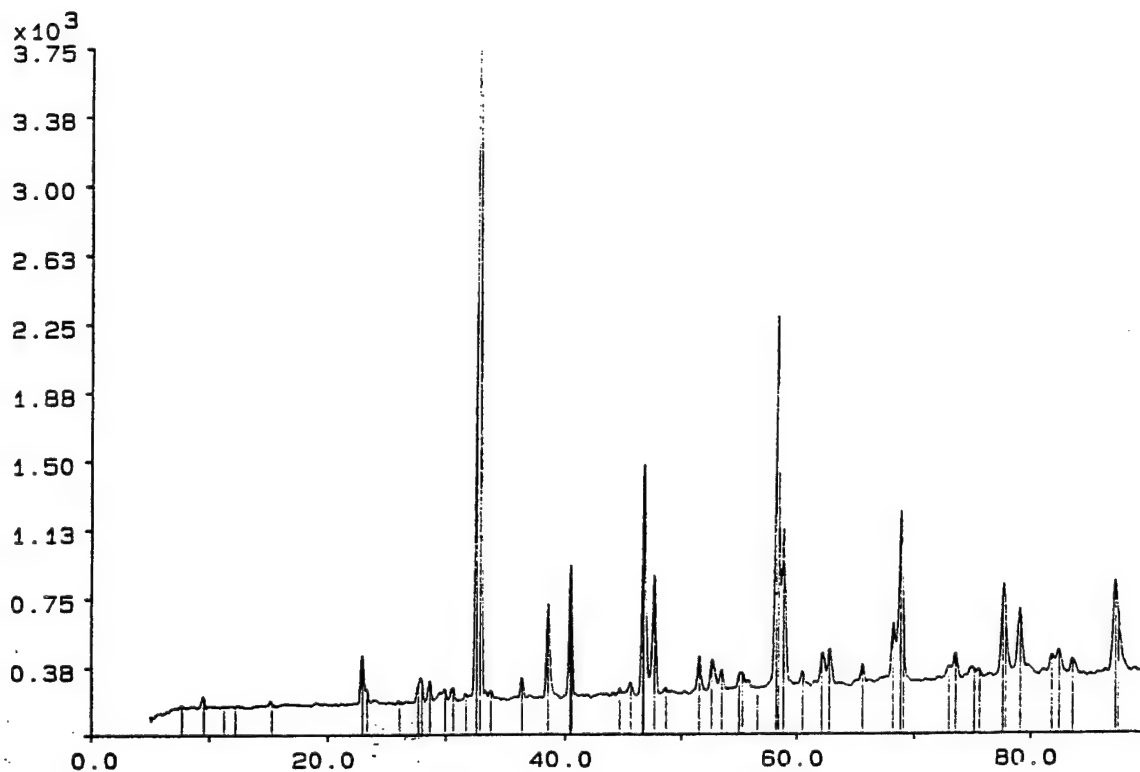
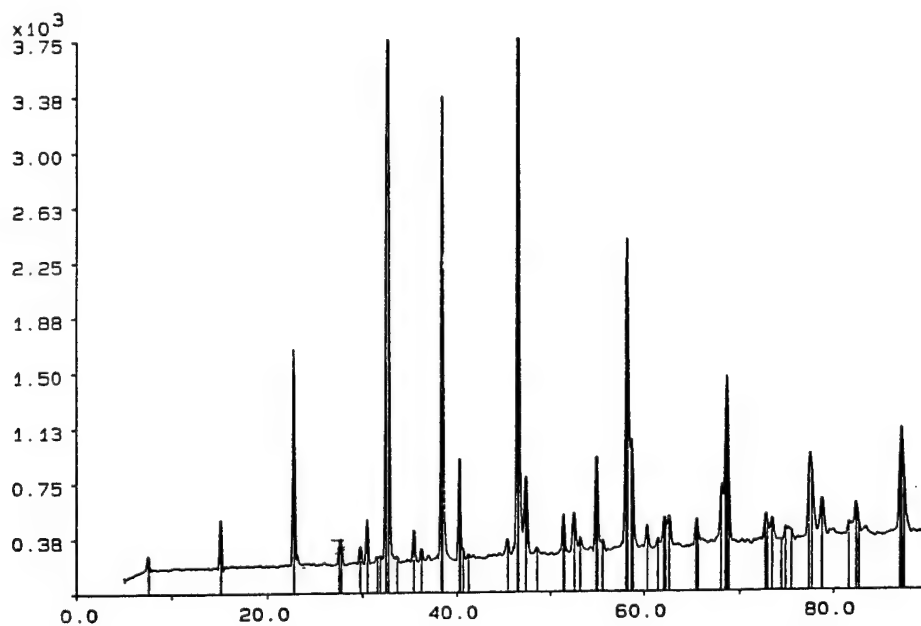


Figure 43. 0.5 % Gallium Substitution in the $Y_{1-2,3}$ Compound.

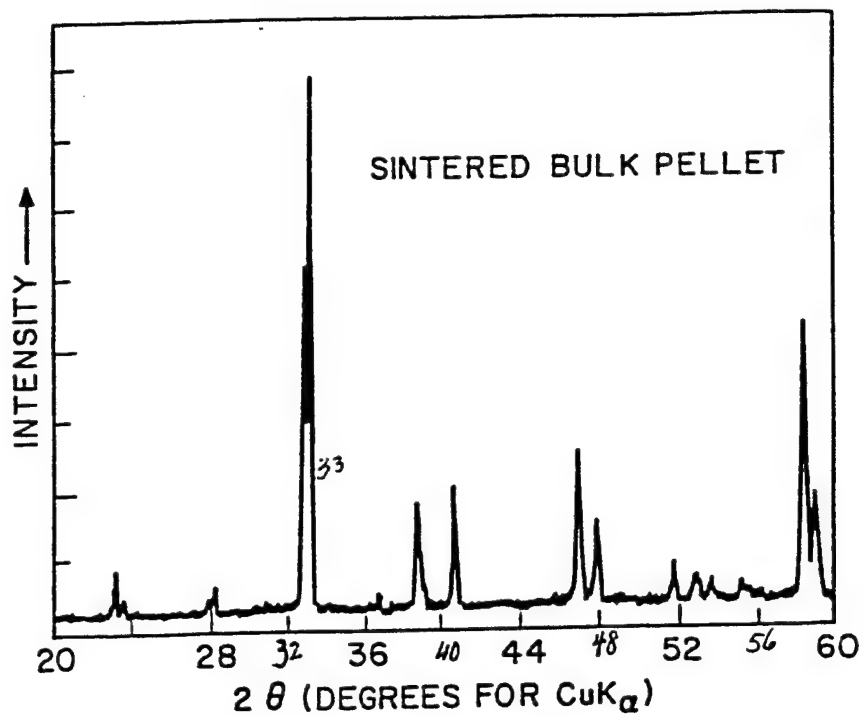


(a) $\text{Y}_1\text{Ba}_2\text{Cu}_3\text{O}_{7-\delta}$ at 20° for CuK_α .



(b) $\text{Y}_1\text{Ba}_2(\text{Cu}_1\text{O}_x\text{Ga}_x)_3\text{O}_{7-\delta}$.

Figure 44. X-ray Diffraction Patterns for (a) $\text{Y}_1\text{Ba}_2\text{Cu}_3\text{O}_{7-\delta}$ at 20° for CuK_α , (b) $\text{Y}_1\text{Ba}_2(\text{Cu}_1\text{O}_x\text{Ga}_x)_3\text{O}_{7-\delta}$, and (c) $\text{Ba}_2\text{YCu}_3\text{O}_{9-\delta}$.



(c) Sintered Tape and on a Powdered Sample From a Bulk Sintered Pellet of $\text{Ba}_2\text{YCu}_3\text{O}_{9-\delta}$.

Figure 44. X-ray Diffraction Patterns for (a) $\text{Y}_1\text{Ba}_2\text{Cu}_3\text{O}_{7-\delta}$ at 20° for $\text{CuK}\alpha$, (b) $\text{Y}_1\text{Ba}_2(\text{Cu}_1\text{O}_x\text{Ga}_x)_3\text{O}_{7-\delta}$, and (c) $\text{Ba}_2\text{YCu}_3\text{O}_{9-\delta}$ (continued).

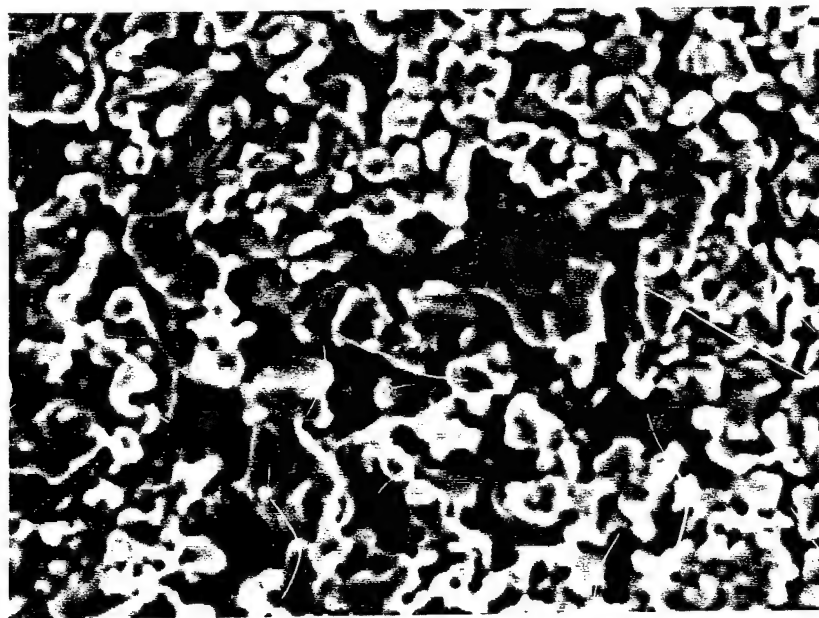


Figure 45. 0.5% Indium Substitution in the $\text{Y}_{1.23}$ Compound.

5.2.1 Starting Chemicals.

- Bismuth Oxide: 1.8210 g.
- Calcium Carbonate: 0.7820 g.
- Strontium Carbonate: 1.1540 g.
- Cupric oxide: 1.2432 g.
- Nitric Acid.
- Acetone.
- Urea.

5.2.2 Laboratory Equipment.

- High-Temperature Furnace: capable of reaching 1,200° C.
- Microprocessor: furnace temperature controller with programmable heating and cooling.
- Quartz Tube: forming the high-temperature chamber, 24-mm o.d. with both ends extending outside of the furnace by 20 cm. One end being connected to an oxygen supply tank and the other to an oil-sealed bubbler.
- Tank of oxygen with pressure regulator.
- Alumina crucibles.
- Pellet presser.

5.2.3 Preparation Procedure. The procedure involves three grinding steps and three thermal treatment process.

- Grinding the appropriate amounts of oxide and carbonates in an agate mortar.
- Placing the powder mixture in a porcelain crucible and forming a slurry by adding Con. HNO_3 .
- Allowing the mixture to dry in air followed by overnight drying at 100°C .
- Grinding the solid again in an agate mortar and pestle.
- Placing the powder in an alumina crucible and heating it in the high-temperature furnace by raising the temperature to 860°C in 3 hr. Maintaining it at 860°C for 24 hr, followed by very slow air-cooling to room temperature at about 1°C/min .
- Grinding the powder for the last time. Pressing the powder into a pellet at 50,000 psi.
- Placing the pellet and crucible in the high-temperature furnace. Using the programmable controller to raise the temperature to 860°C in 3 hr and maintaining it for 24 hr, followed by slow-cooling for 96 hr. This last stage is especially crucial and can only be accomplished in a reproducible manner by a programmable controller.

5.2.4 Test and Characterization Procedure. A simple test of the superconducting properties involves the Meissner Effect. The sample in the superconducting state will levitate when placed above a magnet. Substitution of 4% Sb for bismuth in $\text{Bi}_2\text{Sr}_2\text{Ca}_2\text{Cu}_3\text{O}_{10}$ was accomplished and characterization was performed (see Figures 46–48) as follows.

- SEMs by Gail Meyers are given for the previous sample in Figure 46. Figure 46a shows platelets, and Figure 46b shows bars. The bars are calcium rich. Both samples were superconducting above liquid-nitrogen temperature by means of the Meissner Effect.



(a) Platelets.



(b) Bars.



(c)



(d)

Figure 46. SEM Micrographs of SbBiCaSrCuO After Sintering Process.

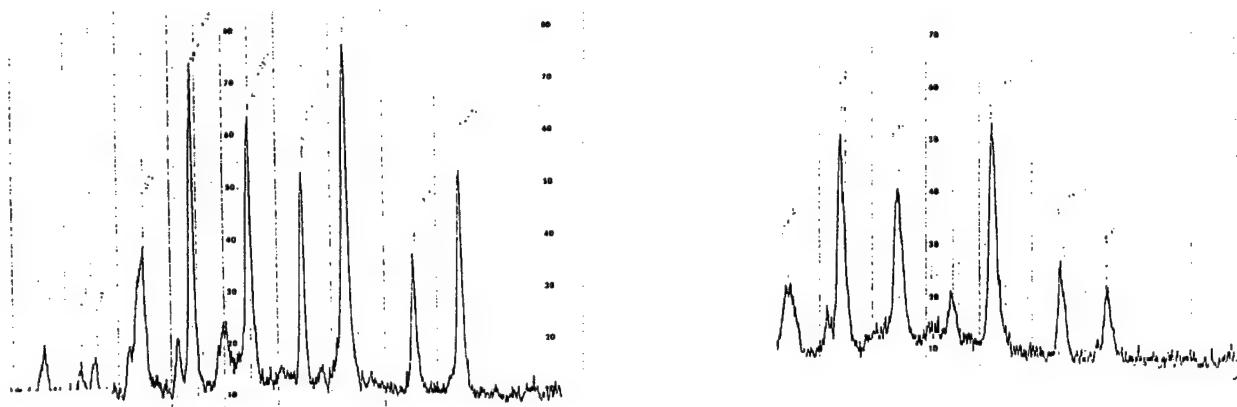


Figure 47. Valence, Charge-Transfer, and Carrier Type.

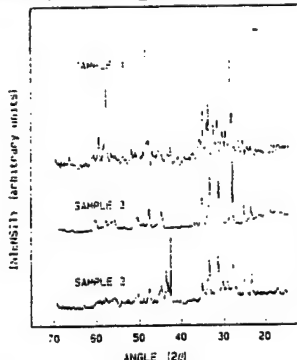


Figure 48. X-ray Scans for Samples 2-4.

- X-ray diffraction results are given in (Figure 48) and compare to the work done by Jones et al. [177]. Substitution of gallium for copper in Bi_{2223} was attempted; however, the resulting product did not pass the levitation test by means of the Meissner Effect at liquid-nitrogen temperature. Substitution of $1/2\text{Gd}(4f^7 5d^1 6s^2)$ for $1/2\text{Y}(4d^1 5s^2)$, produced a material with T_c above liquid-nitrogen temperature. However, an experiment aimed at producing $\text{Gd}_{1/2}\text{Y}_{1/2}\text{Ba}_2(\text{Cu}_{1-x}\text{Ga}_x)_3\text{O}_{7-\delta}$ did not pass the levitation test at the liquid-nitrogen temperature.

When conducting solid-state substitutions for tailored materials engineering (to test such aspects of the theory as the need for a multivalence cation that is diamagnetic in its atomic state) we utilized the oxides Ga_2O_3 , Nb_2O_5 , In_2O_3 , CdO , and MnO_2 . The results of these substitution studies confirmed the developing theory with respect to the previously mentioned predictions (i.e., only multivalence cations that were diamagnetic in their atomic state produced high- T_c material).

In the bismuth-based materials, the average weight loss in the first heat treatment was about $20 \pm 3\%$ (weight loss occurs because the starting materials are oxides and carbonates). The second thermal treatment weight loss was $5 \pm 1\%$. The third thermal treatment weight loss was $2 \pm 0.5\%$. Sintering does not change the weight. Table 6 summarizes the substitutional chemistry.

Goodenough and Manthiram [178, 179] of the University of Texas at Austin have suggested to M. F. Chen to pursue a project concerning calcium substitution for yttrium because barium- and calcium-substituted compounds tend to contain large amounts of oxygen vacancies. The project that Goodenough suggested specifically related to the fabrication of $Y_{1-x}Ca_xBa_{1.6}La_{0.4}Cu_3O_{7-x}$, and to compare structure and charge-transport properties with our data on $YBa_2Cu_3O_{7-\delta}$. Fourteen samples (two sets) were thus fabricated in our laboratory with various compositions, and the Iodometric titration was performed to determine the total concentration of oxygen for each sample. The direct measurements of mobile holes have not yet been accomplished because the funds for the project expired prior to the availability of suitable National Magnet Laboratory user time (all of our user time had been devoted to the samples that were materials-designed in our own program). The effect of increasing the concentration of calcium substitution causing an increase in crystal grain size is shown in Figure 49.

Goodenough and Manthiram have pointed out, in private discussions, the following regarding mobile holes [178].

- All copper oxide superconductors have a significant number of holes.
- Oxidation in excess of normal valence Cu(2) is necessary to prepare stoichiometric La_2CuO_4 , which is an antiferromagnetic semiconductor having no holes.
- $La_{2-x}Sr_xCuO_4$ is superconducting for $x > 0.05$. $T_c = 40$ K, with $x = 0.15$, having 0.15 holes/Cu.
- $YBa_2Cu_3O_6$ is an antiferromagnetic semiconductor having no holes.

Table 6. Substitutional Chemistry

Substitutions	Substituted Ion	Preparation Reagents	% High- T_c in liquid	Test N_2
Material: $Y_1Ba_2Cu_3O_{7-\delta}$				
In	Y	In_2O_3	50	No
Cd	Y	$Cd(CH_3COO)_2$	50	No
In	Y	In_2O_3	25	No
Cd	Y	CdO	25	No
Ca	Y	CaO	10	No
Gd	Y	Gd_2O_3	50	Yes
Gd	Y	Gd_2O_3	75	Yes
Gd, Ga	Y, Cu	Gd_2O_3, Ga_2O_3	50, 3	No
Ga	Cu	Ga_2O_3	0.5	Yes
Sb	Cu	Sb_2O_5	2	No
Re	Cu	Re_2O_7	10	—
Material: $Bi_2Sr_2Ca_2Cu_3O_{10}$, $Bi_2Sr_2CaCu_2O_8$, $BiSrCaCu_2O_6$, and $Bi_xSr_yCa_zCu_wO_m$				
V	Cu	V_2O_5	100	No
V	Cu	V_2O_5	25	No
Pb	Bi	PbO	3	Yes
Mn	Cu	MnO_2	100	No
Nb	Cu	Nb_2O_5	30	No
Nb	Cu	Nb_2O_5	50	No
Nb	Bi	Nb_2O_5	5	No
Sb	Bi	Sb_2O_5	100	No
Sb	Bi	Sb_2O_5	50	No
Sb	Bi	Sb_2O_5	30	No
Sb	Bi	Sb_2O_5	5	Yes
Re	Bi	Re_2O_7	50	No
Re	Bi	Re_2O_7	5	No

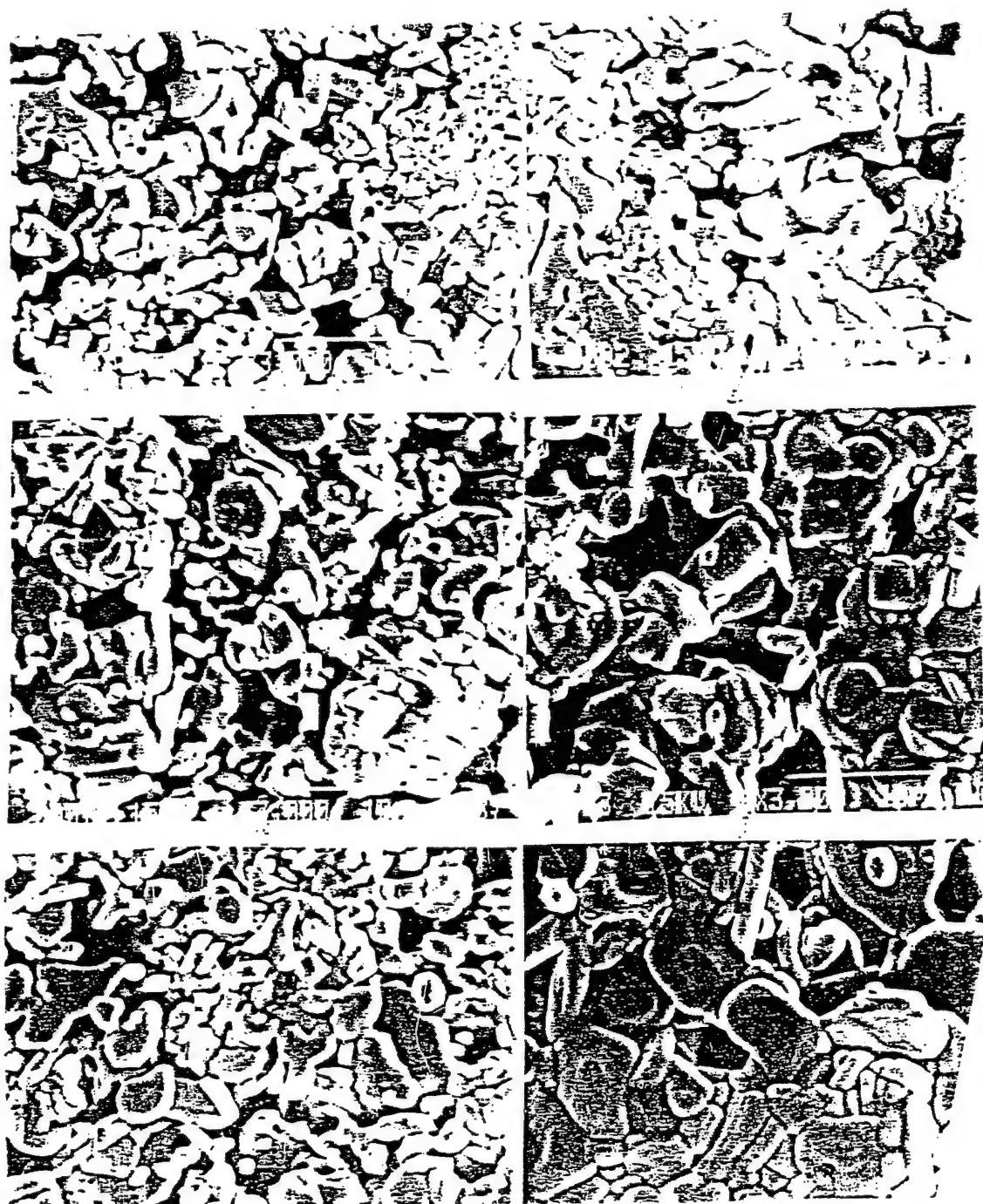


Figure 49. As the Concentration of Calcium Substitution Increases, the Crystal Size Increases.

- $\text{YBa}_2\text{Cu}_3\text{O}_{7-\delta}$ ($0.06 < \delta < 0.5$) is superconducting with $T_c = 92 \text{ K}$ at $\delta = 0.06$ having 0.3 holes/Cu.
- $\text{Bi}_2(\text{Sr,Ca})_3\text{Cu}_2\text{O}_{8.17}$ is superconducting with $T_c = 86 \text{ K}$ having 0.17 holes/Cu.

- $\text{Ti}_2\text{Ba}_2\text{Ca}_{n-1}\text{Cu}_n\text{O}_{4+2n+\delta}$ ($n = 1, 2, 3$) is superconducting with T_c ranging from 80 to 12 K.

Two sets of seven pellets of $\text{Y}_{1-z}\text{Ca}_z\text{Ba}_{1.6}\text{La}_{0.4}\text{Cu}_3\text{O}_{7-\delta}$ were prepared with various z concentrations from $z = 0$ to $z = 0.6$. The compound for $z = 0$ should be tetragonal, with a $T_c = 50$ K. With increasing z , we anticipate a rise in T_c up to $T_c = 80$ K, but with the symmetry remaining tetragonal, as z approaches $z = 0.4$, we also anticipate that, for a fixed oxygen pressure, the total oxidation of the CuO array remains fixed [179].

We performed thermal gravimetric analysis and Iodometric titration to find total oxygen content. I_2 was titrated with standardized $0.02 \text{ NNa}_2\text{S}_2\text{O}_3$. Starch was used as an indicator. The following procedure was utilized [180].

- Sodium Thiosulfate 0.02 N .
- Dissolve $4.964 \text{ g Na}_2\text{S}_2\text{O}_3 \cdot 5\text{H}_2\text{O}$.
- Add $1 \text{ g Na}_2\text{CO}_3$.
- Dilute to $1,000 \text{ ml}$ distilled water.
- $Y =$ milliliters of $\text{Na}_2\text{S}_2\text{O}_3$ required for sample.
- $b =$ milliliters of $\text{Na}_2\text{S}_2\text{O}_3$ required for blank.
- $0.1333 \text{ mg of O} = 1 \text{ ml } 0.02 \text{ NNa}_2\text{S}_2\text{O}_3$.
- $$\frac{(Y - b) \times \text{normality of Na}_2\text{S}_2\text{O}_3 \times 0.133 \times 100}{0.02 \times \text{milligrams of sample}} = \% \text{ O.}$$
- $(Y - b) \text{ ml} \times 0.1333 \text{ mg/ml} = \text{milligrams of O.}$

The average oxidation state of copper and, hence, the total oxygen content of the sample was determined by dissolving about 100 mg of the sample in a solution consisting of 15 ml of 10% KI and about 5 ml of 3.5 N HCl. The solution was diluted with about 10 ml of distilled water, and the liberated I_2 was titrated with standardized sodium thiosulfate with starch as the end-point indicator. All analyses were done in duplicate. The final oxygen stoichiometry had an error limit of ± 0.02 . We measured the x-ray diffraction pattern of $Y_1CaBa_{1.6}La_{0.4}Cu_3O_{7-x}$ at 20 K using the Phillips diffractometer. This yielded essentially the same pattern as $Y_1Ba_2Cu_3O_{7-\delta}$.

6. Experimental and Theoretical Results From the USAMTL Research Program.

6.1 The Hall Effect in $Y_1Ba_2Cu_3O_{7-\delta}$. In this section, we address the high- T_c superconducting ceramic oxide $Y_1Ba_2Cu_3O_{7-\delta}$ in polycrystalline form shown crystallographically in Figure 50, and believed to be a defect substitutive derivative of the K_2MnF_4 structure (Figure 30) in the form $(Y_1^{3+}Cu_1^{3+})_1(Ba_2^{2+}Cu_2^{2+})_1O_{8-\epsilon}$, where $\epsilon \approx 1.1 - 1.5$.

We measured the Hall effect at low to high B-field in polycrystalline samples in order to determine the dominant carrier in the normal state. Previous studies in some of the high- T_c materials had shown a positive Hall coefficient in these materials in the normal state. Thus, by studying the positive hole concentration as a function of temperature, we believed that we may be able to relate the work to the hypothesized exciton concentration characteristics. One of the purposes of our work was to determine whether $Y_1Ba_2Cu_3O_{7-\delta}$ would show a sharp peak and trend in the positive Hall voltage near T_c , as was shown for $LaSrCuO_4$ by Hundley et al. [150] and Figure 51). In the latter study, the value of R_H became zero as the temperature decreased below T_c , then became slightly negative before sustaining a zero value as temperature continued to decrease into the zero-resistance state.

Our Hall effect experiments were performed at values of magnetic field to 15 T. Data taken at 6.8 and 5.0 T are given in Figures 52 and 53. These data show a rising positive Hall voltage with decreasing temperature, this effect beginning at temperatures somewhat above T_c and being

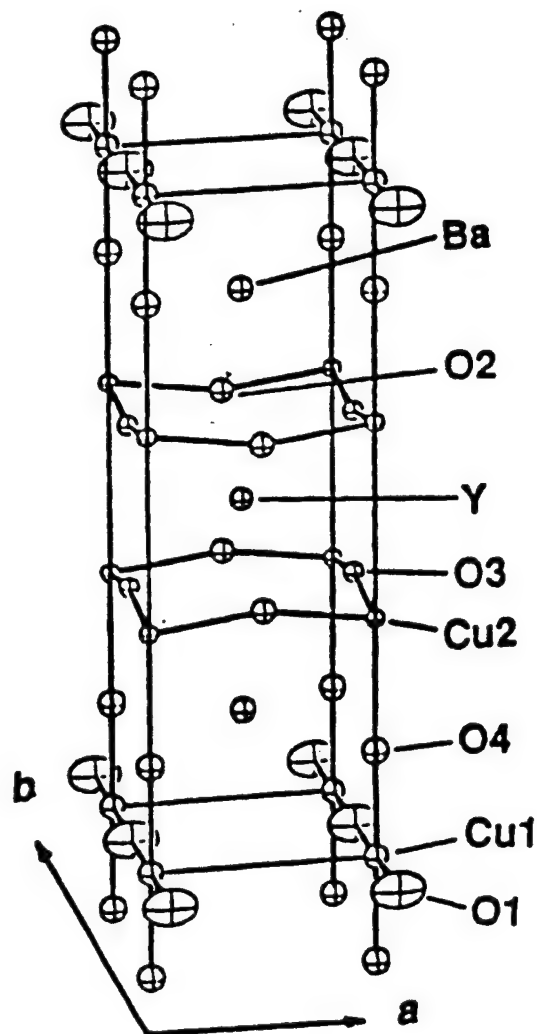


Figure 50. Structure of the Superconductor $\text{Y}_1\text{Ba}_2\text{Cu}_3\text{O}_{7-\delta}$.

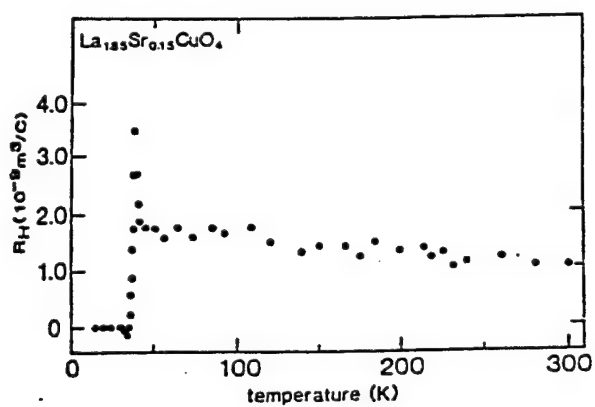
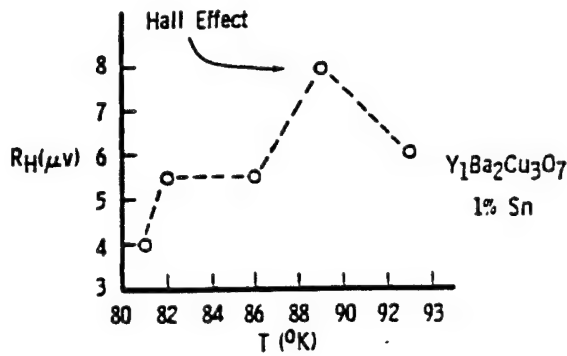
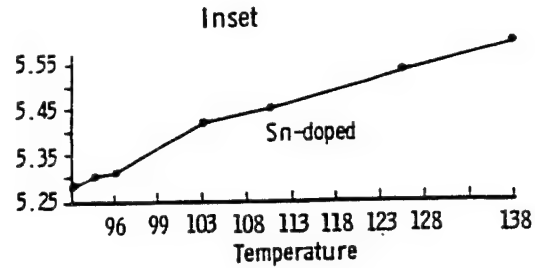


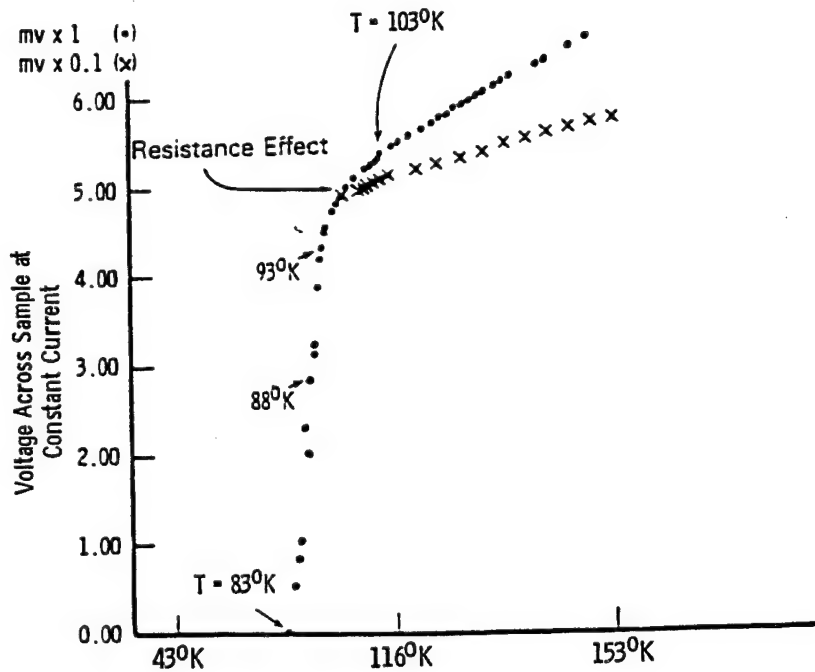
Figure 51. The Hall Data on $\text{La}_{1-x}\text{Sr}_x\text{CuO}_4$ [150]: Hall Constant in $\text{La}_{1.85}\text{Sr}_{0.15}\text{CuO}_4$ vs. Temperature.



(a)



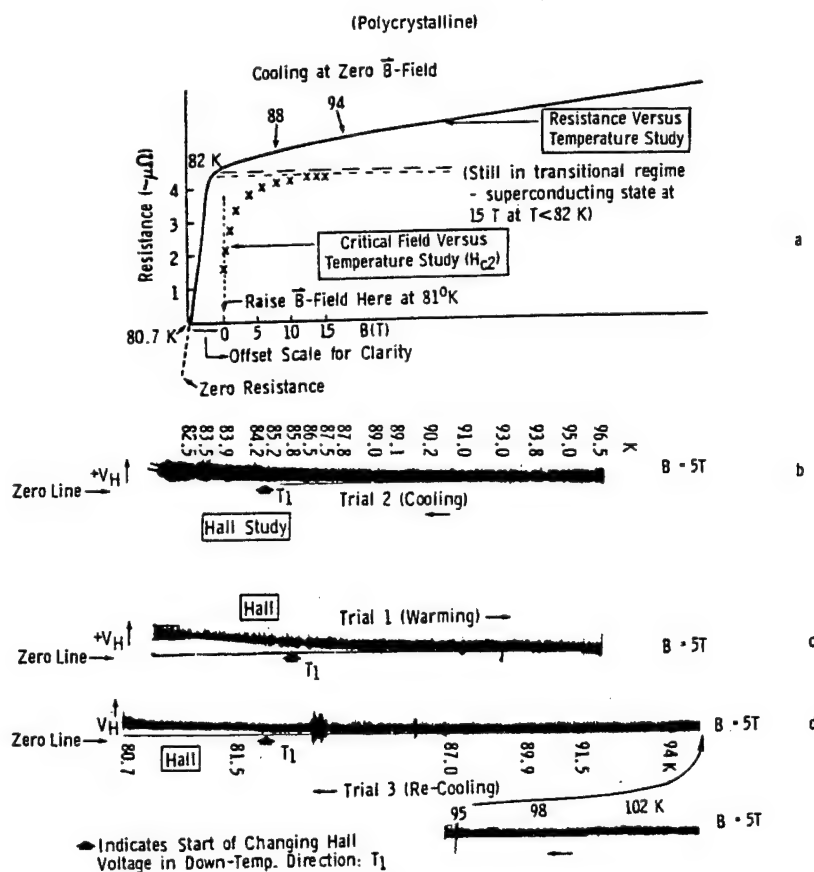
(b)



(c) Four-Terminal Resistance Data.

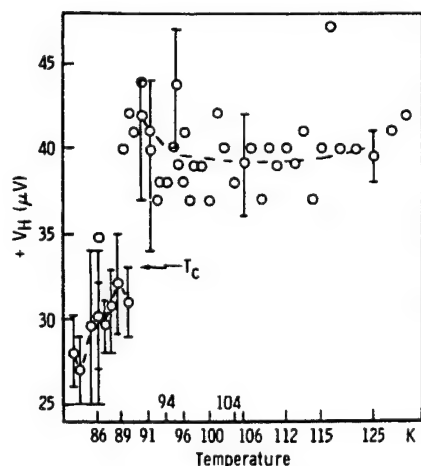
Figure 52. Hall Effect Experiments at 6.8 and 5.0 T.

accentuated with a slope change at approximately the temperature, T_o , corresponding to the deviation from linear behavior in resistance vs. temperature. The results bear strong similarity with the peaked signal reported by Hundley et al. [150]. We performed the experiment at 6.8 T in a point-by-point manner, reversing both the current and the magnetic field at each equilibrium temperature. However, so as to preclude missing a maximum or minimum N turning-point-temperature (in R_H vs. T), we also monitored V_H continuously as a function of temperature for a single polarity of current and magnetic field. This continuous data showed essentially the same trend as the point-by-point method, proving that stray voltages due to any very slight mismatch of Hall contacts or thermal

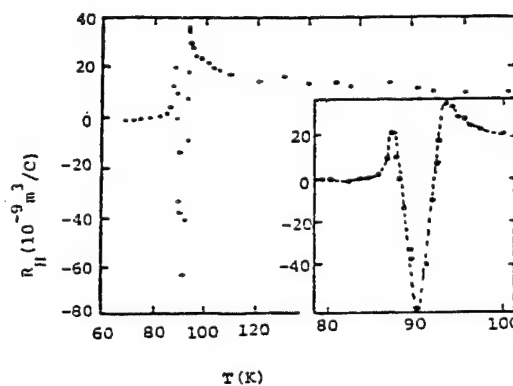


intermediate region between the superconducting and normal states at 81 K as a function of increasing B to 15 T. These data indicate that recovery to the normal state has not occurred, even at fields as high as 15 T and temperatures near T_c ; they also indicate a very strong B dependence of resistance up to 5 T.

In Figure 54a, we present our Hall data taken at 15 T, which suggest a positive anomaly spike just above T_c , followed by a lowering of $+V_H$ and including some oscillatory or irregular behavior. We utilized a very high magnetic field of 15 T to determine the effect relative to the lower fields utilized in the experiments shown in Figures 52 and 53. The effect of this extreme magnetic field (or magnetic strain) is apparently to cause the high degree of fluctuation at $T < T_c$ indicated by the error bars. In Figure 54b, we reproduce the data of Zhao et al. [183], which show similar behavior for the compound $Ba_{1.2}Y_{0.9}V_{0.9}Cu_3O_{7-\delta}$, but also include, at a lower temperature, a region of changes in sign to $R_H < 0$. The data in Zhao et al. [183] are explained by the authors as being due to differences between the interior of grains and the grain boundary itself. (The latter can still support a Hall voltage, even though the grain "islands" are superconducting.)



(a) At 15 T.



(b) $R_H < 0$.

Figure 54. Hall Effect vs. Temperature for Yttrium Barium Cuprate [183].

If an exciton-mediated mechanism is indeed present as an initiator of high- T_c superconductivity, one would expect an increase in exciton concentration as the temperature was decreased to the T_c region. This would be expected because of the increase in exciton lifetime as heat is withdrawn from

the sample. The core of an exciton is a positive hole that is either bound on an oxygen, is due to a charge excitation or fluctuation from one valence state of copper to a second valence state, or is simply a free hole. Thus, if exciton concentration increases, there should be a decrease in positive carriers because some of the formerly free holes are weakly binding electrons in unrecombined states in Hydrogenic orbit. Hence, the hole carriers that take on the electron in unrecombined Hydrogenic orbit cannot participate in charge conduction. This is true of bound, as well as free, excitons. The net result of a decrease in positive carriers in a material with a positive Hall coefficient should be an increase in $+R_H$ (as we observe).

As shown in Figures 53 and 54, we observe a change in slope (to a higher slope) in $+R_H$ vs. temperature at a temperature greater than T_c . To explain this second-order slope change, we have to refer to single-crystal Hall effect data found in Penny, Von Molnar, and Kaiser [184] and reproduced in Figure 55. These data show that for $B \parallel c$, the Hall coefficient is positive with a normal $1/R_H$ temperature dependence. In this case, the charge-carrier orbits are caused by the Hall voltage circulate in the a-b plane or the base plane of the coulombicly bonded pyramidal building block of the structure where conduction is dominated by holes (hopping type). However, for B perpendicular to c , an anomalous temperature dependence is observed, and the Hall voltage is, instead, negative. The circulating currents in this latter case are in the b-c or a-c planes and are thus related to the delocalized electrons of the $Cu(l)$, which is d-p π -bonded to the $O(l)$ ions via a chain structure. In a two-carrier Hall effect system, the analysis becomes quite complicated, and the Hall coefficient is given by

$$R_H = (1/e) / [(p\mu_h^2 - n\mu_e^2) / (p\mu_h + n\mu_e)^2].$$

In order to attempt to describe the increase in slope that we observe in R_H vs. T , we assume that any differences in the temperature dependence of the mobilities can be neglected and normalize the aforementioned relationship. Since the B parallel to c condition should exert far more influence than the B perpendicular to c condition, we then add the data of Penny, Von Molnar, and Kaiser [184] (from ~ 300 K to 100 K, excluding the precipitous rise in Hall number at T slightly less than 100 K).

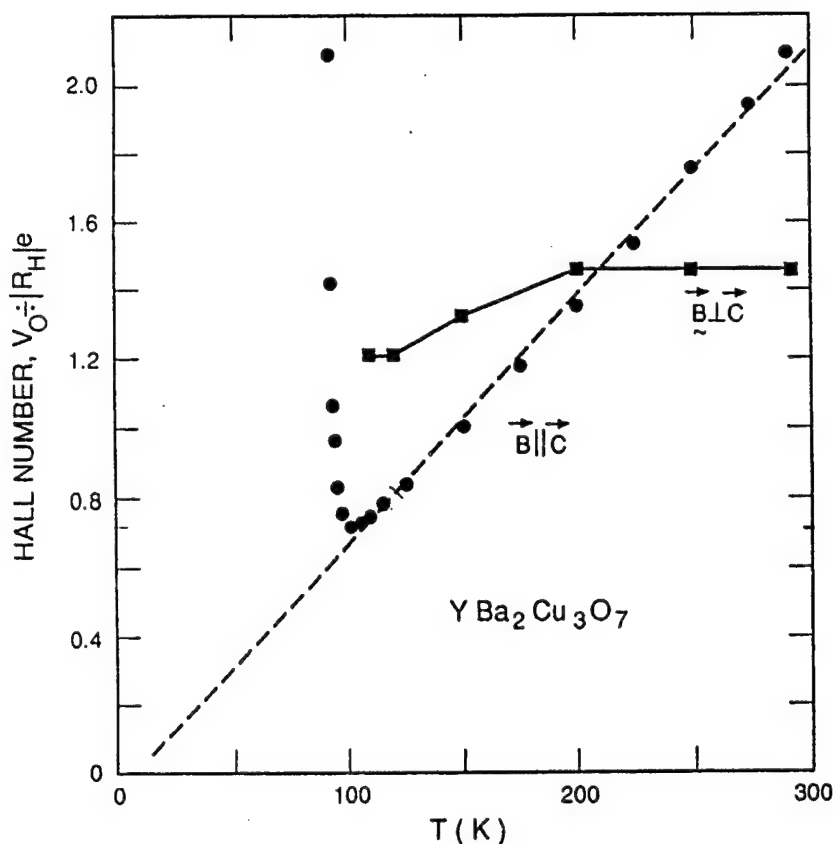


Figure 55. Single-Crystal Hall Data. $V_O/|R_H|e$ for a Single Crystal of $\text{YBa}_2\text{Cu}_3\text{O}_7$ [184]. $V_o = 175 \text{ \AA}^3$ is the Volume Per Formula Unit.

In this addition, we give a 2:1 (and then a 2.2:1) weight factor to the $B\parallel c$ data and obtain the dependence given in Figure 56. These curves are in approximate accord with our data of Figures 53 and 54, but because Hall number is plotted, rather than Hall voltage, they are reversed in apparent sense. This accord suggests that our assumptions were essentially valid regarding the weighted contribution of the $B\parallel c$ case.

The effects of both decreasing temperature and incipient Cooper pairing may cause a decrease in carrier scattering with excitons. Normally, such scattering may be a factor in inducing electron-hole recombination. Hence, the process of Cooper pairing due to exciton mediation may indeed be self-building (upon itself). However, at a certain concentration of Cooper pairing, there is likely to exist competition between Cooper-pairing forces and exciton binding energy (which is weak). In

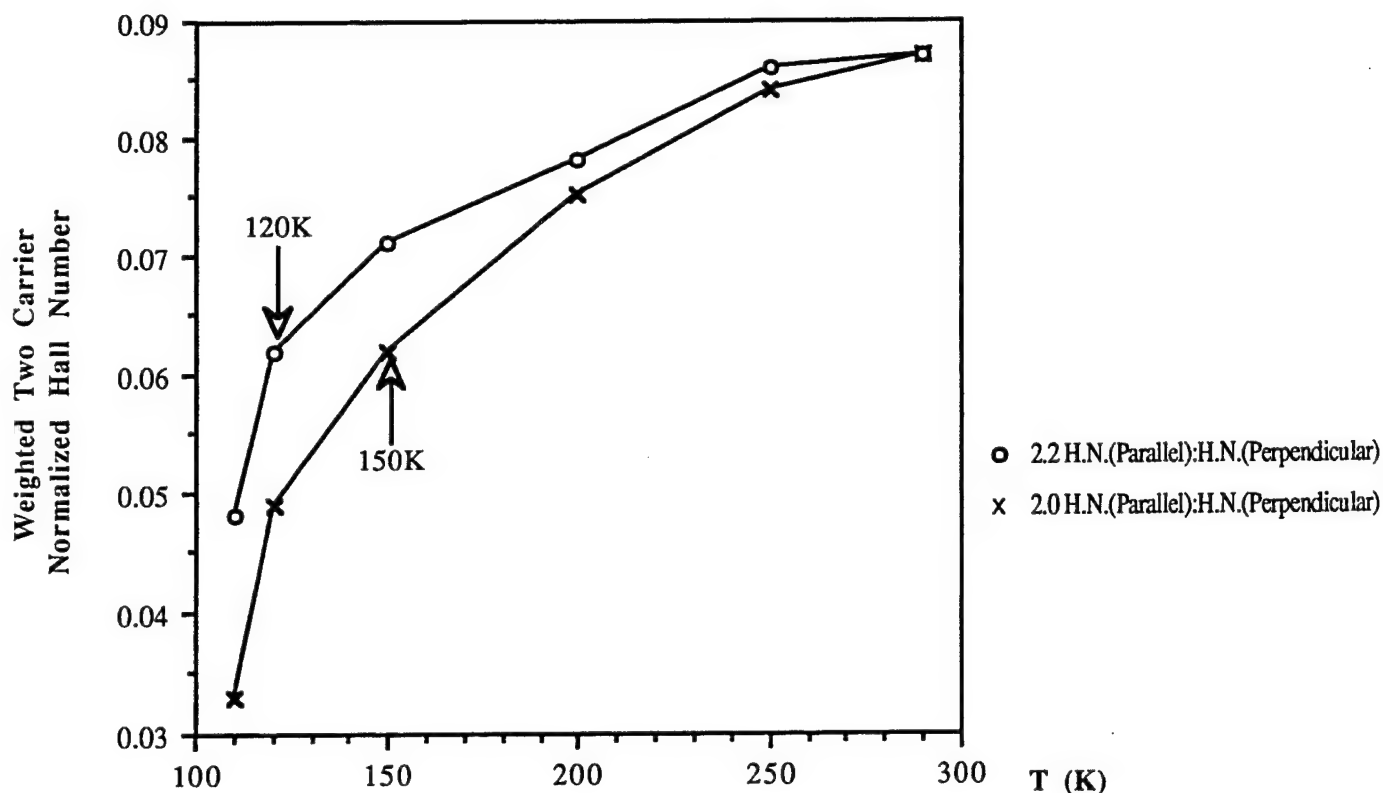


Figure 56. Weighted Two-Carrier Normalized Hall Number vs. Temperature Showing Second-Order Slope Change.

such a competition, the Cooper-pairing coulombic forces should prevail and cause the ionization of the excitons. In such an event, the expectation would be an increase in both the hole and electron concentrations in the conduction system. The result should be visible in terms of a sudden decrease in the Hall coefficient of a p-type material. This is exactly what we observe in the Hall effect data. Furthermore, an ionization event of this type could cause a change in the dominant carrier, which would be indicated by a changeover to a negative Hall coefficient, as shown in the ceramic material Hall effect studies in Hundley et al. [150], Vezzoli et al. [181], and Zhao et al. [183]. The physical explanation for the delta-function-like effect near T_c in R_H vs. T for ceramic materials is interpreted to be due to the trapping of holes at grain boundaries reducing the number of mobile holes, and some of these trapped holes take on electrons into excitonic states, thereby becoming bound excitons.

More recent work [181] also shows very anomalous behavior in R_H vs. T (shown in Figure 57) near T_c and lends credence to the peaked and oscillatory character of the earlier data [185].

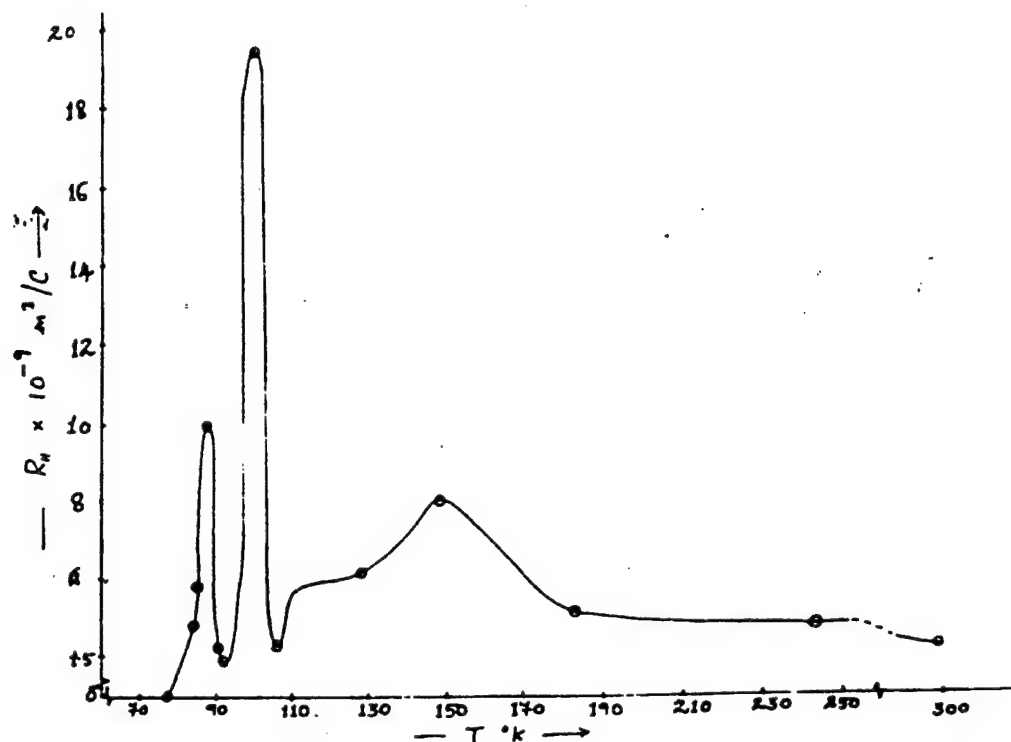


Figure 57. Variation of Hall Coefficient (R_H) With Temperature (TK) to Be So (i.e., the Charges Are Highly Mobile at and Below T_c , Even Though the Material is Under the Influence of Magnetic Field, Giving a Finite Hall Voltage at T_c .)

6.2 Antiferromagnetism in the YBaCuO System. It has been known that, broadly viewed, the coexistence of ferromagnetic ordering and low- T_c superconductivity is confined to narrow temperature intervals, but that antiferromagnetism and low- T_c superconductivity can coexist over an extended temperature range. With the discovery of the new high- T_c materials, however, antiferromagnetism and superconductivity were believed to be thermodynamically separated by a cusp in a phase diagram as reproduced in Figure 58 [186–188], and were therefore thought not to coexist. Notwithstanding this, very elegant work by Budnick, Chamberland, and Baines [186]; Budnick et al. [187, 188] using muon spin rotation techniques has reported that there is indeed a subtle form of overlap of these two characteristic properties of high- T_c materials as shown in Figure 58.

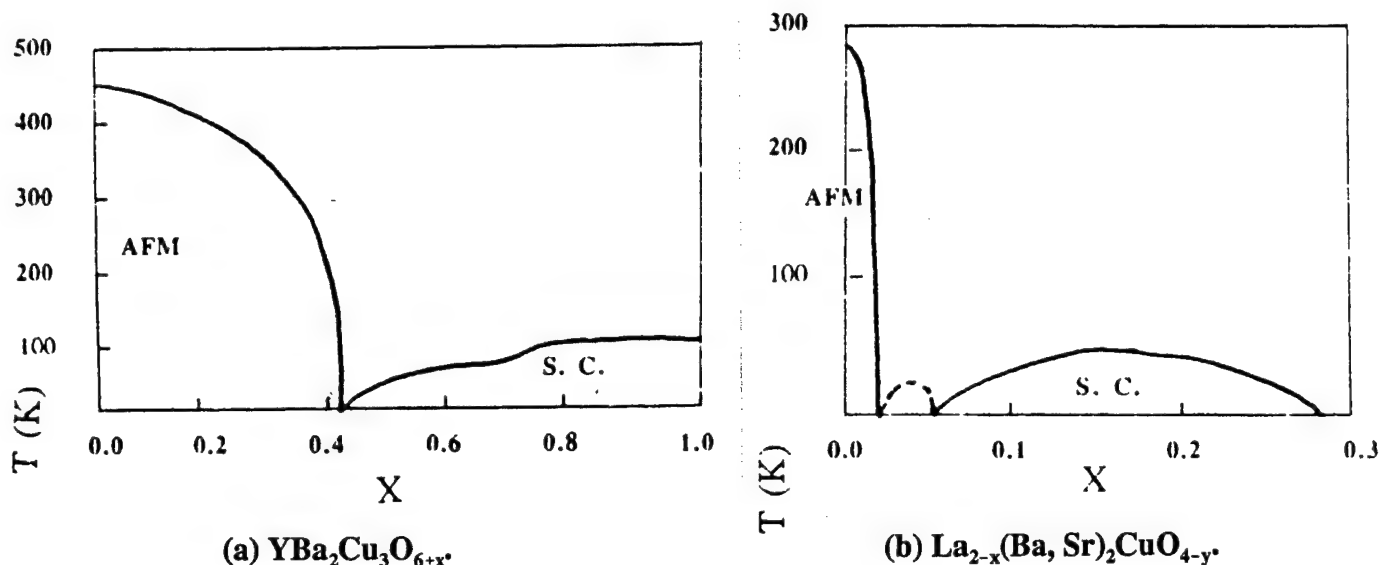


Figure 58. Experimental Phase Diagrams for (a) $\text{YBa}_2\text{Cu}_3\text{O}_{7-x}$ and (b) $\text{La}_{2-x}(\text{Ba, Sr})_2\text{CuO}_{4-y}$.

Because of the correlation between the $\text{Y}_1\text{Ba}_2\text{Cu}_3\text{O}_{7-\delta}$ and the antiferromagnetic K_2NiF_4 structural archetypes, we performed experiments in the summer of 1987 to examine the possibility of static antiferromagnetism at the Cu(2) sites in $\text{Y}_1\text{Ba}_2\text{Cu}_3\text{O}_{7-\delta}$. We were advised [189] to conduct this study at very low magnetic fields (<0.1 T) using the MIT SQUID. The results are shown in Figure 59, and although reflecting considerable scatter/fluctuation, this figure suggests a Neel condition at $T_N \sim 400$ K $\pm \Delta$ [190, 191]. This observation may admittedly be associated with nonuniformities in the material; however, it was not detected at higher magnetic fields of 0.5 T and 1.0 T. Shortly after our experiments were analyzed, the detailed neutron diffraction work of Tranquada et al. [145] was published, showing for nonsuperconducting stoichiometries of $\text{Y}_1\text{Ba}_2\text{Cu}_3\text{O}_x$, where $6.0 \leq x \leq 6.5$, a dynamic Neel temperature existed for the Cu(2) spins 390 ± 10 K. The very important work of Tranquada et al. [145] was discussed intensely at the American Physical Society meeting in New Orleans in March 1988, and antiferromagnetism in these stoichiometries was confirmed by other laboratories. Even earlier, antiferromagnetism was detected in the lanthanum strontium cuprate high- T_c superconductor [192–194].

The significance of antiferromagnetism relative to superconductivity is understood actually in terms of fluctuations or deviations from the antiferromagnetism state, which are referred to in general as spin fluctuations. The spin fluctuations specify the reversals of the direction of spin or reversals of the sign of m_s at a very high rate. However, herein, we address a specific form of the

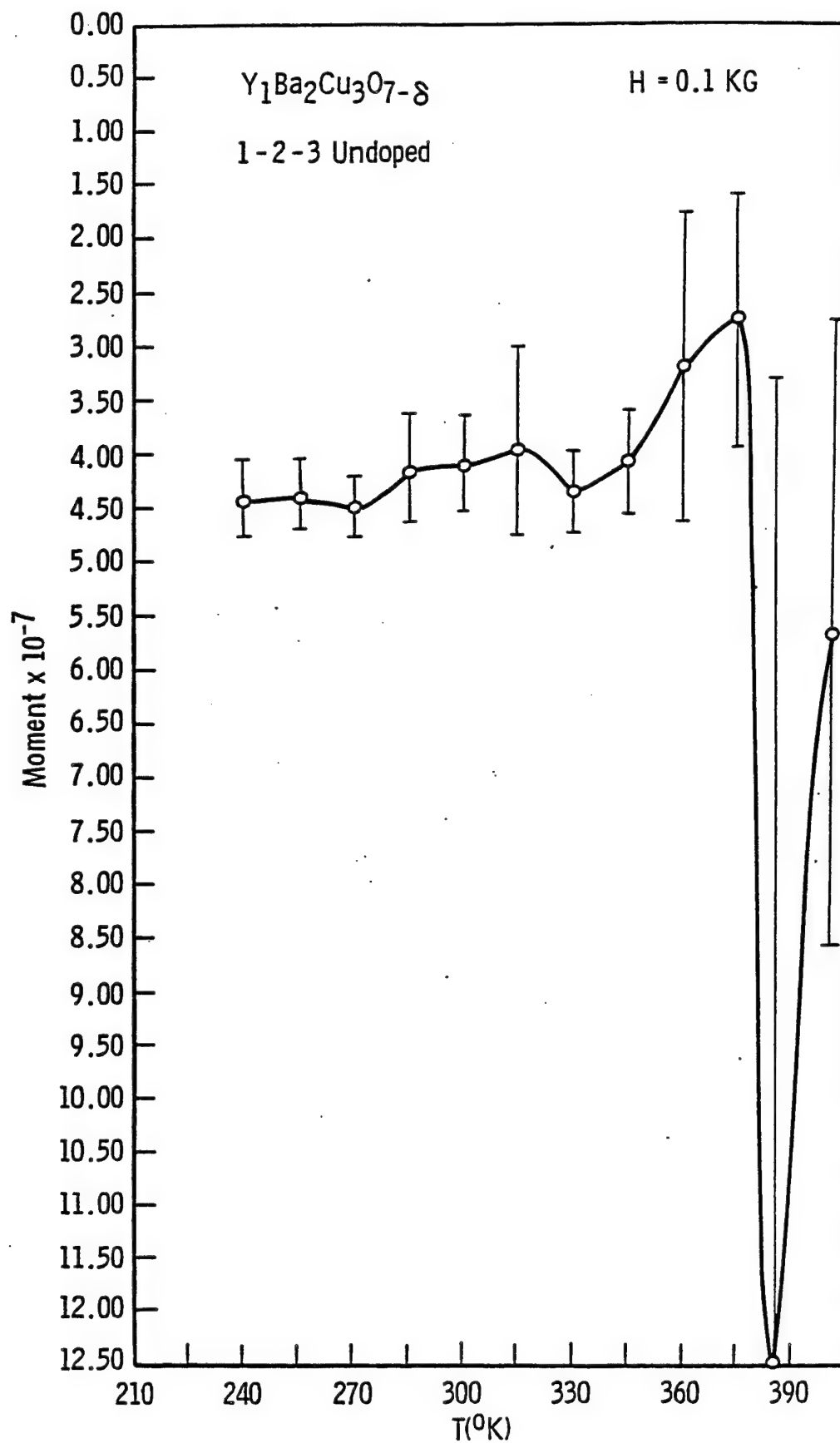


Figure 59. MIT SQUID Results.

spin fluctuation, which is localized at the Cu(I) site and out of phase with the antiferromagnetism system at the planar sites in the $Y_1Ba_2Cu_3O_{7-\delta}$ material. These deviant spins or unstable states, which are localized or bound, upset the delicate balance of perfect spin compensation, which is characteristic of antiferromagnetism, and can themselves act as mediators inducing Cooper pairing via spin-spin correlations with conduction electrons. The antiferromagnetism that is related to the RE spin in $RE_1Ba_2Cu_3O_{7-\delta}$ has been identified such as for $Gd_1Ba_2Cu_3O_{7-\delta}$ showing a $T_N \sim 0.3$ K [148]. Gadolinium is strongly paramagnetic, and its moment is likely to attack Cooper pairs in its vicinity; it was believed that the central ion (Gd, Er, Ho, etc) was magnetically isolated from the superconducting region of the unit cell [148]. This unfavorable spatial domain for superconductivity was then proven theoretically [195]; however, it was shown to exist over only a much smaller range than originally supposed. For example, the case in which gadolinium replaces yttrium, the range at which the paramagnetic moment of the gadolinium has a destructive effect on Cooper pairs extends only about 0.6 Å from the valence shell of the central ion.

The antiferromagnetic stoichiometries of $O_{6.0}$ and $O_{6.5}$ indicate that the compounds $Y_1Ba_2Cu_2^{2+}Cu_1^+O_6^{2-}$ and $Y_1Ba_2Cu_3^{2+}O_{6.5}$, respectively, do not allow for the all-important spin fluctuations that seem essential to high- T_c superconductivity. In the former compound, the Cu_1 chain ions are in the $d^{10} s^0$ state, which has no effect in upsetting the antiferromagnetism in the $Cu(2)$ planes since it contains no unpaired d-state spins. In the latter compounds, all the copper ions are in 2+ valence and, hence, in d^9 states, allowing for complete antiferromagnetism at planar copper and chain copper sites, thus also not causing a deviation from antiferromagnetism. Therefore, it is clear that neutron diffraction measurements, capable of detecting long-range dynamic antiferromagnetic ordering will verify antiferromagnetism for these stoichiometries. In the $O_{6.6}$ stoichiometry, as a contrasting example, the resulting compound should have a cation composition $Y_1Ba_2Cu_{2.8}^{2+}Cu_{0.2}^{3+}$, and the $Cu(I)$ d^9 states in this case occupy only a portion of the nonplanar copper sites. This partial occupancy (approximately 80% in this case) can then cause an upset or deviation of the balance of spin compensation that exists in the planar region. Thus, in such a stoichiometry, long-range antiferromagnetic order will not be observed, nor will it be observed for O_x stoichiometries where $6.5 < x < 7.0$. However, since the charge on the copper valence states is fluctuating at very high frequency ($< 10^{13}$ Hz), there will arise statistically influenced cases where

short-range time-dependent antiferromagnetic order may indeed exist and may be measurable at low fields (such as with a SQUID). These conditions may establish the overlap region of antiferromagnetism and high- T_c superconductivity, as discussed earlier.

6.3 The Role of RE Substituted for Yttrium in High- T_c $Y_1Ba_2Cu_3O_{7-\delta}$

6.3.1 Experimental Data on RE Substitution. In Figure 60, the work of Chu [196] is plotted as a function of the RE that is substituted for Y^{3+} , and in Figures 61 and 62, the data are plotted in a similar fashion [197]. These data show enhancement of the zero-resistance temperature and, even more so, an enhancement of the equally important temperature that identifies deviation from linear R vs. T behavior (with peak enhancement associated with the RE ions of maximum spin). It is also shown in these figures that in the deviation from linear R vs. T behavior, there is asymmetry and anomaly in the Ho^{3+} , Er^{3+} , and Lu^{3+} data as compared to the La^{3+} and Nd^{3+} data points. In Figure 63 [198, 199], the spin and effective magnetic moment are plotted vs. the RE series and correlated with the decrease in T_c caused when these RE elements with 4f electrons are substituted into lanthanum. In this figure, we clearly observe that the effective magnetic moment is not equal (or symmetric) for Ho^{3+} and Er^{3+} as compared to Nd^{3+} and Pm^{3+} —and neither are the corresponding values of $-\Delta T_c$ (nor the corresponding values of ΔT_0 or $\Delta T_{(R=0)}$ in Figures 60 and 61). In Figure 64, we additionally plot the paramagnetic Curie point and the domain transition for Gd^{3+} , Ho^{3+} , and Er^{3+} and note peaked behavior at Ho^{3+} , which correlates with peaked effective magnetic moment (also plotted, but as open circles [200]).

In the Laves phases AB_2 , where $B = Ge, Ru, Os, Ir, \text{ or } Pt$, and A is either a RE with 4f electrons (symbolized by A') or $Y, Sc, Lu, \text{ or } La$ (which do not contain 4f electrons [symbolized by A'']), it is known that $A''B_2$ are always superconducting, but $A'B_2$ are ferromagnetic. The Curie temperatures of the $A'B_2$ compounds show a correlation with the number of valence electrons similar to the criterion for the appearance of superconductivity. Comparison of Figures 60–63 indicate that the asymmetry and anomaly in the closed-circle data of Figure 60 (deviation from linear R vs. T) may be related to the asymmetry of the effective magnetic moment and Curie point and domain transition in Figures 63 and 64. These correlations suggest that the yttrium or the RE substitute may

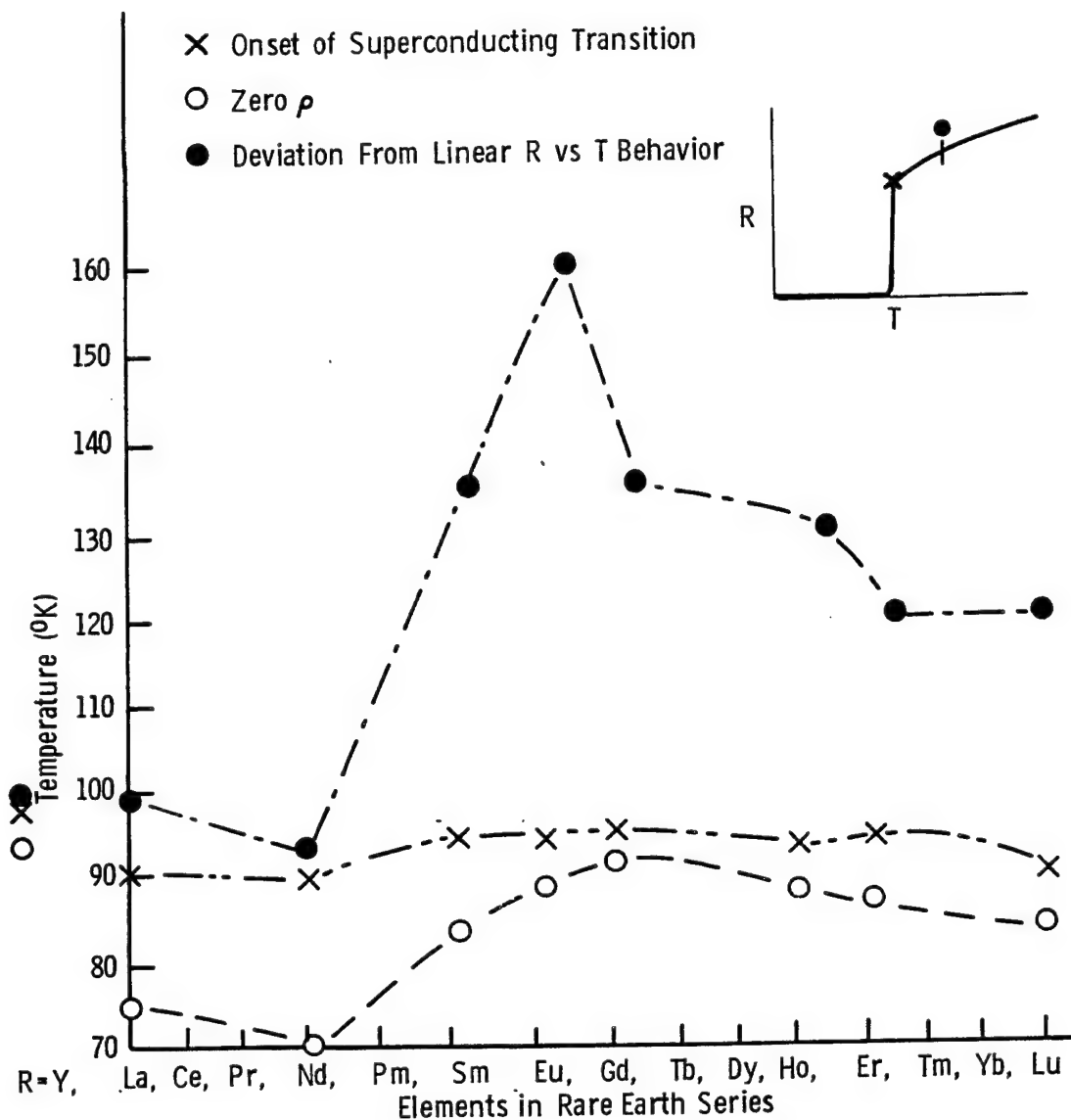


Figure 60. Transition Temperatures vs. Element (R) in $R_1\text{Ba}_2\text{Cu}_3\text{O}_{7-\delta}$ [196].

contribute some net factors in high- T_c $\text{Y}_1\text{Ba}_2\text{Cu}_3\text{O}_{7-\delta}$ that favor superconductivity, contrasting their destructive influence on the superconductivity of low- T_c materials. Very recent work on $\text{Y}_{(1-x)}\text{Tb}_x\text{Ba}_2\text{Cu}_3\text{O}_{7-\delta}$ and $\text{Y}_{(1-x)}\text{Ce}_x\text{Ba}_2\text{Cu}_3\text{O}_{7-\delta}$ [201] shows that the effects of Tb and Ce are in accord with Figures 60 and 61.

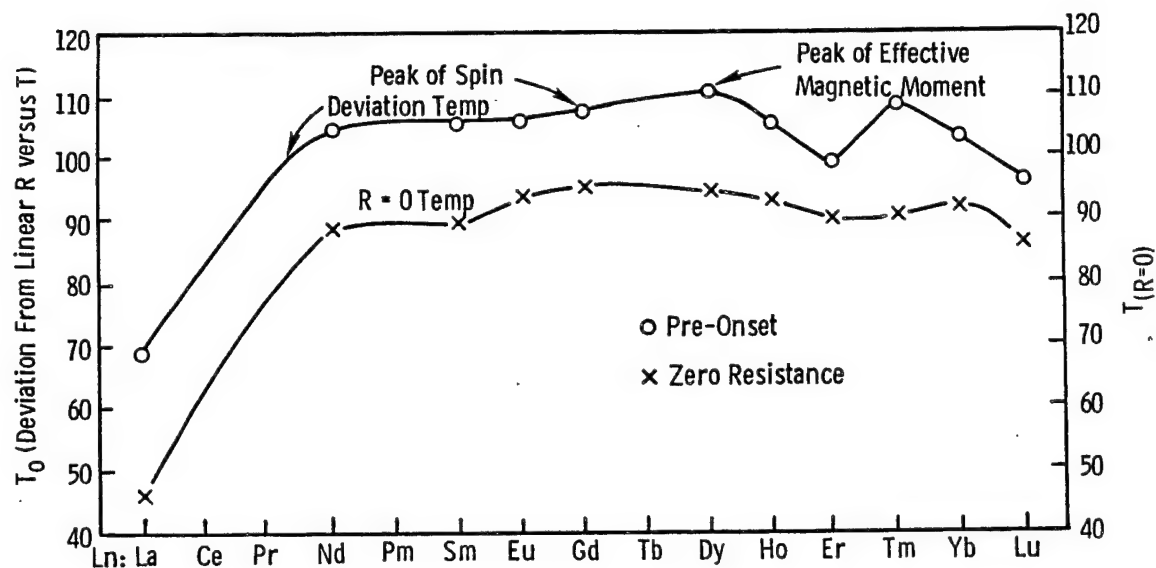


Figure 61. Graph of the Preonset and Zero-Resistance Temperatures for RE $\text{Ba}_2\text{Cu}_3\text{O}_{7-\delta}$.

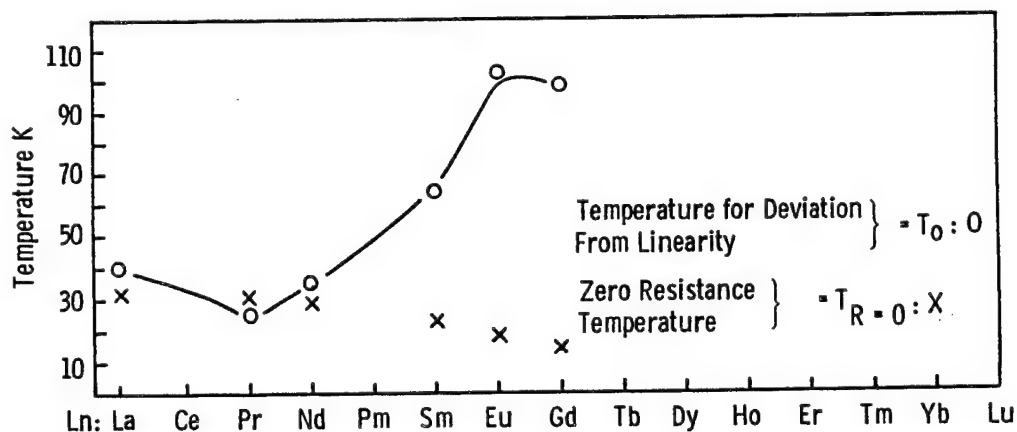


Figure 62. $\text{Ln}_{0.2}$ (RE) Substituted Into $\text{La}_{1.6}\text{Sr}_{0.2}\text{Ln}_{0.2}\text{CuO}_4$.

The cause of the enhancing effect on T_0 and $T_{(R=0)}$ shown in Figures 60 and 61 is not yet fully established. It is appealing, however, to search for an explanation of this effect in terms of magnetic phenomena that are believed to be a possible triggering mechanism of high- T_c superconductivity, such as the previously described spin fluctuations from antiferromagnetism. In our earlier study [195], it was shown by a modified Rudderman-Kittel analysis that the magnetic moment of the RE ion, which is substituted for yttrium in $\text{Y}_1\text{Ba}_2\text{Cu}_3\text{O}_{7-\delta}$, tends to polarize the localized unpaired and uncompensated d^9 valence spin existing at Cu(I) sites when a charge-transfer excitation occurs, creating an odd number of Cu^{2+} states at those lattice locations. (This charge transfer occurs to create neutralized unit cell conditions when the oxygen $\text{O}_{7-\delta}$ stoichiometry changes as δ increases from

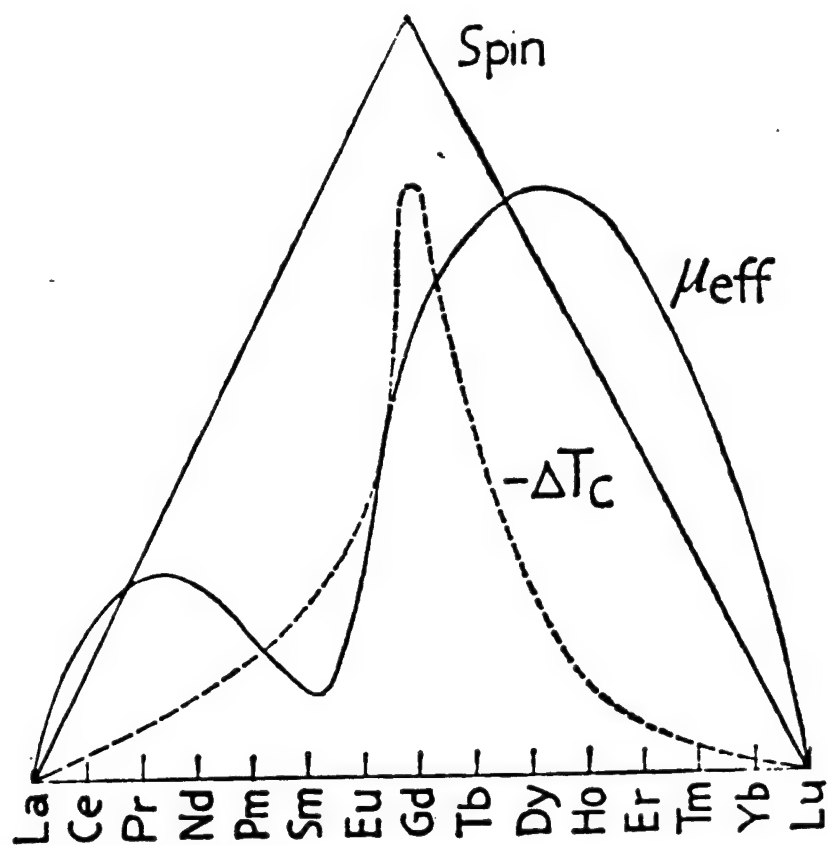


Figure 63. Spin and Effective Magnetic Moment vs. RE Series.

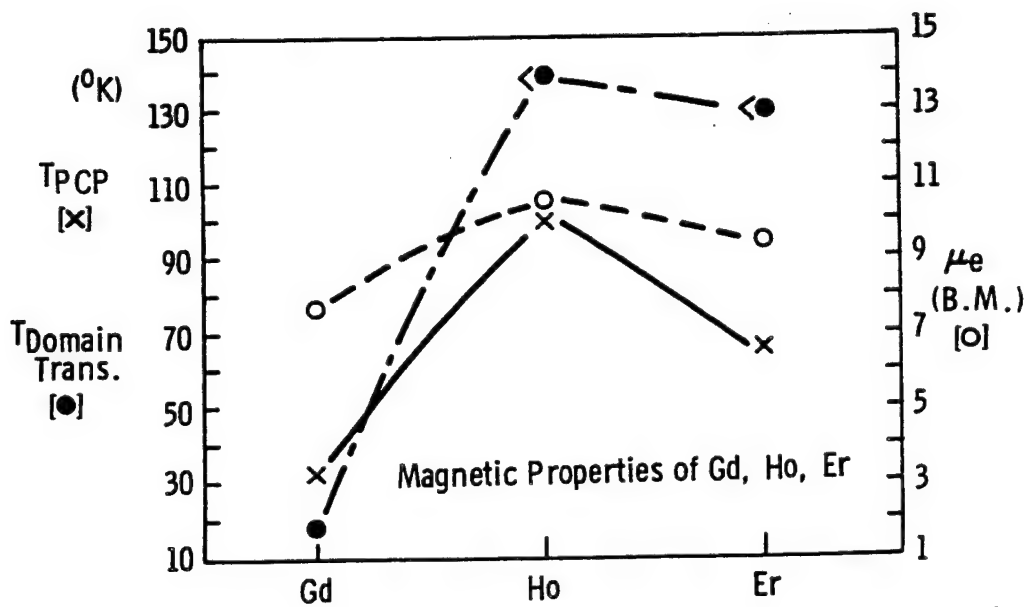


Figure 64. Curie Point and Domain Transition.

0 to a value <0.50 .) The calculation indicated that an indirect exchange correlation in the form of a spin density wave exists between the spin of Gd^{3+} (or other appropriate RE) and that of the d^9 anomalous $Cu(I)^{2+}$. The indirect correlation establishes a short-range antiferromagnetism coupling between the two spins. This antiferromagnetism indirect correlation is enhanced as the effective magnetic moment and spin of the paramagnetic ion increases. The net result is the ordering of these local d^9 $Cu(I)$ spin fluctuation moments. This ordering should promote ease of spin-spin coupling as a contributor to the mechanism that establishes high- T_c superconductivity and is discussed in a subsequent section and shown diagrammatically in Figure 65. Quantum-mechanically, the net result of this correlation is a spin density wave that can be described by invoking a formalism using the particles referred to as spinons. Even in materials that are generally regarded as simple paramagnetic substances, such as RE compounds, there exist some interionic interactions (albeit weak interactions) that are also associated with a temperature below which ferromagnetic or antiferromagnetic behavior prevails. In substances that have a Curie or Neel temperature near or above room temperature, these interactions are quite large (such as Cu^{2+} in $Y_1Ba_2Cu_3O_{7-\delta}$). It is probable that in many such cases, these dipole-dipole interactions are not simple or direct, but are coupled through the electrons of intervening atoms, especially in oxides and halides. The ferromagnetic or antiferromagnetic interactions are normally decreased when the magnetic species are physically separated from each other by intervening ions. In the case of $RE_1Ba_2Cu_3O_{7-\delta}$, the effect of the planar Cu^{2+} ions, as well as the planar and pyramidal apical oxygen ions, will influence the dipole-dipole interaction between the RE^{3+} and the Cu^{2+} unpaired spin at the formerly Cu^{2+} chain site. In these polarized indirect exchange interactions, the possibility also exists for ferromagnetic and antiferromagnetic polarizations, as well as the previously pointed-out spin density wave. Antiferromagnetism in the planes seems to be a precursor for high- T_c superconductivity for the purpose of stabilizing the spin system. The spin fluctuations then form antiferromagnetism causing mediation of spin-spin pairing of Cooper electrons.

When a RE is substituted into the lanthanum strontium cuprate structure [202], according to $La_{1.6}Sr_{0.2}RE_{0.2}CuO_4$, the deviation from linearity in R vs. T shows the opposite tendency (a second-order change toward increasing resistance with decreasing temperature) for gadolinium, europium, and samarium, compared to the trend when substitutions are made into $Y_1Ba_2Cu_3O_{7-\delta}$.

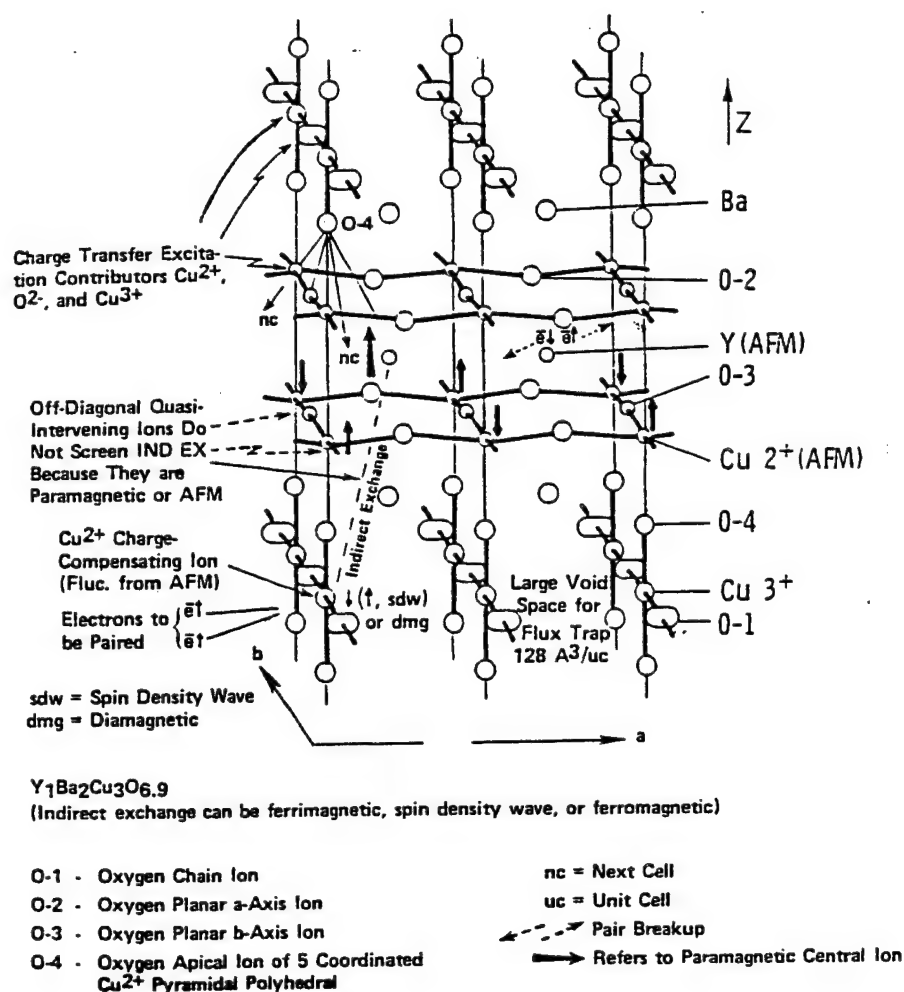


Figure 65. Spin-Fluctuation Contributing Mechanism for High- T_c Superconductivity.

For neodymium, praseodymium, and lanthanum, the deviation is identical to the shoulder of the resistance drip (namely approximately T_c). Nonetheless, this temperature still shows the same peaking trend (Figure 62), as does the T_0 enhancement effect in Figures 60 and 61. However, the almost linear decreasing $[202]$ trend of $T_{(R=0)}$ shown in Figure 62 contrasts the soft crested behavior in $T_{(R=0)}$ in Figures 61 and 62. This suggests that the magnetic factors influencing T_0 are in some ways similar for $\text{RE}_1\text{Ba}_2\text{Cu}_3\text{O}_{7-\delta}$ and $\text{La}_{1.6}\text{Sr}_{0.2}\text{RE}_{0.2}\text{CuO}_4$, but the magnetic properties affecting $T_{(R=0)}$ are different for the two materials.

The reason why in conventional (low- T_c) superconductors the magnetic impurities cause very large reduction in T_c , in comparison to the effect of nonmagnetic impurities, is related to the rotational freedom of the spin direction of each impurity atom or ion. In high- T_c superconductors, the effect of magnetic impurities is small and of the same order as the effect of nonmagnetic impurities. This seems to imply that the impurity spin in the new high- T_c superconducting oxides is not free to rotate and is thus relatively fixed. The further implication is that being fixed is an indication of magnet ordering, which is intrinsic to the host material (such as antiferromagnetism of the RE^{3+} sites) and localized behavior, rather than impurity-impurity interactions and very long-range correlations.

The importance of the temperature (T_0) identifying deviation from linearity in R vs. T in many of the ceramic high- T_c superconductors is borne out in our observations that the positive Hall coefficient vs. temperature data show an increasing slope at this temperature, and more recent data show small oscillations in resistance vs. time at constant temperature commencing at T_0 (shown in Figures 66 and 67).

The independence of superconductive and magnetic behavior in $Gd_1Ba_2Cu_3O_{7-\delta}$ indicates strong anisotropy. Magnetization measurements below T_c at intermediate values of field indicate antiferromagnetism for Gd^{3+} (an f configuration S-state ion). Because Gd^{3+} has zero orbital angular momentum, the gadolinium ion does not interact to first order with the crystal field and retains degeneracy of its half-integral spin $S = 7/2$. Investigations of $Ho_1Ba_2Cu_3O_z$ indicate that high- T_c superconductivity coexists largely independently with strong Ho^{3+} paramagnetism, suggesting that superconductivity is excluded from at least parts of layers containing the Ho ion (in accord with our calculation). This exclusion reduces the dimensionality of the superconducting state. This viewpoint is consistent with calculations of electronic band structure.

6.3.2 Details of the Calculations of the Paramagnetic Central Ion Capacity to Decouple Cooper Pairs and the Indirect Exchange Polarization. The plan of this calculation is to (1) evaluate the Cooper-pairing energy or gap (this can be accomplished from scanning tunneling microscopy and from J_c [T] analysis), (2) evaluate the spatial dependence of the field of the

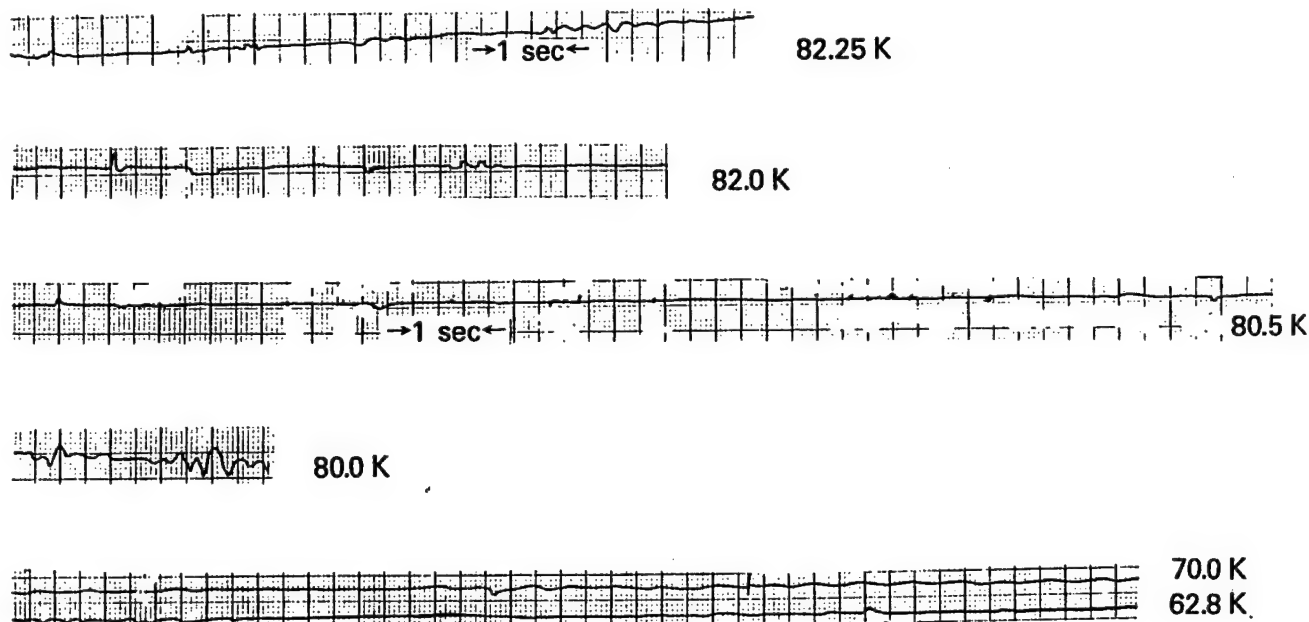


Figure 66. Oscillations in Electrical Resistance During Transition at $B = 0$ to Superconductivity as a Function of Time at Constant Temperature for $\text{Y}_1\text{Ba}_2\text{Cu}_3\text{O}_{7-\delta}$.

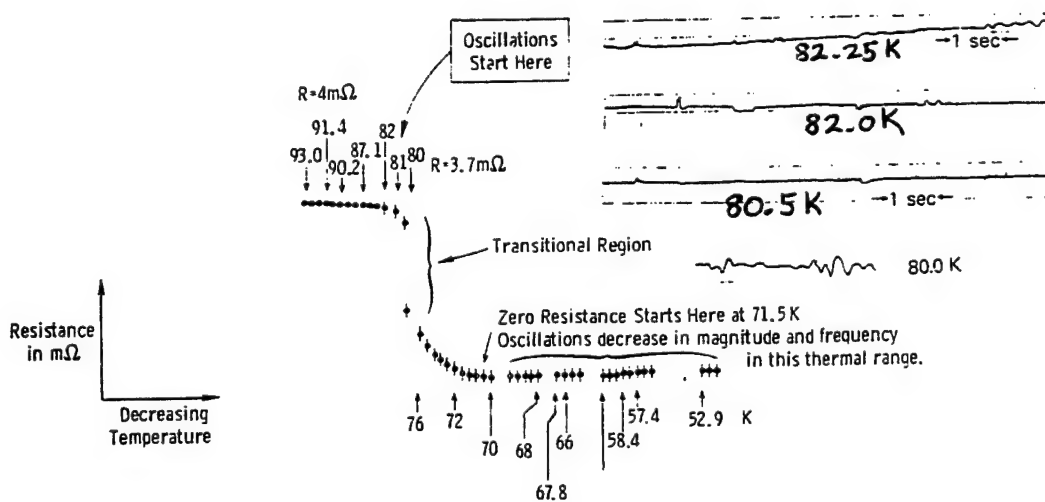


Figure 67. Oscillations in Electrical Resistance During Transition at $B = 0$ to Superconductivity as a Function of Time at Constant Temperature for $\text{Y}_1\text{Ba}_2\text{Cu}_3\text{O}_{7-\delta}$ (Small Oscillation Data Observed at Temperature Data Points Shown With Vertical Bars).

paramagnetic central ion (and associated energy), and (3) evaluate the level of interaction between antiferromagnetism-coupled RE central ions such as $Gd^{3+}(S_{7/2})$ with the d^9 spin fluctuation ion in the Cu-O chain region.

We embark upon this calculation under the simplifying condition of zero external magnetic field ($B_{ext} = 0$). When Cooper-pair conducting electrons, because of the varying phase of their wave function, suddenly find themselves in a spatial position where they are exposed to a field (B_p) due to the paramagnetic moment of the central RE ion (such as Gd^{3+}), then they must experience a time-changing local magnetic field and submit to Maxwell's third equation or Faraday's law:

$$dB_p/dt = -\nabla \times E_p. \quad (11)$$

Thus, a local field is superimposed upon the Cooper pair. Even though a superconducting material will not microscopically support an electric field, the microscopic supercurrent (at $T > 0$ K) interprets this internal field ($-E_p$) in terms of an induced linear momentum P_p , which supplements the additional total linear momentum ($P_s = 2mv_s$) of a Cooper pair in the supercurrent condition S. The pair refers to an electron with $P = p + mv_s$ and an electron with $P = -p + mv_s$. Thus, there exists a microscopic occupation of this momentum state, and this occupation is in the form of pairs.

We write the wave function in the London form $\Psi(r_1, r_2, r_3, \dots, r_N) = \exp\{i\sum_j \chi(r_j)\} \Psi_0(r_1, r_2, r_3, \dots, r_N)$, where $\chi(r_j)$ = phase of the condensate wave function at a function of position, and $\Psi_0(r_1, r_2, r_3, \dots, r_N)$ = ground state wave vector with no charge flow. The total local momentum is then $p_s + p_p = (\hbar/2\pi)\nabla\chi$. Since $\nabla \times \nabla\chi$ (or curl grad) = 0, we write $\nabla \times (p_s + p_p) = 0$. This then specifies potential flow. The force (F), which gives rise to crystal momentum is thus conservative, since $F(\Delta t) = m(v_s + v_p)$ and $\nabla \times (F\Delta t) = \Delta t \nabla \times F = 0$. Thus, the force giving rise to the supercurrent is independent of the path of charge flow, provided the electrons remain paired. The kinetic momentum (P) is the parameter that governs how high a current density (J) a Cooper pair can sustain before undergoing pair scission. This is because the kinetic momentum governs the KE of the pair, and when this energy exceeds the binding energy of the Cooper pair, then the pair undergoes scission. At that point, the measurable current density (I/A) will have exceeded the critical current

(J_c) for that value of temperature. However, for the case in which pair breakup is due to proximity of the paramagnetic ion and its decoupling power, we must consider the internal field established by the paramagnetic ion. We write the kinetic momentum P as follows: $P = P_s + P_p - 2eA(r)/c$, where $A(r)$ the vector magnetic potential defining the internal field due to the paramagnetic ion such that $\nabla \times A(r) = B_p(r)$. The current density (J) in general terms is expressed as $J(p) =$ partial derivative (with respect to P) of the Gibbs free energy $F_s(P)$ of the state of macroscopic occupation defined by P . Thus, the critical current (J_c) above which superconductivity is destroyed or locally above which a Cooper pair breaks apart is written

$$J_c(P) = \partial F_s(P) / \partial P, \quad (12)$$

and evaluated at the value of momentum $P = P_c$ corresponding to local J_c . At this condition, $F_s = F_N$, where F_N is the Gibbs free energy of the normal state. Thus, we have $J_c(P) = \partial F_N(P) / \partial P$ evaluated at $P = P_c$.

Because this expression is a function of P , then it is implicitly also a function of temperature (T). The higher T will cause greater energy $(1/2)mv^2 = KT$ and will influence the wave vector $k = p/(h/2\pi)$. Also, because the kinetic momentum is influenced by the proximity to the paramagnetic ion (since the, paramagnetic ion is the source of the highest internal perturbing field), then a component of J_c is also a function of the position coordinate r . Therefore, in the case being discussed, the total critical current density arises from a component (J_f) due to the supercurrent's accelerating field and a component due to the paramagnetic ion (J_p). Thus,

$$J_c = J_f + J_p.$$

Since J_c is fixed by F_s and by T , the closer a Cooper pair becomes to the paramagnetic ion, the lower is the allowable field current such that $J < J_c$. At a minimum distance r_p , the Cooper pair must break down due to proximity to the paramagnetic perturbing source, even at $J_f = 0$. It is this distance for which we seek a solution. Then for small changes in P caused by closer proximity to the paramagnetic central ion, we can write

$$J_c(P) = \Delta F_N / \Delta P,$$

and

$$\Delta P = \Delta F_N / J_c(P).$$

Hence, from our equation for P in terms of A , we can conclude

$$\Delta F_N / J_c(P) = \Delta \{P_s + P_p - 2e(mxr)/cr^3\}, \quad (13)$$

where P_s is the linear momentum that is not a function of r , but a function of J ; m = magnetic moment of the paramagnetic ion. For an exact solution, equation (13) must be solved for r . The value of $(mxr)/r^3$ is utilized for the vector magnetic potential, A , in the dipole field approximation. Thus, when a Cooper pair moves from position r_1 to position r_2 , we represent the value of J_c at the terminus of this move as

$$J_c = (F_{2N} - F_{1N}) / \{(P_{s2} - P_{s1}) + (P_{p2} - P_{p1}) - (2e/c) [(mxr_2/r_2^3) - (mxr_1/r_1^3)]\}, \quad (14)$$

evaluating parameters with subscript 1 at r_1 , and subscript 2 at r_2 .

Equation (14) is difficult to evaluate because of the free-energy terms. We can, however, evaluate the value of r_2 at which the Cooper pairs decouple, due to the paramagnetic central ion by equating the magnetic energy (at $J_f = 0$) to the gap energy, which is itself equal to the binding energy of a Cooper pair. From scanning tunneling microscopy work [197], we observe that

$$2\Delta = 3.53 k(T_c),$$

or

$$\Delta = 225 \times 10^{-16} \text{ erg.}, \quad (15)$$

but we know that

$$\Delta = -(1/2) \int \mathbf{M} \cdot \mathbf{B} dV = -(1/2) m_1 \cdot \mathbf{B} = (1/2) m_1 \cdot (\mu \nabla \phi), \quad (16)$$

where m_1 = magnetic moment of the Cooper pair. At the instant of decoupling ($m_1 = 2 \mu_B = 3.46 \mu_B$) where B = magnetic field due to the paramagnetic central ion of magnetic moment m_2 , μ = magnetic permeability, and ϕ = scalar magnetic potential = $(m \cdot r)/r^3$.

Taking the parallel or antiparallel moment condition of $\Theta = 0$ and differentiating with respect to r , we have $\Delta = 2\mu_B \{ \mu_B (1 + \chi)m_2/r^3 \}$, where χ = magnetic susceptibility.

We evaluate this for the paramagnetic ion gadolinium, where $m_2 = 10 \mu_B$; $\chi = 775,000 \times 10^{-6}$ cg units and, derive $r_2 = 0.52$ Å. This is a reasonable magnitude because we know the value must be considerably less than the distance from the central ion to the Cu^{2+} planes, which are essentially the Y-O(2) and Y-O(3) distances, which are 2.409 Å and 2.386 Å. Thus, if a Cooper pair approaches Gd^{3+} to within about one-half of an angstrom, it will undergo scission and decouple its formerly antiparallel paired spin. For Er^{3+} this number is 0.45 Å.

Although yttrium is not expected to have a significant magnetic moment, $\text{Y}_1\text{Ba}_2\text{Cu}_3\text{O}_{7-\delta}$ shows a moment of 0.5 μ_B formula units. If the yttrium has some covalency, then it may be associated with a small moment and breakup pairs in only its immediate environment.

6.3.3 Frequency and Time Considerations of Interaction Between the Cooper Pair and the Paramagnetic Ion. We must now determine whether the Cooper pair "sees" the magnetic moment of the center ion (RE^{3+}) as oscillating or as stationary so we can determine if enough time exists for a magnetic-decoupling reaction to take place. If the spin of the central ion is oscillating at such a high frequency that, during the time of critical proximity of the Cooper pair, the pair experiences an oscillating moment of the paramagnetic ion, then there will be no net force to decouple the pair.

The maximum velocity of the Cooper pair is about 10^8 cm/s or 10^{16} Å/S. This means that the pair is within 1 Å of the paramagnetic center ion for about $t \approx 0.1$ fs (10^{-16} s). The magnetic spin of the center ion oscillates at $\nu = 10^{11}$ Hz in the host material. (This frequency may be even higher in an isolated ion condition.) Thus, within the crystal grain, the period of oscillation of the paramagnetic ion is of the order of 10^4 fs; hence, it appears stationary to the passing Cooper pair, which remains

in its vicinity for less than 1 fs. We can conclude that the calculation of the previous section is valid for the real-time regime.

6.3.4 Polarization of Cu^{2+} Spin Fluctuations by the Paramagnetic Central Ion. Normally, the Ruderman-Kittel [203, 204] theory is employed to study the effect of paramagnetic impurities, such as manganese. Briefly, an impurity such as manganese retains some of its Hund's rule magnetization in the solute state and, by this identical mechanism, polarizes the spins of the conduction electrons in its vicinity. The resulting spin polarization, however, is curiously not well localized in the vicinity of the impurity, but, remarkably, is long-range and oscillatory. This means that a second impurity atom at an arbitrary distance from the first admits to ferromagnetic or antiferromagnetic interaction with the first impurity atom, depending on whether the second atom is positioned at the trough or the peak (crest) of the polarization wave.

In the case addressed herein, we must note that the number of paramagnetic central ions is about five times the number of spin fluctuations at the Cu(1) sites. Thus, if the Cu^{2+} spin fluctuation ion at the chain site is viewed as the impurity, although copper is diamagnetic in the bulk metal configuration, the Cu^{2+} spin fluctuation ion becomes either ferromagnetically coupled or antiferromagnetic coupled (with the centrosymmetric polarizing ion) in the context herein when polarized as a fluctuation by the paramagnetic central ion (such as gadolinium).

The calculation of the indirect-exchange coupling constant, according to the Ruderman-Kittel approach, derives from second-order perturbation theory. This is written in abbreviated form [203, 204] as

$$J(\mathbf{R}_{ij})_{\text{ind ex}} = + [J^{\text{Hu}}/2N]^2 \sum \{2\cos(\mathbf{q} \cdot \mathbf{R}_{ij})/[E(\mathbf{k} + \mathbf{q}) - E(\mathbf{k})]\}, \quad (17)$$

with the summation being such that $k < k_F$, and $|\mathbf{k} + \mathbf{q}| > k_F$.

These interactions can be utilized to link the spins and as such be employed in the effective Heisenberg Hamiltonian only under very specific conditions. Two of these conditions are (1) the

Fermi sea remains in the ground state and is not substituted for by a long-range order state, and (2) the elementary excitations must be free particle-like (coulomb repulsion must not cause incipient long-range ordering of the conduction gas).

If the correlation energy in the electron gas can be neglected, then the Hartree-Fock ground state is not the conventional Fermi sea, but is apt to be a spiral configuration described as a spin-density wave. This possibility would render the Ruderman-Kittel approach less appropriate, and thus applicable only to nonordered magnetic materials.

It has been shown [205], however, that indirect-exchange (super exchange) theory can be applied to metals containing elements of the RE series (lanthanides) because the f-shell radii of the RE atoms are so small (additional electrons enter inner orbits) that even nearest-neighboring atoms do not have significant direct overlap.

One considers the Hamiltonian

$$H_{\text{ind ex}} = -\sum_i J_i \mathbf{S}_i \cdot \mathbf{S}_j \quad (18)$$

and calculates the eigenstates where the spins \mathbf{S}_i are situated on locations on a uniform lattice. The q_0 term is defined as the wave vector for which the interaction constant $J(q_0)$ attains a maximum. Then for metals containing lanthanides, when $q_0 = 0$, all spins are parallel, and the ground state is ferromagnetic. However, when q_0 is a wave vector on one or more points of symmetry of the Brillouin zone boundary such as $(\pm 1, \pm 1, \pm 1)$ in the simple cubic Bravais lattice, then the ground state is an antiferromagnetic configuration. If q_0 is not any of these unique wave vectors, then the ground state is a spiral spin variation. Since the location of the Cu^{2+} fluctuations from antiferromagnetism are not likely to be definitively ordered on the lattice chain sites, we should expect some spiral configurations and some antiferromagnetic correlations, with the $q_0 = 0$ ferromagnetic case being most rare. Thus, if the ions that host the spin fluctuations are ordered on a sublattice, then their antiferromagnetic (or ferrimagnetic) interaction correlation with the Gd^{3+} ion (for example) should foster at least a slightly higher T_c .

The Ruderman-Kittel interaction must be solved numerically and is cast in terms of k_F , which is defined as $2\pi/\lambda_F$, where λ_F = wavelength of conduction electrons when constrained by the Pauli exclusion principle, and they become polarized by the magnetic impurity. The important parameter $N_{c/a}$ (dimensionless) is the number of conduction electrons per magnetic atom, and is associated with k_F . In the cubic lattice case, an antiferromagnetic correlation exists for $1/4 < N_{c/a} < 3/2$ (for bcc and fcc) or $< 5/2$ (for simple cubic). In $\text{Gd}_1\text{Ba}_2\text{Cu}_3\text{O}_{7-\delta}$, there is one magnetic ion per unit cell (Gd^{3+}), but, near T_c , there is about one conduction carrier per unit cell. Thus, the parameter $c/a \sim 1$ and would indicate antiferromagnetic indirect exchange for a simple cubic unit cell. The value of $J(0)$ is found to be proportional to the Curie Temperature; hence, antiferromagnetic indirect-exchange correlations may be a maximum for Gd^{3+} as the RE constituent compared, for example, to Ho^{3+} and Er^{3+} . To determine whether the type of correlation is the stable ground state at low temperature, it is necessary to examine the spin wave spectrum $\hbar\omega(r)2S[J(0) - J(k)]$. The indirect polarization is shown in Figure 65, and the adjacency of cells is emphasized in Figure 68 in order to visualize successive polarizations at the $\text{Cu}(I) d^9$ substitutional states.

Thus, the previous discussion indicates the strong possibility that in $\text{RE}_1\text{Ba}_2\text{Cu}_3\text{O}_{6.9}$ the RE paramagnetic ion polarizes some of the fluctuations from antiferromagnetism in an antiferromagnetic correlation (with respect to the centrosymmetric RE, and, thus, with respect to each other. The correlation is likely, however, to be mixed and include ferromagnetic interactions, especially spin density waves as well. Crucial to this analysis is the Cu^{2+} plane ions and the copper chain ions being characteristically different in some ways from what they would be if they were strictly subject to the BCS formalism of low- T_c superconductivity. This difference is borne out by recent NMR and NQR studies, including spin-lattice effects [206], which also show degradation of the sharp NMR spectrum of the copper chain ions due to oxygen loss and a strikingly different electron dynamics between the copper plane and copper chain ions. Appreciable disorder is reported in this work in the Cu^{2+} planes, which is probably due to the puckering and the effects of five-fold coordination. The $\text{RE}_1\text{Ba}_2\text{Cu}_3\text{O}_{7-\delta}$ unit cell is itself elongated orthorhombic; however, for the purpose of the present analysis, due to its symmetry, we can consider the center one-third of the cell that is a nearly cubic section and still retain all of the essential chemical physics of the polarization effect. Here, it must be realized that (Figure 65) for every $\text{Cu}^{3+}d^8 \rightarrow \text{Cu}^{2+}d^9$ (antiferromagnetism spin

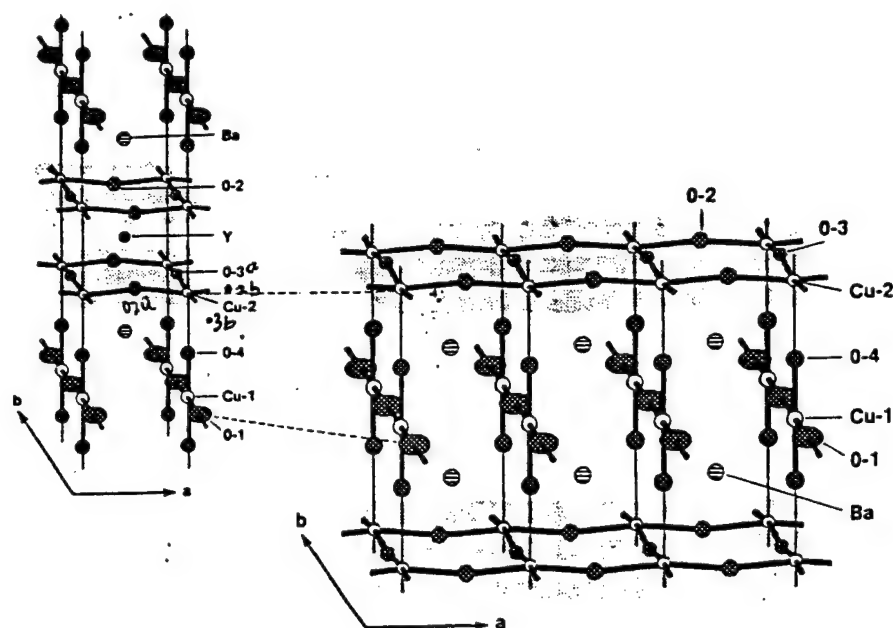


Figure 68. The Structure of $\text{Y}_1\text{Ba}_2\text{Cu}_3\text{O}_{7-\delta}$ [111, 112] Showing Lattice Parameters:
 $a = 3.8231 \text{ \AA}$, $b = 3.8864 \text{ \AA}$, $c = 11.680 \text{ \AA}$, Space Group P_{mmm} , Orthorhombic Bravais Lattice. Chains in the b - c Planes Are CuO_3 . Layers in the a - b Plane Are CuO_2 . Bond Lengths Are
 $\text{Cu}(1) \text{ Cu}^{+3} - \text{O}^{-2}(1) \text{ (in Plane)} = 1.943 \text{ \AA}$,
 $\text{Cu}(1) \text{ Cu}^{+3} - \text{O}(4) \text{ (Below Plane)} = 1.850 \text{ \AA}$,
 $\text{Cu}(2) \text{ Cu}^{+2} - \text{O}(2) \text{ (in } a\text{-Direction of Puckered Plane)} = 1.928 \text{ \AA}$,
 $\text{Cu}(2) \text{ Cu}^{+2} - \text{O}(3) \text{ (in } b\text{-Direction of Puckered Plane)} = 1.962 \text{ \AA}$, and
 $\text{Cu}(2) \text{ Cu}^{+2} - \text{O}(4) \text{ (in } c\text{-Direction)} = 2.303 \text{ \AA}$.
The Numbers 1, 2, 3, and 4 Refer to the Identified Oxygen Ion. These Lattice Parameters Suggest Jahn-Teller Distortion in d^9 (Cu^{+2}) With Elongation in d_{z^2} , Hence Favoring the e_g State to Be in the Configuration $(d_{z^2})^2 (d_{x^2-y^2})^1$.

fluctuation) site in $\text{O}_{6.9}$ stoichiometry, there is more than one Y^{3+} or RE^{3+} central ion nearest neighbor (because of each $\text{Cu}(1)$ belonging to eight unit cells). At T_c , the temperature is above the Neel temperature for the RE ions; hence, these ions are not antiferromagnetically related (with each other) at T_c , and we interpret this to mean that their average paramagnetism (majority spin) strongly enforces parallel or antiparallel correlation with the spin fluctuation unpaired state. This means that relative to each other, the spin fluctuation sublattice will have essentially a similar relationship as the average moment of the polarizing paramagnetic central ions have to each other and be either parallel to the RE spins or antiparallel to them or related to them by a spin density wave. The second and next nearest neighbor should have only minor effects on this polarization.

6.3.5 Calculations of Approximate Energy and Torque for Polarization. The geometry and structure of the $Y_1Ba_2Cu_3O_{7-\delta}$ cell shows that the distance from Y^{3+} to the Cu^{2+} , which exists at a chain site (for charge neutrality reasons) is 6.45 Å with no directly on-diagonal intervening atoms (or ions) situated directly between them. We now calculate the torque $\tau = m \times B = mB (\sin\Theta)$. Taking $\Theta = 90^\circ$ for a worst-case requirement for alignment (polarized ordering), we have $\tau = mB = m_{Cu^{2+}} \mu \nabla[(m_{RE} \cdot r)/r^3]$.

In the aforementioned analysis, we take $m_{Cu^{2+}} = 0.5 \mu_B$. Then we have $\tau = 0.027 \times 10^{-3} \text{ eV} = 0.27 \times 10^{-4} \text{ eV}$. This value has an order of magnitude slightly less than that for spin-orbit coupling and slightly more than that for hyperfine electron-nuclear coupling, and, hence, is of the correct order for magnetic spin-spin coupling [207].

6.3.6 Ferrimagnetic Correlations. The case is now treated for correlations between the RE^{3+} central ion and the copper antiferromagnetic spin correlations that are neither ferromagnetic nor antiferromagnetic, but ferrimagnetic [208]. The interactions between magnetic ions in some materials are negative rather than positive, and hence lead to unequal antiparallel alignment of neighboring or interacting magnetic moments. Ferrimagnetic compounds are characterized by exchange interactions and two or more interpenetrant sublattices, which are spontaneously magnetized in different directions. The two most fully studied crystal types that are known to be ferrimagnetic are classified as spinels and garnets. The spinel structure is an A_2BX_4 compound such that X is a nonmagnetic divalent ion such as oxygen, sulfur, or selenium; and B is a divalent metal such as Mn, Fe, Ni, Co, Cu, Pb, or Mg. In the case of $RE_1^{3+}Ba_2Cu_3O_{7-\delta}$ the B ions are Cu^{3+} and Y^{3+} . The A ion in a spinel is a trivalent ion of a metal such as Mn, Fe, Co, Al, or Ga. In the case of the superconductor, it is Ba^{2+} and Cu^{2+} . If the "B" are not all of the same metal (as is the case in the superconductor), the net result can be a mixed correlated material. In the spinel structure, it is shown that one-third of the A and B ions are in the spin-up orientation, and the other two-thirds are in the spin-down direction.

In the $RE^{3+}Ba_2Cu_3O_{7-\delta}$ structure interpreted as a $(RE_1^{3+}Cu_1^{3+})(Ba_2^{2+}Cu_2^{2+})_1O_{8-w}$ defect derivative of the K_2MnF_4 structure, there are several ways to envision the sublattices. This is

accomplished through considering the elongated orthorhombic cell of the superconductor as being subdivided into a triple Perovskite structure.

Based upon analogy to the work described in the earlier section on Rudderman-Kittel indirect exchange, the possibility for ferrimagnetic correlations between the ions (that constitute the spin fluctuation systems) with themselves and with the RE central ion is very reasonable. The question then that naturally arises is, "What is the magnetic state of those fluctuations from antiferromagnetism that are not correlated?" Here, we are perhaps assisted by noting that in the high- T_c superconductors, the major ions such as copper, bismuth, and thallium are ions that, when in atomic metallic form, are diamagnetic (with respective susceptibilities of -5.46 , -280.1 , and -50.9×10^{-6} -cg units). These elements are ideal for high- T_c superconductivity because of their multivalence and the manner with which they can coordinate oxygen into five- and six-fold nearest neighbors. The partial metallic bonding and the cation-neutralizing charge-transfer excitations in bismuth, thallium, and copper in the high- T_c superconductors may be the factor that allows their atomic (metallic) diamagnetism to be so important. It is interesting to note that of all the divalent anions that can participate in the A_2BX_4 structural types, only oxygen is not diamagnetic and, at the same time, only oxygen seems to be compatible with high- T_c materials as the principle anion. This suggests that a diamagnetic anion may interfere with superexchange, and thereby destroy antiferromagnetic indirect-exchange correlations. From this, we form the interpretation that the noncorrelated Cu^{2+} ions at formerly Cu^{3+} sites are diamagnetic. The frequency of oscillation of the noncorrelated diamagnetic Cu^{2+} fluctuations from antiferromagnetism is apt to be much greater than the spin-flip oscillation of the RE^{3+} ions, and, even if the period is of the order of the time of proximity of a Cooper pair, the transient paramagnetism (when in an ionic rather than a metallic or atomic state) would be too weak to break up a pair.

Diamagnetism of isolated ions results from the orbital motion of electrons as a consequence of the force that each electron experiences when moving in a magnetic field. Although diamagnetism is a universal property of tight and complete general spin pairing, it is outweighed by paramagnetism when electrons undergo transitions to other unique quantum states of differing magnetic moment due to the applied magnetic field. Since it would be an unrealistic assumption to conjecture that the Cu^{2+}

spin fluctuation from antiferromagnetism does not undergo transition, we can suspect that those that are uncorrelated undergo oscillations due to charge-transfer excitations between diamagnetic and paramagnetic states.

It is believed that the orbital contributions to the spin indirect-exchange interactions are small in (Y^{3+} or RE^{3+}) $Ba_2^{2+}Cu_3O_{7-\delta}$ because the orbital moment is essentially quenched due to the intense, nonuniform electric field arising from the oxygen ions that surround the paramagnetic RE and the weakly paramagnetic barium. Again, by analogy with the spinel archetype of ferrimagnetism, the exchange correlation in an A_2BX_4 spinel is influenced by whether the ferromagnetic ion is distributed over only the VI-coordination sites or both the VI- and IV-coordination sites. The latter case characterizes inverse spinels in which one-half of the A ions are in tetrahedral interstices, and the other half and all of the B ions are in the octahedral interstices. This occurs when the preference toward octahedral coordination is greater for the B ions than for the A ions. In the aforementioned superconductor, it seems clear that Cu^{2+} can exist at planar sites, and, depending upon δ , at chain sites as well. Furthermore, Cu^{2+} can exist at chain sites and may, on occasion, substitute for Y^{3+} or RE^{3+} . Because of these added complexities or deviations, the indirect-exchange and superexchange correlations are affected, and the net result causes the spontaneous moment per molecule unit to be equal to the average moment of the B ion; or in the case of the superconductor, the spontaneous moment will be the weighted average moment of the RE and the chain $Cu(1)^{2+}$. The deviations probably also ensure the presence of some noncorrelation spins and some intrinsic disorder that must ultimately be a limiting factor on T_c .

6.3.7 Quantized Flux Trapped in a High- T_c Superconductor When $H > H_{c1}$: Vortice Lines of Quantized Flux. During the past 4 yr of study, it has become clear that in the new high- T_c oxide superconductors correlations are more localized and of a shorter range than in low- T_c conventional superconductors such as niobium. This is certainly indicated from the vast difference in the coherence length of high- T_c materials (10–17 Å) as contrasted to low- T_c superconductors ($\approx 1,000$ Å). However, because of the oxide's high value of H_{c2} we must ask ourselves over what spatial range is flux quanta trapped when $H_{c1} < H < H_{c2}$ (readmission of flux beneath the penetration depth from the external field) [37].

The London value for flux quanta enclosed in a topological region of closed loops with cross-sectional perimeter dl is $\phi = A \cdot dl = n(hc/e)$. This relationship is independent of material and is derived from the quantum-mechanical requirement or condition for a single-valued solution to the wave function in the case when the current density J is Gauge-invariant. The value for hc/e is $4 \times 10^{-7} \text{ G/cm}^2$. Experimental evidence shows quantization in the form $n(hc/2e)$ in which the factor of $1/2$ arises from pairing.

From our studies of resistance vs. B at in $Y_1Ba_2Cu_3O_{7-\delta}$ having $T_c = 81.7 \text{ K}$, we find that $H_{c2} \gg 15 \text{ T}$ (150,000 G); however, H_{c1} is much less than 1 kG. The quantization evidence that had been experimentally proven for tin and lead cylinders (in three orthogonal Helmholtz coils) is interpreted by Onsager [209] and by Byers and Yang [210] as direct proof of Cooper pairing.

From Stokes theorem, the line integral $\int A \cdot dl$ = the surface integral $\int (\nabla \times A) \cdot ndS$. We can write $\nabla \times A = B$, and take $H_{c1} = 150 \text{ G}$. If we then can approximate A as independent of l , and B as independent of S , then using a value of H that is much greater than the lower critical field and of the order of the upper critical field ($H_{c2} \sim 100 \text{ T}$), we can write $\int dS = n(2 \times 10^{-7} \text{ G/cm}^2)/100 \text{ T}$. This yields $S = 20 \times 10^{-14} \text{ cm}^2$. For $n = 1$, the result shows a radius for the vortice (region of interior-trapped flux) of 25 Å. This is a reasonable value because it correlates fairly well with the coherence length of the high- T_c superconductors.

6.3.8 Calculation of Cooper-Pair Concentration. The coherence length in a high- T_c material is believed to be about on the average 15 Å, contrasting as previously mentioned the 1,000-Å coherence length of conventional low- T_c superconductors such as niobium and vanadium. The volume of a sphere of radius 15 Å can be envisioned as the domain of freedom of a single Cooper pair during the interval of its transient lifetime. This volume is simply $(4/3) \pi r^3 \approx 13.5 \times 10^{-21} \text{ cm}^3$. Based on space filling, this indicates a minimum carrier concentration of Cooper pairs of 7.4×10^{19} Cooper pairs/cm³. However, interpenetration of Cooper pairs is expected to force an increase in this number. We have measured the positive hole carrier concentration from Hall effect studies in the normal state in $Y_1Ba_2Cu_3O_{7-\delta}$ at a few degrees above the critical temperature to be about 6×10^{20} to 1×10^{21} holes/cm³. The concentration of bound holes that are the result of the charge-transfer

excitations is about $10^{22}/\text{cm}^3$. This shows that the Cooper pair idealized concentration is at least an order of magnitude or so less than both the free- and bound-hole concentrations. It is also at least an order of magnitude less than the total free-carrier concentration in the superconducting state. Therefore, on the average, no more than about 1 free electron in 10 enter into a paired state.

We should be able to recalculate the Cooper-pair concentration from a binding energy and J_c analysis and approach the idealized condition by employing the value of J_c for the best crystalline films of $\text{Y}_1\text{Ba}_2\text{Cu}_3\text{O}_{7-\delta}$ ($J_c = 5 \times 10^5 - 1 \times 10^6 \text{ A/cm}^2$). We can write the critical current in terms of the critical momenta (p_c) of the Cooper pair, the values of p_c being associated with an energy that exceeds the binding energy (or gap) of the Cooper pair:

$$J_c = (p_{cp})p_c/m,$$

where m = effective mass of Cooper pair. The gap energy can then be described as

$$\Delta = (p^2/2m) = \{[(mJ_{c2}/P_{cp})^2]/2m\},$$

or

$$\Delta = [(m/2) (J_c/P_{cp})]. \quad (19)$$

From scanning tunneling microscope studies, we have shown that $2\Delta = 3.53 K T_c$ or $\Delta = 22.5 \times 10^{-15} \text{ erg} \approx 14 \text{ meV}$ (for $\text{Y}_1\text{Ba}_2\text{Cu}_3\text{O}_{7-\delta}$). The effective mass of the electron at this energy is $m_e = 9 \times 10^{-28} \text{ g}$, which we multiply by two in order to consider the pair. Using the conversion factor of about 0.62×10^{19} electrons per coulomb, we calculate a minimum of a $P_{cp} \approx 0.6 \times 10^{18}$ Cooper pairs/ cm^3 for $J_c \approx 5 \times 10^5 \text{ A/cm}^2$, and $P_{cp} = 2.4 \times 10^{18}$ Cooper pairs/ cm^3 for $J_c = 2 \times 10^6 \text{ A/cm}^2$.

This value is within an order of magnitude of the "idealized" concentration given in the previous analysis. The small linear term in the specific heat of $\text{Y}_1\text{Ba}_2\text{Cu}_3\text{O}_{7-\delta}$ may be related to some normal conduction electrons existing below T_c as being due to defects or impurities. The aforementioned correlation in the calculations using two different approaches tends to suggest that the Cooper pairs do not appreciably interpenetrate each.

The temperature dependence of the Hall constant near T_c implies a temperature dependence of the conductivity. This is most likely to be essentially due to the temperature dependence of the carrier concentration near T_c where Cooper pairs may be forming at preonset conditions. It is not yet experimentally established whether holes or electrons are paired in the supercurrent; however, the observation that the Hall coefficient enters the zero-value state (corresponding to zero resistance) from a negative value lends credence to our interpretation that electrons are the carriers that are Cooper-paired. Hence, the minority carrier in the normal state is the carrier that is starting to be paired at temperatures just above T_c (where deviation from linearity in resistance vs. temperature begins). Since pairs seem to be forming in this preonset temperature range (and this will be borne out in subsequently discussed magnetic field studies), it is worthwhile to further study the bound hole that acts as the mediator and the internal electric field that induces the charge transfer to establish the bound hole. This study will be presented in subsequent sections on the mediator/pair Coulombic interaction and the internal perturbation electric field.

6.4 Magnetically Related Properties of the Bismuth-, Gallium-, Antimony-, and Gadolinium-Containing High- T_c Superconductors.

6.4.1 The Effect of the Applied Magnetic Field on Resistance vs. Temperature Behavior in the Normal, Preonset, Transitional, Foot, and Zero-Resistance Regions. In Figures 69–71, we respectively plot for $\text{Bi}_2\text{Sr}_2\text{Ca}_2\text{Cu}_3\text{O}_{10}$ the R vs. B data for various precise values of T during the transition to the superconducting state and the extracted data of R vs. $1,000/T$ for differing values of B . One of the unique accomplishments of our study relative to most of the work in the field is that we devoted considerable attention to studying the nonequilibrium regimes, such as the transitional, preonset, and foot regions, rather than studying exclusively the normal and zero-resistance states. The data of Figure 69 show that the effect of the B -field in elevating resistance is stronger as the temperature is lowered within the transitional zone. The data of Figure 70 show that, in the transitional region, the B -field causes a diverging of the R vs. $1,000/T$ data which, when back-extrapolated to intersection, do so at what is believed by us to be the best T_c . We identify this as T_c by comparison with R vs. T data for this compound at zero B -field and by examining the Hall-effect data for that temperature at which the positive Hall voltage drops precipitously to zero (Figures 72

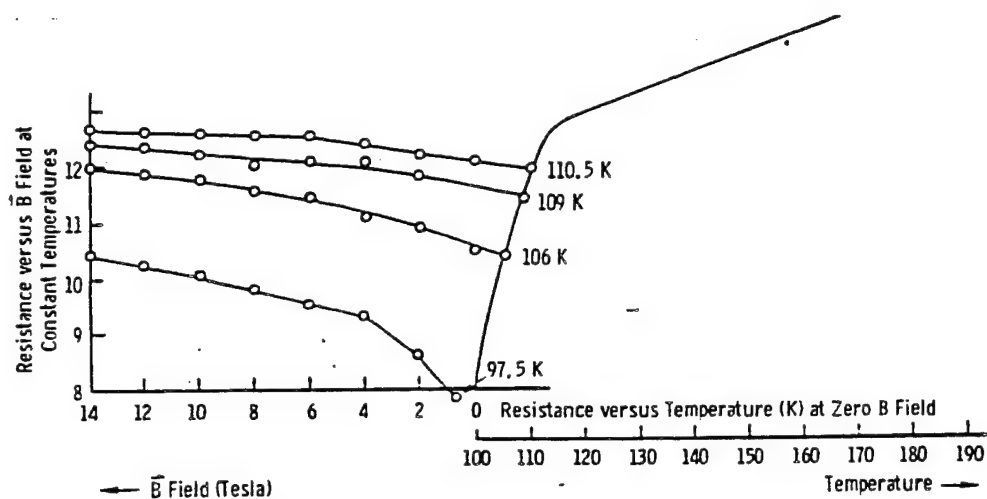


Figure 69. Electrical Resistance vs. B-field at Constant Temperature in the Intermediate State for BiSrCaCuO High- T_c Superconductor.

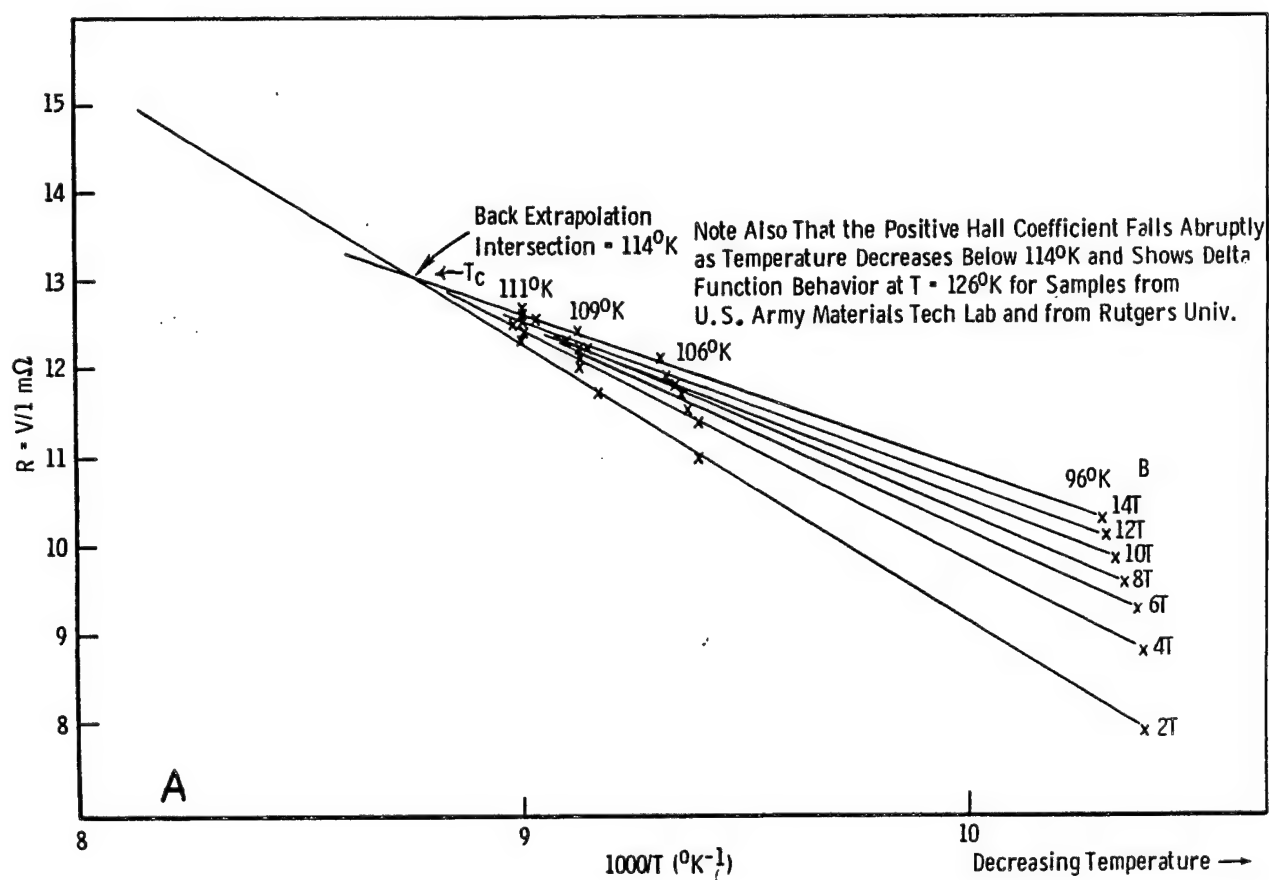


Figure 70. Electrical Resistance vs. Reciprocal Temperature for $\text{Bi}_y\text{Ca}_z\text{Sr}_w\text{Cu}_r\text{O}_x$ as a Function of Applied Magnetic Field During Transition to Superconducting State.

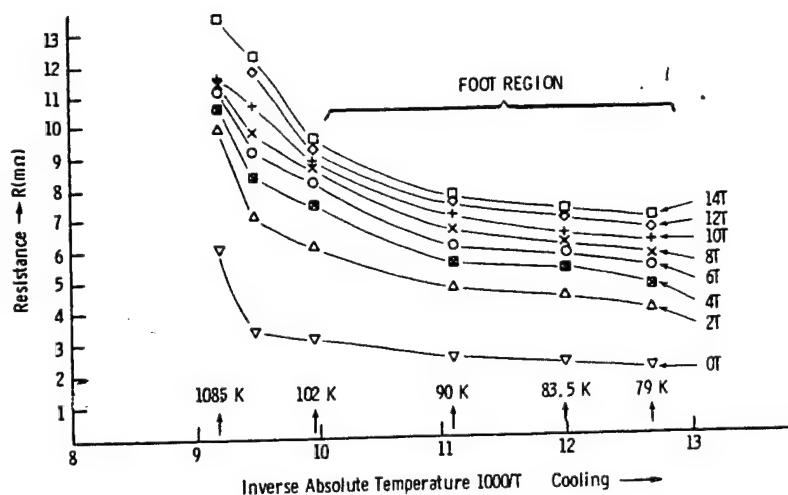


Figure 71. Resistance vs. $1,000/T$ for BiSrCaCuO as Function of Magnetic Field.

and 73). Figure 71 gives the R vs. $1,000/T$ data corresponding to temperatures in the foot region of the R vs. T curve for the BiSrCaPbCuO high- T_c superconductor. This curve does not show the intersecting linear behavior displayed in Figure 70, but suggests an extrapolated intersection at a temperature lower than the region of distinct slope change in the data (≈ 102 K). These differences indicate a substantial difference in the physics of the governing mechanism in the transitional region vs. that of the foot region. In Figure 74, we show our data on the recovery of resistance as a function of magnetic field to 17 T at temperatures corresponding to the zero-resistance region for $Y_1Ba_2Cu_3O_{7-\delta}$. This figure shows almost a linear behavior, and a similar behavior is shown in the equivalent R vs. B for the zero-resistance state of the bismuth-containing high- T_c superconductor. This contrasts the more temperature-dependent behavior and nonlinear character observed in the transitional zone [211].

The Hall data for the bismuth-containing high- T_c superconductor are plotted for three separate samples of the bismuth-containing superconductor. Figure 72 gives the digital and analogue (inset) data for the sample prepared in our own laboratory and shows a delta-function-like peak at 126 K

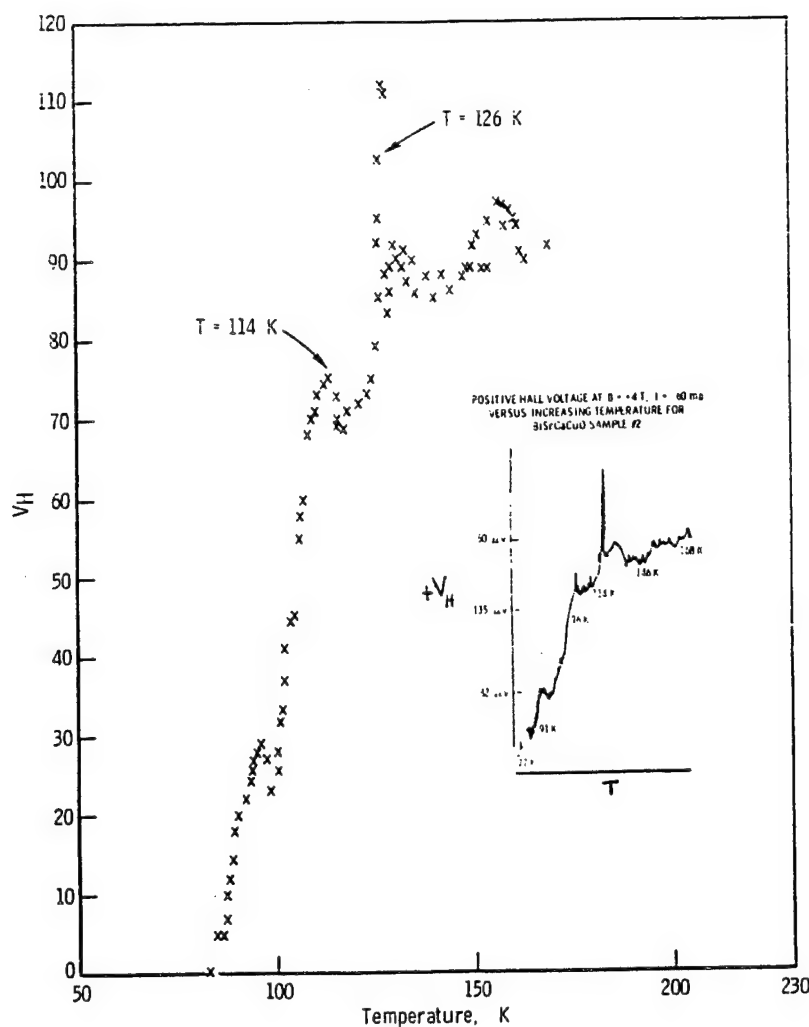


Figure 72. Hall Effect vs. Temperature K at $B = 4$ T for BiSrCaCuO (Heating Cycle ~ 0.1 K/min).

(a peak characteristic of the polycrystalline ceramic material as described earlier), a secondary peak anomaly at 114 K, with possibly a third peak at ~ 96 K. The presence of three peaks may be due to the presence of the principal phase of $\text{Bi}_2\text{Ca}_2\text{Sr}_2\text{Cu}_3\text{O}_{10}$, as well as the presence of two additional slightly differing phases that are very difficult to separate from the yield of the solid-state chemical synthesis reaction. In Figure 73, the data for a sample synthesized by Moon and Safari at Rutgers University are shown, also displaying peaks at 126 and 114 K. In both sets of data, the applied magnetic field was selected to be 4 T in order to obtain appropriate Hall voltages at 60-mA current. Figure 75 gives the analogue Hall data for a previously prepared sample at our laboratory and indicates the presence of two peaks.

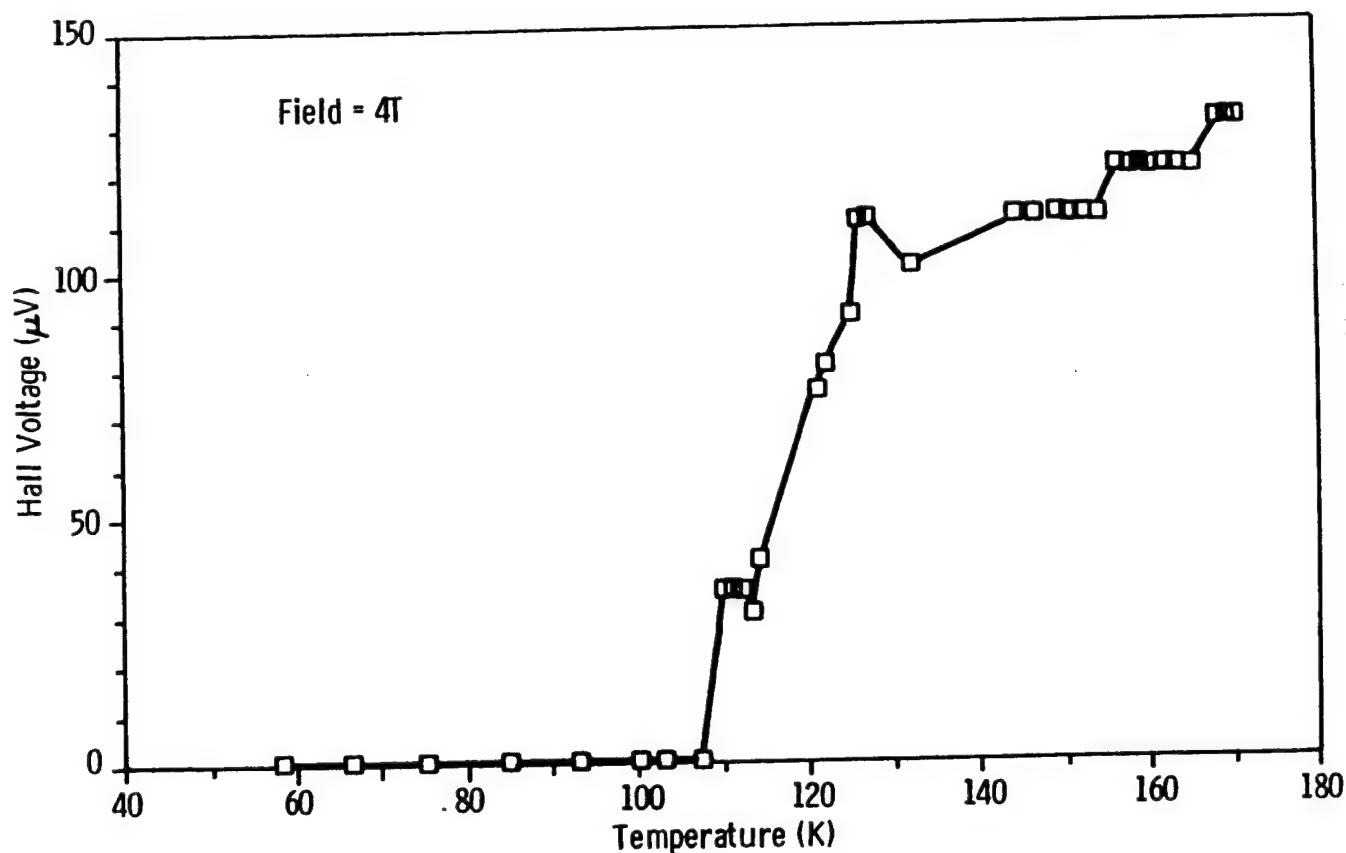


Figure 73. Hall Effect vs. Temperature for BiSrCaPbCuO, Suggesting Singularity and Showing Abrupt Drop to Zero. Sample Was Fabricated at Rutgers University Center for Materials Science and Electrical Engineering Department.

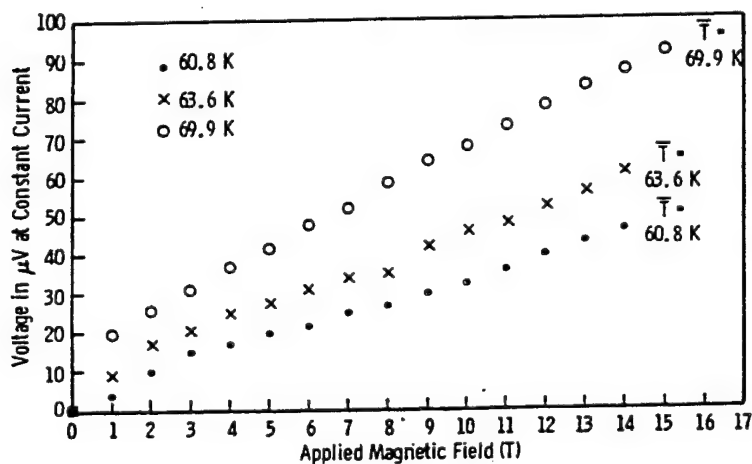


Figure 74. Resistance vs. B-field for Several Values of Temperatures in $Y_1Ba_2Cu_3O_7$. Graph of Recovery of Electrical Resistance From the Zero-Resistance Level as Function of Applied Magnetic Field in Tesla at Three Different Values of Temperature for $Y_1Ba_2Cu_3O_7$ Polycrystalline Bar Using Bitter Magnet.

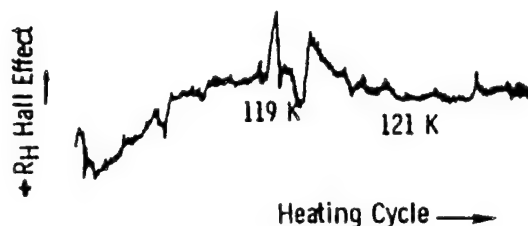


Figure 75. Hall Voltage vs. Temperature in Kelvin for $\text{Bi}_{1.5}\text{Ca}_2\text{Sr}_{0.5}\text{Cu}_3\text{O}_x$ Sample No. 1 at $B = +5 \text{ T}$.

These data correlate very well with measurements on single-crystal $\text{Bi}_2\text{Sr}_2\text{CaCu}_2\text{O}_{8-\delta}$ conducted by Zettil [212] showing an anomaly in $+R_H$ near T_c . This suggests that the cause of an anomaly in the Hall voltage vs. temperature, in the neighborhood of T_c , is fundamentally related to the mechanism of high- T_c superconductivity and does not arise purely from the nature of the ceramic sample (grain boundaries, etc), albeit that the peaked character is accentuated by the ceramic character of a polycrystalline sample.

Figure 76 shows the magnetic field sweep (period = 60 s) experiments that we conducted for the high- T_c superconductor $\text{Y}_{0.5}\text{Gd}_{0.5}\text{Ba}_2\text{Cu}_3\text{O}_{7-\delta}$ at temperatures in the normal state, as well as the preonset, transitional foot, and zero-resistance regions of the R vs. T curve shown in Figure 77. The location of the preonset region in this set of experiments was actually first pinpointed by seeking the temperature at which the magnetic field sweep (to 20 T) caused an increase in the four-terminal electrical-resistance measurement and then confirmed after the B-field sweep experiments by measuring R vs. T as shown in Figure 77. The inset to Figure 76 gives the change in resistance during a 30-s sweep from $B = 0$ to $B = 20 \text{ T}$ as a function of very accurately controlled ($\pm 0.05 \text{ K}$) temperature. Inspection of this inset figure shows a straight line containing the data points the are related to the normal state, the preonset region, and the transitional zone. The data points for the $R = 0$ and foot regions fall off of this straight line. In that the preonset data points link via a straight line the normal and transitional-state data points, we then interpret this figure to indicate that in the preonset zone Cooper pairing has already begun in an incipient fashion, but has not proceeded in high enough a concentration to create a sharp resistance drop. Another way of interpreting this

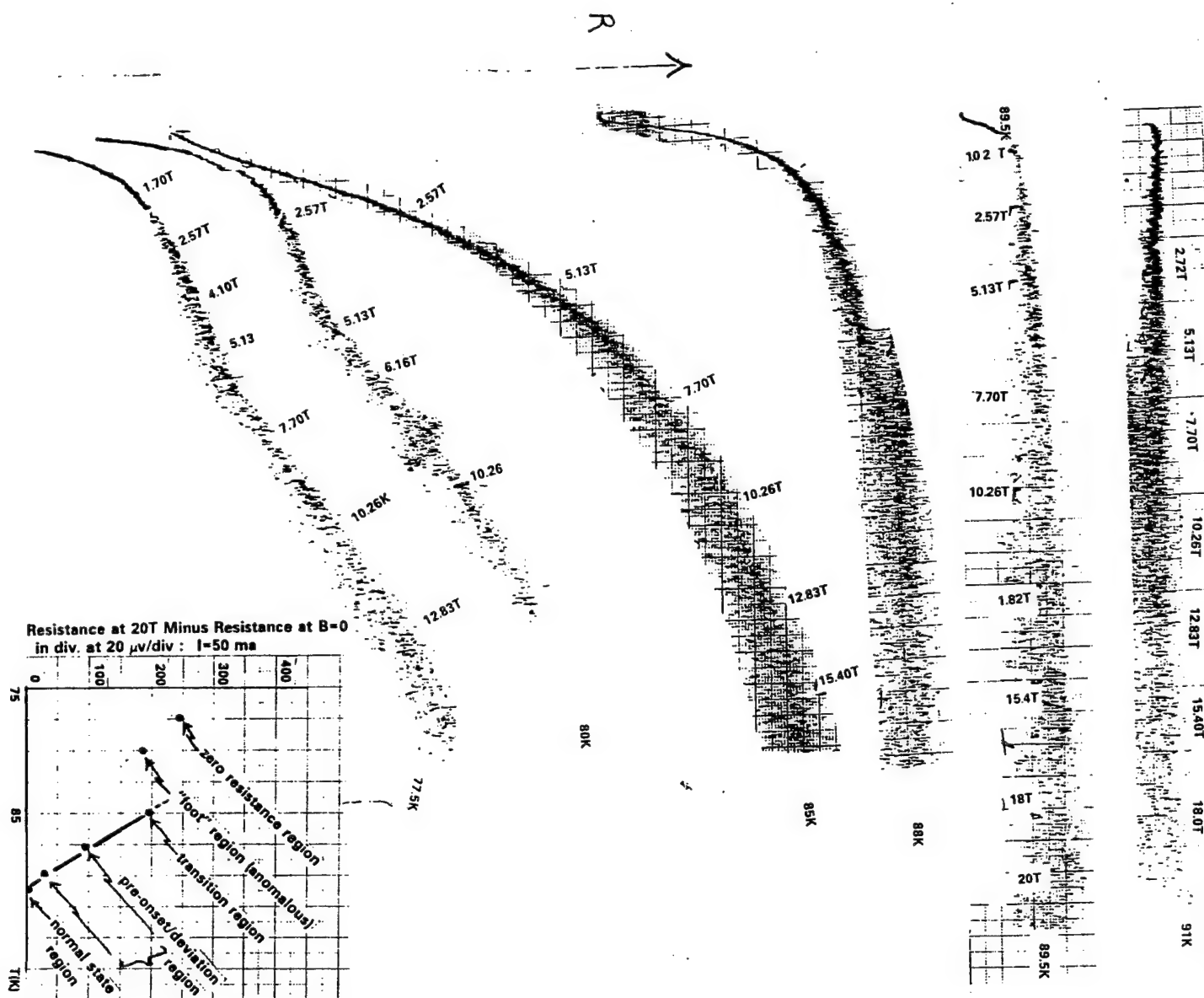


Figure 76. Change in Resistance vs. B-field at Temperatures From Normal State to Zero-Resistance State: Up-Field Sweep 20 T in 60 s, ΔR in div at 20 $\mu\text{V}/\text{div}$ Using 50 ma.

insufficient concentration is to hypothesize that, in the preonset zone, the lifetime of the mediator is insufficient to cause ample Cooper pairing to induce a transition to a supercurrent regime.

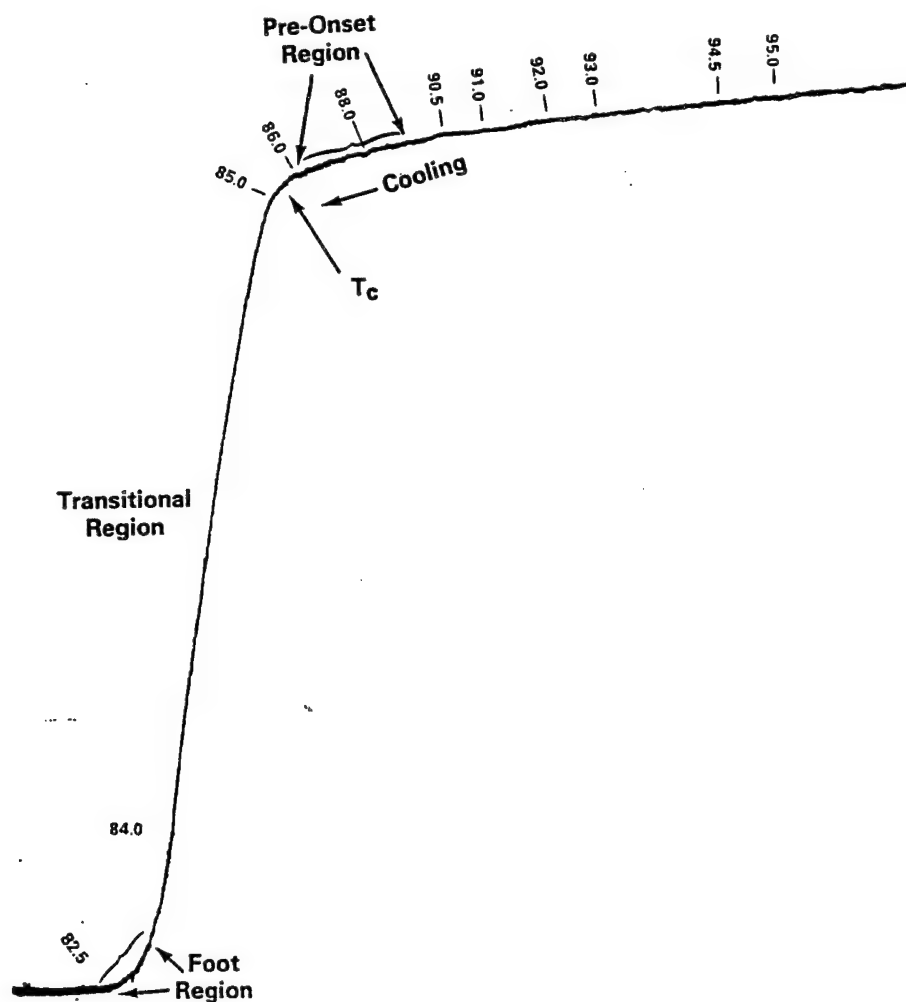


Figure 77. Resistance vs. Temperature $Y_{0.5}Gd_{0.5}Ba_2Cu_3O_{7-x}$

Although the preonset characteristic of deviation from linearity in R vs. T is shown more clearly in ceramic materials than in single crystals, there is no evidence to indicate that certain phenomena characteristic of ceramics (such as typical nonmagnetic impurities) have any effect on the gross structures of R vs. T , on T_c , or on $T_R = 0$. The enhancing of charge-transport nonlinearities and anomalies observed in ceramic polycrystalline materials is related to the effects of grain boundaries in accentuating carrier or particle scattering or trapping processes. The nonlinearity observed in R vs. T data for ceramic materials has not changed very significantly from the much earlier high- T_c samples, whereby processing was inferior, and typical impurities were of higher concentration; hence, is believed to be characteristic of polycrystalline bulk samples.

Figure 78 shows the R vs. $1,000/T$ data for the preonset region of the R vs. T curve as affected by the applied magnetic field. This figure contrasts the counterparts for the transitional and foot zones (Figure 70 and 71). In Figure 78, there is no sign of convergent extrapolation except for low fields (<5.5 T). From Figure 77, we can see that the preonset region meets the transitional region at about 85 K ($\approx T_c$); therefore, the convergence at low field in Figure 78 at $T \approx 93$ K relates to a phenomenon occurring at $T > T_c$ (i.e., at T_o , the preonset temperature). The obvious difference between Figure 78 and Figures 70 and 71 indicates that there is a difference between the processes (or the stage of the processes) at work in the preonset zone and at work in the transitional region. This suggests that T_c may be a kinetically related phenomenon.

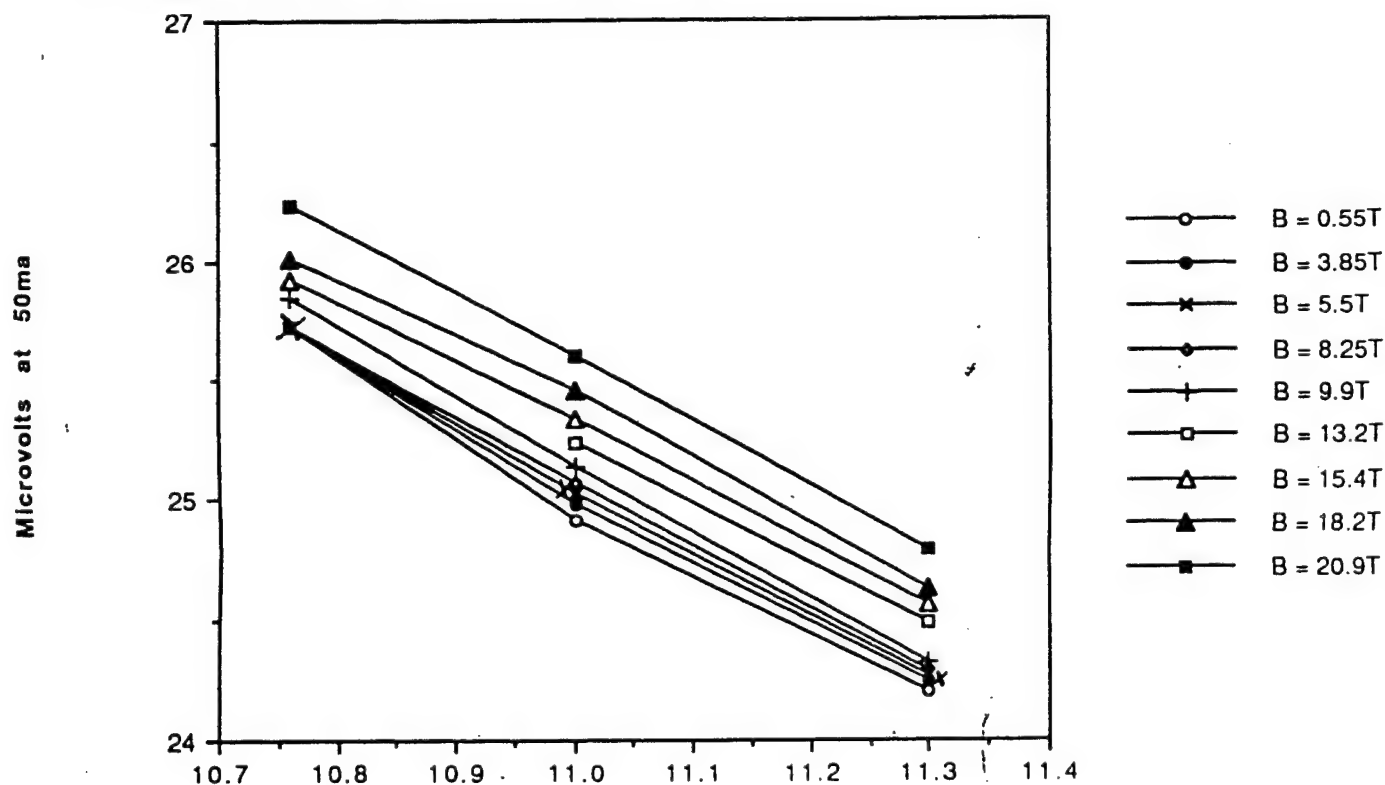


Figure 78. Potential ($\mu\text{V}/50\text{ma}$) vs. $1,000/T$ in Inverse $^\circ\text{K}$.

6.4.2 The Zero-Resistance Region Time Dependence of Flux Readmission. We have conducted a preliminary study of the recovery of electrical-resistance in $\text{Y}_1\text{Ba}_2\text{Cu}_{3-x}\text{Ga}_x\text{O}_{7-\delta}$ using magnetic-field sweep studies. In characterizing this polycrystalline material, we have shown by energy dispersive spectroscopy measurements that $x = 0.2$ to 0.8% . Further characterization by

induced-electron emission tentatively suggests that Ga^{3+} substitutes for Cu^{3+} at chain sites. The material shows strong levitation, high density, very low porosity, large grain size, and very high electrical conductivity in the normal state. In Figures 79 and 80, we give the R vs. T data for the aforementioned compound and, in Figures 81 and 82, we present our data on the recovery of electrical resistance at 83.7 K in the zero-resistance state as a function of the sweep rate of the magnetic-field intensity. The data show that the effect of rate is most clearly observed at low field where the response of resistance recovery is lowest for the fastest sweep rate (18 T in 30 s). Thus, for the most rapid sweep rate, the resistive properties were not recovered until a magnetic field of 1.5 T was exceeded. The time response for resistance recovery is about 1 s. This kinetic parameter and dependence is in keeping with a phase-transition phenomenon and is thought to be associated with field-induced fluxoid depinning time criteria as related to the pinning property of defects. Additional gallium-substituted samples yielded the same or similar results; however, substitution of indium for gallium caused the loss of superconductivity. This is believed to be due to the absence of multivalence in indium.

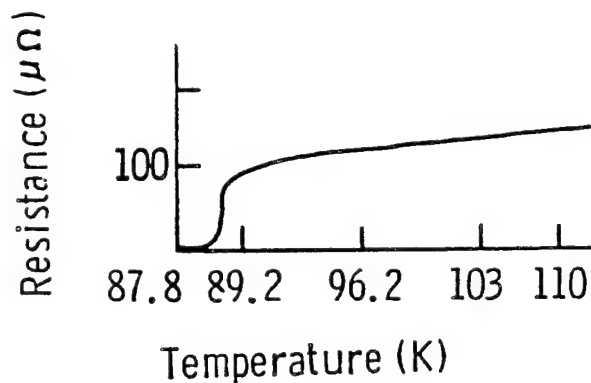


Figure 79. Resistance vs. Temperature Data for $\text{Y}_1\text{Ba}_2\text{Cu}_{3-x}\text{Ga}_x\text{O}_{7-\delta}$.

6.4.3 The Cation Diamagnetism. The diamagnetism associated with the multivalence cation when the charge-transfer excitations drive it into the metallic or atomic state gives rise to orbital motion in the filled d^{10} state. This behavior is akin to nonrestrictive current loops. The orbital motion is altered by an externally applied magnetic field so as to oppose the applied B-field. This alteration remains intact indefinitely until the B-field is again changed. Examples of the charge-transfer excitation reactions that drive the multivalence cation transiently into the zero-valence metallic state are, for example, $\text{Cu}^{2+} + 2e^-$ (from O^{2-}) $\rightarrow (\text{Cu}^0 + \text{O}^0)_{1-x} + (\text{O}^{1-})_x$ which gives rise to

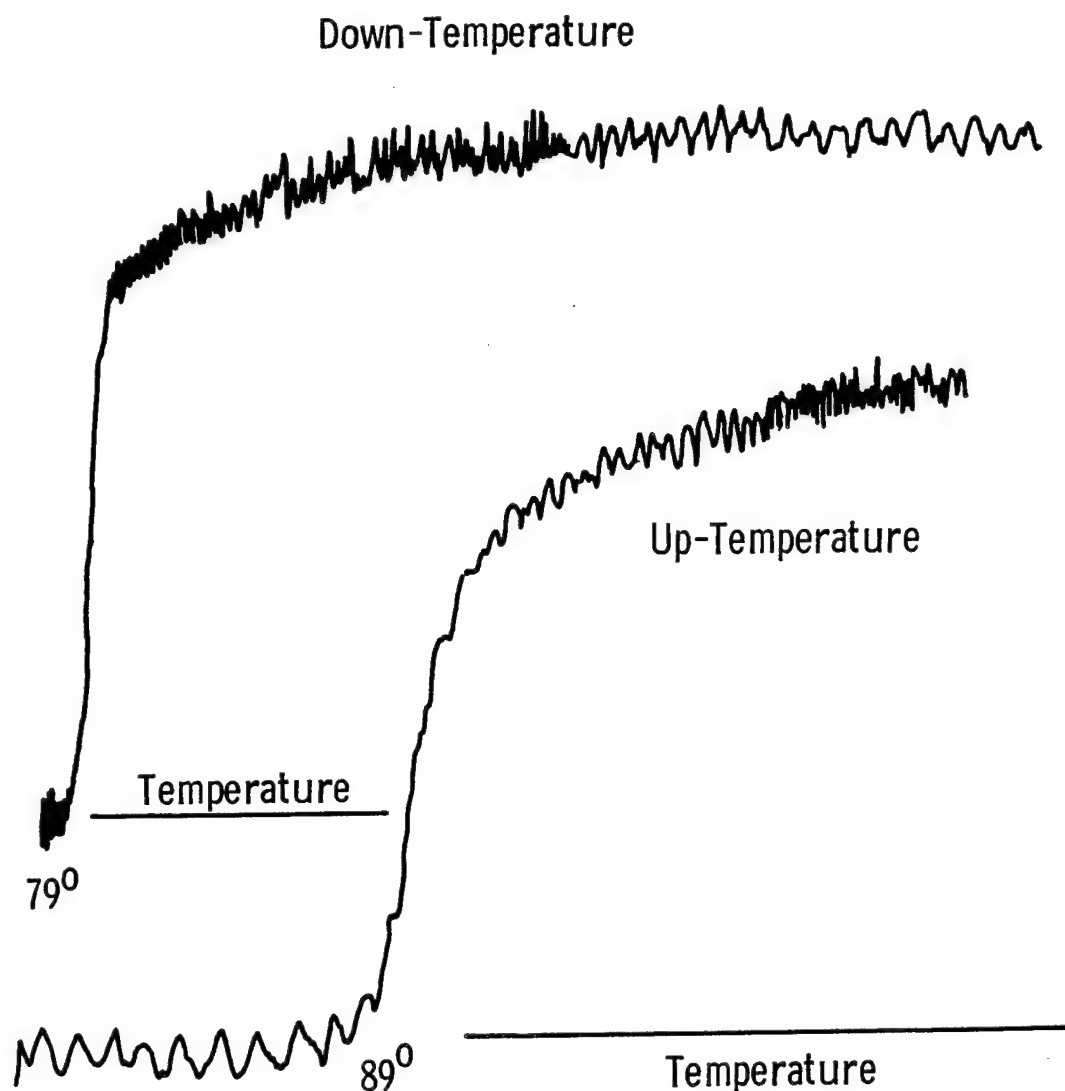


Figure 80. Resistance vs. Temperature for $Y_1Ba_2Cu_{3-x}Ga_xO_{7-\delta}$ at Zero Magnetic Field (Fifth Cycle).

a transient state of metallic or atomic copper (specified as Cu^0), or $Cu^{2+} + 2e^- \rightarrow Cu^0 + O^0$, or $Cu^{3+} + 3e^- \rightarrow Cu^0 + O^0 + O^{1-}$.

The known high- T_c superconductors have, as stated earlier, two general chemical and magnetic characteristics in common in their materials science. They all utilize principal cations that are capable of multivalency such as Cu, Bi, Tl, Pb, Ga, and Sb, but that are also diamagnetic (negative magnetic susceptibility) when in their metallic phase. In the aforementioned charge-transfer reactions, two phenomena inescapably occur. First, bound holes are established on the oxygens (or,

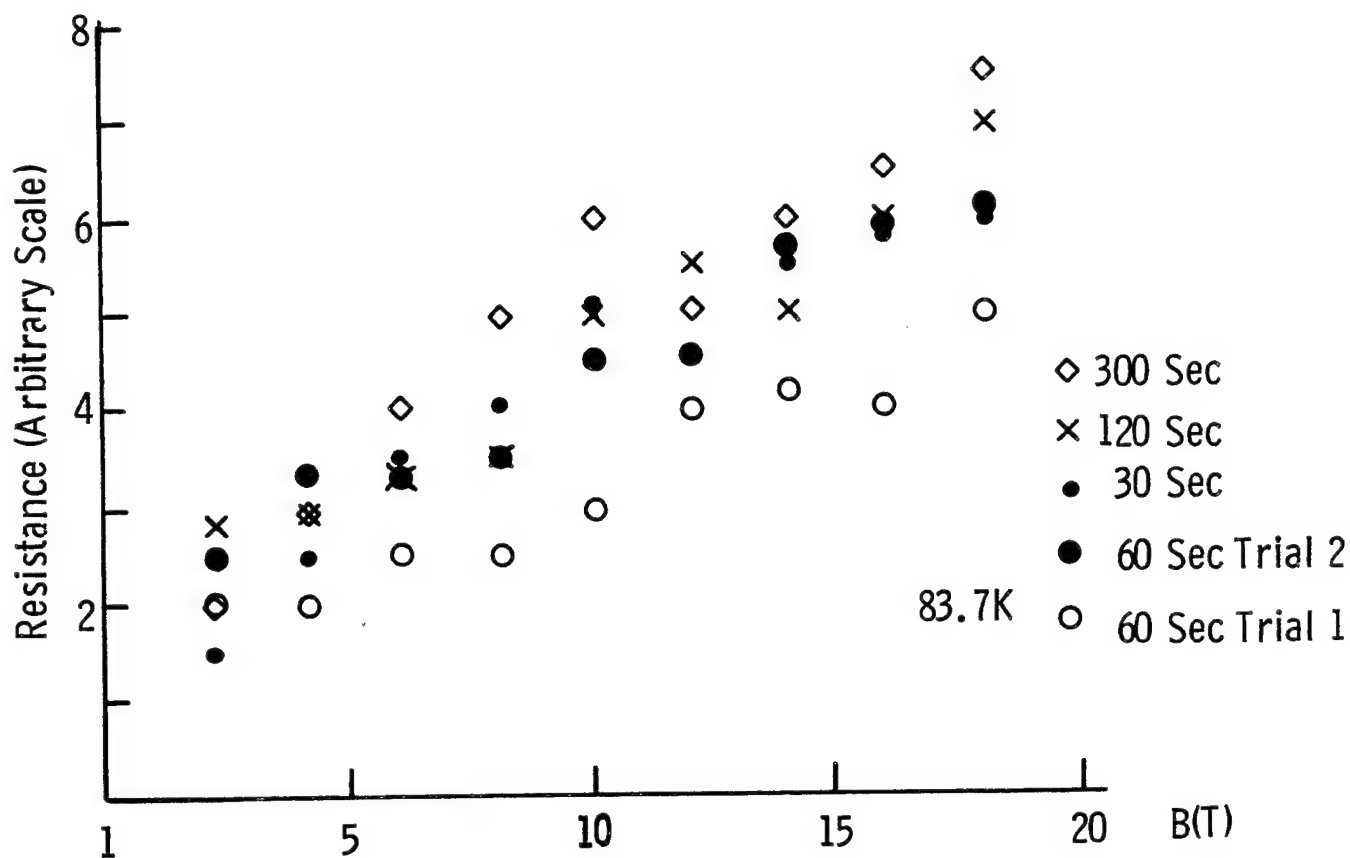


Figure 81. $\text{Y}_1\text{Ba}_2\text{Cu}_{3-x}\text{Ga}_x\text{O}_{7-\delta}$ Recovery of Electrical Resistance as B-field Is Raised From 2 to 18 at Different Sweep Rates.

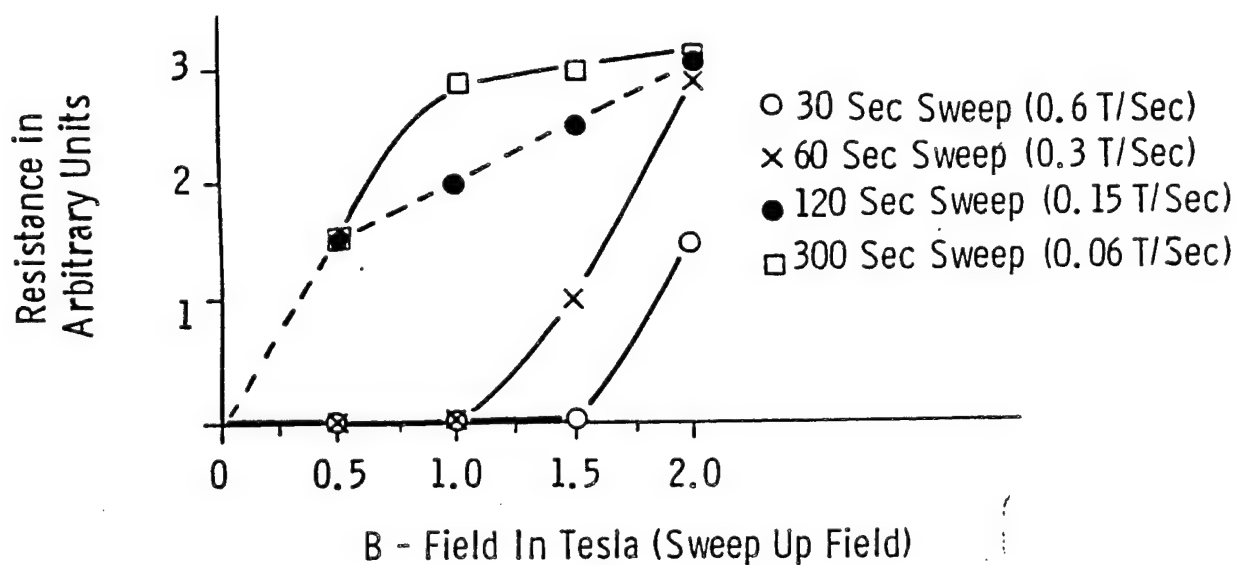


Figure 82. Reduced Data of Recovering Resistance of Superconducting $\text{Y}_1\text{Ba}_2\text{Cu}_{3-x}\text{Ga}_x\text{O}_{7-\delta}$ as a Function of Magnetic-Field Sweep Rate.

for every oxygen that is transiently totally neutralized, there are two bound holes created). It is these bound holes that we believe are the mediators that have a coulombic attractive force with conduction electrons, such that the normally repulsive electron-electron force between certain pairs of electrons is overcome. This effect causes the zero-electrical-resistance state. Secondly, a diamagnetic state is established on the multivalence cation synchronized with every instant of neutralization. It is this diamagnetic state that we believe leads to the property of perfect diamagnetism in superconductors. Therefore, the two properties of zero electrical resistance and perfect diamagnetism are intimately linked together, a characteristic that was observed in the early studies of low- T_c superconductors and has been a paradoxical puzzle ever since.

6.4.4 The Anion Atomic or Zero-Valence Paramagnetism. Of the group VIA elements, only oxygen can act as the principal anion of the known high- T_c compounds. Contrasting the diamagnetism of sulfur, selenium, and tellurium is the paramagnetism of oxygen. The main reason why oxygen is the appropriate group VI anion may be strictly due to its favorable radius in consideration of being coordinated into five- and six-fold nearest-neighbor structural units. Radius ratio considerations indicate that for sulfur, selenium, or tellurium as the anions, the Cu^{2+} will be unable to coordinate five or six anions; however the Bi^{1+} , Bi^{3+} , Tl^{1+} , and Tl^{3+} ions would still be able to hold five- or six-fold coordination. This raises the question regarding the uniqueness of oxygen in the few high- T_c superconductors that do not contain copper. Therefore, because of the observation of enhancement of the preonset and zero-resistance temperatures caused by the spin and magnetic moment of the paramagnetic REs that can substitute for yttrium, we cannot ignore that the paramagnetism of the neutralized oxygens (to which the mediating holes are bound) may have an effect on spin polarization. Consequently, there may also be a relationship of this paramagnetism to the equal-and-opposite spin requirement for Cooper pairing and/or to the spin fluctuations from antiferromagnetism. The transient or time-dependent torque caused by the latter interaction can be calculated through the cross product of the magnetic moment of the spin fluctuation and the internal B-field established by the paramagnetic oxygen. This torque can cause an ordering effect that may be essential to superconductivity at high- T_c . Therefore, the anions S^{2-} , Se^{2-} , and Te^{2-} , which, when neutralized into their atomic states, become diamagnetic, may for that reason not be suitable as principal anions for high- T_c materials.

6.4.5 The Effect of Magnetic Field on Low-Frequency Small Oscillations in Resistance vs. Time at Constant Temperature Below the Preonset Temperature. We have observed $\text{Y}_1\text{Ba}_2\text{Cu}_3\text{O}_{7-\delta}$ (Figures 66 and 67) under high sensitivity and the presence of small oscillations in resistance vs. time occurring at a frequency of about 1–10 Hz (at constant temperature) beginning at the temperature T where the R vs. T data first departs from linearity. These oscillations seemed to occur in a random clustered group fashion. We have observed small oscillations of low frequency also in the BiSrCaCuO superconductor and found that they are magnetic-field dependent (Figures 83 and 84). The origin of these oscillations has not been established; however, they may be related to a behavior that is a consequence of any instabilities of the mediator (hole or virtual exciton). They may also be related to a similar phenomenon observed in low- T_c materials such as vanadium, tantalum, and tin and ascribed to propagation of domain boundaries [213–220].

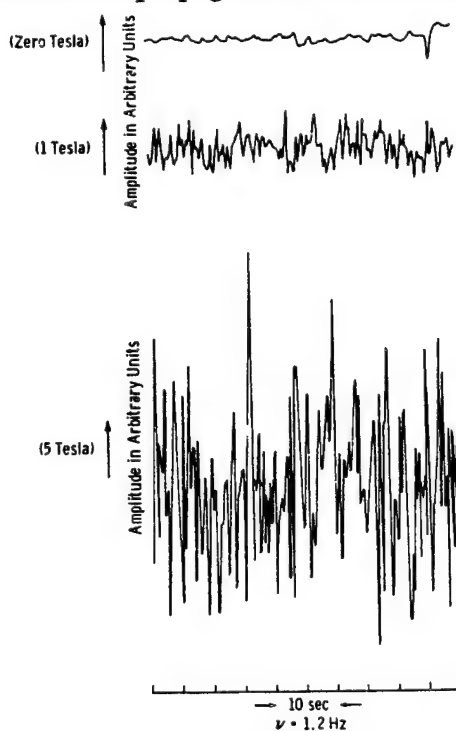


Figure 83. Raw Data for Small Oscillations in BiSrCaCuO High- T_c Superconductor.

6.5 The Exciton Analysis and the Fundamentals of the Interaction of the Hole Constituent of the Bound or Virtual Exciton With Candidate Conduction Electrons for Cooper Pairing. Classically, the mediation of Cooper pairing by bound excitons (or virtual excitons) is viewed in terms of a coulombic attraction between the bound hole hydrogenic core of the exciton and a

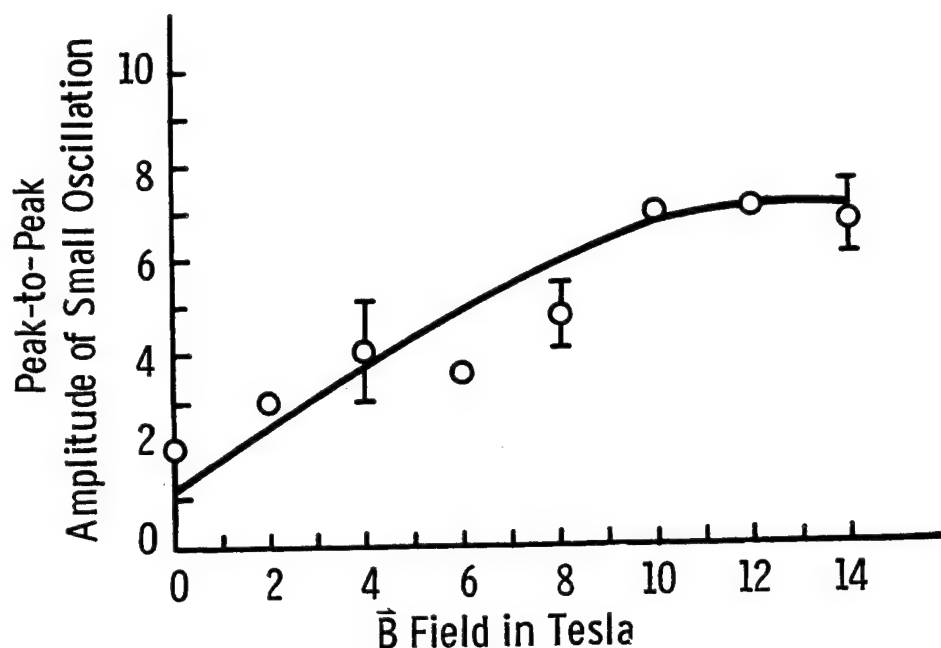


Figure 84. BiSrCaCuO High- T_c Superconductor (Sample No. 2) Amplitude of Small Oscillation vs. Applied Magnetic Field.

conduction electrons creating regions of enhanced positive charge, which themselves propagate a new charge distribution that is experienced by a second possible-to-be-paired conduction electron.

The full mathematical representation of this interaction will be presented later. Quantum-mechanically, this interaction is perceived as an excitation of the exciton (or its bound hole constituent) from the ground state to a higher energy state, this excitation being caused by interaction with a conduction electron. As the excited state of the exciton (or hole) then decays, the energy emitted is absorbed by a second conduction electron, which, if of opposite spin and opposite linear momentum, can transiently pair with the first conduction electron. This approach can be formalized by employing the effective mass theory for excitons and calculating the energy of the individual states given by

$$E = \{E_G - (R/n^2) + [(h/2\pi)^2 (K^2/2) (m_c + m_v)]\}, \quad (20)$$

where $R = (\text{Rydberg constant}) = \mu e^4 / [2 (h/2 \pi)^2 (\epsilon_0)^2] n$ = principal quantum number; m_c and m_v refer to conduction-electron mass and valence-electron mass, respectively.

Clearly, the exciton, although an excited state itself, is capable of further excitation to quantized states much like the characteristics of the H atom.

In hypothesizing the importance of the exciton and/or bound hole, we are impelled to search out phenomena near the temperature T_c that may contribute to the concentration of these mediating particles. Near the onset conditions of superconductivity, the dielectric relaxation time of the material (τ_d) and the diffusion length lifetime (τ_l) may become about equal, thereby causing the polarizability to diverge and enhancing charge separation. This enhancement will operate in favor of an increased or sustained concentration of regions of positive charge (such as bound holes or virtual excitons), which can coulombically act as mediators for Cooper pairing of conduction electrons.

The exciton model requires a coulombic binding between holes in the valence band and electrons in the conduction band. In such a regime, the binding energy of the exciton (E_B) must be slightly greater in magnitude than the band gap (E_G). It can be shown that the condition $E_B > E_G$ causes a lowering of the collective ground-state energy of the electronic system by forming partially shielded excitonic-like charge clouds, which are coupled to Cooper pairs. It is clear from the excitonic wave equation that the exciton binding (or ionization) energy is a very significant parameter in any phenomenon that involves excitons. Therefore, as stated earlier, the competition between Cooper-pairing forces and exciton binding forces must be considered in the temperature range of T_c , and may account for an ionization of both bound and free excitons that releases holes and, particularly, electrons into the charge-transport system, inducing the positive Hall coefficient to decrease precipitously and undershoot zero to become negative before stabilizing at zero for the zero-resistance state.

The elementary single-exciton wave equation for a two-band model [221] is

$$[(k^2/2\mu^*) + |E_B|]X_k = \sum_p V(k-p)X_p, \quad (21)$$

where $V(k)$ is the Coulomb potential, k = wave number = $p/(h/2\pi)$, and μ^* is the reduced electron mass of the electron hole pair. This shows the exciton gap as Δ_{ex} approaches zero as $E_B \rightarrow E_G$. The binding energy E_B is given approximately by $|E_B| \approx h\mu^* R/m\epsilon_0^2$, where R is the Rydberg constant, and ϵ_0 is the interband part of the materials static dielectric constant.

In the band model picture to support an exciton-enhanced or exciton-dominated mechanism for high- T_c superconductivity, heavy d-like holes interact with light p-like electrons, causing transient holes on the oxygens. The d-hole behavior might be described as a plasmon from the point of view of a collective mode (or as an exciton from the perspective of an individual mode). The plasmon is a quantum excitation of the electron conduction plasma. By a "collective excitation" is meant an interaction of sufficient range and strength, such that whatever excitation a constituent is given is immediately transmitted to its neighbors, thereby almost instantly becoming a property of the entire collection of particles rather than any individual constituent. Thus, a collective excitation shows no resemblance to the constituent particles supporting its existence. (A quasi-particle, instead, shows a strong resemblance to the constituent particles of a many-body problem.) From the sense of this distinction, it would appear that collective quantum phenomena should be associated with the extended charge-transfer excitations on the Cu d-states ($Cu^{2+} - Cu^{3+}$), and quasi-particle elementary excitations may be associated with the localized behavior of the O 2p states.

The plasmon or plasma oscillation can be visualized by recognizing that the coulomb interaction is a sufficiently long-range force that it is able to it organize the activity of the electrons into collective motion, upon which the individual motions are superimposed [222]. When a hole appears in an electron $Cu^{2+} - Cu^{3+}$ the whole electron cloud contracts inward by a small measure to endeavor to "fill" the hole and preserve a uniform density. In doing so, it necessarily takes on KE $m_e^* v_e^2/2$, but must overshoot its target (because of the velocity term). In the overshoot, an excess charge will exist at the center of the cloud relative to the perimeter region. The collective cloud then tries to eliminate the relative excess charge by expanding. The process then continues and results in a long-wavelength oscillation in the density of the cloud. This is referred to as a plasma oscillation and will

cause a polarization, which, in turn, will establish a field $E = -4\pi P$. Each charge is then returned to equilibrium by a force eE , and the frequency of the plasma oscillation is given as $\omega = (4\pi ne^2)^{1/2}$ or about 10^{16} s^{-1} . The pairing of electrons is then accomplished via the first conduction electron perturbing or exciting a hole and the second conduction electron being coupled by absorbing the resulting plasmon as the electron cloud responds to the perturbed hole.

The previous discussion has been an introduction to exciton and plasmon theory. Before treating the perturbation theory and the quantitative coulombic interaction between conduction electrons and centers of positive charge, we present a section on critical current density. This should be instrumental in understanding how the Cooper pairs that are created by the aforementioned process undergo scission, and, thus, how the create-and-destroy cycle is completed.

6.6 Critical Current in $\text{Y}_1\text{Ba}_2\text{Cu}_3\text{O}_{7-\delta}$ vs. Temperature Dependence: The Recovery Regime. In Figure 85, we present the electrical-resistance (4-terminal) vs. decreasing temperature data (middle curve without pulses) obtained upon rapidly cooling the superconducting material to liquid-nitrogen ambient. The thermocouple in these experiments was placed within 1 mm of the sample. The first-order decrease in electrical resistance in Figure 85 identifies the transition to the superconducting state.

On the rewarming direction (toward right at lower region of Figure 85 using an expanded scale), we show the response of the sample to 35 applied current pulses (of magnitude 2.0 A, duration 1 s, and a current density supply of about 60 A/cm^2). These pulses are superimposed upon the existing DC to produce the resistance vs. temperature curve on the X-Y recorder in the lower trace of Figure 85. In this experiment, the electrode configuration (no. 1 in Figure 86) was utilized. (In the rewarming direction, the current-voltage behavior was clearly observed to be hysteretic when the same scales were utilized.) There is no response observed on the X-Y recorder nor from the digital microvoltmeter over the temperature range of the first 16 of these pulses. We believe that in the bulk of the sample, this rewarming range does not exceed T_c . The electrical DC resistance is still measured as essentially zero on all instruments, with the digital voltmeter oscillating from plus to

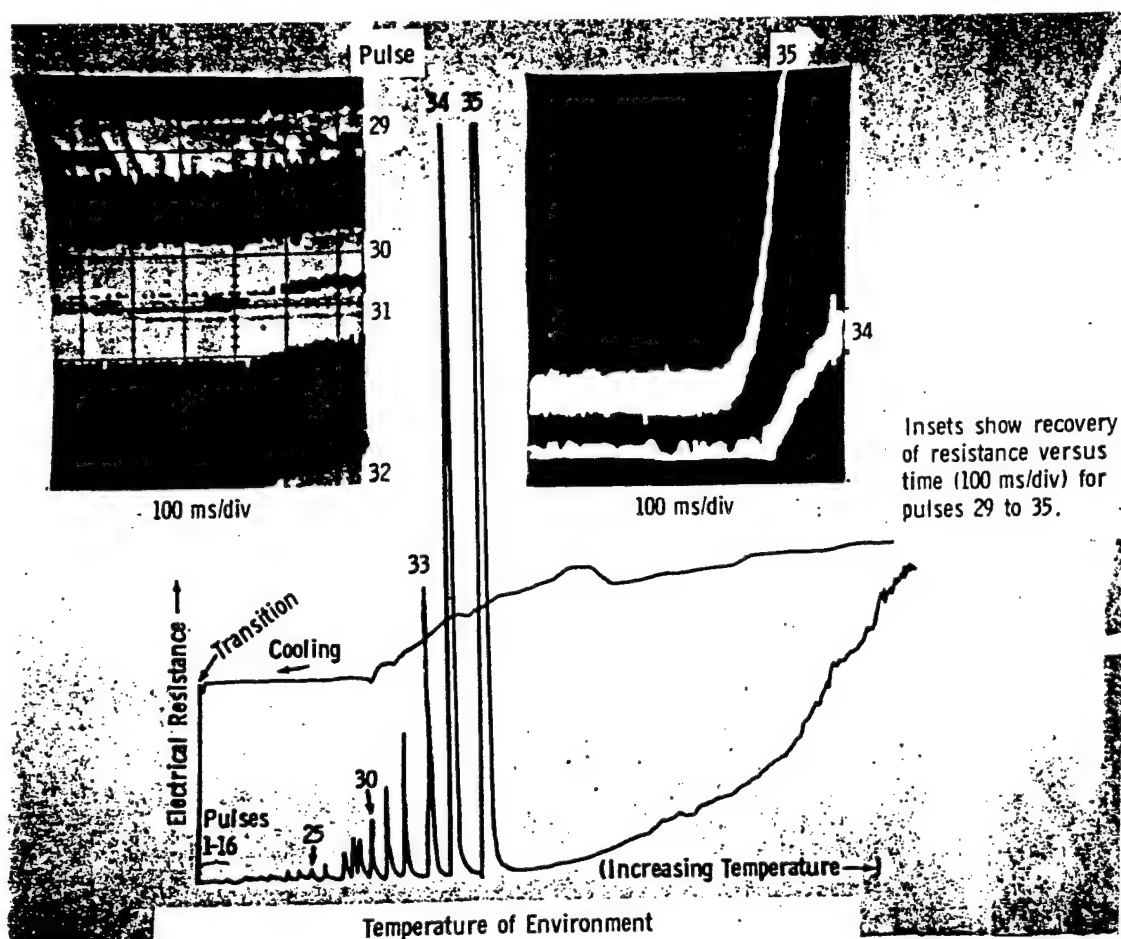


Figure 85. Raw Data for Recovery of $\text{Y}_1\text{Ba}_2\text{Cu}_3\text{O}_{7-\delta}$ Superconductor.

minus within values of a small fraction of a microvolt. Subsequent to the aforementioned region is a zone of constant response (the 17th to the 22nd pulse).

Above a given temperature range, however, the instrumentation shows a voltage response to the applied pulse that increases with temperature. The voltage (and hence resistance) returns to the zero measured level at the end of the superimposed applied pulse. A region of small increasing response pulses extends from the 23rd to the 26th pulse in Figure 85. A region of much greater response magnitude then dominates the behavior from the 27th to the 35th pulse in Figure 85. In the upper insets of the figure, oscillograms are given to show the response to the voltage across the sample to the applied superimposed pulse as a function of time on a millisecond scale. It can be seen from

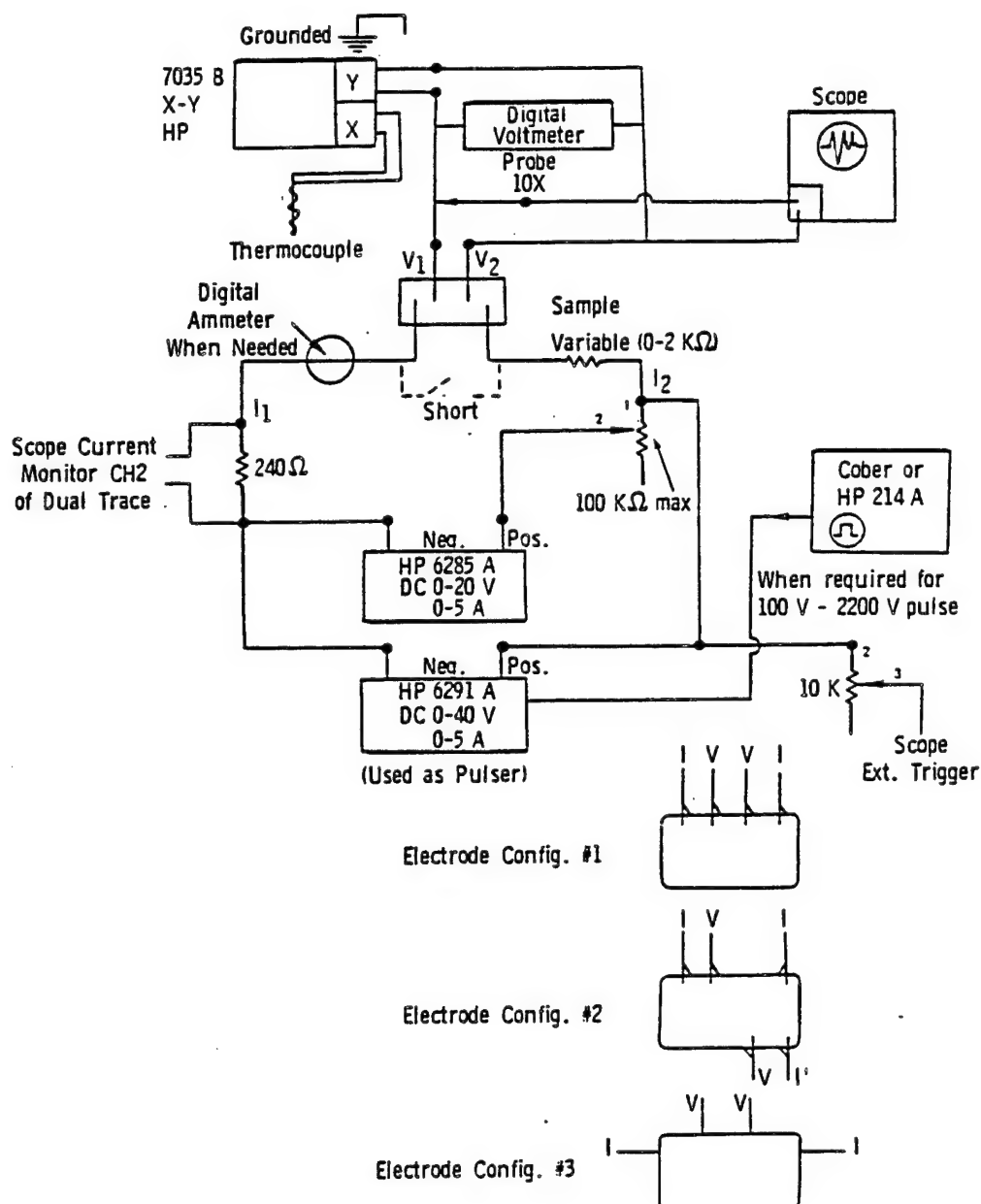


Figure 86. J_c Circuit Schematic.

these oscillograms that as the ambient temperature increases, the slope of the response pulse also increases. The pulse height of response is plotted against rewarming temperature in Figure 87 for two separate experiments. In the inset of this figure is given the J_c vs. T data for a thin film of $Y_1Ba_2Cu_3O_{7-\delta}$, fabricated at IBM [223], showing a slope change at about 88–89 K (basically agreeing with our results of Figures 85 and 87. Figures 85 and 87 are the equivalent of a critical current vs. temperature curve (J_c vs. T) because at temperatures above 80 K (the X data points), the material will

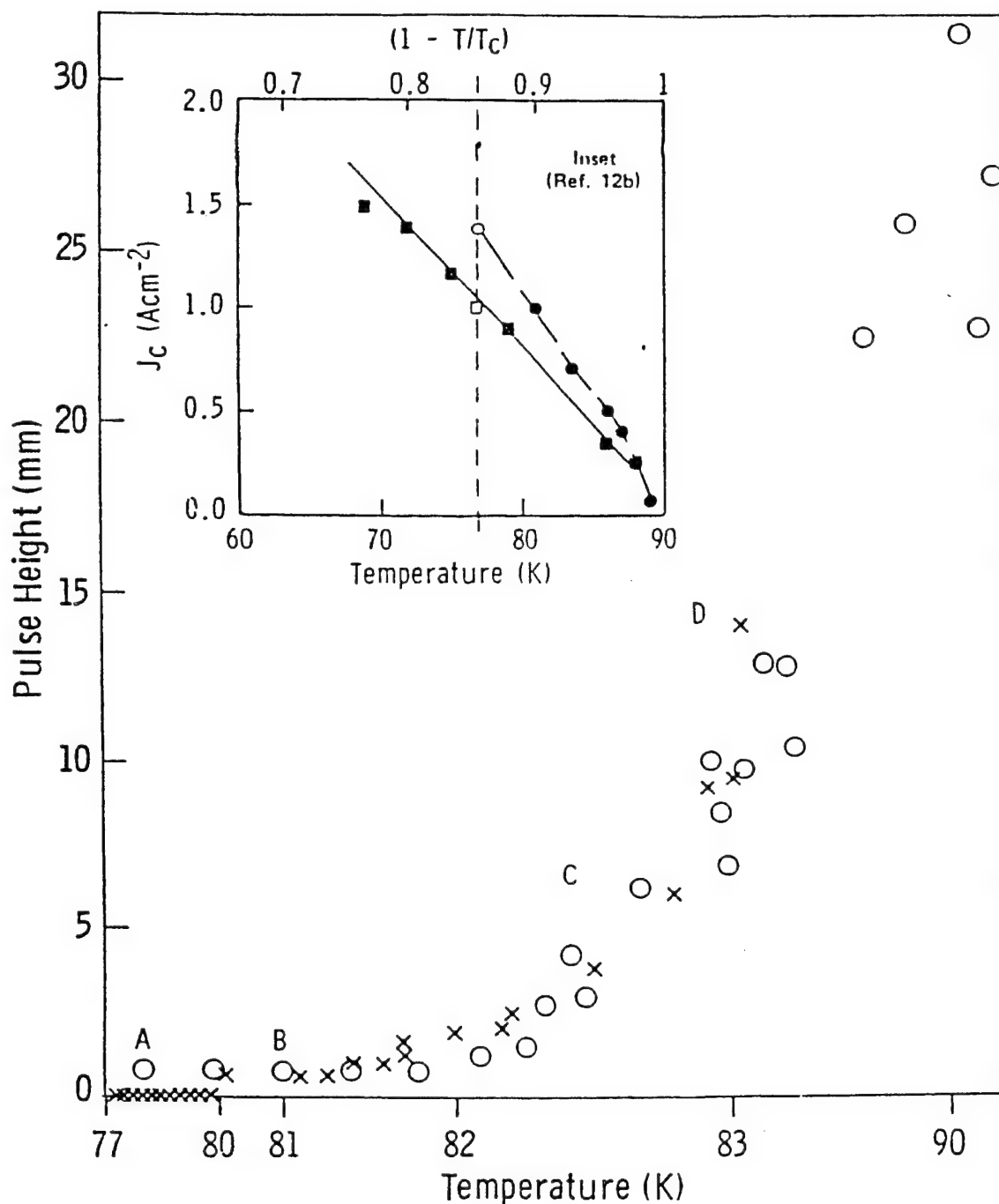


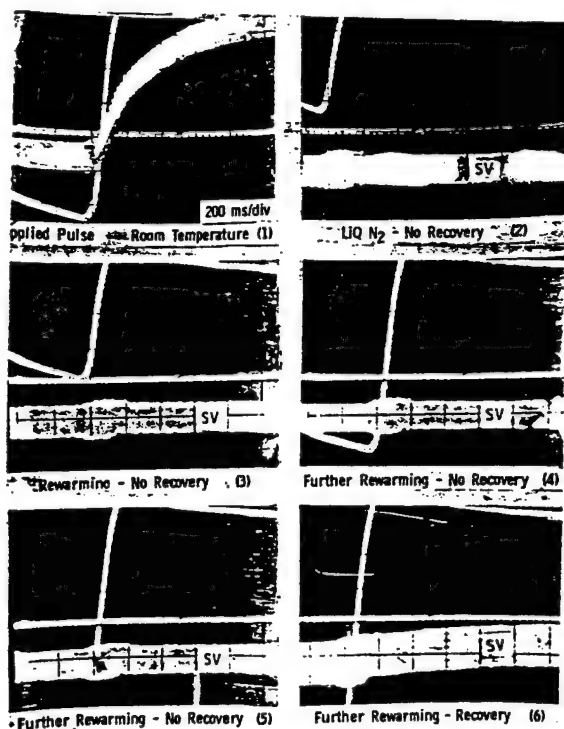
Figure 87. Magnitude of Superimposed Pulse vs. Temperature for $\text{Y}_1\text{Ba}_2\text{Cu}_3\text{O}_{7-\delta}$ Superconductors.

support an electric field, thereby showing electrical resistance. This occurs because J_c has been exceeded by the current that accompanies the applied pulse. In both experiments of Figure 87, a region of no response is followed by a region of constant response and then followed by two separate regions of increasing magnitude response labeled C and D. The inception of these regions of

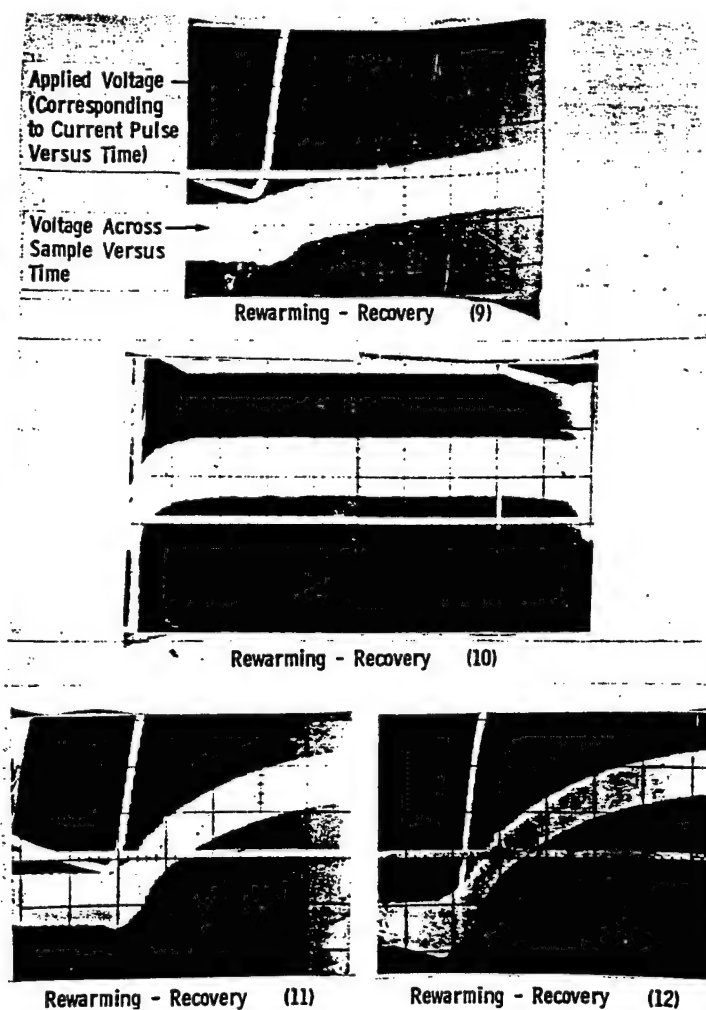
response are not associated with any change departing from zero resistance, which we could measure in the steady state. Not until after the 35th pulse does the DC steady-state resistance begin to measurably rise as temperature increases. This then refers to still another recovery region. The experiment was then repeated using electrode configuration no. 2 from Figure 86 with the voltage electrodes across the bulk of the sample, yielding similar results in that the region of real potential response to the applied pulse was not associated with a measured regaining of DC resistance. Oscillograms showing the eventual response to the superimposed voltage pulse as a function of rewarming are shown sequentially in Figure 88. An actual positive response is not observed until the rewarming condition corresponding to the sixth oscillogram (lowermost right). In Figure 89, the slope of this recovery is plotted (for different regions of interest) from the data of Figure 88. It is clearly shown that this slope increases with increasing temperature. Substituting copper metal for the sample and then redoing the entire set of aforementioned experiments indicated the static response of a typical metal undergoing no transformation and, hence, no unusual dependence on the temperature of the environment.

The previous data indicate a millisecond response time to the recovery of the resistance (or more precisely the acceptance of a bonafide field) when J_c is exceeded with increasing temperature for superimposed current-limited pulses. This millisecond response time may have both nonthermal and thermal mechanisms responsible for its origin. Any thermal contribution would have to be due to a small I^2R arising from the very small contact resistance and later arising after the initial reassumption of resistance upon exceeding J_c .

It is clear from Figures 85 and 87 that J_c is an inverse function of temperature. The magnitude of the response increases with increasing temperature because the difference between the constant current pulse at a given rewarming temperature, $J(I, T)$, and the critical current for that temperature, $J_c(t)$, is increasing with increasing temperature. Hence $V = Ed = (d/\sigma) [J(I, T) - J_c(t)]$. The greater the difference term, the greater the amount of resistance that is developed. This causes the KE to exceed the Cooper-pairing energy. The difference term in the previously mentioned relationship is directly related to electrical resistance.



(a)



(b)

Figure 88. Applied Current Pulse and Recovery of Resistance With Increasing Temperature.

Further indications of regions of recovery from the superconducting state to the normal state and the possibility of transitory phases are given in Figure 90. It is shown therein that the initial region of recovery, employing millisecond pulses, is accompanied by transient voltage collapses. These are shown in the left-hand area of Figures 90a, b, and d and in the uppermost trace (110 V) in Figure 90c. The traces in Figures 90a, b, and d are translated manually on the oscilloscope to the right, corresponding to increasing temperature for clarity to the reader. In Figure 90c, we observe that the transient collapse in voltage is not observed for applied voltage 20 to 50 V, but only for 100 V pulses (and presumably higher). In Figure 90d, the uppermost right-hand traces refer to the

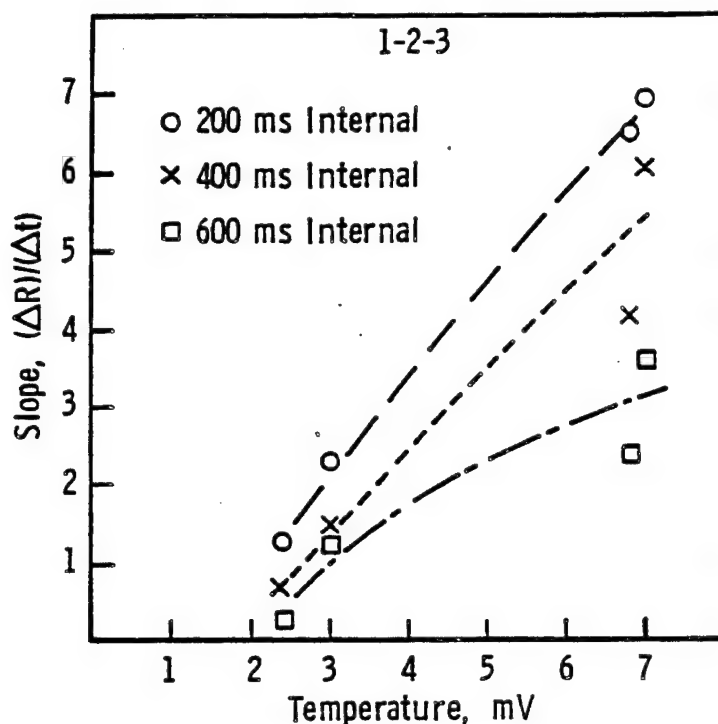


Figure 89. Recovery-of-Resistance Slope vs. Temperature for $Y_1Ba_2Cu_3O_{7-\delta}$ Superconductor.

zone of the final stages of recovery. Intermediate between the region of transients and the region of final recovery is a region (designated as region 2) where a flat trace is shown and a transient is not clearly observable. This is in consonance with the data of Figures 85 and 87. In the lower right of Figure 90d we give the normal-state pulsed behavior, as well as the low-temperature state at 50 and 100 V applied potential, respectively.

Figure 91 gives pulsed response and recovery data employing still a third sample with electrode configuration no. 3 in Figure 86. This experiment was conducted in order to determine whether placing the voltage electrodes on the edge of the same side of the sample caused a change in the results. This was performed in order to compare results from a configuration having a greater measurement contribution from surface currents to configurations with greater measurement contributions from bulk currents. The results from the experiments described in Figure 91 are very similar to those from Figures 85 and 87-90, which had electrodes across the sample. Thus, the temperatures corresponding to the onsets of the voltage response to the superimposed pulse were not associated with configuration of the electrodes.

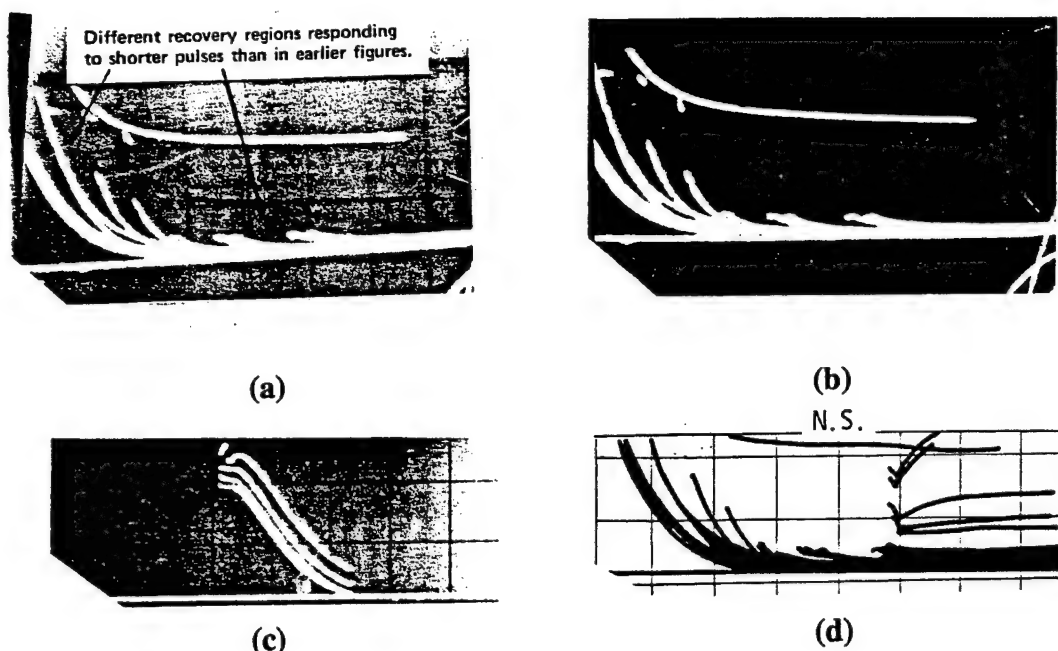


Figure 90. Oscillograms for Transition Into and Recovery From the Superconducting State. (a) The Pulses to the Left Show a Voltage Collapse or Breakdown Transient, Whereas the Pulses in the Center Show a Low-Resistance Flat Region. The Uppermost Trace Across the Oscillogram Refers to the Normal-State Behavior. (b) Oscillograms Showing Superconductor's Recovery of Resistance Response to Voltage Pulse. The Individual Pulses Are Displaced to the Right With Increasing Temperature for Clarity. (c) Voltage vs. Time (200 μ s/div) in Superconductor During Rewarming at (From Bottom to Top) at 20, 50, and 100 V Applied Amplitude. Note Voltage Collapse or Breakdown Transient in Uppermost Oscillogram. (d) Upper Left and Center Same as (a) and (b). Upper Right Shows Region of Recovery of Normal State or Lowermost Traces Are Superconductor Near T_c . Almost Horizontal Trace = Normal State Before Cooling (Designated N.S.).

We must address the question whether the data of Figures 85 and 87–91 are simply or partially representative of a pulsed Joule-heating effect related to contact resistance. If I^2R heating were exclusively causing the material to be pulsed out of the superconducting state because of additional heat over and above ambient, then we should expect a continuous monotonic response curve rather than the discontinuous recovery behavior shown in Figure 87 (the discontinuity at about 85 K in Figure 91). Furthermore, we would also expect that pulses of widely varying width (and duty cycle), such as those employed in Figure 85 and those employed in Figure 88, should yield very different recovery and response behavior. However, both sets of these data indicate more than a single recovery region. Additionally, since the material is a superconductor, the Joule-heating while in the

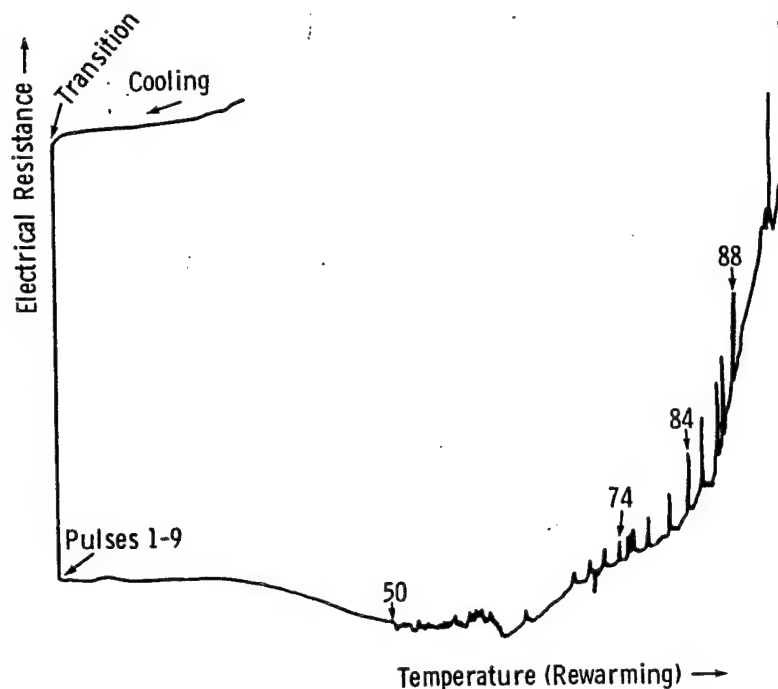


Figure 91. Recovery From the Superconducting State.

superconducting state, could only arise from contact resistance. The contact resistance in the present experiments was about a maximum of $1.0 \text{ m}\Omega$ as determined from two-terminal measurements. After initial bulk resistance is reassumed, additional I^2R effects are unavoidable. Hence, it is possible that thermal components are to some small degree involved (or superimposed) in these data, but it is not possible that Joule-heating can exclusively explain the J_c vs. T slope-change data.

AC susceptibility studies [224] have shown that, in O-annealed polycrystalline superconducting samples of this material, there are two regions of J_c behavior vs. field amplitude. These are derived by studying the peak-loss characteristics, as well as the Meissner transition (which itself shows two regions of behavior). Because of lack of single-crystal data, it is not clear whether the origin of these two types of behavior is due to fundamental properties of the superconductor, such as structural polyhedra, or is due to coupling effects arising from crossing grain boundaries. It is shown that the data, giving rise to the aforementioned regions of behavior, changes dramatically when the sample is pulverized into a fine powder (because of changing grain-to-grain mismatch). Hence, it is likely that grain boundaries at least influence the behavior noted in Goldfarb and Chen [224–226] and,

thus, may influence some of the behavior in our own studies. However, the inset of Figure 87 [213] gives J_c vs. temperature for thin films fabricated at IBM and shows a slope change at about 88 K, which corresponds to what we show as the regions C-D slope change in Figure 87 at about 82.7 K and in Figure 91 at about 85 K. These correlations argue definitively against polycrystalline characteristics being responsible for the observation of more than one region of recovery in J_c vs. T.

In Figure 92, we show the superconductor response to a voltage pulse of about 4–20- μ s duration and magnitude varying from 50 V to 2,200 V. Figure 92 gives an oscillogram corresponding to a small-magnitude and a large-magnitude double pulse. The double pulse is shown at 77 K and reflects decay to zero resistance in ~ 1.4 μ s. The larger magnitude pulse is also shown at room temperature on a different scale. It is shown that in entering into the superconducting state, there are two regions of voltage decay: (1) a region of "overshoot" or inductive emf and (2) a region of what appears to be resistive decay. These two regions have time constants of about 100 ns and about 1–1.4 μ s, respectively. In Figure 92f and g, we present multiple traces showing the effect of rewarming using an applied pulse of 2,200 V, giving a current density of 3×10^3 A/cm², and not indicating any tendency to break out of the superconducting state. There was no DC applied field in these studies, but simply a short applied pulse not superimposed on any other signal. Figures 92b and c show decay of the voltage at 200 and 500 ns/div time scales. Figure 92c also includes an oscillogram of the net result when a parallel copper short is placed across the superconductor at low temperature (lower trace). Figures 90d and e give the resulting traces when copper wire is substituted for the sample at room and low temperatures, respectively. Figure 92f gives, from bottom to top, the voltage decay across the superconductor at 77 K, the trace upon considerable rewarming, and the trace corresponding to voltage at a position in the circuit ahead of the superconductor. The source voltage shows only an inductive-type decay and does not include the longer resistive decay observed in the superconductor. Figure 92a gives the rewarming data until the normal state is recovered at room temperature. The inductive contributions to these data suggest an inductive coupling emf, which appears inescapable in experiments of this type. The resistive decay seems to be considerably longer than what would be expected from a typical nonequilibrium viewpoint. The possibility must be considered that this resistive decay of about a microsecond may be at least in part due to the capacitance of the sample accentuated by its polycrystalline nature.

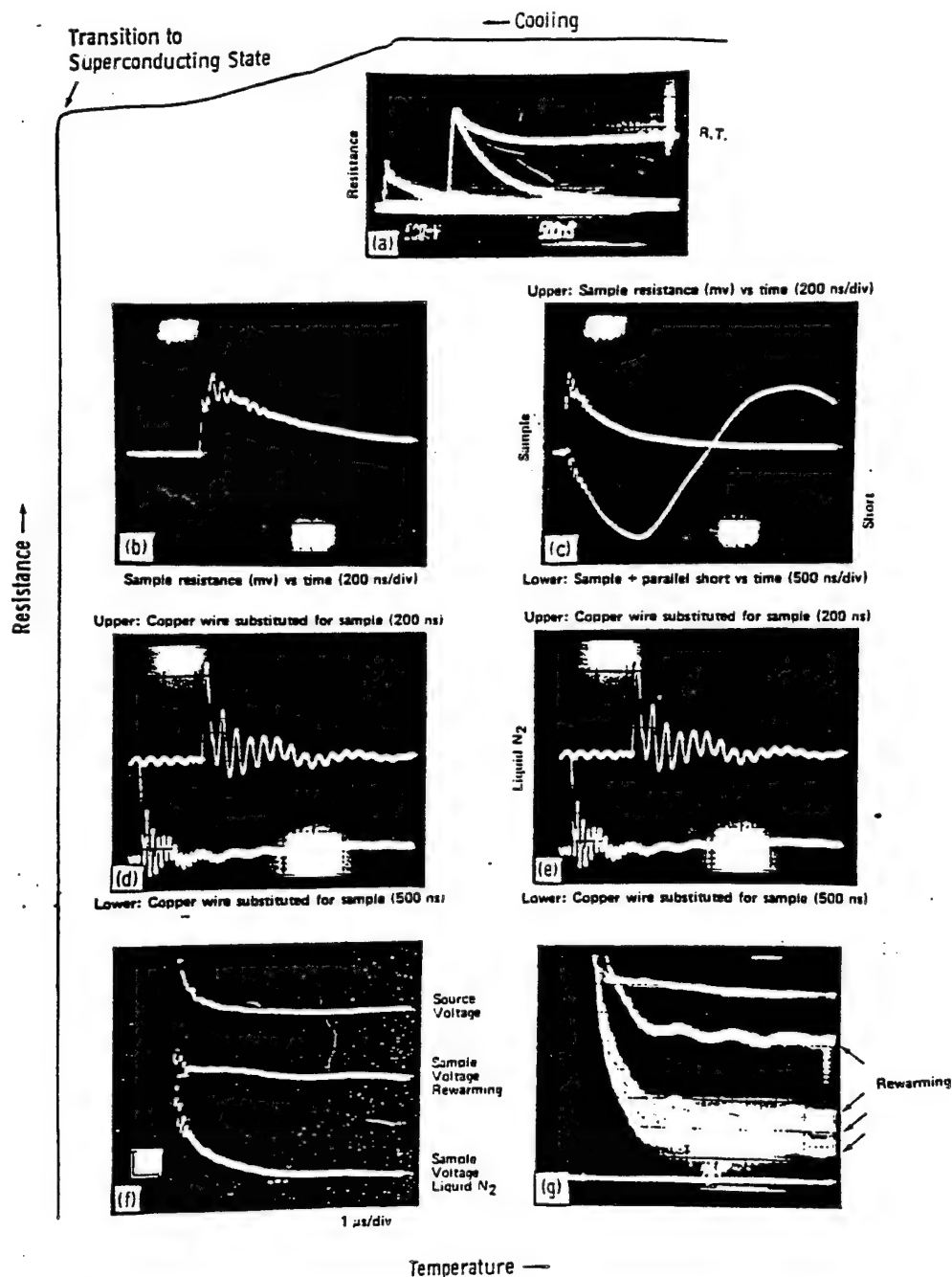


Figure 92. Voltage Response to Short Pulse in the Superconducting State.

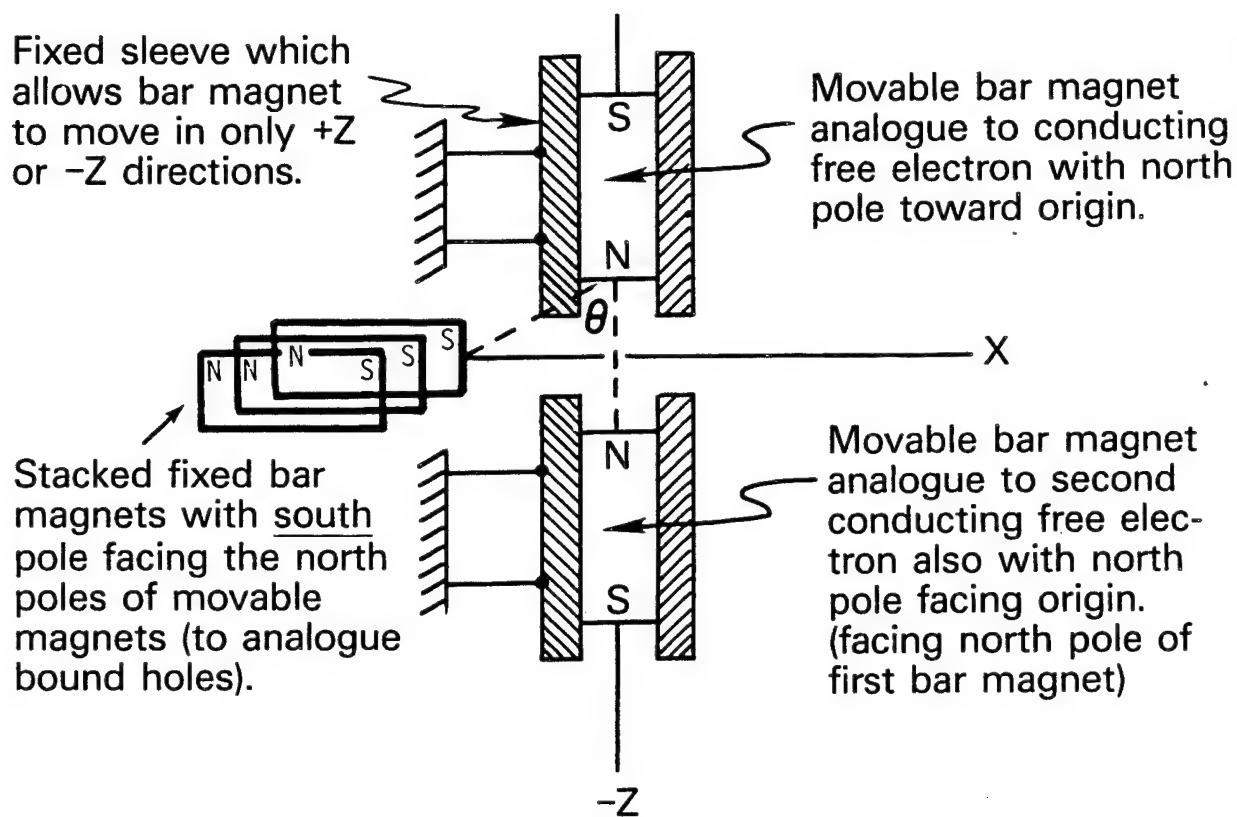
Capacitance effects may certainly arise from grain boundaries in the sample. Secondly, this time period could be associated with the time required to establish appropriate Cooper-pair distribution through the sample and along the surface. This is in consonance with kinetics that would be expected on this time scale if a phase transition of the Ginzburg-Landau type were key to the mechanism of the transition into the superconducting state.

When in the superconducting state, but prior to the application of a voltage, the material must exhibit some ratio of itinerant Cooper-paired electrons to normal electrons. This is because the delocalized electrons under no electric field undergo motion randomly dictated by kT . Pairing under zero external electric field will then depend upon the probability of interaction between an itinerant conduction electron and the mediating boson, as well as the interaction between the mediating boson and another conduction electron with opposite spin and momentum. This probability depends upon the spheres of influence of these particles (i.e., the coherence length of the electron pair and the proximity of the boson). When an electric field is applied (with $J < J_c$), then electron motion (paired and nonpaired) is no longer random, but, rather, directed. The region of influence then of the subject particles changes, and a modification of Cooper pairing takes place, changing the ratio of paired to normal electrons. This field-created modification in Cooper pairing must require a finite time prior to reaching a state of resistancelessness. We suspect that on a local level, this time interval will be much less than 1 μ s. However, the time for this pairing (in the sense of a distribution) to influence the entire bulk interelectrode gap (and hence be measurable in our experiment) may be much longer and approach at least 1–2 μ s.

Along these lines, it seems appealing to conduct time-dependence decay experiments at the onset temperature and during the narrow temperature region where the resistance is collapsing toward the superconducting state. Equally important would be the performance of time-dependent decay studies in the preonset region of the R vs. T behavior, especially very near the onset (T_c) conditions.

6.7 Quantitative Treatment of Cooper Pairing, Based on Bound Holes or Virtual Excitons as Mediators in $Y_1Ba_2Cu_3O_{7-\delta}$.

6.7.1 Polar Analogues in Magnetostatics. To conceptualize the action of a bound particle to cause attraction between two otherwise repelling mobile entities, we suggest a very simple analogue in magnetostatics. In Figure 93, we show two bar magnets with equal field strength at positions, $0, 0, Z$ and $0, 0, -Z$ with their north poles facing toward each other, and allow them to be free to move (confined only by a frictionless sleeve) in only the $+Z$ - or $-Z$ -directions. We then ask what is the simplest way that we can cause these two mobile bar magnets to move toward each other,



When there are enough fixed bar magnets such that cosine components of attractive force with north poles of movable magnets exceeds the latter's mutual repulsive (north-north) force, the movable magnets will move toward each other.

Figure 93. Bar Magnet Analogue to Cooper Pairing.

rather than away from each other, as they would move if they were close enough and not acted upon by any other forces except their own mutual magnetism. The two bar magnets thus represent two free electrons, which, under typical conditions, will repel each other. If we place an assemblage of fixed bar magnets (one on top of the other) at locations for example $X, 0, 0$, or $-X, 0, 0$, with their south poles facing the origin, we clearly see that when the cosine component of the total attractive force between these fixed south poles and the north poles of the free bar magnets along the z-axis exceeds the repulsive force between the two north poles of the free magnets, then the latter will move toward each other as if they admitted to a net attraction. Thus, the fixed bar magnets on the x-axis in this simple analogue represent the bound hole or virtual exciton mediators cited earlier as a high- T_c mechanism (or the positive hole constituents of the virtual excitons, or simply localized

centers of perturbed positive charge these centers undergo only very limited motion, so the analogue with fixed br magnets is satisfactory).

6.7.2 The Coulombic Interactions. For simplification, at first, we shall consider only one complete CuO_3 quasi-pyramid as in Figure 94. We utilize the term "quasi-pyramid" because the base of the pyramid is not quite a perfect plane due to the puckering of the planar oxygens (O_2 and O_3) in the structure. We shall assume that due to the high internal electric field (which will be treated in the next section and clearly the assumption will be proven to be justified), there is one bound hole localized on each of the oxygens in the pyramid, and, due to the charge-transfer excitation, there is an average of two bound holes associated with the planar Cu^{2+} . In reality, for a given pyramid at any given instant, there are only two bound holes associated with the oxygens that arise from the neutralization of the Cu^{2+} ; however, three or more bound holes can be caused by the transient neutralization of the Cu^{2+} . It is likely that two of these three holes will be associated with the apical O_4 . In the nonneutralized case, the Cu^{2+} should furnish two bound holes in the form of constituents of virtual excitons. We have combined these two situations to obtain seven bound holes to take into consideration additional positive charge, which could be furnished by the boundary conditions and to analogue the seven bound holes per unit cell for the structure. A correction to the appropriate number of bound holes is accomplished by a monopole-weighting term, which will be introduced shortly.

The coulombic attractive force between any one of the bound holes and a conduction electron in the base plane of the pyramid is $F_{eh} = (kq_e q_h/r^2)$ where $-q_e = q_h = -e = -\text{charge on the electron}$, $k = 1/4\pi\epsilon_0$, and where r = distance between bound hole (h) and conduction electron e_2 . If the lifetime of the bound hole is (τ_{lh}) is longer than the time Δt_e when the conduction electron is in the neighborhood of being affected by the field of the hole, then the force F_{eh} will classically govern the perturbation of the bound hole. From a classical standpoint, the motion of the bound hole due to the conduction electron in the interacting neighborhood can be described by Newton's Second Law $F_{eh} = m_h a_h$, where a_h is the acceleration of the bound hole (of mass m_h) during the time Δt_e . The distance S that the hole moves (to a position of enhanced positive charge) is $S = (1/2) [ke^2/m_h r^2]$

In order to calculate the value of Δt_e , we must know the electron velocity v , which has been approximated in the past from Hall mobility studies as 10^8 cm/s. An electronic-type theory for high- T_c can be tested in this regard by utilizing the modified Conwell-Weisskopf [227-228] approach to calculate the mean free time of the electron and noting that the average mean free time τ_{mft} is a maximum for $v = \{7kT/m_e^*\}^{1/2}$. For $T = 100$ K and $m_e^* = m_e$ for a free electron, this gives $v = 1.1 \times 10^7$ cm/s. Since, at the preonset condition (temperature for deviation from linearity in resistance vs. temperature data) for high- T_c superconductivity in $Y_1Ba_2Cu_3O_{7-\delta}$ is about 100 K, and since we are interested in the calculations for the minimum time required for a mediating interaction between the bound hole and the free electron, we safely take $v = 10^8$ as a maximum. Then the value of Δt_e for e_2 to traverse approximately the region of the plane of the pyramid (approximating this distance as 3 Å) is $\sim 0.3 \times 10^{-15}$ s or somewhat less than 1 fs.

The modified Conwell-Weiskopf treatment gives the average mean free time that we can approximate as the lifetime of the hole before collision causes recombination. This is derived as

$$\tau_{mft} = \{[8K^2 (KT)^{3/2} (2m^*)^{1/2}] / [\pi^{3/2} Z^2 e^4 N \ln[1 + (7kKT/2Ze^2 N^{1/3})^2]]\}, \quad (22)$$

where k = dielectric constant, $+Ze$ = charge of scattering center, N = concentration of ionized impurity centers, and K = Boltzmann constant. If we assume that the ionized impurity scattering center is the bound hole having $Z = 1$, and $N = 10^{20} - 10^{22}$ cm $^{-3}$, N being assumed to be about equal to the free-hole value from our Hall data, and utilize the high-frequency dielectric constant $k = (n \pm 1)^2 = 1 - \omega_p^2 / \omega(\omega \pm \omega_B)$, where n = index of refraction, ω_B = frequency of precession of the electron, ω_p = plasma frequency for a tenuous plasma in which the damping of the motion of free electrons due to collisions becomes negligible, and ω = frequency at which k is being measured, then the calculated value of mean free time is $\tau_{mft} \approx \tau_{Lh} \approx 5.1 \times 10^{-11}$ s to 5.2×10^{-14} s, depending upon the values of k and N . Using the best available values for k and N , we derive $\tau_{mft} \approx 3 \times 10^{-12}$ to 3×10^{-13} s, and take this value as approximately the lifetime of the bound hole, τ_{bh} . Thus $\tau_{Lh} > \Delta t_e$, and hence, the lifetime of the hole-scattering center is long enough to allow for an interaction while the conduction electron is in the neighborhood of the bound hole. This implies that from the lifetime standpoint, the hole is tested to be a bonafide candidate for a high- T_c mediator.

6.7.3 Initial Conditions and Perturbations. Even at temperatures considerably greater than T_c , the internal electric field, due to the nature of the structure, induces charge-transfer excitations that lead to bound holes and virtual excitons. However, at such temperatures, the short lifetime of these excitons/holes strongly restricts the possibility of mediation of conduction electrons. Because of the short lifetime of excitons at $T \gg T_c$, we can at first approximate the bound holes shown in Figure 94 as stationary and not displaced by a moving conduction electron. The average electron-electron repulsion between an electron (e_2) in the plane of the pyramid and an electron (e_1) above the plane (at distance r_{12} apart) is the sum of their unmodified repulsive interaction and an attractive component based on interaction with the stationary holes. To compensate for the short lifetime of the virtual exciton or bound hole (τ_{Lh}) at $T \gg T_c$, we assign the hole some fractional charge ζ^*Ze where $0 < \zeta^* \ll 1$, and for a single virtual exciton $Z = 1$. Then when the lifetime of the hole increases as T becomes larger and almost attains T_c , the value of ζ^* increases to ζ_f^* , and the holes become displaced by the action of electron e_2 (because of ample interaction time for nontrivial displacement). We define ΔS^* as the average distance that electron e_2 displaces the positive constituent of the virtual exciton (or the positive bound hole). Thus, the magnitude of ζ^* can be viewed as a coefficient of effectiveness or a product of the ratio of real lifetime at temperature T to maximum lifetime at $T = 0$ K times a factor that characterizes the degree of monopolar character of the mediator (this parameter being adjustable to account for a correction in the number of bound holes per pyramid as well). The displacement of the holes then further changes the attractive component of the force between the hole and the conduction electron e_1 above the plane. The electron-electron force is specified as $F_{e1-e2} = F_R + F_A$, where R = repulsive and A = attractive. Then

$$F_{e1-e2} = - \{ [ke2\beta_{e1}/(r_{12})^2] [r_{12}/|r_{12}|] \} + \sum_i^n \{ [k\zeta_f^* ne^2/(r_{e1-h})^2]/(r_{e1-h})/r_{e1-h} \}, \quad (23)$$

where n = number of bound holes per pyramid, r_{e1-h} = distance between the bound hole and the conduction electron e_1 , and β_{e1} = multiplier (< 1.0) to account for the small initial attractive force component due to the stationary holes.

Now we can consider the realistic situation involving displacement of the bound holes. We know that the initial (i) force representing the $e_1 - e_2$ is repulsive and that $\zeta_i^* \ll 1$. However, the

value of ζ^* is very important because it will influence the delicate balance in the repulsive and attractive terms such that by displacing the holes, the resulting change in the attractive component (when ζ^* increases and r_{e1-h} becomes shorter) is to become larger than the repulsive component. Then, for a given value of ζ^* we calculate the value of r_{12} such that $F_A \geq F_R$.

Because the balance between repulsive and attractive components is changed by the increased lifetime and the motion of the bound holes, we can then employ a Schrodinger wave equation approach using a time-independent perturbation and solve for the perturbed potential V' due to the displacement of the holes. Thus, $V' = V + v$, where V is the electron-electron potential prior to the motion of the holes. Thus,

$$-[(h/2\pi)^2/2m] (d^2 \Psi'/dx^2) + V\Psi'_n + v\Psi'_n = E'_n \Psi'_n, \quad (24)$$

where $\Psi'_n(x) = \sum_L a_{nL} \Psi_L(x)$. The coefficients a_{nL} , determine how much of each of the $\Psi_L(x)$ is contained in $\Psi'_n(x)$. The expectation value of the perturbing potential is $\langle V(x) \rangle = \Psi_n^*(x)v(x)\Psi_n(x)$. Then the shift in energy of the n^{th} eigenvalue due to the perturbing potential $v(x)$ is equal to the value of $v(x)$ averaged over the n^{th} unperturbed eigenstate times a weighting factor. The latter factor is simply the probability density $\Psi_n^*(x) \Psi_n(x)$ for that eigenstate. Thus,

$$E'_n - E_n = a_{nn} = \int_{-\infty}^{\infty} \Psi_n^*(x)v(x)\Psi_n(x)dx. \quad (25)$$

The coefficients a_{nm} specify what magnitude of each of the unperturbed eigenfunctions $\Psi_m(x)$ is mixed with the dominant unperturbed eigenfunction, $\Psi'_n(x)$. Then

$$a_{nm} \approx [1/(E_n - E_m)] \{ \int \Psi_m^*(x) v(x) \Psi_n(x) dx \}, \quad (26a)$$

excepting $a_{nn} \approx 1$, and

$$\Psi'(x) = \sum_m a_{nm} \Psi_m(x). \quad (26b)$$

Thus, from this point onward, the approach of Cooper in the BCS theory of superconductivity can be pursued for the case of two electrons with opposite spin. Cooper [9, 10] solved the Schrodinger equation for a pair of electrons of opposite momenta k and $-k$ in a potential well by assuming that the interacting electrons could not get into the Fermi sphere, thus incorporating the exclusion principle by specifying $|k| > k_f$ [229-231].

6.7.4 Displacement of Positive Charge and Work Done by e_2 Conduction Electron. In Figure 94, we place a conduction electron (e_2) in the neighborhood of one of the oxygen ions (O(2) for example), and we calculate the coulombic attractive force F_i on each of the entities of nonnuclear positive charge centers in the pyramid. In this manner, we can derive for $\zeta_f = 1$ the values given in Table 7. We sum up the work done by the electron e_2 on the bound holes (or virtual excitons) as $\sum f_i dL_i = 3.4 \times 10^{-19}$ joules, where $L = \Delta S_h^*$ = displacement of each bound hole. The initial KE of the conducting free electron is $(1/2)mv_{e2}^2 = 4.6 \times 10^{-19}$ J. Then the final velocity of the conduction electron after displacing the holes toward the conduction electron is

$$V_{f(e2)} = \{(2/m_e) [(1/2) (m_e v_{e2}^2)] - \sum_{i=1}^n \int_0^{L_i} f_i \cdot dL_i\}^{1/2} = 1.2 \times 10^7 \text{ cm/s},$$

where v_{e2} is the initial velocity of electron e_2 and is taken as 1.0×10^8 cm/s as before. The magnitude of $V_{f(e2)}$ will be a minimum because the condition $\zeta_f = 1$ gives rise to a maximum work done.

Since an accelerating charge radiates energy, we can calculate the radiation rate of the accelerated hole (due to the attraction from the conduction electron) as $R = [(2/3) (e^2 a^2/C^3)] \approx 1.2 \times 10^{-17}$ J/s/hole (where a = acceleration of bound hole, and c = velocity of flight). Since the motion of the hole is only for the time $\Delta t \leq 0.3 \times 10^{-15}$ s, this gives an energy of about 3.5×10^{-33} J/hole or about 4×10^{-12} J/cm³, which is a relatively small energy.

6.7.5 Potential Function for $e_1 - e_2$ Interaction Derived From Conservation of Momentum and Conservation of Energy. We begin this section by specifying conditions for the conduction electron e_1 , which exists somewhere above the plane of the pyramid. We let p_1 = initial momentum

Table 7. Interaction of Electron e_2 at O (2 Å) Site in Base Plane of Pyramid With Bound Hole Cores of Bound or Virtual Excitons

Interaction	r (Å)	Maximum Displacement of Holes (Å)	Force of Interaction Newtons (N)	Work Done by e_2 on Holes in Joules (J)
e_2 - Cu^{2+} hole	1.91	0.2 each	6.2×10^{-9} each	1.24×10^{-19} each
e_2 - O(2B) hole	3.82	0.05	1.5×10^{-9}	0.075×10^{-19}
e_2 - O(3B) hole	2.70	0.10	3.1×10^{-9}	0.310×10^{-19}
e_2 - O(3A) hole	2.70	0.10	3.1×10^{-9}	0.30×10^{-19}
e_2 - O(4) hole	3.00	0.08	2.5×10^{-9}	0.20×10^{-19}
Average	2.67	0.12	3.8×10^{-9}	$\sum_i = 3.38 \times 10^{-19}$

of the e_1 electron so that $p_1 = m_e v_{e1} = (h/2\pi)k_1$. Then by specifying Δp_1 to represent the change in the momentum of e_1 due to the displacement of the bound holes by the e_2 electron, we can simply write $\Delta p_1 = m_e \Delta v_{e1}$.

The shift in the position vectors of the assemblage of bound holes will create a change in the coulombic force (F), which is a component that contributes to the overall force that governs the velocity and overall motion of the above-plane conduction electron e_1 . Then, $\Delta F t_e = m_e \Delta v_{e1}$ (i.e., the velocity v_{e1} is based on the resolution of all of the forces acting on conduction electron e_1 during time Δt ; these forces are integrated to give an energy e_1 equal to $p_1^2/2m$). Thus, $\Delta v_{e1} = \Delta F \Delta t_e / m_e$.

After the coulombic interaction with the moving holes, the new momentum of the conducting electron e_1 is

$$p_1' = m_e v_{e1} + m_e \Delta v_{e1} = m_e v_{e1} + \Delta F \Delta t_e.$$

The initial momentum of the conduction electron e_2 in the plane is $p_2 = m_e v_{e2}$. The final momentum is $p_2' = m_e v_{f(e2)}$. From conservation of energy we have

$$(p_2')^2/2m_e = p_2^2/2m_e - \sum_i \int_0^{L_i} f_i dL_i \quad (27)$$

From the conservation of momentum, we know that the total sum of the changes in the linear momentum of the electron in the plane (e_2), the assemblage of n holes, and the electron above the plane (e_1) is zero. Thus,

$$(m_e)v_{e2} - p_2' - n\zeta_f^* m_h v_h = p_1' - m_e v_{e1}, \quad (28)$$

where v_h = velocity of the bound hole = $a_h \Delta t_e$.

Solving equations (27) and (28) for $(p_2')^2/2m_e$ in terms of p_1' , and equating to (e) (V_{e1-e2}) gives us an expression for the potential function relating e_1 and e_2 , and the bound holes:

$$V_{e1-e2} = (1/2m_e e) \{m_e v_{e2} - \Delta F \Delta t_e - n\zeta_f^* m_h v_h\}^2. \quad (29)$$

Equation (29) then represents the potential between electrons e_1 and e_2 as modified by the coulomb attraction between the displaced bound holes. The value of ΔF is derived from the hole motion due to the action of electron e_2 . The greater the value of n (the number of bound holes per pyramid) and the greater the displacement L_i , the larger the probability of an attractive net force at a critical value of r_{12} . The parameter r_{12} is contained within the relationship for p_1' . This is because the velocity of electron e_1 after the interaction with the bound holes (v_{fe1}) depends upon the attractive coulombic force between each hole and electron e_1 . The net attractive force is derived by taking the gradient of the potential that will be proportional to the inverse square of r_{12} .

6.7.6 Calculation for Net Attraction Between Two Conduction Electrons as Mediated by Displaced Positive Charge Contribution of Virtual Exciton. Figure 95 gives, using the previously mentioned approach of bound holes or virtual excitons as mediators, the computer-calculated plots

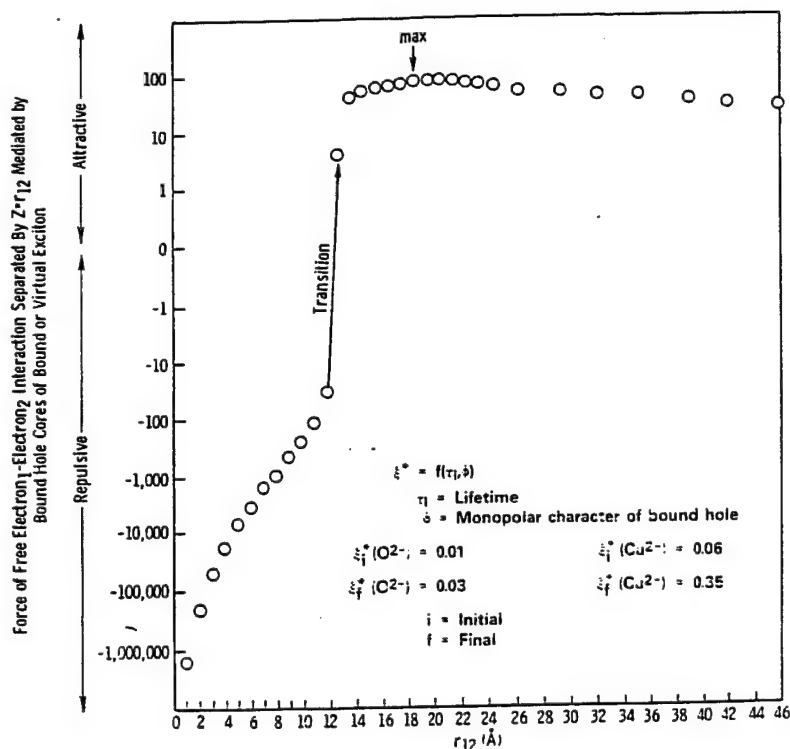


Figure 95. Net Force Between Free Electron e_1 and e_2 After Displacement of Bound Holes.

of the distance between two free electrons in excess of which the net attractive hole-mediated coulombic force felt by two electrons is attractive and thus overcomes the normal electron-electron repulsive force. This calculation employed only a single CuO_5 pyramid that rests in parts of four adjacent unit cells. The graph in Figure 95 shows that at an interelectron distance r_{12} of about 12–14 Å, the attractive net force overcomes the repulsive force between two free electrons. In the case when these two electrons have opposite spin and opposite linear momentum, then they can become transiently Cooper-paired. In Figure 96, we show the results of a similar calculation that employed a cluster of four pyramids with coplanar base planes. The critical value of r_{12} for this more complicated calculation is about 11–12 Å. A calculation was also conducted for both conduction electrons being in the CuO_2 plane yielding similar results. The in-plane calculation requires weighing the holes associated with the O_4 ion more heavily. Being a bridging agent the O_4 apical ion is apt to be more favorable for hosting bound holes than would be the other oxygen ions. It should be noted that the calculations leading to what is shown in Figures 95 and 96 are very sensitive to the initial conditions regarding the lifetime of the holes and the degree of monopolar character of

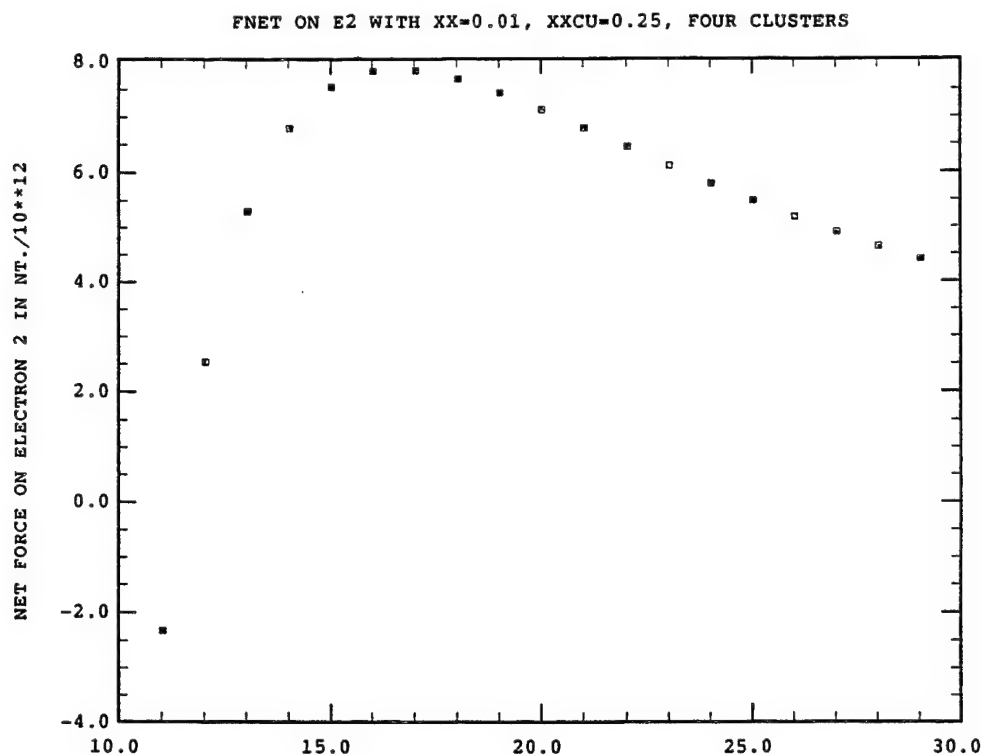


Figure 96. Graph of Turn-Around Conditions From Repulsive to Net-Attractive Electron-Electron Interaction, Based on Interaction With Positive Hole Cores of Bound Excitons on Four-Pyramid Cluster Having Common Base Plane. First Conduction Electron Is in Base Plane of Pyramid Cluster. Second Conduction Electron Is Above the Plane in a Direction Opposite to Apical O(4).

the holes. Calculations in which the energy is very sensitive to initial and boundary conditions often connect to conditions of chaos, and such a possibility is open to future analysis. Table 8 summarizes the results of this treatment.

The approach to calculate what is given in Figures 95 and 96 was that for a given value of ζ . We determined the value of r_{12} such that $F_A \geq F_R$. Or conversely, if we utilize the known experimental average coherence length for the ceramic material of 15 Å as r_{12} , we calculate the appropriate ζ_f for $F_A \geq F_R$. Experimental values of coherence length are ~7 Å in the z-direction and ~17 Å in the x-y-directions.

The calculation shows that for a value of $\zeta_i^* < 0.14$, the electron-electron interaction force is always repulsive for $n = 7$ holes/pyramid, so we therefore take ζ_i^* as between zero and 0.14 and then

Table 8. Summary of Theoretically Derived Properties of High- T_c Superconductivity in $Y_1Ba_2Cu_3O_{7-\delta}$

	Characterization	Pertinent Value
1	Pyramids per Unit Cell	2 (Eight 1/4 Pyramids)
2	Number of Bound Holes Per Pyramid Due to Charge Transfer Excitation and Bound Exciton	7
3	Free Electrons Per Pyramid	0.86
4	Mobility of Free Electron	$3.3 \text{ cm}^2/\text{V-s}$
5	Initial Velocity of Free Electron	$1 \times 10^8 \text{ cm/s}$
6	Final Velocity of Free Electron After Perturbation of Bound Holes	$1.1 \times 10^7 \text{ cm/s}$
7	Interaction Time of Free Electron With Bound Holes	$0.3 \times 10^{-15} \text{ s}$
8	Average Lifetime of Bound Holes	3×10^{-14} through $1 \times 10^{-12} \text{ s}$
9	Average Displacement of Bound Holes	0.1 \AA
10	Direction of Internal Electric Field at Ion Positions; Ion Having Maximum Absolute Magnitude of Internal Electric Field	$+Z$ 04
11	Displacement of $2P_z$ Electron of Oxygen Ion; Extent of Monopolar Character to O^{2-} Bound Hole	0.1 \AA 5–10%
12	Principal Plane of Free Electron Motion	CuO_2 Plane (Base Plane of Pyramid)
13	Increase in Lifetime of Bound Holes as Temperature Decreases	Two to Three Fold
14	Interelectron Spacing for Positive Attraction	$12\text{--}18 \text{ \AA}$
15	Minimum Temperature for Bound Exciton Mediation to Create Superconducting Pairs	40 K

calculate the hole displacement and the electron-electron ($e_1 - e_2$) separation, based on the new position of the holes and on a final ζ_r^* for attractive interaction to overcome the repulsive interaction.

The final value of ζ^* , which we refer to as ζ_f^* , represents the increased lifetime of the holes (positive charge contribution to virtual exciton) at $T = T_c$. We performed the aforementioned calculation by varying ζ_f^* from 0.14 to 1.00 and giving the two free electrons the same x-y-coordinates, but varying interelectron spacing in the z-direction.

Since the electron constituent of the virtual exciton due to the charge-transfer excitation spends very little time near the Cu(2) hole, the ζ^* factor for the copper hole is largely a function of lifetime (because the large diameter of this exciton gives its core hole essentially a monopolar character relative to the electron e_1 above the plane). However, the much smaller virtual or bound exciton localized on the oxygens may differ considerably from a monopole relative to its interaction with e_1 and is actually more akin to a dipole (because of the electronegativity of O). Thus, when T decreases to T_c and the lifetime of both types of virtual excitons increases, the ζ^* factor for the Cu^{2+} holes should increase much more so than the ζ^* factor for the O^{2-} holes. Hence, we conducted the calculation by taking the values as shown in the legend of Figure 95 (which was also used in the calculation in Figure 96). Coulombically, the contribution of the Cu^{3+} is implicitly considered in this analysis because it promotes the charge-transfer excitations that lead to the excitons or bound holes because of the action of an internal electric perturbation local field gradient, which will be treated in section 6.8.

The interelectron spacing for positive net attraction of e_1 and e_2 as a function of the fraction of effective charge on each of seven bound holes in the CuO_5 pyramid is very sensitive to the effective bound charge; hence, initial conditions are very critical. Figure 97 gives the approximated theoretical graph of coherence length vs. temperature for superconducting $\text{Y}_1\text{Ba}_2\text{Cu}_3\text{O}_{7-\delta}$, showing a great sensitivity as T_c is approached such that near 84.5 K, the coherence length diverges, which mathematically suggests pair scission.

6.7.7 Calculation of Temperature for Adequate Hole Lifetime ($\tau_{Lh} = \Delta t$) Using Coulombic-Interaction Model. The calculation of T_c for low- T_c superconductors, which has been shown in an earlier section, was derived from the theory of specific heat and normal modes of vibration of the lattice. However, a calculation for high- T_c , employing electron-hole attraction rather than ion

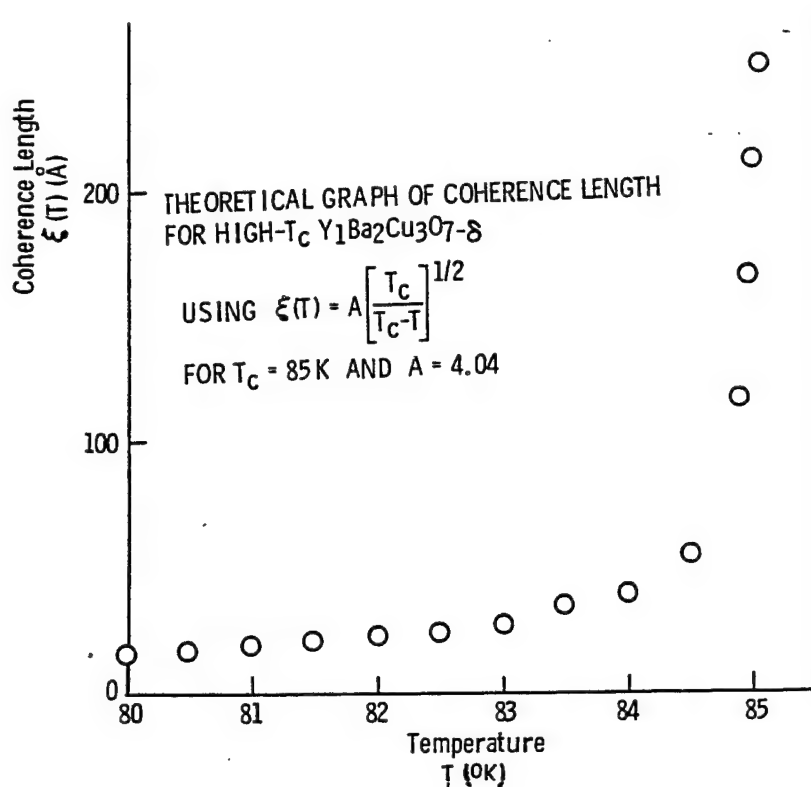


Figure 97. Theoretical Plot of Coherence Length vs. Temperature.

vibrations as mediators, should involve a calculation of the temperature for which the lifetime of bound holes is adequately long to qualify for being mediator particles.

We can approximate a temperature at which the average velocity of electrons will be such that the mean free time between collisions with holes is longer than Δt_e . Thus, $\tau_{bh} \approx \tau_e \geq \Delta t_e \approx 10^{-15}$ s, where bh = bound hole, and e = electron that is a candidate for collision and recombination with the bound hole. We specify that $\tau_{bh} \approx 3.4 \times 10^{-13}$ s from the charge-transfer excitation and mean free time discussion in an earlier section. We can independently calculate this value from knowing the hole mobility (μ_h) for $Y_1Ba_2Cu_3O_{7-\delta}$ as $3.3 \text{ cm}^2/\text{V}\cdot\text{s}$ [223–226]. Then from $\tau_h = m_h \mu_h / e$, we can calculate $\tau_h \approx \tau_{bh}$ as 10^{-13} to 10^{-14} s.

We now calculate the average velocity of the electron constituent of the exciton from the orbital frequency (10^{14} Hz) and the assumed radius for the exciton. The temperature for that average velocity can be calculated from the known relationship of the mean square velocity [227, 228] as

$$\langle v \rangle \approx [(3 KT/e) (e/m^*)^{1/2}], \quad (30)$$

where K = Boltzmann constant, and m^* = effective mass at the appropriate energy.

For the virtual exciton associated with the Cu^{2+} , we take an average radius equal to the distance to the copper chain site based on the $\text{Cu}^{2+} - \text{Cu}^{3+}$ charge-transfer excitation interaction. For the virtual exciton associated with the oxygens, we assume a much smaller exciton radius of about 0.5 Å in keeping with the model of electron displacement by the high internal electric field. We then take a weighted average for the velocity of the electron that is related to the virtual exciton as $v_{\text{ex}} = (1/7) (2v_{\text{exCu}} + 5v_{\text{exO}})$. Using equation (30), this yields a temperature of 62 K, which is in reasonable agreement with the midpoint of the range of T_c in the high- T_c materials.

6.8 The Properties of High- T_c Superconducting Materials That Relate to Characteristics of Marginal Ferroelectrics.

6.8.1 Overview. High- T_c superconducting oxides are composed of structural elementary building blocks, including pyramids, planes, and chains, in such a manner so as to be expected to create a large internal local electric perturbation field. In addition, the presence of $d^9\text{Cu}^{2+}$ creates a Jahn-Teller distortion, affecting the position of the apical oxygen (O_4) ions. Observations have also been reported of spontaneous polarization, piezoelectricity, pyroelectricity, and circular dichroism in this class of materials. These structural and property criteria suggest that high- T_c Perovskite-like superconductors in their normal state may be in the microscopic domain a special case of marginal ferroelectric materials. The importance of ferroelectric polarization in the pretransition normal state relates to a number of phenomena that are reported to be associated with the high- T_c mechanism, such as phonons, polarons, and charge-transfer excitations. The unique structure of the $\text{Y}_1\text{Ba}_2\text{Cu}_3\text{O}_{7-\delta}$ indeed gives rise to local perturbation electric fields that we have calculated by a multicell point-charge computer code herein described. The resonant charge-transfer excitation establishes a virtual exciton, which creates electron-electron coupling in the form of Cooper pairs. This analysis is intended to show the origin of the bound hole from the internal perturbation local field approach.

6.8.2 Introduction to Ferroelectric Properties as Related to High- T_c . In the road to high- T_c superconductivity, there were two generally acknowledged channels of approach. One, derived from theories of the metallization of H, emanated from pressure-induced energy band displacement and related to excitonic levels, being advanced by several Russian [33–35] and one American scientist [39] and leading to materials studies such as of CuCl, BiSb, and CdS. The other derived from considering collective quantum states [71, 72] that related to phonons as well as excitons (or plasmons) and stressed ferroelectric-like oxides; heavy Fermion materials; Chevrel phases; and, in particular, ferroelectric materials. The former approach led to observations of effects akin to high- T_c superconductivity [74–84]. The latter led to finding high- T_c superconductivity reproducibly in the new Perovskite-like materials [91–96, 111–117].

Links that have been suggested between high- T_c superconductivity and ferroelectric materials were initially met with much criticism and controversy. However, the recent spontaneous polarization study of Kurtz et al. [232], which was calculated from their strain data, gave an implication that high- T_c $\text{Gd}_1\text{Ba}_2\text{Cu}_3\text{O}_{7-\delta}$ was a relaxor ferroelectric-type material. Further support for this notion is given in reports of pyroelectric and piezoelectric effects near the surface in single crystal $\text{Y}_1\text{Ba}_2\text{Cu}_3\text{O}_{7-\delta}$ [233]. The authors of this latter work propose an intrinsic bipollaronic microscopic mechanism causing an asymmetric displacement of the O_4 ions (breaking crystal centrosymmetry) and causing a macroscopic polarization per unit volume directed along the c-axis. In our present study, we have shown using a 75-unit cell array coulombic point-charge calculation (as well as a modified orbital calculation) that the highest internal electric perturbation field in the $\text{Y}_1\text{Ba}_2\text{Cu}_3\text{O}_{7-\delta}$ structure exists at the O(4) site, where the field is also of opposite direction than at the copper, barium, O(1), O(2), and O(3) sites. The results of this study indicate that the normal-state conductivity in $\text{Y}_1\text{Ba}_2\text{Cu}_3\text{O}_{7-\delta}$ is due largely to the chain contribution to the structure, implying that conductivity in the pyramidal or planar region is likely to be dominated by hopping. The results of our perturbation internal electric field study are shown in Figures 98–102 and in Table 9. The results are described in more detail and further developed in a subsequent subsection herein and are certainly compatible with observations suggesting a microscopic poled behavior. A further suggestion that relates to at least modest ferroelectricity in $\text{Y}_1\text{Ba}_2\text{Cu}_3\text{O}_{7-\delta}$ is the report of circular dichroism [234], which indicates broken symmetry below a specific temperature, whereby parity

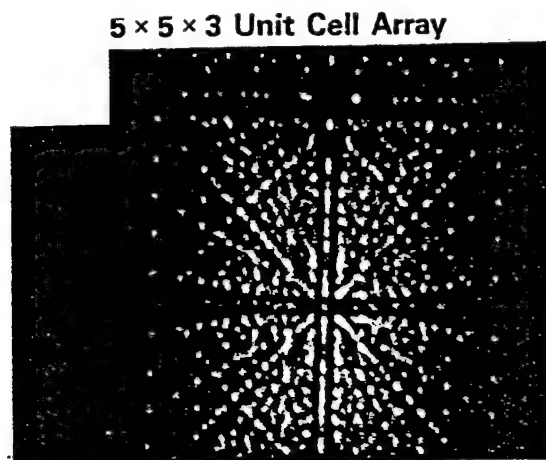


Figure 98. Computer Screen Array of Lattice Sites in $Y_1Ba_2Cu_3O_{7-\delta}$ Structure.

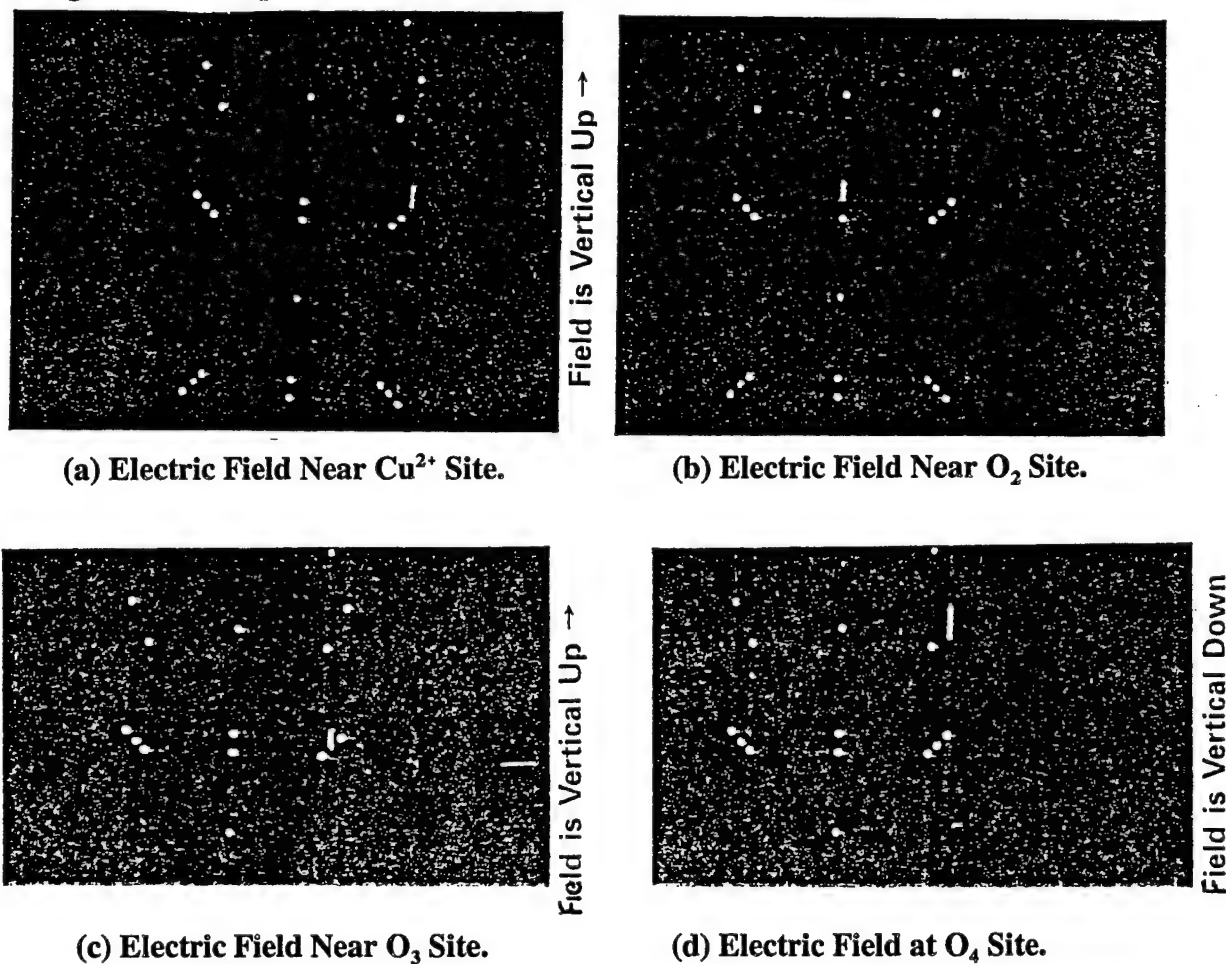


Figure 99. Display of Calculated Internal Electric Field Magnitude and Direction at (a) Cu^{2+} , (b) O_2 , (c) O_3 , and (d) O_4 Sites.

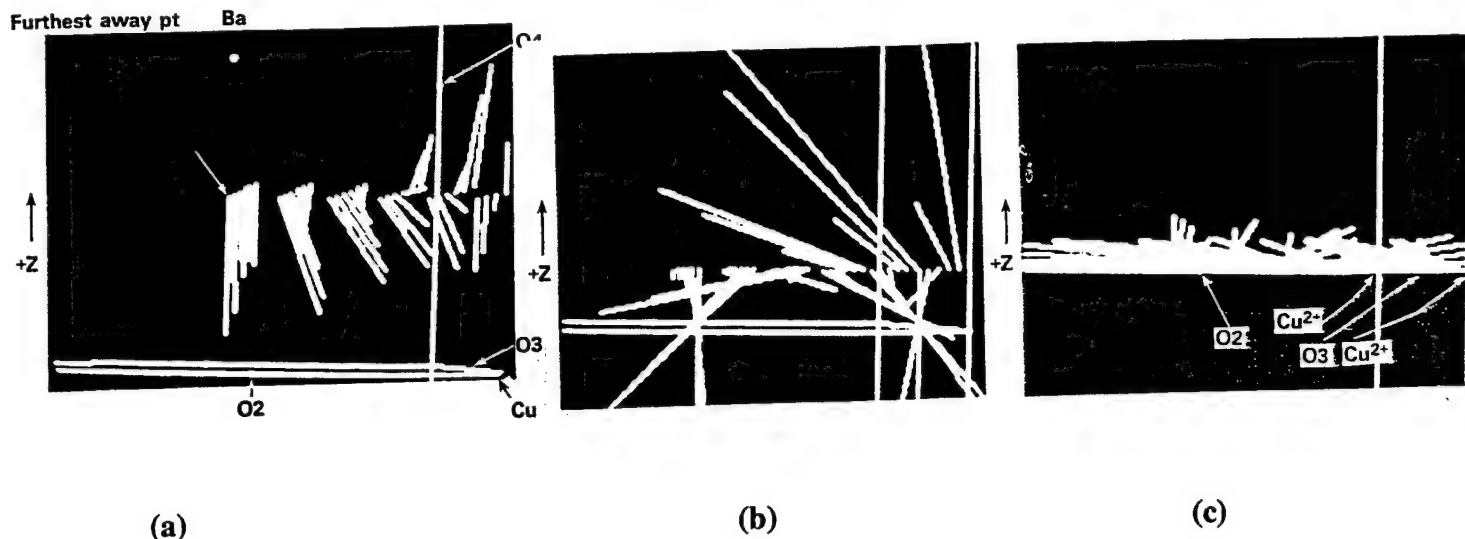
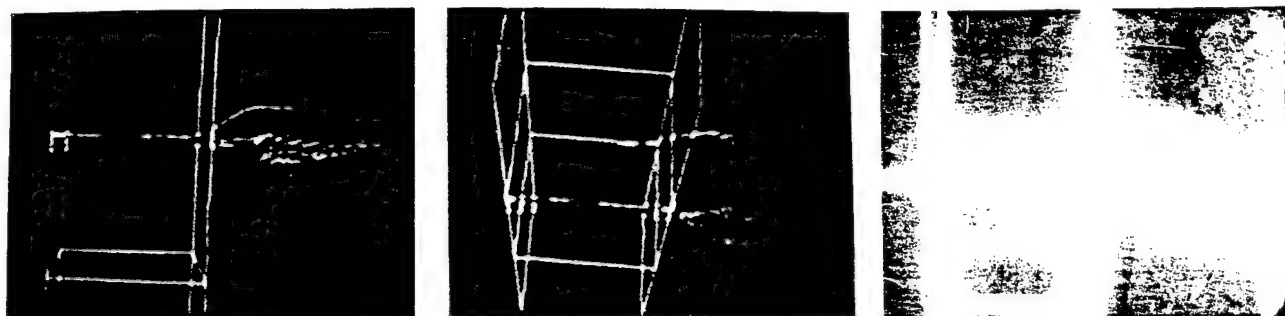


Figure 100. Computer Calculation for Internal Field Lines at Center Unit Cell of 75-Cell Array of $Y_1Ba_2Cu_3O_{7-\delta}$ Using One-Quarter Pyramid. (a) Emanating From 6×6 Array of Points in Probe Plane Parallel to CuO_2 Pyramid Base Plane and Passing Through Pyramid at About One-Half the Pyramid Height. Notice Twisting of Paths out of Probing Plane. (b) Same as (a), Except the Probe Plane Passes Through at About One-Quarter the Pyramid Height. Notice Twisting of Paths out of Probing Plane. (c) Same as (a) and (b), Except That Probing Plane Almost Coincides With Base Plane of Pyramid. Note That Vectors Are of Lower Magnitude and There Is Less Out-of-Plane Twisting. Note Also Vertical Field Lines at Ion Sites.

symmetry and time-reversal symmetry are simultaneously broken. Additionally, the compatibility of the structures and compositions of high- T_c materials with the A_2BX_4 archetype ferroelectric spinel-type systems is further justification of the likelihood of a close coordination between high- T_c materials and marginal ferroelectric materials. However, although the bipolaron is a natural consequence of ferroelectric phenomena, it is unlikely that the bipolaron could indeed be the principal mediating particle to establish Cooper-pairing if one considers the established Fermi surface.

The possible link between ferroelectric behavior and high- T_c superconductivity became apparent in our own theoretical work when we established that bound holes must be localized on the oxygens and must be related to virtual excitons associated with the multivalence cations. We conclude that



(a) 90° (Vertical).

(b) Front Rotation to 30°.

(c) Front Rotation to 70°.



(d) 0°.

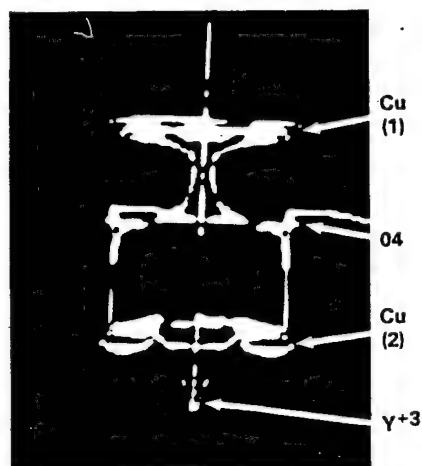
(e) Front Rotation to 45°.

(f) Rear Rotation of 33°.

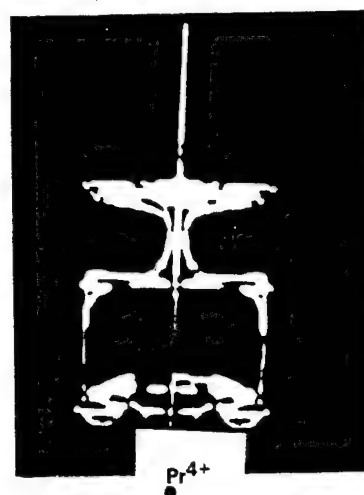
Figure 101. Internal Electric Field Lines for $Y_1Ba_2Cu_3O_{7-\delta}$ Single-Cell Probe Points in x-Direction Through Neighborhood of Cu^{2+} : Edge Effects.

the charge-transfer excitation, which leads to the establishment of the bound hole system, is due to the high internal electric perturbation field, which will be quantitatively described shortly.

6.8.3 General Theory of Ferroelectric Materials. Ferroelectricity is a phenomenon occurring in certain materials, whereby electric moments have the tendency of parallel orientation with



(a) Center Cell $7 \times 7 \times 5$ Array.



(b) Internal Electric Field in Front Face of Unit Cell $\text{Pr}_1^{4+}\text{Ba}_2\text{Cu}_3\text{O}_7$.

Figure 102. Comparison of Field Paths for $\text{Y}_1\text{Ba}_2\text{Cu}_3\text{O}_{7-\delta}$ With $\text{Pr}_1\text{Ba}_2\text{Cu}_3\text{O}_{7-\delta}$.

Table 9. Perturbation Field at Ion Sites

Ion	Charge	Ex	Ey	Ez
Y	+3	0.0	0.0	0.0
Cu ₂	+2	0.0	0.0	0.38
O ₂	-2	0.0	0.0	0.33
O ₃	-2	0.0	0.0	0.34
Ba	+2	0.0	0.0	-0.32
O ₄	-2	0.0	0.0	-0.67
Cu ₁	+3	0.0	0.0	0.0
O ₁	-2	0.0	0.0	0.0

NOTE: These are normalized (e^2/A) values for the upper half of the unit cell. To obtain electric field strength in Newtons/coulomb multiply by 14.4×10^{10} .

extended domains. This behavior is often typified in ABX_3 and A_2BX_4 structures, both of which also relate to high- T_c materials in the form of layered Perovskites and substitution defect derivatives of

the antiferromagnetic K_2NF_4 structure. A ferroelectric material displays a hysteresis loop in its polarization (P) vs. electric field (E) dependence, which yields the spontaneous P_s (the polarization present at zero external field). The P vs. E characteristic also gives the coercive field.

Materials that are ferroelectric and structurally relate to high- T_c superconductors are the ABX_3 structures $KNbO_3$ and $KTaO_3$, and the A_2BX_4 spinel structures $(NH_4)_2SO_4$ and $(NH_4)_2BeF_4$. Such materials exhibit a Curie temperature above which P_s vanishes, and a temperature T^* at which the dielectric constant peaks. We believe the latter temperature to be related to high- T_c materials.

If a ferroelectric material is perturbed by a stress that is caused by an electric field, the infinitesimal change in the internal energy is given by

$$dU = TdS - \sum_{i=1}^3 X_i dx_i + E \cdot dP, \quad (31)$$

where T = temperature, and S = entropy. It is conceptualized that the polarized phase below the Curie point (T_{cp}) is a slight distortion of the nonpolarized phase above the Curie point. It is further assumed that P_s lies along the Z-axis and $E_x = E_y = 0$. We can then write the Gibbs free energy for a crystalline structure having a center of symmetry (such as $Y_1Ba_2Cu_3O_{7-\delta}$) or a symmetry plane perpendicular to Z as

$$G = G_0 + (1/2)\alpha P^2 + (1/4)\gamma P^4 + (1/6)\delta P^6 \text{ at } T > T_{cp}. \quad (32)$$

In equation (32), G_0 = free energy for zero polarization, and α , γ , δ are materials-related coefficients. This yields the electric field in terms of the polarization

$$E = dG/dP = \alpha P + \gamma P^3 + \delta P^5. \quad (33)$$

Neglecting effects of saturation allows the electric susceptibility X above the Curie temperature to be calculated as

$$X = P/E + 1/\alpha$$

or

$$X = 1/\beta(T - T_0), \quad (34)$$

using the approximation $\alpha = \beta(T - T_0)$, where T_0 is the temperature at which the extrapolated curve of the inverse dielectric constant intersects the temperature axis. The expression $\beta(T - T_0)$ relates to the materials property known as the dielectric stiffness $K = X^{-1}$. The coefficients in equations (33) and (34) for E are such that β and δ are positive in materials known to be ferroelectric (and presumably in high- T_c oxides as well); however, the sign of γ strongly influences the dependence of G on temperature and polarization.

For $\gamma < 0$, the transition at $T > T_4$ is first order (slope or first derivative change in Gibbs function, or discontinuity in volume or entropy vs. intensive thermodynamic variable) with a latent heat and a discontinuity in specific heat c_p . However, for $\gamma > 0$, the transition at $T > T_{cp}$ is second order (change is in second derivative of the Gibbs function) with zero latent heat, but a spike (peak or anomaly) in specific heat. Also for $\gamma > 0$, the Curie temperature $T_{cp} = T_0$, and at $T < T_0$, the slope of K vs. T is negative and twice the magnitude as for $T > T_0$. Then ideally, at $T = T_0$, the dielectric stiffness K approaches zero as ϵ approaches infinity. In practice, however, ϵ remains limited, although it attains very high values in most ferroelectric materials. T_{cp} varies widely in ferroelectric materials, ranging from 120°C in BaTiO_3 to -260°C in KTaO_3 .

Dielectric measurements [235, 236] at 9.2 GHz are reported for $\text{Y}_1\text{Ba}_2\text{Cu}_3\text{O}_{7-\delta}$ to show that the real part of the intrinsic dielectric constant at microwave frequencies exceeds 120, and has a loss tangent ≤ 0.2 .

For a first-order ferroelectric transition, we can write $E = \beta(T - T_0)P + \gamma P^3 + \delta P^5$ and $K = 1/X = \beta(T - T_0) + 3\gamma P^2 + 5\delta P^4$. However, for a second-order ferroelectric transition in the presence of a constant bias field E_B , the polarization vs. field relationship is given by $E + E_B = \beta(T - T_0)P + \gamma P^3$. For $E = E_B = 0$, the aforementioned gives a general value of P_s of the order of $\mu\text{C}/\text{cm}^2$; however, in the presence of a large internal electric field, it yields much higher values of P_s .

6.8.4 Persistent Polarization in Ferroelectric Materials and Perfect Diamagnetism in Superconductors. Polarization of a more or less permanent persistence can be established in ferroelectric materials by various processing techniques, including by melting then solidifying in a strong electric field, thereby forming electrets (permanent dipoles that become oriented in the molten state, and the orientation being retained upon solidification). Permanently polarized entities experience forces and torques that can be calculated from $\mathbf{E} = \int \tau \mathbf{E} \rho_p d\tau$, where $\rho_p = \nabla \cdot \mathbf{P}$, and \mathbf{E} = electric field at $d\tau$ that is obtained by neglecting or ignoring the field of the electric dipole itself. The electric field produced by a permanently polarized entity is the vector sum of the fields provided by all of the individual dipoles of the dielectric.

In a nonuniform electric field, there is a net force on the internal dipoles given by $\mathbf{F} = \nabla(\mathbf{E} \cdot \mathbf{p})$, where \mathbf{p} = dipole moment of the separated charges, and \mathbf{E} = electric field in the domain of which the dipole exists. Since \mathbf{p} is constant, the net force is proportional to the gradient direction of \mathbf{p} . In the $\text{Y}_1\text{Ba}_2\text{Cu}_3\text{O}_{7-\delta}$ superconductor, that direction is \mathbf{Z} . The resulting force then points in the direction in which this component of \mathbf{E} increases most rapidly. Thus, the net result in highly nonuniform fields can be rapidly circling electrons, such as circulating individual loops insulating with respect to each other, but not with respect to themselves.

Interestingly, the negative magnetic polarizations of diamagnetic materials (such as the perfect diamagnetism of superconductors) can be understood if one envisions a loop of material with zero electrical resistance and attempts to establish a magnetic field therein. From Lenz's Law, the current that is induced in such a loop will be in a direction to prevent the establishment of that magnetic field. The resulting current loop would represent a magnetic dipole acting in the direction opposite to the applied \mathbf{B} -field. An array of such loops then represents a diamagnetic material. This reasoning suggests the coexistence of superconductivity (resistancelessness) and diamagnetism (negative magnetic polarization). The orbital electrons in completely filled atomic shells behave very similar to nonresistive circulating current loops. The application of a \mathbf{B} -field perturbs their orbits to some degree such as to oppose the applied field (the new orbital motion remaining until \mathbf{B} again changes).

Thus, polar electret-like behavior in ferroelectric materials and perfect diamagnetism in largely ionically bonded superconductors (such as high- T_c oxides) have some degree of commonality.

6.8.4.1 Peaking Dielectric Constant. The dielectric constant in ferroelectric materials is a function of temperature and normally admits to a maximum turning point. This temperature (T^*) for the peaking dielectric constant for a second-order ferroelectric is shifted by the bias field E_B to which the material is subjected. Hence, the peak does not occur at the Curie point, but at $T^* > T_{cp}$. Differentiating the dielectric stiffness

$$K = \beta(T - T_0) + 3\gamma P^2 \quad (35)$$

with respect to temperature and equating to zero yields, at $T = T^*$,

$$dP/dT = -\beta/6\gamma P, \quad (36)$$

where P = polarization that is induced by the bias field E_B . Since the bias field remains constant, $dE/dP = 0$, which leads to

$$dP/dT = -\beta P [\beta(T - T_0) + 3\gamma P^2]^{-1}. \quad (37)$$

Equations (35)–(37) lead to an expression for the polarization P^* induced at the temperature T^* by the effect of the bias field E_B :

$$P^* = \{[(1/3)\beta\gamma^{-1} (T^* - T_0)]^{1/2}\} (T^* - T_0)^{3/2}. \quad (38)$$

This suggests that in the absence of an external bias field, the most important property that governs the temperature at which the dielectric constant peaks is the actual internal electric field in a local region established by the unique crystal structure itself. We can approximate the shift in T^* as a function of net field E_N by differentiating $(T^* - T_0)$ as a function of E_B . This yields $d(T^* - T_0)/dE_B = (\text{CONST})/E_N^{1/3}$, which takes the form shown in Figure 103. This suggests that

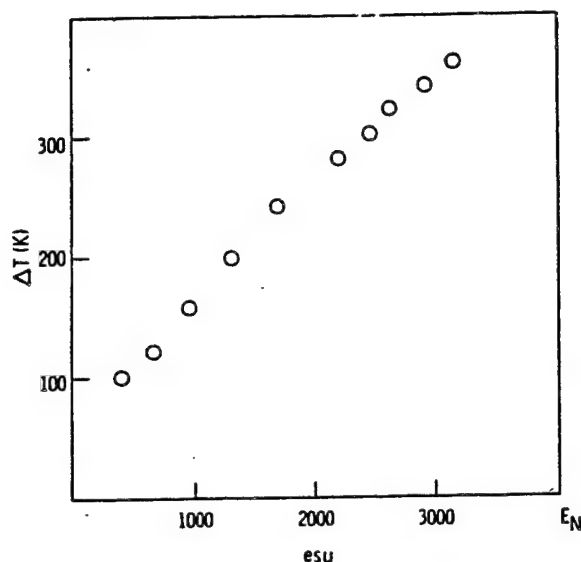


Figure 103. Calculated Graph of $T^* - T_0$ vs. E_N in esu for $T_0 = 400$ K and Temperature Varying From 40 to 300 K.

the highest net electric fields in ferroelectric materials will create large shifts in T^* . The importance of T^* with respect to high- T_c superconductivity is related to charge separation and the ability to build up regions of positive charge, as well as the possible establishment of a polaronic, bipolaronic, or virtual exciton state.

In Figure 104, we plot T^* vs. frequency for $Y_1Ba_2Cu_3O_{7-\delta}$ from the data of Lurtz et al. [235, 236]. We have shown in a previous section of this report that small low-frequency (1–10 Hz) oscillations commence in both $Y_1Ba_2Cu_3O_{7-\delta}$ and in $Bi_2Sr_2Ca_2Cu_3O_{10}$ at the temperature (T_0), at which the resistance vs. temperature data for ceramic materials deviates from linearity. T_0 is above T_c and in the range of T^* and also identifies the temperature that is most strongly enhanced when an RE is substituted for Y in $Y_1Ba_2Cu_3O_{7-\delta}$, this enhancement being directly related to the spin and effective magnetic moment of the paramagnetic RE substitute. We believe that the small oscillations are a consequence of instabilities in the particle or quasi-particle, which is the mediator inducing the Cooper-pairing. The graph in Figure 104 extrapolates to a T^* of about 80–100 K at frequency of 1–10 Hz, favoring our hypothesis regarding the proximity of T^* and T_0 . The reason why the dielectric constant peaks at $T > T_c$ in high- T_c materials is because charge-transfer-established polar

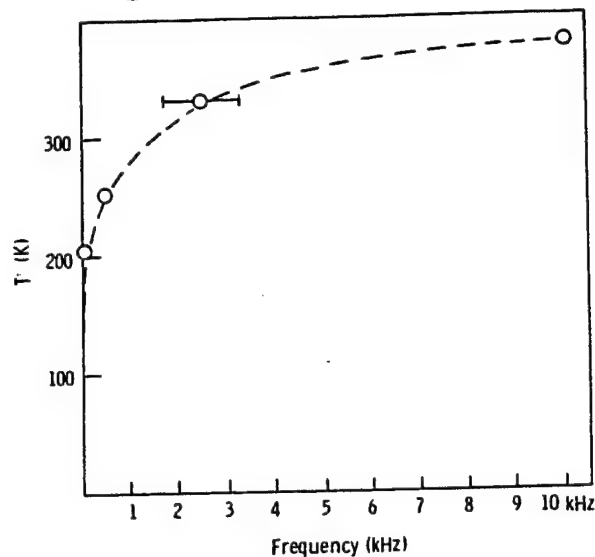


Figure 104. T^* vs. Frequency for $Y_1Ba_2Cu_3O_{7-\delta}$ [235, 236].

states (charge separation) are being favored by the increased lifetime (of holes) fostered by the lowering temperature as T_c is approached. The increased bound and free carrier lifetimes may cause a condition, such that the lifetime is about equal to the dielectric relaxation time, thus causing the polarizability to diverge according to well-established relaxation semiconductor theory.

Another temperature T_e , which may be somewhat key to the ferroelectric related argument is the temperature at which the dielectric loss (ϵ'') peaks. In the present reasoning, this temperature should peak at a value slightly lower than T^* because of competition between Cooper pairing and the binding forces of the mediating particle. In Figure 105, we reproduce the dielectric loss (ϵ'') vs. temperature data of Kurtz, Bhalla, and Cross [235, 236] for $Y_1Ba_2Cu_3O_{7-\delta}$, showing a peak at slightly more than 100 K and an avalanching runaway at about 90 K (which is approximately T_c). The peaking loss is probably a consequence of the bleed-off of charge separation or the breaking down of dipolar moments due to the Cooper-pairing mediating forces (bound holes and virtual excitons) that attract negative charge and make the perfect metal. As temperature is further lowered, the decrease in loss (prior to the runaway of ϵ'' at $\sim T_c$) is likely to be due to re-established dipole moments as competition ends because Cooper pairing becomes nearly complete. Finally, the sharply increasing loss accompanies the transition to the superconductivity state (Cooper-paired supercurrent) and is associated with a condition where the dielectric relaxation time and the diffusion

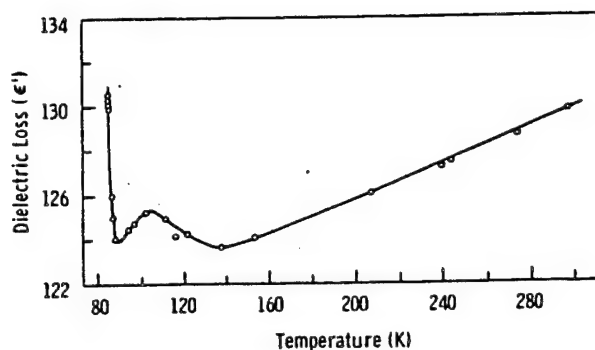


Figure 105. Dielectric Loss ϵ'' vs. Temperature Reproduced From Kurtz, Bhalla, and Cross [235, 236]. Microwave Measurements of ϵ' for the Same Samples. Note that the Small Value of $\tan \delta = \epsilon''/\epsilon' \approx 0.02$ Indicates That Maxwell-Wagner Corrections Due to Intergranular Effects are Minor.

length lifetime become sharply different so the polarization, P , no longer diverges, thus establishing a highly lossy condition. Additionally, the ionization of excitons may contribute to the increase of loss in the final stage of Cooper pairing.

This implies from a materials science standpoint that crystal architectures involving polyhedral building blocks of vastly differing symmetry, thus leading to the highest internal electric fields, will tend to either force Curie temperatures upward, T^* downward, or a combination of both. The approach then implies that materials engineering for higher T_c and new high- T_c superconductors should focus on materials with very high internal electric fields because such fields will bring T^* closer to T_o and T_c and will assist the buildup of charge transfer to establish virtual excitons.

6.8.4.2 The Polarization vs. Temperature Curve. Further consideration of the previous analyses, in conjunction with appropriate constants for δ , β , and γ , allows one to derive a predicted $\log P_s$ vs. T curve (Figure 106) for a tentatively "engineered" high- T_c $\text{La}_{1-x}\text{Sr}_x\text{CuO}_4$ Perovskite-type material. The form of this curve has an appearance similar to that of the experimental dependence of P_s on T shown in the inset [232] to the figure. This direct correlation further suggests a commonality of some kind between the high- T_c materials and the class of ferroelectric materials. This commonality is very difficult to prove because the measurement of strain polarization and the calculation of the polarization curve are both exceedingly difficult to accomplish.

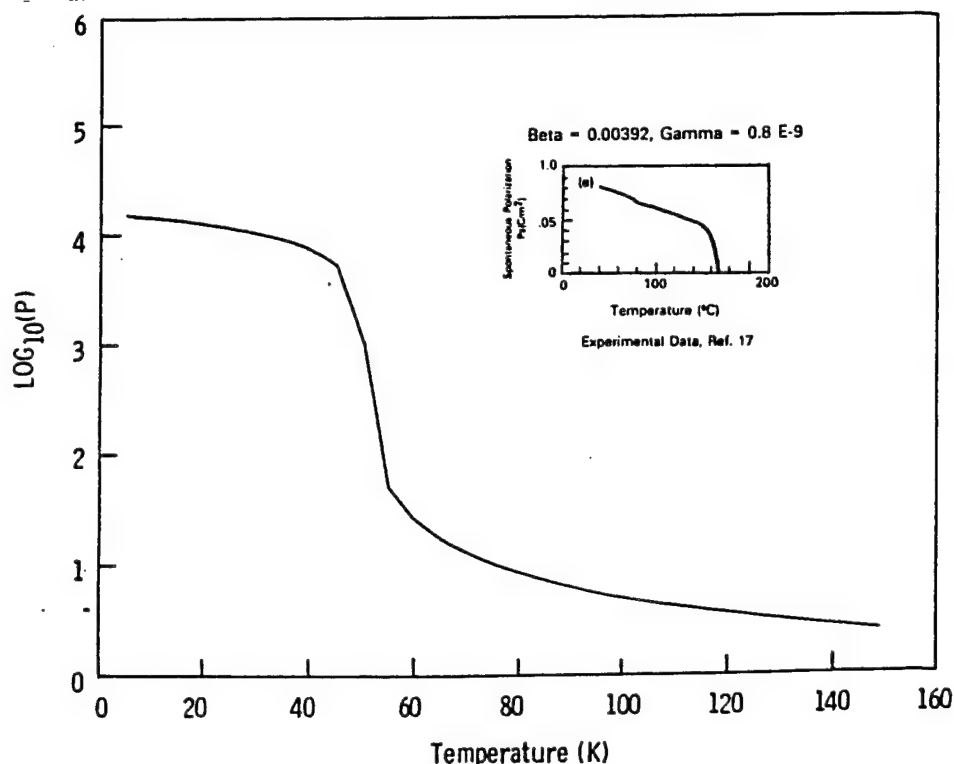


Figure 106. Plot of Log P vs. T for Idealized Ferroelectric High- T_c Superconductor and Comparison With Experimental (Inset) Using $Gd_1Ba_2Cu_3O_{7-\delta}$.

6.8.5 The Internal Electric Perturbation Field Calculation in $Y_1Ba_2Cu_3O_{7-\delta}$.

6.8.5.1 The Computational Model. The computational model that we utilized to calculate the internal electric perturbation field employs a unit cell of point-charge sites, each with a specified charge and a position relative to the cell. This unit cell is replicated to fill a lattice volume by specifying the number of cells in both the negative and positive directions along each of the three principle axes. The coulomb electric field is computed at any field point by summing the contributions from every such charge site. In all cases, the total charge of the replicated unit cell is zero, and its charge distribution is a high-degree multipole. Therefore, as a whole, the coulomb field of the cell drops off rapidly as a function of distance from the cell. This yields the regular background coulombic field and justifies employing a finite-size cell array in the computation to

obtain a field in the central region that accurately represents the field within the interior of a crystal lattice.

The presence of a nonzero perturbation electric field in a solid is ultimately a consequence of the crystal structure and local defects and disorder. In this study, we have treated only the crystal structure itself. Upon scrutiny of this structure of $Y_1Ba_2Cu_3O_{7-\delta}$, it appears clear that the O(4) apical ions, having no mirror plane symmetry within the pyramidal building block, are the fundamental cause of a local perturbation electric field and a field gradient. This is schematically illustrated in Figure 107, where we show that the basic building block structural polyhedra for $Y_1Ba_2Cu_3O_{7-\delta}$ involve the sharing by the O(4) ion of a distorted pyramid (coordinated with a base-centered anion) and a defect (double vacancy) octahedron. The asymmetry in local electrovalent forces at the nonmirrored O(4) could clearly be expected to give rise to a high internal electric field and field gradient.

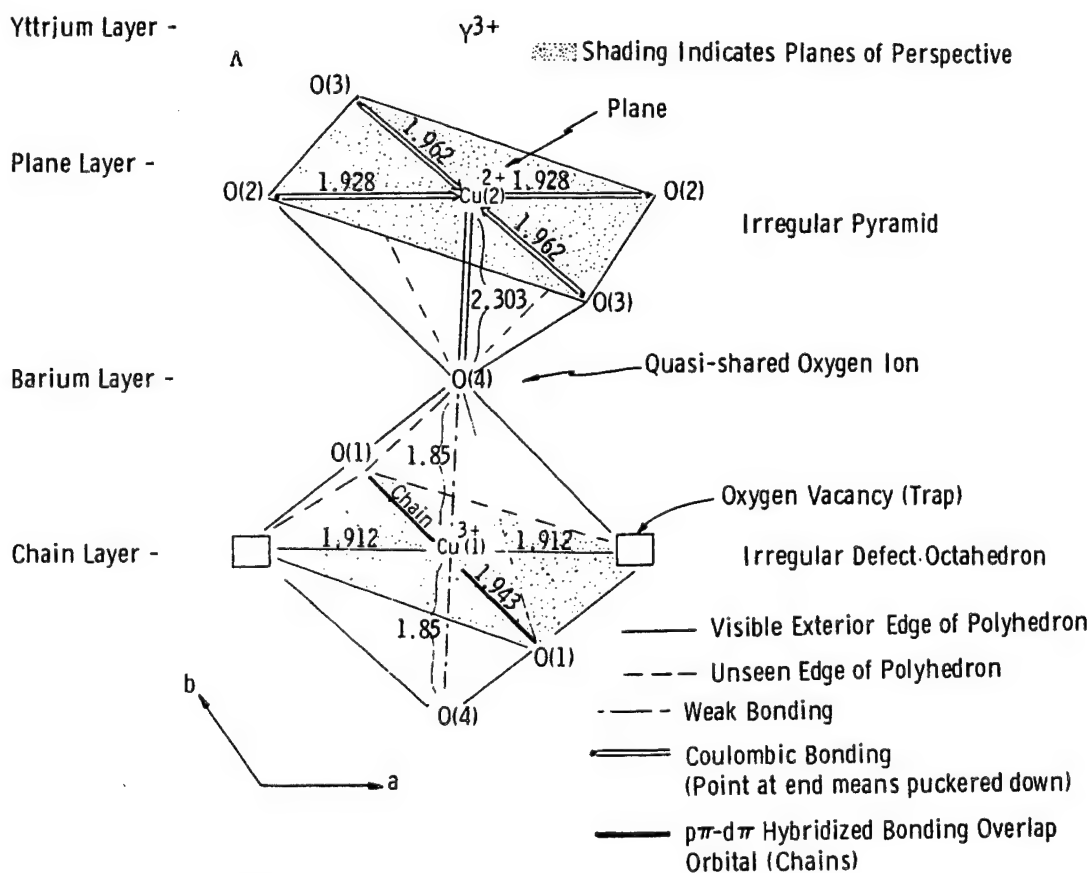


Figure 107. Polyhedral Building Block Units of $Y_1Ba_2Cu_3O_{7-\delta}$.

In order to visualize the field, the program provides the option to compute and display the field vectors at a regular array of field observation points. Alternatively, it can compute and display the field lines that pass through those field points. The entire lattice and field display can be rotated and viewed from any angle and perspective viewing point. This latter property of the code is important in order to determine the very complex internal field and particular planes in which the field paths exist. The model permits the addition of fractional point charges at any position within the lattice, thus enabling the study of such effects as charge transfer among ion sites. It also permits the introduction of predefined orbital-shaped charge distributions to better approximate the quantum-mechanical electron-probability charge-distribution density. The model, as written, does not itself make adjustments to the charge distribution in response to the computed fields; however, such a modification is easily adaptable to the code.

In general, the computed field can be expected to be accurate for regions of the central unit cell that are outside the near-field region of any atom or ion. At or very near an ion site, the portion of the field due to all other charges in the lattice, except the charge at that site, can also be expected to be accurate. This portion of the field has physical significance and is referred to herein as the "perturbation internal electric field" or "perturbation field" (that field to which an ion is exposed or subjected, neglecting its own self-field). The word "perturbation" is used to connote a distorting (relatively short-range) field that would alter the normal symmetric charge distribution of an isolated ion. The computed perturbation field avoids coulomb singularities by ignoring any charge located closer than a certain threshold distance from the field position. Near an ion site, the perturbation field is defined as $\text{total field} = \text{perturbation field} + \text{self-field}$.

The program is written in the "C" language, uses floating-point calculations, and functions on an 8-MHz IBM-AT or look-alike employing EGA graphics. The performance enables each vector to be computed in approximately 1 s and an entire field line in about 10 s. Further improvements of about 4X would be expected if a floating-point chip were employed. For any given charge configuration and field-point array, the field computations are performed once, and then the graphic results are available to be instantly viewed from any vantage point.

Most of the floating-point field computations were accomplished a single time for the regular lattice, and then the results were used to speed up all later field computations. This technique made a distinction between the ions within the center of the unit cell and the ions occupying the remainder of the lattice cells. Within the center cell, the far-field magnitudes, due to all the other cells (except the center unit cell), were computed at a rectangular grid of points and stored for later linear interpolation at any position within the center cell. The near-field, due to only the ions of the center cell, is computed exactly each time. Typically, hundreds of far-field cells are employed, and, since the access to the stored array and the linear interpolation is very fast, the time to compute each field vector was reduced from an initial 75 s to 1 s. This provided a basic change in the nature of the program from noninteractive to highly interactive, and it permitted computer-engineered experimentation and evaluation of many charge situations in an iterative manner. These charge situations simulated or conformed to the effects of charge-transfer excitations that are expected to alter the idealized ionic charges of the point-charge modeled $\text{Y}_1\text{Ba}_2\text{Cu}_3\text{O}_{7-\delta}$ structure.

The program permits the following parameters to be varied:

- number, positions, and fractional charges of ions in the unit cell source coordinates;
- the directions of cell replication;
- the number of cells along each replication axis (both in the positive and negative directions; in the recent case, the Y^{3+} ion was taken as the origin);
- positions and charge magnitudes of other single-charge sites not replicated within the cell array;
- positions and orientations of lobe-shaped fractional charge arrays as an orbital refinement to an electron point-charge model;
- ability to view the entire lattice, a portion thereof, or just the center unit cell;

- specification of a rectangular, cylindrical, or spherical array of positions at which to compute the field;
- display of field vectors at the measurement observation positions or field paths passing through them;
- perspective viewing position (displacement, tilt angle, rotation, and focal distance); and/or
- use of any coordinate system.

6.8.5.2 *Computation of Internal Electric Field of $Y_1Ba_2Cu_3O_{7-\delta}$* The two major objectives in applying the aforementioned computational model to the YBaCuO system are to determine the static electric stresses acting on each ion and to obtain an understanding of how mobile charges within the lattice will be influenced by the total field, especially an inhomogeneous field.

The electric stresses on the ions are associated with the perturbation field, which was discussed previously as being accurate near the ions, even though this model does not explicitly incorporate the continuous quantum-mechanical probability density related to the positional occupancy of the charge. However, the mobile charges are usually moving in the region of the cell far enough from the ion sites where the total computed field is reasonably accurate. Fortunately then, the capabilities of this computational model are adequate to serve our objectives.

A $7 \times 7 \times 5$ array of unit cells was utilized as the lattice, and only the region within the center cell was analyzed in most computations (the exception was the random substitution analysis discussed shortly where a $3 \times 3 \times 1$ cell array in the center of the $7 \times 7 \times 5$ lattice was analyzed). This finite lattice was justified because several field points were computed using the $7 \times 7 \times 5$ array and a larger $9 \times 9 \times 7$ array, and the difference was less than 0.1% throughout the center cell. The field is highly multipolar in nature, and the trend is for it to converge rapidly in value near the center as more cells are added at the outer portion of the lattice.

6.8.5.3 *The Electric Field Using Single-Point Idealized Ionic Sources for Each Ion, According to the Composition ($Y_1^{3+}Cu^{3+}$), ($Ba_2^{2+}Cu_2^{2+}$), $O_{8-\delta}^{2-}$.* Most of the computations were accomplished employing a model of each ion site as a single-point charge having the total charge of the ion concentrated at the center of the ion's nucleus. Thus, we did not normally employ a positive nucleus surrounded by negative electrons—only a single point having a net positive or negative charge equal to an integer multiple of an electron charge. Each field line path was computed by starting at some specified point in the lattice and following the field line that passed through that point. The field line was followed in both directions until it approached within 0.3 Å of an ion site, at which point the path following computation was terminated. The format of the computation algorithm for the electric field vector also changed in character at a radius of 0.3 Å from the ion site. Outside that "arbitrary" radius, the total field was computed; inside, only the perturbation field was computed, neglecting the field contribution from that nearby ion. Also since relatively short-range order effects were being assessed, we neglected screening effects that would be present for values of O_x oxygen stoichiometry, which contributed metallic compounds in their room-temperature state. We believe that screening lengths in this material are of the order of a lattice parameter.

As expected, the electric field was very complex: tangent everywhere on the unit cell boundary, and approximately zero at the eight corner points. The perturbation fields were zero at all yttrium, Cu(1) and O(1) sites. The other sites (see Figure 101), however, had nonzero perturbation fields aligned with either the positive or negative z-direction. The sites in the top portion of a unit cell are described in Table 9; the opposite sites in the cell simply have perturbation fields aligned in the opposite direction. All O(2) sites experienced equal magnitude perturbation fields. The same is true for O(3), O(4), barium, and Cu(2) groups of sites. Although these calculations were performed for $Y_1Ba_2Cu_3O_{7-\delta}$, the approach is valid for all crystals having ionically bonded building block polyhedra, especially ferroelectric-type materials. The strongest perturbation field occurred at the O(4) site, measuring -0.67 (normalized units) in the z-direction. The perturbation fields measured in the base of the pyramid at Cu(2), O(2), and O(3) were strong (0.38, 0.33, and 0.34, respectively) and aligned in the z-direction. The perturbation field computed at barium was -0.32 in the z-direction.

The perturbation field acts to modify the electron distribution of an ion from what would be obtained if the ion were isolated from other charges. The perturbation field measured exactly at the ion sites is not necessarily representative of the entire region within the electron orbitals. For example, the perturbation field 0.2 Å below the O(4) site measured -0.55; at the site, it measured -0.67 and 0.2 Å; and above the site it measured -0.84. Most of this spatial variation can be attributed to the proximity of the O(4) to the Cu(1) ion (with charge +3 employed in the previous computation, but generally $>+2$, on average, in the $\text{Y}_1\text{Ba}_2\text{Cu}_3\text{O}_{7-\delta}$ material). Such perturbation fields would tend to displace the O(4) electron distribution from the nucleus and to distort it significantly in ferroelectric-type crystals (because of their large polar effects).

6.8.5.4 Employing the Refinement of an Electron Distribution. In this calculation, we employed a charge array to approximate the quantum-mechanical probability distribution of the six outer (p) orbitals at one of the O(2) sites, rather than using a single-point charge ion. The objective was to test if the total field would be substantially altered from that of the single-point model in the region beyond a 0.3-Å radius from each site. Each of the electrons was replaced by an array of 26 equal fractional charges in a lobe-like shape. Each lobe was aligned along one of the six principal axes and constructed as follows:

- each charge was positioned on one of six "slices" of appropriate dimensions;
- the slices were equally spaced from each other and aligned perpendicular to the lobe axis;
- each slice contained one charge on the lobe axis;
- the first five slices nearer the nucleus contained four additional charges, one at each of the four corners of a square; and
- the slice specifications are given in Table 10.

Table 10. Specifications of Charge Array Approximation for $Y_1Ba_2Cu_3O_{7-\delta}$

Slice No.	Distance From Nucleus	Total Charge	Diagonal or Square (A)
1	0.22	5/26	0.165
2	0.44	5/26	0.22
3	0.66	5/26	0.33
4	0.88	5/26	0.22
5	1.10	5/26	0.165
6	1.32	1/26	—

The refined charge distribution for the O(2) site had a monopole charge component of -2 (normalized), and higher charge moments of octopole and up. The combined higher moment field (E3) at various positions relative to the nucleus are listed in Table 11 and compared against the monopole field (E0). At a distance of 1.0 A the value of E3 was approximately equal in magnitude to E0 and generally aligned in a different direction. At a distance of 2.0 A, the magnitude of E3 generally dropped off to about 1/8 E0, although in the region just beyond the end of a lobe, E3 strengthened E0 by 40%.

6.8.5.5 Conductivity Within the Base Plane of the Pyramids (CuO_2 Planar Region) in $Y_1Ba_2Cu_3O_{7-\delta}$ It has been observed experimentally that single crystals of $Y_1Ba_2Cu_3O_{7-\delta}$ show far higher conductivity (in the normal state) in the x- and y-directions than in the z-direction. This suggested to us that internal electric fields within the CuO_2 planes of $Y_1Ba_2Cu_3O_{7-\delta}$ may assist in low-voltage hopping conductivity. We tested this hypothesis by computer-calculating the directions of the internal electric field in many planes (as measured using a 6×6 array of observation coordinates), which are perpendicular to the c-axis. Figure 100a shows that the field paths are in the x-y-directions for the test plane, which essentially coincides with the planar region of the unit cell (base plane of the pyramid). All of the other parallel planes that are vertically displaced from the base plane (excepting the planes that contain the chains) show vectors that point sharply in a

Table 11. Field Moments From a Refined Charge Array Distribution at O(2) for $Y_1Ba_2Cu_3O_{7-\delta}$

Position RE Nucleus			Monopole Moment Field			High Moment Field		
x	y	z	EOx	EOy	EOz	E3x	E3y	E3z
0.707	0.707	0.0	-1.40	-1.40	0.0	1.20	1.20	0.0
0.577	0.577	0.577	-1.16	-1.16	-1.16	1.06	1.06	1.06
1.414	1.414	0.0	-0.36	-0.36	0.0	0.03	0.03	0.0
1.155	1.155	1.15	-0.29	-0.29	-0.29	0.04	0.04	0.04
2.0	0.0	0.0	-0.50	0.0	0.0	-0.19	0.0	0.0

disordered fashion out of the x-y-plane, implying that a coherent mobile directional current is not expected in these other planes or perpendicular to them. Interference and scattering effects will more than likely sharply limit currents in any direction other than in the Cu(2) plane or the Cu(l)-O(l)-Cu(l) chain. Most of the electron carriers, which are in the vicinity of the planes, do not become trapped by the residual holes in the planar region because their transit times are too short to allow for recombination. The in-plane electronic conduction is believed to be largely due to $d_{x^2-y^2}$ and P_x and P_y electrons, whereas the in-plane hole conduction seems to be related to p-holes based on O(p)-Cu(d) hopping and direct O(p)-O(p) hopping.

In Figure 108, the observation that the field lines are in the plane of the base plane of the pyramid (the CuO_2 plane) and in the x-y-plane containing the chains is clearly shown. These perspectives illustrate the power of the computer code, allowing the cell to be viewed from any angle and direction so as to assist the observer in determining the direction of the field paths.

6.8.5.6 Charge Substitutions. The lattice of unit cells described so far represents a regular repetitive charge distribution. Since we suspect that some of the electric stresses on the ion sites might cause certain electrons to undergo charge transfer in a ferroelectric-type material, we can analyze the effect on the field when those charge adjustments are engineered and determine whether

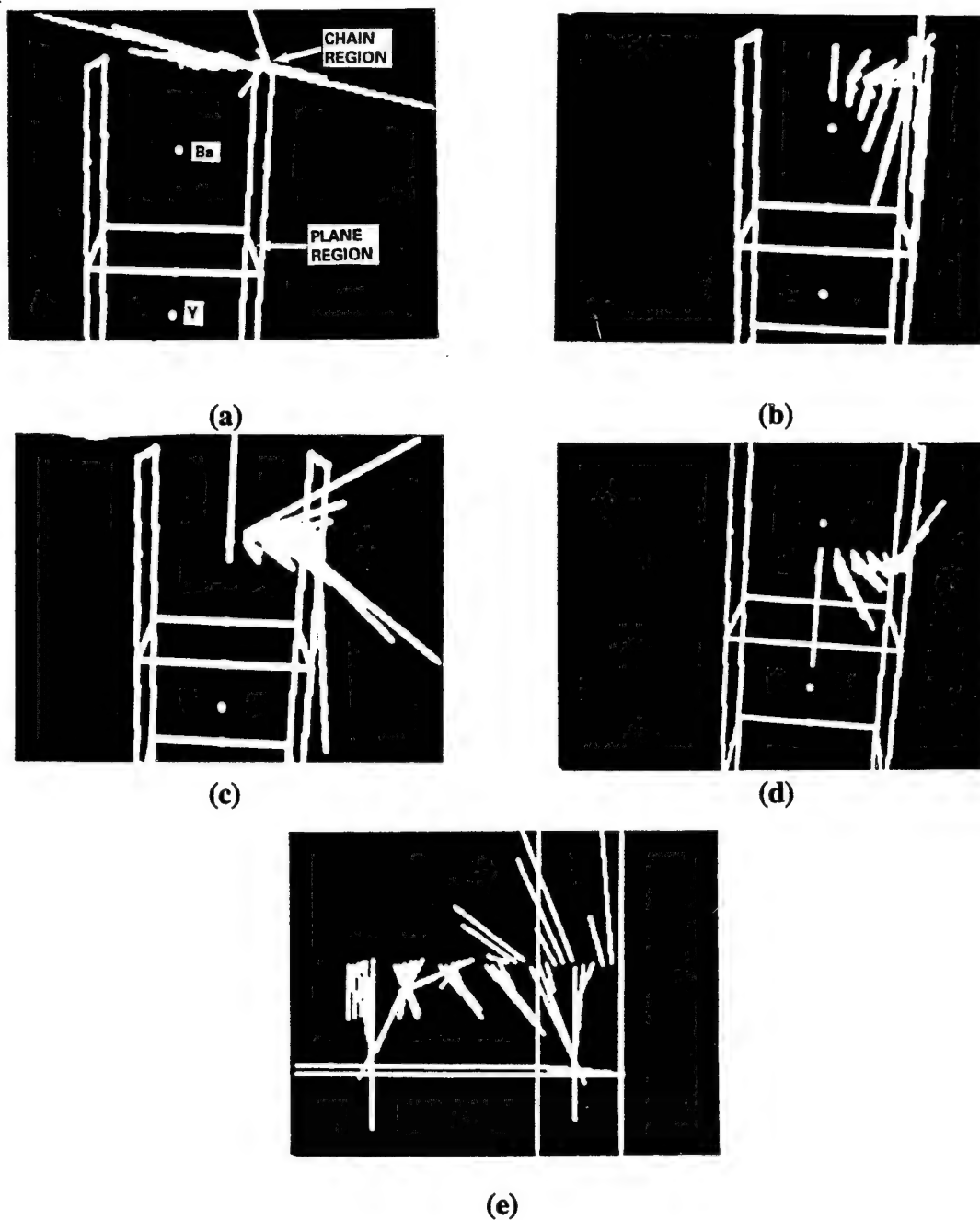


Figure 108. Internal Electric Field Vectors in Probing Planes Perpendicular to c-Axis of Unit Cell of $\text{Y}_1\text{Ba}_2\text{Cu}_3\text{O}_{7-\delta}$ Starting With Plane Containing Upper Cu(1)-O(1)-Cu(1)-O(1) Chain and Ending With Plane Between O(4) and Base Plane of Pyramid.

the adjustments tend to be static, oscillatory, or unstable. Alternatively, molecular orbital hybridization, especially in the chain region involving Cu d_{yz} orbitals, can cause a change in the net ionic charge values relative to the idealized values. Computations were made by using the regular lattice charge distribution and superimposing on it one or several point charges to simulate these

adjustment configurations. One should keep in mind that the field arising from a single-point charge is spherically symmetric, and it is relatively easy to visualize the "adjustment field" resulting from a small number of substitutions. The adjustment field is simply defined through $\text{new field} = \text{original field} + \text{adjustment field}$.

Several integral configurations were computed involving charge substitutions at the Cu(2), O(4), and Cu(1) sites of the center unit cell and the O(4) and Cu(2) sites immediately above the upper chain region and within the next higher cell. All of these sites lie along a single vertical edge in the region containing the chain. The perturbation fields measured at the ion centers only have nonzero components in the z-direction. These are listed in Table 12.

The field values in Table 12 imply that for many resulting electronic configurations arising from charge transfer due to an internal electric field in which $\text{O}(4)^{2-}$ will become $\text{O}(4)^{-1}$ or $\text{O}(4)^0$, the direction and intensity of the perturbation field will drive free carriers toward the nearby chain regions, thus promoting both conductivity and recombination at the chain sites. This then leaves the majority of bound holes in the region of the pyramids. This confirms that a calculation, involving the coupling of candidate electrons for pairing with mediating bound holes must be made employing the holes spatially concentrated in the pyramidal regions of the $\text{Y}_1\text{Ba}_2\text{Cu}_3\text{O}_{7-\delta}$ unit cell. Such holes could possibly even be low-mobility free holes due to the internal electric perturbation field, the longest lifetime bound hole is expected to be associated with the O(4) when it is neutralized to $\text{O}(4)^0$.

The resulting large fields after the charge transfer at the Cu(1) site (due to some of the substitutions) indicate that the neutralization of the O(4) is not stable, and the charge transfer is indeed oscillatory. Typical oscillation frequencies are of the order of 10^{13} – 10^{14} Hz. When the O(4) is involved in a charge transfer with the Cu(1), the individual hole concentration in the pyramidal region is necessarily affected. Therefore, the hole concentration in the individual polyhedral building blocks of the unit cell is time-dependent. Since the charged state of the O(4) is time-dependent, the anisotropies and asymmetries associated with O(4) must also be time-dependent. Because of the very high frequency of the charge-transfer excitation, any measurements of anomalies and

Table 12. Perturbation Fields Under Charge Substitution

Charge Substitutions	Pz at Cu ₂	Pz at O ₄	Pz at Cu ₁
No substitutions	0.38	-0.67	0.0
+1 added at O ₄ = O(4)	0.19	-0.67	0.29
-1 added at Cu ₁ = Cu(1) ⁺²	0.44	-0.38	0.0
+1 added at O ₄ and -1 added at Cu ₁	0.25	-0.38	0.29
+1 added at O ₄ and -1 added at Cu ₂ = Cu(2) ⁺¹	0.19	-0.86	0.23
+2 added at O ₄ = O(4) ^o and -1 added at Cu ₁ = Cu(1) ⁺²	0.06	-0.38	0.58
+2 added at O ₄ and -2 added at Cu ₁ = Cu(1) ⁺¹	0.12	-0.09	0.58
+2 added at O ₄ and -1 added at Cu ₁ and -1 added at Cu ₂	0.06	-0.057	0.53
+1 added at O ₄ and +1 added at O ₄ above and -2 added at Cu ₁ = Cu(1) ⁺	0.28	-0.16	0.0
+2 added at O ₄ and +2 added at O ₄ above and -2 added at Cu ₁ and -1 added at Cu ₂ and -1 added at Cu ₂ above	0.08	-0.40	0.0

asymmetries caused by the excitation, such as changes in polarization and dipole moment (measurements that would assist in delineating a ferroelectric structural characteristic) should require time-of-flight neutron-scattering techniques.

The role of the axial oxygens in high-T_c materials has been recently addressed [236], reporting two different positions for the axial oxygen, which can be explained in terms of Cu-O(4) bond motion in an anharmonic double-well potential. This viewpoint shows the influence of electronic

degrees of freedom entering in the superconducting transition because of coupling between anharmonic phonons and the superconducting order parameter. The viewpoint also gives support to dynamic Jahn-Teller coupling. Additional recent work [237, 238] concentrates on electron-hole asymmetry in terms of a local interaction that breaks electron-hole symmetry. Such a local interaction could be a time-dependent charge transfer.

6.8.5.7 Random Substitutions. Another set of substitutions was performed in order to simulate the conditions arising from the observed fact that high-temperature superconductivity in the $\text{Y}_1\text{Ba}_2\text{Cu}_3\text{O}_{7-\delta}$ structure occurs when the oxygen ion content is slightly below 7 (around $\text{O}_{6.5}$ – $\text{O}_{6.9}$). This represents an irregular pattern of missing negative charge. This situation was simulated by using a random selection process to neutralize or alternatively eliminate 5% of the O(4) ions. Since the O(4) ions contribute 2 of the 7 oxygen ions per unit cell, $5\% \times (2/7)$ yields 0.1 divalent negative charge eliminated out of 7 (or 6.9 oxygen ions remaining per unit cell, on average). We chose to draw charge away from the O(4) sites because, due to the Jahn-Teller distortion and a local asymmetric environment, the O(4) is the most weakly bonded oxygen ion in the pyramids of the cell.

Each randomly selected O(4) ion was computationally eliminated by adding a +2 charge at the ion site, thereby nullifying the total electrical effect of the original -2 charge. In order to maintain local (i.e., over one unit cell) charge neutrality, the addition of the +2 charge requires two electrons to be added nearby in the lattice, so we forced 20% of the Cu(1) ions to take on one electron in an independent random pattern. Thus $20\% \times 1$ Cu(1) ion per unit cell yields 0.2 Cu(1) ions modified per unit cell, and the charge substitutions per unit cell are, on average, $+2.0 \times 0.1$ for O(4) and -1.0×0.2 for Cu(1)—a spatial balance of charge on average. The Cu(1) was selected because it is the likely candidate to gain an electron due to its high idealized charge of +3. In the $\text{O}_{7-\delta}$ stoichiometry, the idealized charge of trivalent positive for Cu(1) can be considered an extrema when charge transfer causes a near-total ionic condition. However, at other instants during the resonance the covalency of the Cu(1)–O(1) bond predominates and the residual ionic charge can be much less than +3. This situation is treated shortly. In the $\text{O}_{7-\delta}$ stoichiometry (or $\text{O}_{6.9}$), for example, charge balance suggests that for K_2MnF_4 structure, 20% of the Cu(1) sites are in a $\text{Cu}^{2+}(\text{d}^9)$ state at electronic equilibrium. This change in state at the Cu(1) site will upset the delicate antiferromagnetism

established at the planar Cu(2) sites and will constitute a spin fluctuation from antiferromagnetism, which itself can be a mediator for high- T_c superconductivity. Because of the spin fluctuations from antiferromagnetism, it becomes very difficult to measure a Neel temperature in the phases of YBCO having a superconducting stoichiometry; however, using a SQUID with very low fields (<150 G), we have found indications, albeit with much fluctuation of data (which may indeed be real rather than systematic), of a T_N at 390 ± 30 K. Then, for these reasons and the observation of the perturbation field at O(4) in Table 9, we chose the Cu(l) charge adjustment to compensate for the oxygen deficiency.

The objective in performing this computation was to determine if there would likely be, by chance, a local clustering of these substitutions that might contribute some large field substantially exceeding the perturbation fields already observed within the unsubstituted lattice. The results are as follows. Field changes of about 0.5 were computed at the nearest-neighboring ion sites within the $3 \times 3 \times 1$ unit cell array in the center of the $7 \times 7 \times 5$ lattice. These compare in magnitude to individual engineered substitutions previously described, which is not unexpected because the substitution mechanism is the same. However, there were no larger or longer range perturbation fields observed that arose from a chance clustering of several neutral O(4) sites or Cu(l) modifications. The percentages of substitutions are small, and there would have to be a very large and fortuitous concentration of neutral O(4) or Cu(l)²⁺ in order to produce much larger fields. This arrangement would not be stable because it would violate neutrality conditions over a large volume.

6.8.5.8 Vector Fields in and Near the Chain Region. It is important to analyze the internal electric fields in the region of the Cu(l)-O(l)-Cu(l) chains because the d-p π bonding in the chains represents a covalency overlap in d_{yz} , which can free other orbitals for conduction. The 3+ valence, which we have ascribed to the Cu(l), refers, as previously mentioned, to the ionic extreme under O²⁻₇ stoichiometry. This extreme ionic state occurs only when the electrons that indeed could be shared are instead in the close environment of O(l). Under that condition of a d^8 state, the electrons in the d_{yz} orbital are nonetheless still suited to participate in covalent-like bonding with the O(l) p_y orbital, and the electron in the d_{z^2} orbital can participate in covalent bonding or conduction toward the pyramidal region in the direction of O(4). When stoichiometry is reduced to O²⁻_{7- δ} the simplest

rearrangement to satisfy the requirement of an oxygen ion deficiency is for some oxygen electrons to transfer to the $\text{Cu}(1)^{3+}$. This is in accord with our viewpoint that Cooper pairing takes place in the region of the pyramidal planes where copper holes remain and oxygen holes are further created. In Figure 109a and b, we show the internal electric field vectors near the $\text{Cu}(1)\text{-O}(1)$ chain, from the perspective of looking down the c -axis for the situations of Figure 109a $\text{Cu}(1)^{3+} - \text{O}(4)$ and Figure 109b after the charge transfer establishing a $\text{Cu}(1)^{2+}$. In both Figures, the internal field is established so as to drive mobile holes toward the $\text{O}(1)$; however, in Figure 109b, the field is somewhat diminished. Free electrons will move in the opposite direction (toward the $\text{Cu}(1)$).

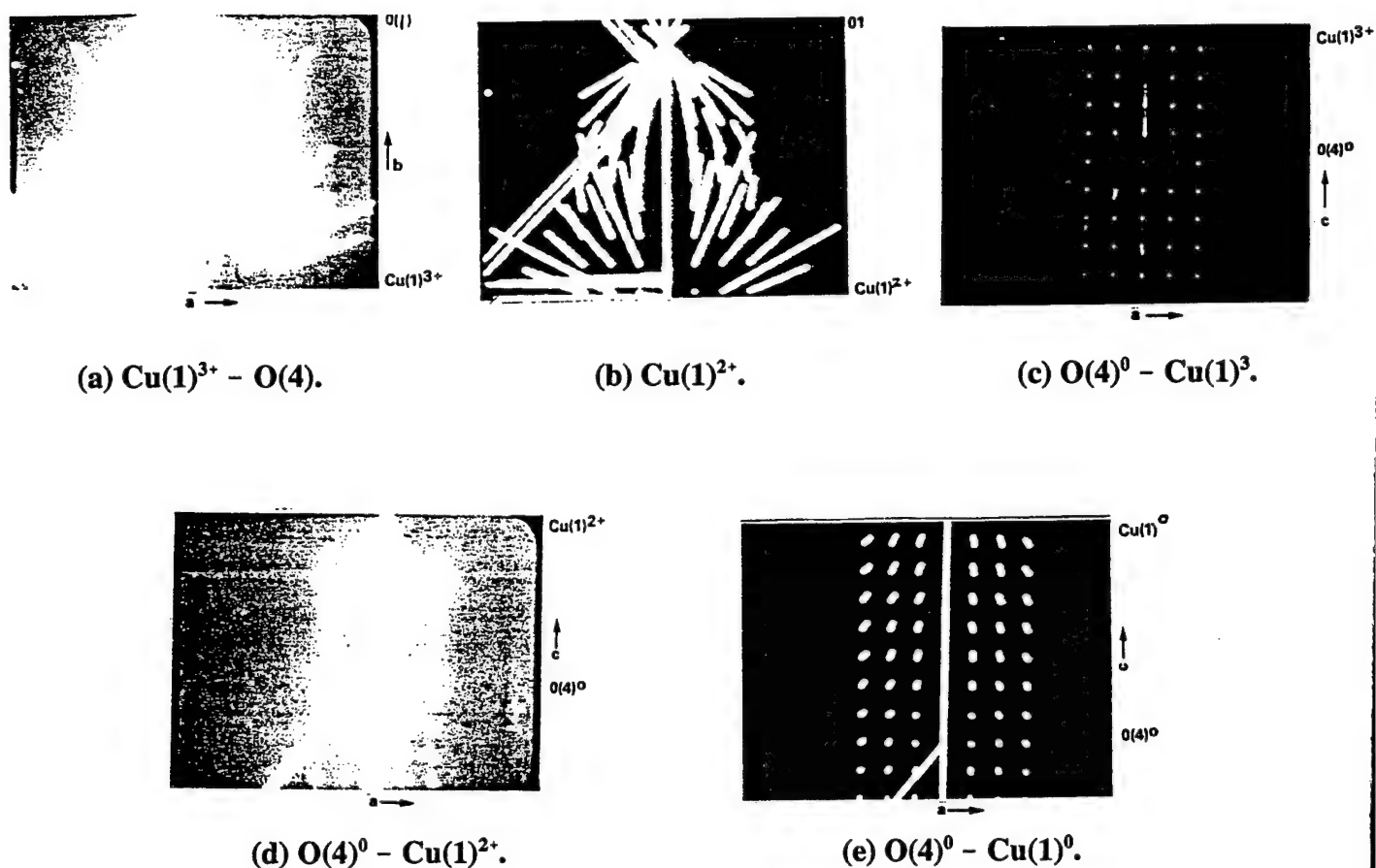


Figure 109. Vector Directions Near Chain Region in $\text{Y}_1\text{Ba}_2\text{Cu}_3\text{O}_{7-\delta}$.

In Figures 109c-e, we show the field vectors from the viewing perspective of the x - z -plane for the conditions of Figure 109c $\text{O}(4)^0 - \text{Cu}(1)^3$, Figure 109d $\text{O}(4)^0 - \text{Cu}(1)^{2+}$, and Figure 109e

$O(4)^0 - Cu(1)^0$. In Figures 109c and d, the field vectors point toward the CuO_2 planes, thereby ensuring holes to be localized in the planar regions. However, in the charge-transfer-neutralized state $O(4)O - Cu(1)^0$, where both are neutralized, the vectors point toward the chain direction (however, with diminished magnitude), thereby driving free electrons toward the CuO_2 planes. This shows the resonant nature of the excitation. No other charge-transfer configuration that we have examined reverses the vector directions. This then indicates the varying physical situation and the resonance phenomena associated with the charge transfer related to $O(4)$.

The study shows that the high internal electric fields are compatible with a spontaneously but marginal ferroelectric material. The term "marginal" is employed to indicate that physical properties fall in the borderline region of ferroelectric behavior, and that only microscopic, not macroscopic, ferroelectricity is present. The internal field gives rise to the charge-transfer excitations, which, in turn, establish poled states associated with at least the $O(4)$, giving rise to the microscopic ferroelectricity.

6.8.5.9 Modifications Due to Molecular Orbital Considerations. Due to partial covalent bonding and molecular orbital hybridization, and considering screening, the effective ionic charge on the copper and oxygens becomes modified to the following values: $Cu(1) = +1.16$; $Cu(2) = +1.6$; $O(2) = -1.98$; $O(3) = -1.94$; $O(4) = -1.54$; $O(1) = -1.85$ [239, 240] (Table 13 herein). The major modification in cationic charge is in the charge of the chain copper. This change from $3+$ under idealized extreme ionicity before charge transfer to $+1.16$ is in part a consequence of overlap between the $Cu d_{yz}$ orbital and the $O p_y$ orbital creating a pi bond. (The $d_{x^2-y^2}$ orbital is associated with a sigma bond). It is also in part due to overlap with $O(4)$ because of charge transferred from the $O(1)$ and $O(4)$ to create the lowered cationic charge on $Cu(1)$ and, in so doing, creating the bound holes on the oxygens for mediating Cooper pairing. The principal reduction in an ionic charge occurs at the $O(4)$ because of the aforementioned charge transfer and partial bonding with the $Cu(1)$.

Substituting the previously modified values into the center unit cell charge conditions and again using the internal local field perturbation code (and specifying the cell from Y^{3+} to the next above Y^{3+} so that the region of interest, namely the $Cu(1) - O(1)$ chain, is almost centered in the unit cell)

Table 13. Internal Perturbation Electric Field Calculated Using Modified Charge Magnitudes of Center Unit Cell in $7 \times 7 \times 5$ Array

Ion	Charge (Modified)	Ez (Modified)	Charge (Original)	Ez (Original)
Y	3+	0	3+	0
Cu ₂	1.6+	+0.45	2+	+0.38
O ₂	1.98-	+0.44	2-	+0.33
O ₃	1.94-	+0.45	2-	+0.34
Ba	2+	-0.07	2+	-0.32
O ₄	1.54-	-0.17	2-	-0.67
Cu ₁	1.16+	0	3+	0
O ₁	1.85-	0	2-	0

results in field intensities shown in Table 13 and compared therein to the idealized unmodified values. Figure 102f gives the vector field paths for the regions in the unit cell that are associated with the modified values of charge and shows only a slight difference when compared to Figure 102a and b for the idealized point-charge situation.

6.8.5.10 Tests for Convergence. A number of checks were performed to make sure that the coulomb field was computed correctly and accurately. The primary method of computing the field for the results discussed herein involved replicating a unit cell of fractional charges throughout a rectangular lattice array. The field measured within the central cell converged to stable values when a $7 \times 7 \times 5$ lattice was used. Additional outer layers of cells contributed total changes of less than 0.01 (3%). Further computational speed improvements were made by precomputing the far-field component at a rectangular grid of positions within the central cell and interpolating that component to the nearby measurement positions that are involved in any later computation. The far field was that portion of the field obtained from all ion sites of the $7 \times 7 \times 5$ lattice external to the central cell, and all later computations involved only measurement positions within the central cell. The near-field component at any measurement position was always computed exactly from the charges on the

boundary and within the central cell. Choosing this boundary to separate far-field source from near-field source and using an interpolation grid spacing of 0.25 Å were found to introduce errors of no more than 0.01 (normalized units) between these interpolated fields and those obtained using the $7 \times 7 \times 5$ lattice without interpolation.

A check was performed to make sure that the results obtained in the central cell by the aforementioned interpolated method agreed with a different and more direct computation that had fewer chances for software error. The check involved simply enumeration of whole ion charges throughout an $80\text{-Å} \times 80\text{-Å} \times 200\text{-Å}$ volume and computing the perturbation coulomb field at each of the different ion sites nearest the volume center. Again, agreements were obtained to within 0.01 (<3%).

Finally, the field was tested to make sure it conformed to the behavior of having 0.0 divergence (except at ion locations) and 0.0 curl. The curl was numerically calculated by evaluating the change of the field between closely spaced positions. For example, $\text{curl}(\mathbf{E}) = (\mathbf{E}_y(x_1) - \mathbf{E}_y(x_0))/(x_1 - x_0) - (\mathbf{E}_x(y_1) - \mathbf{E}_x(y_0))/(y_1 - y_0)$. Using Gauss's Theorem ($\nabla \cdot \mathbf{E} = \text{surface integral } \mathbf{E} \cdot \mathbf{n} da$) the divergence was evaluated by summing over the faces of a small cube surrounding the position of interest and employing field values measured at the center of each of the faces. Both the divergence and curl were numerically computed to be essentially zero throughout the central cell.

6.8.6 Implications of the Internal Field Study Regarding High- T_c Superconductivity and Crystal Chemistry in $\text{Y}_1\text{Ba}_2\text{Cu}_3\text{O}_{7-\delta}$.

6.8.6.1 The Valence of Copper. The observations of high internal perturbation electric fields due to the structure and composition of $\text{Y}_1\text{Ba}_2\text{Cu}_3\text{O}_{7-\delta}$ and the inference of consequent charge-transfer excitations (which will cause a change in the valence state of the principal cation) in what shows characteristics in common with a material that is microscopically marginally ferroelectric indicate that the copper ions will display an average fractional charge of between 2+ and 3+. At equilibrium, the one Cu^{3+} ion at the chain and the two Cu^{2+} ions in the pyramids (per unit cell) suggest that the fractional average charge will be +2.3. Measurements using induced electron

emission (IEE), x-ray absorption fine structure (EXAFS), electron spectroscopy chemical analysis (ESCA), and energy dispersive analysis (EDX), all indicate that the average valence state of the copper ions is 2.33. This is not to say that at any given moment there does not exist Cu^{1+} and Cu^0 at a copper site, but that the neutral and monovalent states arise from the charge-transfer resonance instead of being equilibrium lattice site charges. The mixed-valence condition appears to be true of the principal cations (copper, bismuth, thallium) of all the high- T_c compounds, and, if mixed valency did not exist, then these compounds could be long-range antiferromagnetic in their stoichiometric states. For example, if $\text{Bi}_2\text{Sr}_2\text{Ca}_2\text{Cu}_3\text{O}_{10}$ were characterized by bismuth being constantly in the 3+ state and copper being constantly in the 2+ state, without any change of valence due to charge-transfer excitations, then there would be no departure or deviation from antiferromagnetism at the d^9 Cu sites. However, since this is not the case, and we must consider the alternate states of bismuth and copper, we then should write the chemical formula as $\text{Bi}^{3+}_{(2-x)}\text{Bi}^{1+}_x\text{Sr}^{2+}_2\text{Ca}^{2+}_2\text{Cu}^{2+}_{(3-y-z)}\text{Cu}^{3+}_y\text{Cu}^{1+}_z\text{O}^{2-}_{10}$, where at any ionic steady-state condition $y = 2x + z$ for charge balance. The average valence state of $\text{Cu}^{2.33+}$ in $\text{Y}_1\text{Ba}_2\text{Cu}_3\text{O}_{7-\delta}$ implicitly takes into account the partial covalent bonding in the pyramids and, to a much larger degree, in the chains. This relates to the difference in electronegativity of the multivalence cations and the oxygen. Since all of the coppers are not exactly equivalent electrovalently, and the same is true for the oxygens considering the partial covalent bonding and the molecular orbital hybridization, the relationship between percent ionic character and difference in electronegativity depends upon the precise bond being analyzed. The Cu(2) - O(4) bond is the most sensitive bond in the pyramidal building block and is most vulnerable to effects that cause anomalies and deviations such as polarizability phenomena. Thus, this bond is the likely candidate to be at the root of any linking to ferroelectric behavior. However, since T_c seems to scale somewhat with the metal-metal distance, then, since the total polarization of the unit cell is zero under ideal conditions without considering defects, the macroscopic clear-cut ferroelectric character is necessarily missing from $\text{Y}_1\text{Ba}_2\text{Cu}_3\text{O}_{7-\delta}$. However, within the subunits of the cell or the polyhedral building blocks, or when taking into account microdefects, the high- T_c material reflects a microscopic character of ferroelectricity. For this reason, we refer to the archetype materials-classifying property of high- T_c materials as marginal relaxor ferroelectrics.

6.8.6.2 *The Polyhedral Building Blocks.* The differing building blocks plus the asymmetry in the CuO_5 pyramid, coupled with the mixed valency of copper, seem to indicate that at least two separate differing-symmetry polyhedral building blocks (acting in concert) are necessary to effectuate high- T_c superconductivity. In the local region of interface between polyhedral building blocks of differing symmetry, the internal perturbation electric field can be expected to be very high. In $\text{Y}_1\text{Ba}_2\text{Cu}_3\text{O}_{7-\delta}$, the chains and the pyramids, acting in a joint manner, play essential roles in the establishment of the high internal field. In addition, the chain region supplies conduction electrons and also acts as a recombination center. The pyramidal region supplies the holes or virtual excitons that act as the mediators to cause coupling with conduction electrons and give rise to Cooper pairing. A charge-transfer excitation that alters the chain copper $\text{Cu}(1)^{2+}$ causes, under idealized conditions, a deviation or fluctuation from the antiferromagnetism in the $\text{Cu}(2)^{2+}$ planes. This can establish a further spin-coupling mechanism through unpaired spins at the chain sites in addition to the coupling mechanism furnished by the holes or virtual excitons. Due to the absence of mirror plane symmetry of the apical O(4) and the puckering of the planar oxygens (O(2) and O(3)), the pyramid becomes vulnerable to display structural characteristics in common with ferroelectric materials, such as microscopically oriented polarizations, due to the high internal local perturbation electric field.

After completing the computer code for the internal electric field, it came to our attention that an independent study [241] had endeavored to calculate the electric field at the i th site, due to an electronic dipole p_j of the j th site (or ion). In Lee and Sharma [241], the authors cite the absence of inversion symmetry at the oxygen sites and the high polarizability of oxygen, in conjunction with the internal field produced by the ionic charges (monopoles), as being responsible for the creation of the superimposed dipole field, which has a collective oscillation frequency of about 1,014 Hz. The work also cites the high electronic polarizability of the oxygens as an indicator that the valence electron clouds of the appropriate ions can easily adjust to total thermodynamic conditions by undergoing deformation. This adjustment effect is a conformation to local symmetry in an effort to minimize the energy. Lee and Sharma also suggest that the excitation of the crystal-field-generated self-sustained collective oscillations mediates the electron-electron or hole-hole pairing mechanism. This viewpoint is almost equivalent to our coulombic-induced spacial perturbation of positive charge shown in Figures 94–96. This dipole excitation, as well as the virtual exciton due to charge-transfer

excitations, and, additionally, the polaronic model, all dwell on a large internal local electric perturbation field. The manner in which the exact structure of the IR absorption peaks (at 0.18 and 1.3 eV), which were cited much earlier in this report, indeed relates to the mediators of the underlying mechanism (and their interaction with the lattice) is not yet established. However, the virtual-exciton mechanism approach can describe this relationship more straightforwardly than alternate models.

7. The Empirical Scaling of Low- T_c and High- T_c Materials With Basic Parameters.

7.1 Low- T_c Scaling. Since conventional low- T_c superconductors are known to be governed by the strong-coupled electron-phonon mechanism and, since we believe that such coupling cannot fully explain the properties and mechanism of high- T_c superconductors, it is thus worthwhile to search for a scaling parameter related to the vibration of atoms and to low- T_c that clearly and definitely does not scale in a similar sense for high- T_c materials.

In Figure 2, we plotted T_c vs. physical density (ρ) for conventional low- T_c superconductors. These show a peaking T_c at densities of 6–9 gm/cm³ for materials that have at room temperature positive magnetic susceptibility, and at about 11–14 gm/cm³ for materials with negative magnetic susceptibility at room temperature (circled in Figure 2). In the inset to the figure, the plot of T_c vs. atomic weight is given, also indicating two approximate peaks. The peaking of T_c with density can be understood in terms of the dependency of the frequency term (in the Debye temperature relationship) with density. This can be shown in the following original analysis.

We can write the Debye temperature as

$$\Theta = [(h/2\pi)\omega_m/k] = [(h/2\pi)v_s/k] (6N\pi^2/V)^{1/3}, \quad (39)$$

where N = number of atoms, V = volume, $k = 2\pi/2\lambda$, ω_m = maximum frequency, and v_o = phase velocity. Then $\omega_m = v_o (6N\pi^2/V)^{1/3}$. We then let $X = N/V$, allowing us to write $(6\pi^2)^{1/3}(N/V)^{1/3} = \omega_m/v_o$. We let $A = (6\pi^2)^{1/3}$; we can then write the following expression for ω :

$$\omega = Av_o (\rho)^{1/3}(m)^{1/3}, \quad (40)$$

where $\rho = Nm/V$, and m = summation of the masses of each atom. We assume that ω is not a function of m , and then differentiate the equation (40) for ω with respect to ρ which yields

$$d\omega/d\rho = B[(v_o(1/3)\rho^{-2/3} + \rho^{1/3}dv_o/d\rho)], \quad (41)$$

where $B = A/m^{1/3}$.

To ascertain the conditions under which T_c is a maximum for a given density, we set equation (41) equal to zero and solve for ρ , which yields

$$\rho = [v_o/\{3(|dv_o/d\rho|)\}]. \quad (42)$$

The value of $dv_o/d\rho$ is taken from data on the velocity of long wave sound as a function of density for known low- T_c materials Ti, Nb, Zn, Sn, and Pb. From these data, we can approximate $dv_o/d\rho = 6.7 \times 10^4$ in units of cm/s per gm/cm⁻³. This then explains why for low- T_c phonon-mediated superconductors the value of T_c shows a peak as a function of density. The plotting of T_c for low- T_c Al5 materials (such as Nb₃X or V₃X) gives a generally decreasing trend with atomic weight. This is shown in Figures 110 and 111.

The critical magnetic field above which magnetic flux can no longer be excluded from the interior of a superconductor is given by $H_c = H_o[1 - (T/T_c)^2]$. In Figure 112, we show H_o vs. the number of missing electrons that would fill the partially filled subshells for the superconducting elements. The exceptions that do not fit on the curve of Figure 112 (namely, Ti, Th, Zr, and Pa, which are not plotted) have a d subshell in their outer shell configuration, which presumably adds

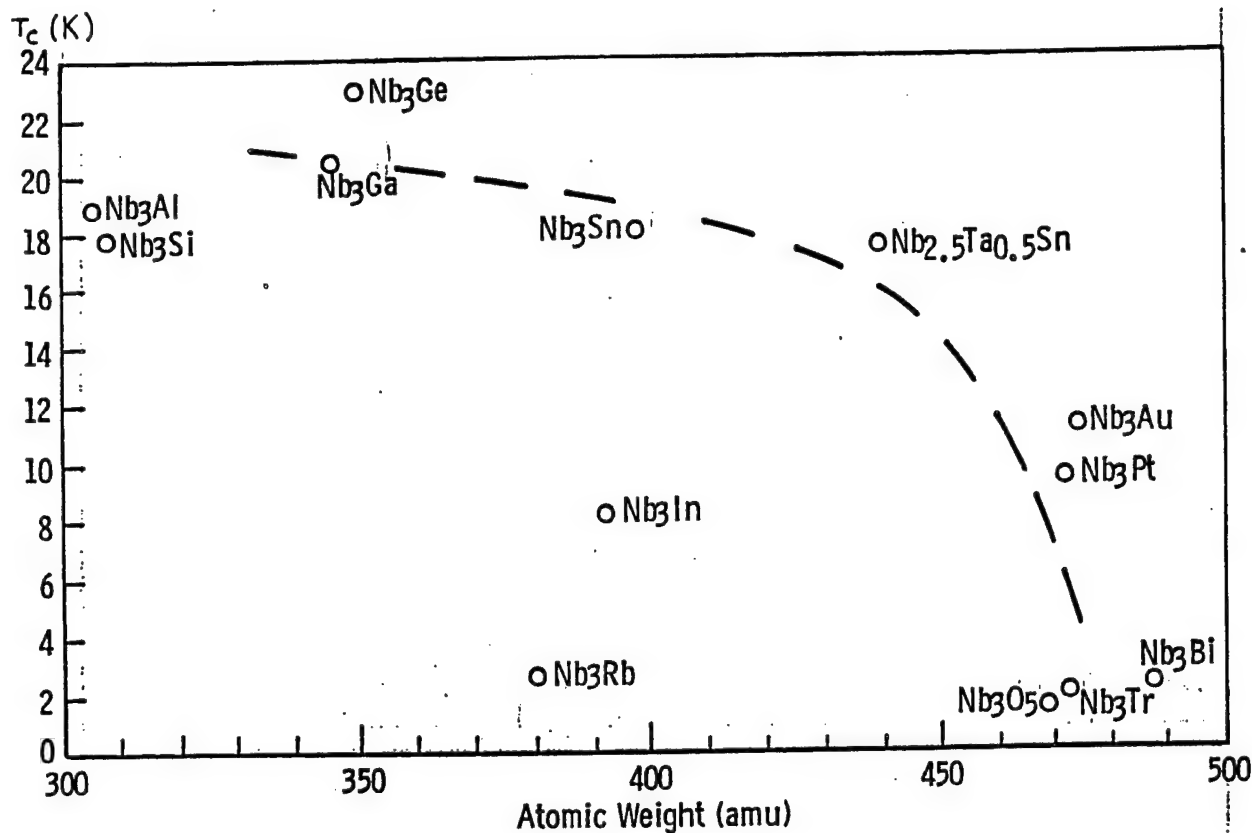


Figure 110. T_c (K) vs. Atomic Weight of Constituents in Nb₃ "A" Structure.

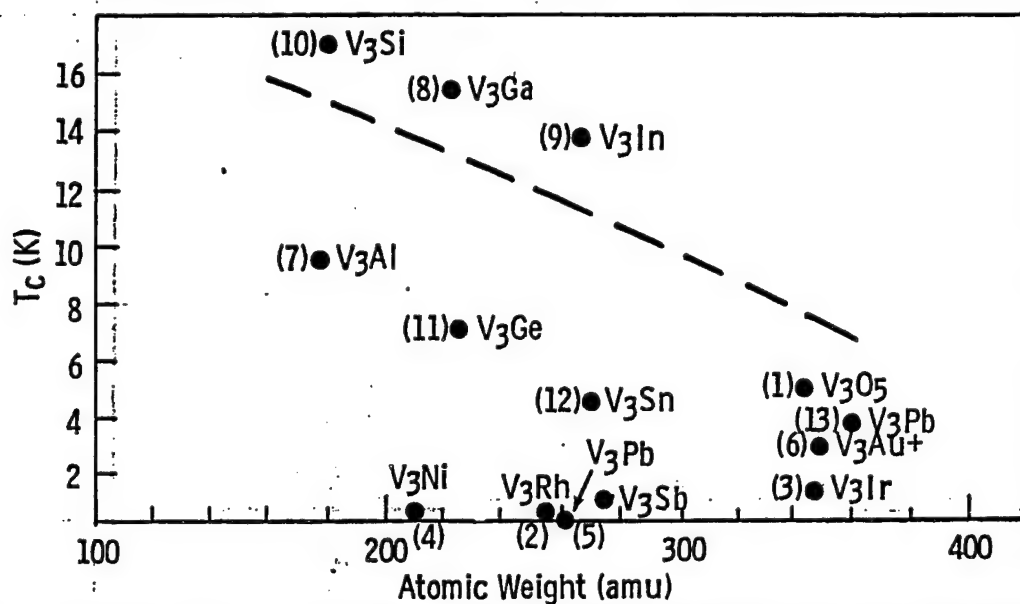


Figure 111. T_c (K) vs. Atomic Weight of Total Constituents in V₃ "B" Structure.

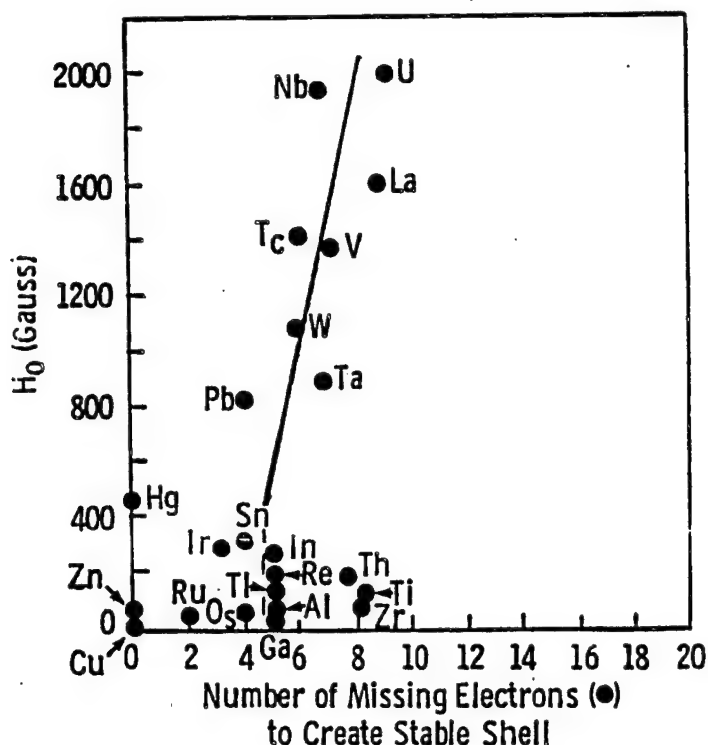


Figure 112. H_0 vs. Number of Missing Electrons to Form Stable Shell in Low- T_c Elemental Superconductor.

another unique factor. The other exception, Hg, has vastly differing electronic properties than the other metals. The fit in Figure 112 for low- T_c materials suggests searching for a related scaling in high- T_c materials because the latter are also known to have missing electrons that leave in their wake bound and free holes.

7.2 High- T_c Scaling. A rather clear-cut general increase of T_c with molecular weight is shown for all of the known high- T_c superconducting oxides except for $\text{Bi}_2\text{Sr}_2\text{Cu}_1\text{O}_6$ and possibly $\text{Ba}(\text{PbBi})\text{O}_3$. (These two latter materials, although being oxides, may actually be essentially phonon-induced superconductors rather than high- T_c materials.) This mass or weight dependence given in Figure 113 shows no peaked behavior and appears very different from that in low- T_c materials given in Figure 2. This suggests a different role of the mass parameter in the two types of superconductors. In the high- T_c materials, the mass dependence seems related to the added complexity of the two (or three) different types of polyhedral building blocks and the more extensive layering in substances having a greater number of ions per unit cell.

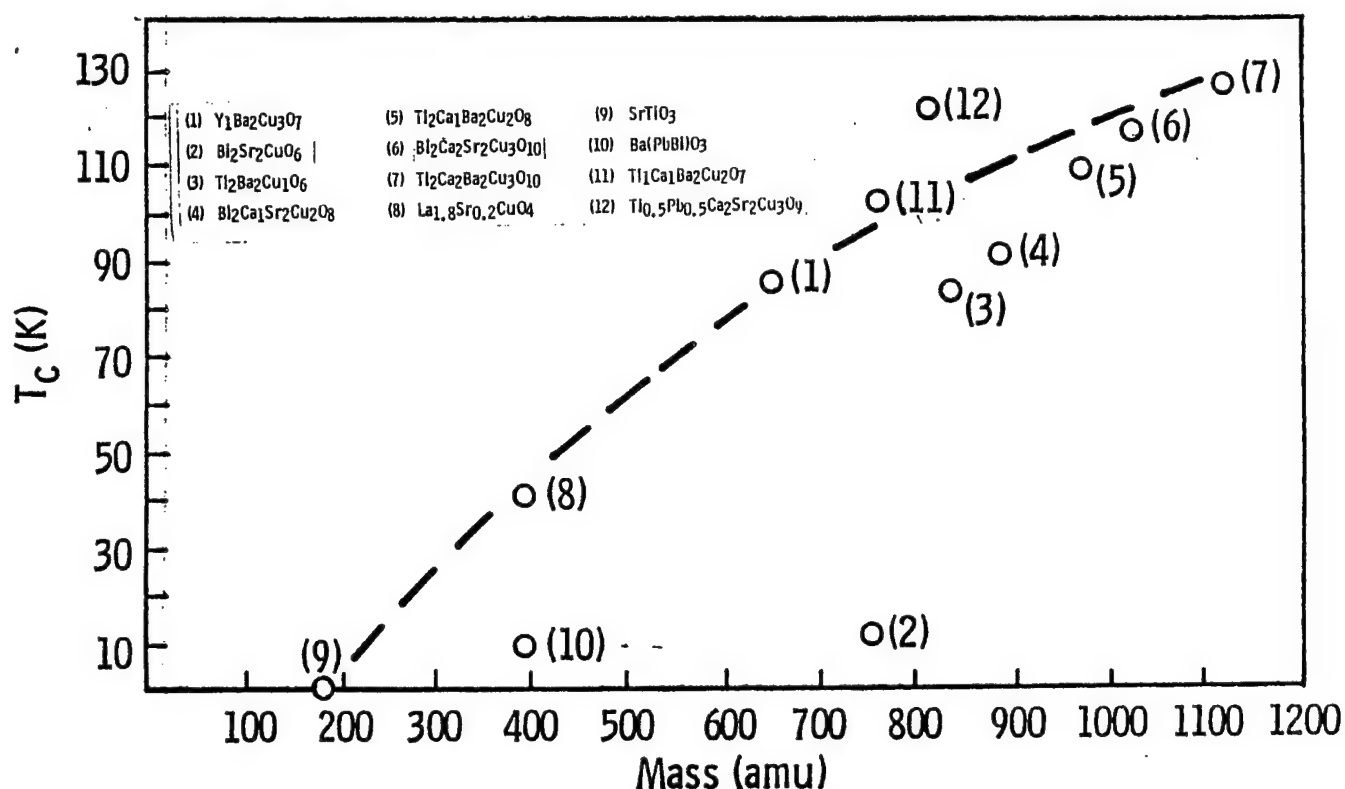


Figure 113. T_c for High- T_c Materials vs. Mass of Formula Unit.

In Figure 114, we show attempts at scaling T_c in high- T_c materials with the number of multivalence cations, as well as with the number of single-valence cations. This figure indicates that the number of multivalence cations per unit cell in high- T_c materials scales better with T_c than does the number of single-valence cations; however, the latter does not reflect a complete absence of scaling. This observation is in harmony with our position that the multivalence cations govern the charge-transfer excitations, which give rise to the bound holes that are the mediators for Cooper pairing, and the single-valence cations are the spacer ions, which are necessary to maintain proper separation between the planes in which the holes are concentrated.

In Figure 115, we plot T_c vs. the total number of bound holes ($P[b]$) per unit cell, which are associated with the charge-transfer excitation that causes the neutralization of the multivalence cations. This charge-transfer excitation can best be described by invoking the notion of the virtual exciton, which refers to the bound hole on the oxygen and the before-recombination state of an electron that transfers from the oxygen to the copper. While in transit from the oxygen to the copper,

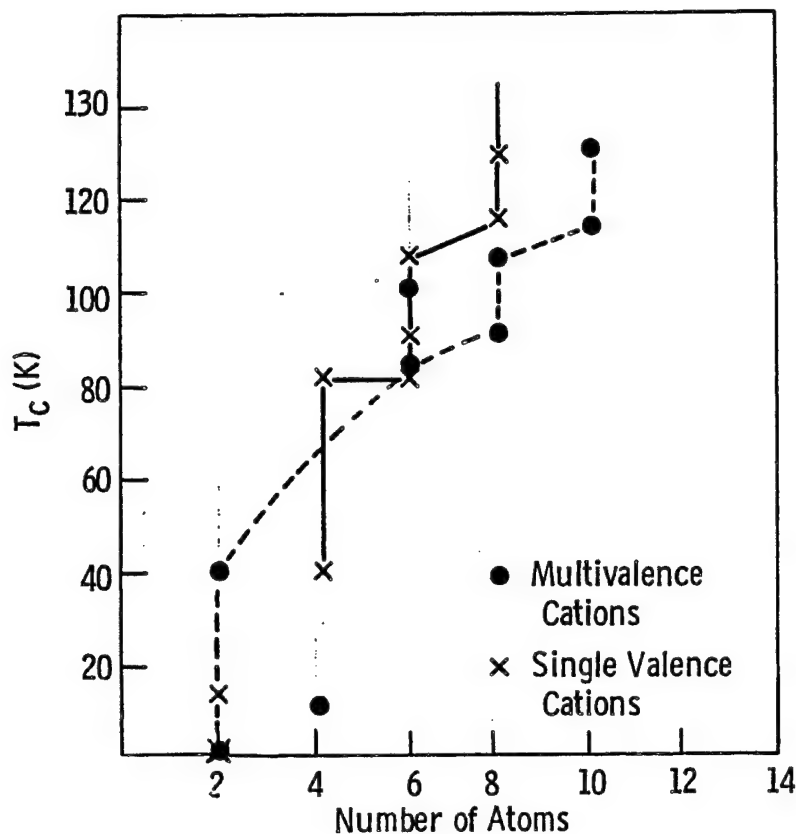


Figure 114. T_c for High- T_c Materials vs. Number of Multi- or Single-Valence Ions.

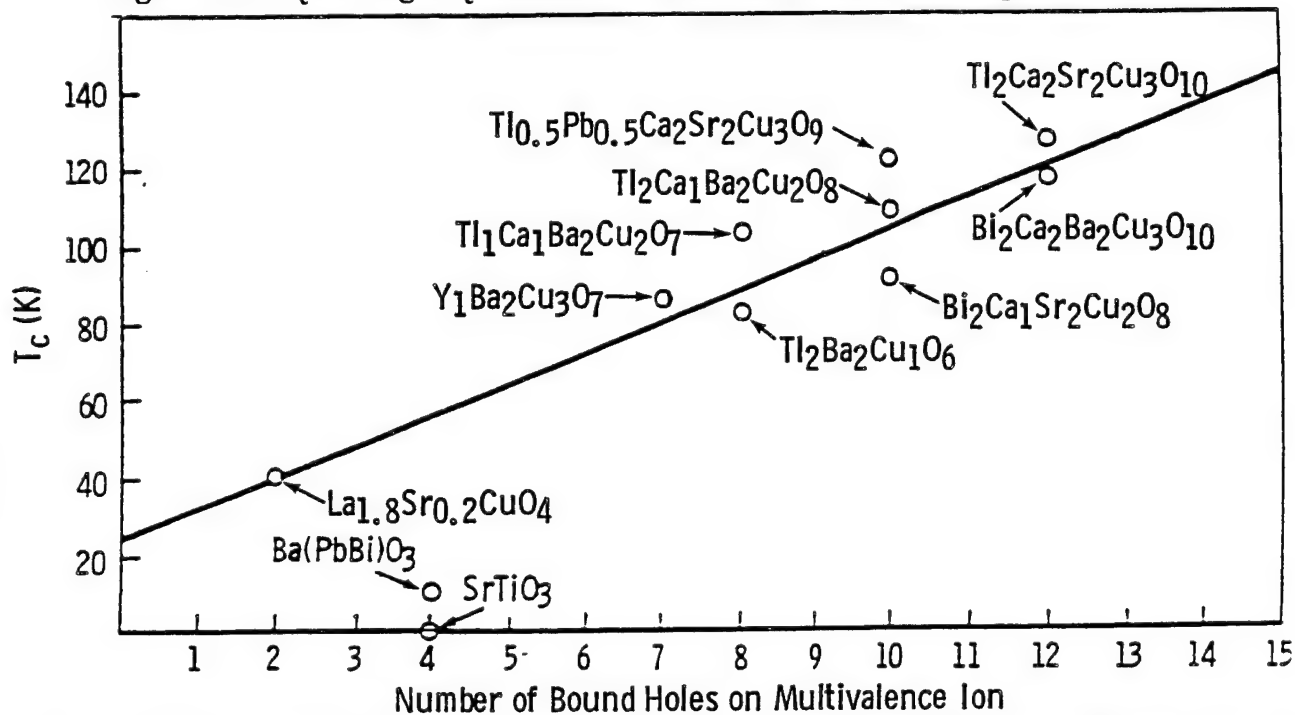


Figure 115. Transition Temperature for High- T_c Materials vs. Number of Holes, Due to Internal Field-Induced Neutralization of Multivalence Metal Atom. (These Holes can be Considered Constituents of Virtual Excitons.)

this electron, and its hole localized to the oxygen, form an excitonic system. Because the lifetime of the system is so short ($\sim 10^{-13}$ s) the system is referred to as a virtual exciton, and, as such, is not required to conform to the conservation of energy law. This relaxation of the conservation law arises from inferences associated with the Heisenberg Uncertainty Principle involving $\Delta E \Delta \tau \leq h/2\pi$.

The number of bound holes associated with a charge-transfer excitation is defined as the number of resulting holes on the oxygens when a multivalence cation is transiently ($3 \times 10^{13}/s$) neutralized by the excitation. Thus, for $Y_1Ba_2Cu_3O_{7-\delta}$, which for charge-transfer neutralization is written in idealized ionic form as $Y^{3+}_1Cu^{3+}_1Ba^{2+}_2Cu^{2+}_2O^{2-}_{7-\delta}$, we derive (from the principles developed in the charge-transfer analysis) the number of bound holes as follows. The charge-transfer $Cu^{3+} + O^{2-} + O^{2-}$ yields $Cu^0 + O^0$, which produces three bound holes on oxygens. Since there are two Cu^{2+} and only one Cu^{3+} per unit cell, we then sum $2 \times 2 + 3 = 7$ bound holes per unit cell. The apical oxygen O(4) in the CuO_5 pyramidal building block is believed to be the optimal candidate ion as the charge-transfer agent.

By this empirical method of calculating $P(b)$, there is found to be a linear correlation for the high- T_c superconductors in T_c vs. $P(b)$ (as shown in Figure 115). The correlation is described by the least-square best fit equation $T_c = 8P(b) + 27$. For $P(b) = 0$, characteristic of low- T_c free-metal superconductors, the fit in Figure 115 gives $T_c \approx 27$ K, which is approximately the same value as that for Nb_3Ge (which has the highest value of T_c for the low- T_c superconductors).

On the other hand, a theoretical superconducting high- T_c lattice involving the highest valence states of the principal multivalent cations, such as Bi^{5+} and Sb^{5+} , and having a 2223X form could achieve a maximum of about 25 bound holes or virtual excitons/unit cell, which, according to Figure 115, would lead to a T_c of about 225 K (if indeed linear extrapolation were justified). According to the early Russian papers [35, 37] describing the feasibility of high- T_c superconductivity, the value of 225 K is the maximum value for T_c that can be associated with an excitonic mechanism for Cooper-pairing.

Since SrTiO_3 , Ba(PbBi)O_3 , and $\text{Bi}_2\text{Sr}_2\text{Cu}_1\text{O}_6$ do not fit the straight line representation in Figure 115, then it is possible that, although these materials are indeed oxide superconductors, nonetheless, the mechanism that governs their superconductivity may be based on electron-phonon coupling rather than virtual excitons.

The compound $\text{Y}_5\text{Ba}_6\text{Cu}_{11}\text{O}_y$ had been reported (in a time frame near the middle of our study) to show a T_c of 235–265 K [242] when synthesized and measured under high-pressure oxygen. The phase was believed to be filamentary; hence, large enough yields to perform a Meissner Exclusion measurement were not produced. However, for charge balance with the 5-6-11-y stoichiometry, the value of $P(b)$ is 25–27 bound holes per unit cell (arising from virtual excitons). This range of $P(b)$ is associated according to Figure 105 with a T_c in the range of 235–265 K as previously reported. This correlation then strongly supports our position that the bound hole constituent of the virtual exciton (or in a broader sense the virtual exciton itself) is the mediator that creates Cooper pairing in high- T_c materials.

8. Conclusions and Interpretations Regarding Materials Science and Mechanism of High- T_c Superconductivity.

8.1 The Materials Science and Materials Engineering. We have determined experimentally that the class of high- T_c superconducting oxides requires a principal metallic constituent ion that possesses the property of multivalence (can exist in ionic and covalent compounds in more than a single-valence state), such as copper, which can assume commonly either +1 or +2 charge (valence) and under certain conditions can enter into compound in a +3 state. The requirement for multivalency is fundamental to the phenomenon that governs high- T_c superconductivity because it promotes charge-transfer excitations that are driven by the high internal local electric perturbation field associated with the high- T_c class of materials. However, the multivalency criteria is actually coupled with a second and limiting criteria, namely the requirement that the major constituent atom, which is multivalent when in an ionic state, is indeed diamagnetic when in its atomic or metallic state. These latter criteria then sharply reduce the number of cations or metal atoms that are bonafide

candidates for the principal constituents of high- T_c superconductors. The resulting elements that then fit into these two criteria are Cu, Tl, Bi, Pb, Sb, Ga, As, Be, B, Cd, Ge, Au, Hg, Ag, P, Sn, and Zn. However, a further crystal stereochemical criteria must be considered, and that is the proper size of the ion such that the radius ratio with oxygen (-2 valence) will fulfill the requirements for five- or six-fold coordination (in order that the appropriate polyhedral building block can be formed, which will lead to a high inhomogeneous internal local electric field). Hence, the charge density of the ion becomes an important criteria relative to a specific lattice site of occupancy. Additionally, the polarizing ability of the cation relative to the anion plays a role in creating the appropriate internal local electric field or internal polarization. When all of these criteria are carefully considered, the only principal cations that satisfy the size, charge, polarizability, and magnetic state required for the constituents of high- T_c superconductors are copper, thallium, and bismuth. (It should be noted that Cu^+ , Tl^{3+} , and Bi^{3+} all have approximately the same size.) Other constituents that fit the multivalence and diamagnetic criteria, but are borderline regarding size, charge density, and polarizability can serve as minor low-concentration cations that still participate in the essential physics of the mechanism that creates the high- T_c state. Examples are Ga^{3+} and Sb^{5+} , which can only be allowed to be present in low concentrations ($<1\%$). If instead these secondary electronically active cations are introduced in larger concentrations, the material no longer is superconducting above liquid nitrogen conditions. In some cases, low-concentration of multivalence cations such as the vanadium ion may possibly participate in charge-transfer excitations because of their multivalency, but cannot contribute to the perfect diamagnetism because their zero-valence state is not diamagnetic. An ion that appears ideal, if indeed it can be materials engineered into active sites in the superconducting lattice, is Bi^{5+} . It is likely that such a substitution will have to be accomplished at high pressure.

With regard to processing, we believe that the best technique to achieve the highest physical densities and the highest values of J_c in bulk ceramic materials is the method of rapid solidification from the melt. This approach requires sophisticated equipment, but shows great promise for homogeneous, single-phase, nearly theoretical density and elevated J_c . Furthermore, processing that involves high-pressure oxygen (~ 70 atm) in the synthesis steps, as well as in the annealing, shows strong potential to elevate T_c because of its tendency to strip electrons off of the multivalence cation

and, in so doing, causing a higher virtual exciton concentration. What is needed in this regard is continued research to stabilize the high-pressure effects such that they do not reverse at ambient conditions.

8.2 The Mechanism of High- T_c Superconductivity. The internal field local perturbation analysis using both point-charge and quantum-mechanical topologies proved the existence of a very high internal field at the copper and oxygen sites, especially at the O(4), where it is most intense and opposite in direction. This internal field, which is a physical consequence of the structures of high- T_c materials due to the differing symmetry of their polyhedral building block species, creates an electrical stress on the material that nature tends to relieve by forcing charge-transfer excitations. The charge transfer involves electrons from the oxygens to the multivalence cations such as Cu. This excitation can be viewed dynamically as a virtual exciton. The charge transfer results in the establishment of holes on the oxygens. These holes are thus the results of a charge transfer to the multivalence cation, which itself occurs at a very high frequency of the order 3×10^{13} Hz. Therefore, the holes have a finite lifetime. However, during this lifetime, the existence of the holes acts as a local region of positive charge that was not present prior to the charge transfer from the oxygens to the multivalence cations. Free electrons that are located in some neighborhood of the region of newly formed (or enhanced) positive charge tend to act such as to fill these positive-charge regions with negative charge in order to create neutrality. In this sense, the regions of enhanced positive charge in position space are unstable. These unstable holes can be conceptualized as resonating because the swarming in of negative charge causes electrons to be stripped of the metallic ions (especially the multivalence ions). This is the opposite of the process that neutralized the oxygens and formed the holes in the first place and is a collective effect. The transient establishment of holes on the oxygens or alternatively on the multivalence cations (also a collective effect), or statistically associated with both, is perturbed by conduction electrons. This perturbation causes a change in charge-distribution density, which then propagates through the lattice. Other conduction electrons are subjected to, or perturbed by, the field of this propagating redistribution of charge density. This effect, from a coulombic standpoint, causes net attraction between the perturbing and the perturbed conduction electrons under conditions when the repulsive force between the two conduction electrons is overcome by the attractive force between the electrons and the bound perturbed holes.

The initial perturbation in the previous description is the action that a conduction electron performs on a transiently established hole. This action can be interpreted coulombically as the doing of electrodynamic work on the hole so that its spatial position is altered, the alteration being an attraction of the bound hole to the conduction electron by about 0.1 Å. The new spatial distribution of charge then propagates and is experienced by a second conduction electron. If the result becomes a net attraction of the two conduction electrons, then one of the criteria of Cooper pairing is established. Alternatively, the perturbation action can be viewed quantum-mechanically as an excitation of the bound hole (associated with the virtual exciton) by the conduction electron; upon relaxation, the bound hole emits a quantum of energy that is absorbed by the second conduction electron. When electrons are attracted to enhanced regions of positive charge, their KE causes what can be described as an overshoot or excess negative charge. This re-establishes a high internal field that is even higher than the initially calculated internal field. This recreated field must be relieved by reinitiation of the charge-transfer process. For these reasons, the charge-transfer excitation resonates.

In order for a zero-resistance state to exist, conduction electrons that carry the supercurrent must be in their state of lowest energy. The electrons that have net attraction toward each other cannot lose energy due to electron-electron repulsion; however, they can be in spin and momentum states that are higher than the ground state and, in such a case, will not be in the state of lowest energy. Hence, in order to maintain then the lowest energy, the spins of the two net attractively correlated electrons must be equal and opposite. Therefore, a mediator to assist in spin-pairing seemingly should contribute to creating superconductivity at high values of T_c . We interpret this mediator to be the spin fluctuations that are created in high- T_c materials when charge transfer causes the establishment of a unpaired valence spin, which breaks the delicately balanced antiferromagnetism at the Cu^{2+} (d^9) sites. In $\text{Y}_1\text{Ba}_2\text{Cu}_3\text{O}_{7-\delta}$, this spin fluctuation is established by the requirement for the decrease in cationic charge as the stoichiometry is reduced from O_7 to $\text{O}_{7-\delta}$. The most likely candidate to suffer decreased cationic charge is the $\text{Cu}(1)$, which ideally exists in the $3+$ state, but which can easily gain an electron and become Cu^{2+} d^9 and, in so, doing will offset the balanced antiferromagnetic compensation existing in the Cu^{2+} base planes of the pyramids. The most likely

source of the electron that creates the Cu^{2+} state at the Cu(1) chain, as well as the phenomenon that causes the anionic reduction from O_7 to $\text{O}_{7-\delta}$, is the O(4) apical ion.

We also conclude, regarding the spin-spin mediator, that the observed effect of the spin and the moment of the centrosymmetric ion in the YBaCuO system in elevating the temperatures for zero resistance and for elevating the preonset temperatures is due to indirect exchange or indirect correlation interaction between the moment and spin of the centrosymmetric ion and the spin of the d^9 , which is established at the Cu(1) chain site due to the reduction from O_7 to $\text{O}_{7-\delta}$. This we interpret as the magnetic contribution to the mechanism of high- T_c superconductivity.

If the two electrons that are both net-attracted and spin-paired have different linear momentum, and, if that momentum is not opposite in that direction, then the BCS formalism shows that they cannot be in their ground state. This requirement of equal-and-opposite linear momentum has the same phenomenology for high- T_c superconductors as it does for low- T_c superconductors.

It is not surprising that only a very small concentration of the total free electrons are actually Cooper-paired to create a supercurrent (approximately 1 in 100 or 1 in 1,000) because of the triple-demanded criteria of net attraction, spin-pairing, and equal-and-opposite linear momentum.

Finally, it should be pointed out that the conclusions of this 4-yr study have been advanced from a multidisciplinary approach to the problem involving materials science, chemistry, and physics. Many of the alternative explanations for the mechanism of high- T_c superconductivity that have been embraced by others were advanced usually through a single-discipline viewpoint. For example, in the very complex physics approaches associated with the electron-phonon interaction, it has become clear that many of the experimental observations, such as the acceptable concentration limits of multivalence cation substitutions in order to preserve high- T_c superconductivity, the charge transport behavior anomalies that were associated with measurements on polycrystalline ceramics, rather than on single crystals and crystal chemistry principles, were being ignored. Some of the experimental observations that were not treated in these mathematical physics approaches relate to critical conditions of charge transfer, multivalence, radius ratios, polarizing nature, scattering effects at grain

boundaries, and the effects of all reciprocal lattices. On the other hand, purely chemical approaches to describe superconductivity have often neglected consideration of Fermi surface, density of states, and coupling parameters. Many of these chemical and physical parameters have now been elucidated by studies that were in some cases motivated by our own work. The theoretical mechanism that we have advanced herein has taken into account all of the reported chemistry, materials science, and physics that are related to this class of materials to include IR absorption phenomena, antiferromagnetic behavior, charge-transport data, charge-transfer excitations, internal perturbation fields, chemical-synthesis substitution limitations criteria, photoemission properties, Fermi surface analysis, stereochemical considerations, lattice dynamics, and physiochemical characterization.

9. References

1. Onnes, K. H. *Akademie*. vol. 14, no. 113, p. 818, Van Wetenschappen, Amsterdam, Netherlands, 1911.
2. Onnes, K. H. *Communication of Physical Laboratory*. vol. 119, no. 120, p. 122, University, Leiden, 1911.
3. London, F. *Superfluids*, vol. 1, Dover, NY, 1961.
4. Ginzburg, V. L., and L. D. Landau. *Zhur. Eksperi. i. Teoret. Fiz.*, vol. 20, p. 1064, 1950.
5. Frohlich, H. *Physical Review*. vol. 79, p. 845, 1950.
6. Maxwell, E. *Physical Review*. vol. 78, p. 477, 1950.
7. Bardeen, J., L. N. Cooper, and J. R. Schrieffer. *Physical Review*. vol. 108, p. 1175, 1957.
8. Lynton, E. A. *Superconductivity*. Methuen and Company Ltd., London, England, 1969.
9. Cooper, L. N. *Physical Review*. vol. 104, p. 1189, 1956.
10. Cooper, L. N. *American Journal of Physics*. vol. 28, p. 91, 1960.
11. Slater, J. C. *Physical Review*. vol. 82, p. 538, 1951.
12. Slater, J. C. *Quantum Theory of Molecules and Solids*. vol. 1, McGraw Hill, NY, 1963.
13. Mott, N. F., and E. A. Davis. *Electronic Processes in Non-Crystalline Material*. Clarendon Press, Oxford, England, 1979.
14. Hubbard, J. *Proc. R. Soc.* vol. A27, p. 237, 1964.
15. Anderson, P. W. *Philosophical Magazine*. vol. 30, p. 839, 1974.
16. Mott, N. F. *Philosophical Magazine*. vol. 29, p. 59 and 613, 1974.
17. Mott, N. F. *Metal Insulator Transitions*. Taylor and Francis, London, England, 1974.
18. Brinkman, W. F., and T. M. Rice. *Physical Review*. vol. B4, p. 1556, 1971.
19. Brinkman, W. F., and T. M. Rice. *Physical Review*. vol. B7, p. 1508, 1973.
20. Kikoin, I. K., and S. V. Goobar. *Journal of Physics*. vol. 3, p. 333, USSR, 1940.

21. Rice, F. O., and E. Teller. *The Structure of Matter*. p. 192, John Wiley, NY, 1949.
22. Eliashberg, G. M. *Journal of Experimental and Theoretical Physics*. vol. 38, p. 996, USSR, 1960.
23. Eliashberg, G. M. "Sov. Phys." *Journal of Experimental and Theoretical Physics*. vol. 11, p. 696, 1960.
24. Eliashberg, G. M. *Journal of Experimental and Theoretical Physics*. vol. 43, p. 1105, USSR, 1962.
25. Eliashberg, G. M. "Sov. Phys." *Journal of Experimental and Theoretical Physics*. vol. 16, p. 780, 1963.
26. McMillan W. L., and J. M. Rowell. *Physical Review Letters*. vol. 14, p. 108, 1965.
27. Foner, S., and B. Schwartz. *Superconducting Machines and Devices*. Plenum, NY, 1973.
28. Foner, S., and B. Schwartz. *Superconductor Materials Science, Metallurgy, Fabrication and Applications*. Plenum, NY, 1981.
29. Bardeen, J. *Superconductivity in Science and Technology*. M. H. Cohen (ed.), University of Chicago Press, Chicago, IL, 1968.
30. Vezzoli, G. C., and T. Burke. *Progress in High Temperature Superconductivity Magnetic Interactions*. vol. 17, L. H. Bennett, Y. Flom, and G. C. Vezzoli (eds.), World Scientific, London, England, 1989.
31. Hurd, C. M. *Electrons in Metals*. Wiley-Interscience, NY, 1975.
32. Essman, U., and H. Trauble. *Physical Letters*. vol. 24A, p. 526, 1967.
33. Keldysh, L. V., and A. N. Kozlov. *Journal of Experimental and Theoretical Physics Letters*. vol. 5, p. 190, 1967.
34. Ginzburg, V. L. *Contemporary Physics*. vol. 9, p. 355, 1968.
35. Abrikosov, A. A. *Journal of Experimental and Theoretical Physics Letters*. vol. 27, p. 219, 1978.
36. Russakov, A. P. *Physica Status Solidi*. vol. B72, p. 503, 1975.
37. Abrikosov, A. A. *Zhur. Eksperim. i. Teoret. Fiz.* vol. 32, p. 1442, 1957.
38. Gorkov, L. P. *Sov. Phys.* vol. 10, p. 593, 1960.

39. Little, W. A. *Journal of Low-Temperature Physics*. vol. 13, p. 365, 1975.
40. Nakajima, S., and Y. Kurihara. *Journal of Physics Society*. vol. 56, p. 3021, Japan, 1987.
41. Marsiglio, F., and J. P. Carbotte. *Solid State Communications*. vol. 63, p. 419, 1987.
42. Marsiglio, F., R. Akis, and J. P. Carbotte. *Physical Review*. vol. B36, p. 5245, 1987.
43. Kresin, V. Z. *Solid State Communications*. vol. 63, p. 725, 1987.
44. Kresin, V. Z. *Physical Review*. vol. B35, p. 8716, 1987.
45. Kresin, V. Z., and S. A. Wolf. *Novel Superconductivity*. S. Wolf and V. Kresin (eds.), Plenum, NY, 1987.
46. Kresin, V. Z. *Novel Superconductivity*. p. 1111, Plenum, NY, 1987.
47. Chang, Y., M. Onellion, D. W. Niles, R. Joynt, G. Margaritondo, N. G. Stoffel, and J. M. Tarascon. *Solid State Communications*. vol. 63, p. 717, 1987.
48. Ihara, M., M. Hirabayashi, N. Terada, Y. Kimura, K. Senzaki, and M. Tokumoto. *Journal of Applied Physics*. vol. 26, no. L463, Japan, 1987.
49. Ruvalds, J. *Physical Review*. vol. B35, p. 8869, 1987.
50. Ruvalds, J. *Novel Superconductivity*. p. 455, Plenum NY, 1987.
51. Zhao, Z., L. Chen, A. Yang, Y. Huang, G. Chen, R. Tang, G. Liu, C. Cui, L. Chen, L. Wang, S. Guo, S. Li, and J. Bi. Private communication. preprint.
52. Perkowitz, S., G. L. Carr, B. Lou, S. S. Yom, R. Sudharsanan, and P. S. Ginley. *Solid State Communications*. vol. 64, p. 721, 1987.
53. Lobo, R. *Physical Review Letters*. vol. 21, p. 145, 1968.
54. Landau, L. D. *Zeitschrift Physica*. vol. 3. p. 644, Sowjetunion, 1933.
55. Frohlich, H. *Polarons and Excitons*. C. G. Kuper and G. D. Whitfield (eds.), Plenum, NY, 1962.
56. Donath, W., and R. A. Marcus. *Polarons and Excitons*. p. 110, C. G. Kuper and G. D. Whitfield (eds.), Plenum, NY, 1962.
57. Emin, D. Private communication. Sandia Laboratories.

58. Aleksandrov, A. S., V. N. Grebenev, and E. A. Mazur. *Pis'ma Zh. Eksp. Teor. Fiz.* vol. 45, p. 357, 1987.
59. Little, W. A., J. P. Collman, and J. T. McDevitt. *Materials Research Society Anaheim Symposium.* vol. 37, 1987.
60. Little, W. A. *Novel Superconductivity.* p. 342, Plenum, NY.
61. Kuramoto, Y., and T. Watanabe. *Solid State Communications.* vol. 63, p. 821, 1987.
62. Robaszkiewicz, R., R. Micnas, and J. Ranninger. *Physical Review.* vol. B36, p. 180, 1987.
63. Scalapino, D. J., R. T. Scalet, and N. E. Bickers. *Novel Superconductivity.* p. 475, Plenum, NY, 1987.
64. Anderson, P. W. *Science.* vol. 235, p. 1196, 1987.
65. Anderson, P. W. *Novel Superconductivity.* p. 295, Plenum, NY, 1987.
66. Anderson, P. W. *Physical Review Letters.* vol. 59, p. 2497, 1987.
67. Pauling, L. *Physical Review Letters.* vol. 59, p. 225, 1987.
68. Varma, C. W., S. Schmit-Rink, and E. Abrahams. *Solid State Communications.* vol. 62, p. 681, 1987.
69. Varma, C. W. *Novel Superconductivity.* p. 355, Plenum, NY, 1987.
70. Vezzoli, G. C. Lecture. The Massachusetts Institute of Technology, Physics Department, 8 Dec 1980.
71. Matthias, B. *Physical Review.* vol. 92, p. 874, 1953.
72. Lefkowitz, I. Private communication. U.S. Army Research Office, 1981.
73. Apfel, J. H., and L. N. Hadley. *Physical Review.* vol. 100, p. 1689, 1955.
74. Chu, C. W., A. P. Russakov, S. Huang, S. Early, T. H. Geballe, and C. Y. Huang. *Physical Review.* vol. B18, p. 2116, 1978.
75. Lefkowitz, I., J. S. Manning, and P. E. Bloomfield. *Physical Review.* vol. B20, p. 4506, 1979.
76. Vezzoli, G. C., and J. Bera. *Physical Review.* vol. B23, no. 6, p. 3022, 1981.
77. Vezzoli, G. C. Laboratory Notes. Picatinny Arsenal, Dover, NJ, February 1980.

78. Vezzoli, G. C. *Physical Review*. vol. B26, no. 8, p. 4140 (see note p. 4145), 1982.
79. Piermarini, G. J., F. A. Mauer, S. Block, A. Jayaraman, T. H. Geballe, and G. W. Hull. *Solid State Communications*. vol. 32, p. 275, 1979.
80. Wilson, J. A. *Philosophical Magazine*. vol. B38, p. 427, 1978.
81. Brandt, N. B., S. V. Kuvshinnikov, A. P. Russakov, and V. M. Seminov. *Journal of Experimental and Theoretical Physics Letters*. vol. 27, p. 33 and 37, 1978.
82. Vezzoli, G. C., M. Otooni, P. Houser, and S. Krasner. *Materials Research Bulletin*. vol. 17, no. 4, p. 485 1982.
83. Homan, G. C., D. P. Kendall, and R. K. MacCrone. *Solid State Communications* . vol. 32, p. 521, 1979.
84. Brown, E., C. G. Homan, and R. K. MacCrone. *Physical Review Letters*. vol. 45, no. 6, p. 478, 1980.
85. Miller, R., F. Dacheille, and R. Roy. *Physical Review*. vol. 37, p. 4913, 1966.
86. Vezzoli, G. C. Lecture. Picatinny Arsenal, Dover, NJ, Feb. 1982.
87. Mattes, B., and W. Foiles. Private communication. University of Michigan, MI, 1987.
88. Freeman, A. J., J. J. Yu, and C. L. Fu. *Physical Review*. vol. B36, p. 7111, 1987.
89. Freeman, A. J., J. J. Yu, and C. L. Fu. *American Physical Society Meeting*. New Orleans, LA, March 1988.
90. Williams, S., and J. Zink. Private communication. University of California Los Angeles, CA, 1987.
91. Bednorz, J. G., and K. A. Muller. *Zeitschrift Physica*. vol. B64, p. 189, 1986.
92. Muller, K. A., and J. G. Bednorz. *Science*. vol. 237, p. 1133, 1987.
93. Frederickse, J. F., Schooley, W. R. Thurber, E. Pfeiffer, W. R. Hosler. *Physical Review Letters*. vol. 16, p. 579, 1966.
94. Binnig, G., A. Baratoff, H. E. Hoenig, and J. G. Bednorz. *Physical Review Letters*. vol. 45, p. 1352, 1980.
95. Baratoff, A., and G. Binnig. *Physica*. vol. 108B, p. 1335, 1981.

96. Baratoff, A., G. Binnig, J. G. Bednorz, F. Gervais, and J. L. Servoin. *Superconductivity in d- and f-Band Metals*. vol. 191, W. Backel and W. Weber (eds.), KeinforschungszentrUm Karlsruhe, Karlsruhe, Germany, 1982.
97. Johnston, D. C. *Materials Research Bulletin*. vol. 8, p. 777, 1973.
98. Johnston, D. C. *Journal of Low-Temperature Physics*. vol. 25, p. 145, 1976.
99. Sleight, W., J. L. Gillson, and P. E. Bierstedt. *Solid State Communications*. vol. 17, p. 27, 1975.
100. Thanh, T. D., A. Koma, and S. Tanaka. *Applied Physics*. vol. 22, p. 205, 1980.
101. Batlogg, B. *Physica*. vol. 126B, p. 275, 1984.
102. Chakraverty, B. K. *Journal of Physics*. vol 40, no. L99, Paris, France, 1979.
103. Chakraverty, B. K. *Journal of Physics*. vol. 42, p. 1351, Paris, France, 1981.
104. Muller, K. A. *American Physical Society Meeting*. New York City, NY, March 1987.
105. Michel, C., L. Er-Rakho, and B. Raveau. *Materials Research Bulletin*. vol. 20, p. 667, 1985.
106. Bednorz, J. G., M. Takashige, and K. A. Muller. *Europhysics Letters*. vol. 3, p. 379, 1987.
107. Bednorz, J. G. Private communication. 1987.
108. Bardeen, J. Private communication. 1987.
109. Uchida, S., H. Takagi, K. Kitazawa, and S. Tanaka. *Journal of Applied Physics*. vol. 26, no. L151, Japan, 1987.
110. Takasi, H., S. Uchida, K. Kitazawa, and S. Tanaka. *Journal of Applied Physics*. vol. 26, no. L123, Japan, 1987.
111. Chu, C. W., P. H. Hor, R. L. Meng, L. Gao, Z. J. Huang, and Y. Q. Wang. *Physical Review Letters*. vol. 58, p. 405, 1987.
112. Chu, C. W., P.H. Hor, R. L. Meng, L. Gao, and Z. J. Huang. *Science*. vol. 235, p. 567, 1987.
113. Cava, R. J., R. B. Van Dover, B. Battlogg, and E. A. Rietman. *Physical Review Letters*. vol. 58, p. 408, 1987.
114. Murphy, D. W., S. Sunshine, R. B. van Dover, R. J. Cava, B. Batlogg, S. M. Zahurak, and L. F. Schneemeyer. *Physical Review Letters*. vol. 58, no. 18, p. 1888, 1987.

115. Moodenbaugh, A. R., M. Suenaga, T. Asano, R. N. Shelton, H. C. Ku, R. W. McCallum, and P. Klavins. *Physical Review Letters*. vol. 58, no. 18, p. 1885, 1987.
116. Franck, J. P., J. Jung, and M. A. -K Mohamed. *Physical Review*. vol. B36, no. 4, p. 2308, 1987.
117. Tarascon, J. M., L. H. Greene, W. R. McKinnon, G. W. Hull, and T. H. Geballe. *Science*. vol. 235, p. 1373, 1987.
118. Zhao, Z. X. Private communication. Inst. of Phys. Academia, Sinica, 1988.
119. Mattheiss, L. F. *Physical Review Letters*. vol 58, p. 1028, 1987.
120. Wu, M. K., J. R. Ashburn, C. T. Torng, P. H. Hor, R. L. Meng, L. Gao, Z. J. Huang, Y. Q. Wang, and C. W. Chu. *Physical Review Letters*. vol. 58, p. 908, 1987.
121. Tarascon, J. M., L. H. Greene, W. R. McKinnon, and G. W. Hull. *Physical Review*. vol. B35, p. 7115, 1985.
122. Hazen, W. Private communication. 1988.
123. Jorgensen, J. D., M. A. Beno, D. G. Hinks, L. Soderholm, K. J. Volin, R. L. Hitterman, J. D. Grace, I.K. Schuller, C. U. Sogre, K. Zhang, and M.S. Kleefisch. *Physical Review*. vol. B36, p. 3508, 1987.
124. Birgeneau, R. J., H. J. Guggenheim, and G. Shirane. *Physical Review*. vol. B1, p. 2211, 1979.
125. Cotton, F. A., and G. Wilkinson. *Advanced Inorganic Chemistry*. Interscience, NY, 1966.
126. Vezzoli, G. C., R. Benfer, and W. Spurgeon. *Novel Superconductivity*. p. 1017, Plenum, NY, 1987.
127. Wilson, J. A. "Solid State Physics." *Journal Physics*, vol. 21, p. 2067, 1988.
128. Lytle, F. W., R. B. Gregor, and A. J. Panson. *Ibid.* p. 1049.
129. Lytle, F. W., G. Van der Laan, R. B. Gregor, E. M. Larson, C. E. Violet, and J. Wong. *Physical Review*. vol. B41, no. 13, p. 8955, 1990.
130. McHenry, M. E., A. Collins, M. M. Donovan, C. Counterman, K. H. Johnson, R. C. O'Handley, and G. Kalonji. *Novel Superconductivity*. p. 563, Plenum, NY, 1987.
131. O'Handley, R. Private communication. Massachusetts Institute of Technology, 1988.
132. Johnson, K. Private communication. Massachusetts Institute of Technology, 1989.

133. Affronte, M., and D. Pavuna. *High-Temperature Supereconductivity: Physical Properties, Microscopic Theory, and Mechanisms*. G. C. Vezzoli, J. Ashkenazi, S. Barnes, and B. Kline, Plenum, NY, 1992.
134. Gallo, C. F., L. R. Whitney, and P.J. Walsh. *Novel Superconductivity*. Plenum, p. 385, NY, 1987.
135. Beasley, M., and T. Geballe. *Physics Today*. vol. 37, p. 60, 1984.
136. Kamaras, K., C. D. Porter, M. G. Doss, S. L. Herr, D. B. Tanner, D. A. Bom, J.E. Greedan, A. H. O'Reilly, C. V. Stager, and T. Timusk. *Physical Review Letters*. vol. 59, p. 919, 1987.
137. Maeda, H., Y. Tanaka, M. Fukutomi, and T. Asano. *Journal of Applied Physics Letters*. vol. 27, no. L209, 1988.
138. Chu, C. W., P. H. Hor, R. L. Meng, L. Gao, Z. J. Huang, J. Bechtold, M. K. Wu, and C. Y. Huang. *MRS Anaheim Symp.* vol. 15, 1987.
139. Zandbergen, H. W., Y. K. Huang, M. J. V. Menken, J. N. Li, K. Kadowaki, A. A. Menovsky, G. Van Tendeloo, and S. Amelinckx. *Nature*. vol. 332, p. 620, 1988.
140. Hazen, R. M., L. W. Finger, R. J. Angen, C. T. Prewitt, R. L. Ross, C. G. Hadidiacos, P. J. Heaney, D. R. Veblen, Z. Z. Sheng, A. El. Ali, and A. M. Hermann. *Physical Review Letters*. vol. 60, p. 1656, 1988.
141. Sheng, Z. Z., A. M. Hermann, A. El Ali, C. Almasan, J. Estrada, T. Datta, and R. J. Matson. *Physical Review Letters*. vol. 60, p. 937, 1988.
142. Sheng, Z. Z., and A. M. Hermann. *Nature*. vol. 332, p. 55, 1988.
143. Gao, L., Z. J. Huang, R. L. Meng, P. H. Hor, J. Bechtold, Y.Y. Sun, C. W. Chu, Z. Z. Sheng, and A. M. Hermann. *Nature*. vol. 332, p. 623, 1988.
144. Heiman, D. Private communication. Massachusetts Institute of Technology, 1988.
145. Tranquada, J. M., D. Coz, W. Kliman, H. Moulder, G. Shirane, M. Suenaga, P. Zaliker, D. Vaknin, S. Sinha, M. Alvarez, A. Jacobson, and D. Johnson. *Physical Review Letters*. vol. 60, p. 156, 1988.
146. Ashkenazi, J. Private communication. University of Miami, 1991.
147. Takeda, S. *Materials Research Bulletin*. vol. 25, p. 293, 1990.
148. Thompson, S. *Physical Review*. vol. 36, no. 1, p. 1, 1987.

149. Ong, N. O., Z. Z. Wang, and J. Clayhold. *Novel Superconductivity*. p. 1061–1066, Plenum, NY, 1987.
150. Hundley, M. F., A. Zettl, A. Stacy, and M. L. Cohen. *Physical Review*. vol. B35, no. 16, p. 8800, 1987.
151. Berko, S. Private communication. Brandeis University, 1990.
152. Freeman, A. J., and J. J. Yu. Private communication. Northwestern University, 1990.
153. Pickett, W. Private communication. *University of Miami Workshop on Mechanisms and Electronic Structure of High- T_c Materials*, Naval Research Laboratory, February 1990.
154. Arkho, P. *University of Miami Workshop on Mechanism and Electronic Structure of High- T_c Materials*. Los Alamos National Laboratories, February 1990.
155. Pickett, W. *Science*. vol. 2, January 1992.
156. Varma, C. *NIST Conference on Magnetic Interactions in High- T_c Superconductors*. Gaithersburg, MD, October 1988.
157. McKelvey, J. *Solid State and Semiconductor Physics*. Harper and Row, NY, 1966.
158. Lytle, F. Private communication. Boeing Aircraft Company, Seattle, WA, 1987.
159. Cava, R. Private communication. Bell Telephone Laboratories, *American Physical Society Conference*, Cincinnati, OH, March 1991.
160. Schlögl, M. Private communication. Max Planck-Fritz Haber Institute, Stuttgart Germany, 1990.
161. Meservey, R. Private communication. The Massachusetts Institute of Technology, 1987.
162. Kurtz, S., L. E. Cross, N. Setter, D. Knight, A. Bhallas, W. W. Cao, and W. N. Lawless. *Materials Letters*. vol. 6, no. 10, p. 317, The Pennsylvania State University, PA, 1988.
163. Schuttler, H. -B. *University of Miami Workshop on Mechanism and Electronic Structure of High- T_c Superconductors*. February 1990.
164. Zhong, J., and H. -B. Schuttler. Private communication. University of Georgia, Atlanta, 1990.
165. Chen, C. -X., and H. -B. Schuttler. *Physical Review*. vol. B41, no. 13, p. 8702, 1990.
166. Schuttler, H. -B., J. Zhong, and A. J. Fedro. Private communication. Miami, FL, 1990.

167. Fedro, A. J., and H. -B. Schuttler. *Physica*. vol. C185-189, p. 1673, 1991.
168. Schuttler, H. -B., and A. J. Fedro. *Physical Review*. vol. B45, no. RC, p. 7588, 1992.
169. Chen, C. -X., H. -B. Schuttler, and A. J. Fedro. *Physical Review*. vol. B (RC), no. 41 (4), p. 2581, 1990.
170. Interrante, L. V., Z. P. Jiang, and D. J. Larkin. *American Chemical Society Symposium Series*. vol. 377, p. 168-180, 1988.
171. Eibchutz, M., R. J. Cava, R. J. Krajowski, J. J. Peck. *Applied Physics Letters*. vol. 58, no. 17, April 1991.
172. Fukuhara, M., A. S. Bhalla, N. M. Laxman, R. E. Newnham. *Journal of Materials Research*. vol. 4, no. 2, March/April 1989.
173. Rotman, D. *Industrial Chemistry*. p. 20-23, October 1987.
174. Cava, R. J. *Scientific American*. p. 42-49, August 1990.
175. Collings, E. W. *Cryogenics*. vol. 28, November 1988.
176. Robinson, D. A. *Journal of Physics*. vol. C21, p. 4091-4096, 1988.
177. Jones, T. E., W. C. McGinnis, R. D. Ross, E. W. Jacobs, J. W. Schindler, and C. D. Rees. *American Chemical Society Symposium Series*. vol. 377, p. 155-167, Naval Systems Center, San Diego, CA, 1988.
178. Goodenough, J. B., and A. Manthiram. *Journal of the American Chemical Society*. vol. 109, p. 6667, University of Texas, Austin, TX, 1987.
179. Goodenough, J. B., A. Manthiram, and S. J. Lee. *Journal of Solid State Chemistry*. vol. 73, p. 278, University of Texas, Austin, TX, 1988.
180. Furman, N. H. *Scott's Standard Methods of Chemical Analysis*. Sixth Ed., vol. I, p. 785, D. Van Nostrand Company, Inc., NY, March 1962.
181. Vezzoli, G. C., T. Burke, B.M. Moon, B. Lalevic, A. Safari, H.G.K. Sundar, R. Bonometti, C. Alexander, C. Rau, and K. Waters. *Journal of Magnetism and Magnetic Materials*. vol. 79, p. 146, 1989.
182. Moon, B. M. Private communicaion. Royal Institute, Stockholm, 1992.
183. Zhao, Y., J. Xia, Z. He, S. Sun, Q. Zhang, Y. Qian, Z. Chen, and G. Pan. *Physical Letters*. vol. 5, p. 221, China, 1988.

184. Penney, T., S. Von Molnar, and D. Kaiser. *Physical Review*. vol. B38, p. 2918, 1988.
185. Seshadri, A. T., and B. Subrahmanyam. *High Temperature Superconductivity Physical Properties, Microscopic Theory, and Mechanisms*. G. C. Vezzo, J. Ashkenazi, S. Barnes, and B. Kline (eds.), Plenum, NY, 1992.
186. Budnick, J., B. Chamberland, and C. Baines. *Physical Review Letters*. vol. 62, p. 102, 1989.
187. Budnick, J., B. Chamberland, D. P. Yang, Ch. Niedermayer, A. Golnik, E. Recknagel, M. Rossmannith, and A. Weidinger. *Europhys. Letters*. vol. 651, 1988.
188. Budnick, J., B. Chamberland, A. Weidinger, Ch. Niedermayer, A. Golnik, R. Simon, E. Recknagel, and C. Baines. *Progress in High-Temperature Superconductivity: Magnetic Interactions*. vol. 17, p. 206-215, G. C. Vezzoli, L. H. Bennett, Y. Flom (eds.), World Scientific, London, England, 1988.
189. Frenkel, R. Private communication. Miami, FL, 1990.
190. Austin, A., G. C. Vezzoli, and R. N. Katz. *Experiments Performed Using the MIT SQUID Magnetometer in the Fall of 1987*. unpublished.
191. Vezzoli, G. C. *Conference on High- T_c Superconductivity Magnetic Interactions*. Gaithersburg, MD, October 1988.
192. Moncton, D. *Science*. vol. 236, p. 780, 1987.
193. Thompson, J. R., S. Sekula, D. Christen, B. Sale, L. Boatner, Y. Kim. *Physical Review*. vol. B36, no. 1, p. 718, 1987.
194. Collins, R. T., Z. Schlesinger, M. W. Shafer, and T. R. McGuire. *Physical Review*. vol. B39, no. 10, p. 5817, 1988.
195. Vezzoli, G. C. *Journal of Magnetism and Magnetic Materials*. vol. 82, p. 335, 1989.
196. Chu, C. W. *Physical Review Letters*. vol. 58, no. 18, p. 1891, American Physical Society Meeting, NY, March 1987.
197. Maple, M. B., Y. Dalichaouch, J. M. Ferreira, R. R. Kake, B. W. Lee, J. J. Neumeier, M. S. Torikachvili, and K. N. Kurvz. *Physica*. vol. B148, p. 155, 1987.
198. Matthias, B. T., H. Suhl, and E. Corenzwit. *Journal of Physics and Chemistry of Solids*. vol. 13, p. 156, 1959.
199. Matthias, B. T., H. Suhl, and E. Corenzwit. *Physical Review Letters*. vol. 1, p. 92, 1958.

200. Pop, I. *Stud. Cercetari.* vol. 17, no. 7, p. 755, Rumania, 1965.
201. Fincher, C., and G. B. Blanchet. *Physical Review Letters.* vol. 67, no. 20, p. 2902, 1991.
202. Tarascon, J. M., L. H. Greene, W. R. Mckimon, and G. W. Hull. *Solid State Communications.* vol. 63, p. 499, 1987.
203. Rudderaman, M. A., and C. Kittel. *Physical Review.* vol. 96, p. 99, 1954.
204. Bloembergen, N., and T. J. Rowland. *Physical Review.* vol. 97, p. 1679, 1955.
205. Budnick, J. Private communication. University of Connecticut, 1992.
206. Warren, W. W. *Physical Review.* vol. B36, p. 5727, 1987.
207. Mattis, D. C. *The Theory of Magnetism.* Harper and Row, NY, p. 193, 1965.
208. Martin, D. H. *Magnetism in Solids.* p. 240, The MIT Press, Cambridge, MA, 1967.
209. Onsager, L. *Physical Review Letters.* vol. 7, p. 50, 1961.
210. Byers, N., and C. N. Yang. *Physical Review Letters.* vol. 7, p. 46, 1961.
211. Vezzoli, G. C., M. F. Chen, F. Craver, A. Safari, B. M. Moon, B. Lalevic, T. Burke, and M. Shoga. *Journal of Magnetism and Magnetic Materials.* vol. 88, p. 351–364, 1990.
212. Zettl, A. Private communication. University of California, Berkeley, 1988.
213. Lalevic, B. *Journal of Applied Physics.* vol. 31, p. 234, 1962.
214. Lalevic, B. *Physical Review.* vol. 128, p. 1070, 1962.
215. Lalevic, B. *Journal of Applied Physics.* vol. 35, p. 1785, 1964.
216. Weber, R. *Physical Review.* vol. 72, p. 1241, 1947.
217. Kaplan, B., and J. G. Daunt. *Physical Review.* vol. 89, p. 907, 1953.
218. Baird, D. *Can. Journal of Physics.* vol. 37, p. 120, 1959.
219. Andrews, D. H., R. M. Milton, and W. DeSorbo. *J. Opt. Soc. Am.* vol. 36, p. 520, 1946.
220. Proc. Roy. Soc. vol. A82, p. 194. London, England, 1948.

221. Ching, W., Y. Xu, G. L. Zhao, K. W. Wong, and F. Zandiehnam. *Physical Review Letters*. vol. 59, p. 1333, 1987.
222. Ziman, J. M. *Electrons and Phonons*. p. 159 The Clarendon Press, Oxford, England, 1960.
223. Chudhari, P. Private communication. IBM Yorktown Heights, 1991.
224. Goldfarb, L., and D. X. Chen. *Journal of Applied Physics*. vol. 63, p. 400, 1988.
225. Ekin, J., T. M. Larson, N. F. Bergen, A. J. Nelson, A. B. Swartzlander, L. L. Kazmerski, A. J. Panson, and B. A. Blankenship. *Applied Physics Letters*. vol. 52, no. 21, p. 1819, 1988.
226. Panson, A. J., and B. A. Blankenship. *Appl. Phys. Letters*. vol. 52, no. 4, p. 331, 1988.
227. Conwell, E., and V. F. Weisskopf. *Physical Review* vol. 77, p. 388, 1950.
228. Brooks, H. *Physical Review* vol. 83, p. 879, 1951.
229. Cooper, L. N. *Physical Review Letters*. vol. 3, p. 17, 1959.
230. Cooper, L. N. *Physical Review Letters*. vol. 6, p. 689, 1961.
231. Cooper, L. N. *Physical Review Letters*. vol. 8, p. 367, 1962.
232. Kurtz, S. K., L. E. Cross, N. Setter, D. Knight, A. Bhalla, W. W. Cao, and W. N. Lawless. *Materials Letters*. vol. 6, no. 10, p. 317, 1988.4
233. Mihailovic, D., and A. J. Heiger. Private communication. University of California Santa Barbara, 1989.
234. Lyons, A. Private communication. Bell Telephone Laboratories, 1988.
235. Kurtz, S. K., A. Bhalla, and L. E. Cross. *USA-USSR Seminar on Ferroelectrics*. Boulder, CO, July 1989.
236. Kurtz, S. K., A. Bhalla, and L.E. Cross. *Ferroelectrics*. in press.
237. Mustre de Leon, J., S. D. Conradson, P. G. Allen, I. Batistic, and A. R. Bishop. *High-Temperature Superconductivity: Physical Properties, Microscopic Theory and Mechanisms*. J. Ashkenazi, S. Barnes, G. C. Vezzoli, and B. Kline (eds.), Plenum, NY, 1992.
238. Hirsch, J. *High-Temperature Superconductivity: Physical Properties, Microscopic Theory and Mechanisms*. J. Ashkenazi, S. Barnes, G. C. Vezzoli, and B. Kline (eds.), Plenum, NY, 1992.

- 239. Johnson, K. Private communication. Massachusetts Institute of Technology, 1991.
- 240. Johnson, K. *High-Temperature Superconductivity: Physical Properties, Microscopic Theory and Mechanisms*. J. Ashkenazi, S. Barnes, G. C. Vezzoli, and B. Kline (eds.), Plenum, NY, 1992.
- 241. Lee, H., and R. Sharma. *Physical Review*. vol. B43, no. 10, p. 7756, 1991.
- 242. Chen, J. T., L. X. Qian, L. Q. Wang, L. E. Wenger, and E. M. Logothetis. *Third Annual Conference on Superconductivity and Applications*. Buffalo, NY, p. 19–21, September 1989.

NO. OF
COPIES ORGANIZATION

2 DEFENSE TECHNICAL
INFORMATION CENTER
DTIC DDA
8725 JOHN J KINGMAN RD
STE 0944
FT BELVOIR VA 22060-6218

1 HQDA
DAMO FDQ
DENNIS SCHMIDT
400 ARMY PENTAGON
WASHINGTON DC 20310-0460

1 CECOM
SP & TRRSTR L COMMCTN DIV
AMSEL RD ST MC M
H SOICHER
FT MONMOUTH NJ 07703-5203

1 PRIN DPTY FOR TCHNLGY HQ
US ARMY MATCOM
AMCDCG T
M FISETTE
5001 EISENHOWER AVE
ALEXANDRIA VA 22333-0001

1 PRIN DPTY FOR ACQUSTN HQS
US ARMY MATCOM
AMCDCG A
D ADAMS
5001 EISENHOWER AVE
ALEXANDRIA VA 22333-0001

1 DPTY CG FOR RDE HQS
US ARMY MATCOM
AMCRD
BG BEAUCHAMP
5001 EISENHOWER AVE
ALEXANDRIA VA 22333-0001

1 DPTY ASSIST SCY FOR R&T
SARD TT T KILLION
THE PENTAGON
WASHINGTON DC 20310-0103

1 OSD
OUSD(A&T)/ODDDR&E(R)
J LUPO
THE PENTAGON
WASHINGTON DC 20301-7100

NO. OF
COPIES ORGANIZATION

1 INST FOR ADVNCD TCHNLGY
THE UNIV OF TEXAS AT AUSTIN
PO BOX 202797
AUSTIN TX 78720-2797

1 USAASA
MOAS AI W PARRON
9325 GUNSTON RD STE N319
FT BELVOIR VA 22060-5582

1 CECOM
PM GPS COL S YOUNG
FT MONMOUTH NJ 07703

1 GPS JOINT PROG OFC DIR
COL J CLAY
2435 VELA WAY STE 1613
LOS ANGELES AFB CA 90245-5500

1 ELECTRONIC SYS DIV DIR
CECOM RDEC
J NIEMELA
FT MONMOUTH NJ 07703

3 DARPA
L STOTTS
J PENNELLA
B KASPAR
3701 N FAIRFAX DR
ARLINGTON VA 22203-1714

1 USAF SMC/CED
DMA/JPO
M ISON
2435 VELA WAY STE 1613
LOS ANGELES AFB CA
90245-5500

1 US MILITARY ACADEMY
MATH SCI CTR OF EXCELLENCE
DEPT OF MATHEMATICAL SCI
MDN A MAJ DON ENGEN
THAYER HALL
WEST POINT NY 10996-1786

1 DIRECTOR
US ARMY RESEARCH LAB
AMSRL CS AL TP
2800 POWDER MILL RD
ADELPHI MD 20783-1145

NO. OF
COPIES ORGANIZATION

1 DIRECTOR
US ARMY RESEARCH LAB
AMSRL CS AL TA
2800 POWDER MILL RD
ADELPHI MD 20783-1145

3 DIRECTOR
US ARMY RESEARCH LAB
AMSRL CI LL
2800 POWDER MILL RD
ADELPHI MD 20783-1145

1 DR MICHAELINE CHEN
529 GROVE ST
NEEDHAM MA 02192

ABERDEEN PROVING GROUND

4 DIR USARL
AMSRL CI LP (305)

REPORT DOCUMENTATION PAGE			Form Approved OMB No. 0704-0188	
Public reporting burden for this collection of information is estimated to average 1 hour per response, including the time for reviewing instructions, searching existing data sources, gathering and maintaining the data needed, and completing and reviewing the collection of information. Send comments regarding this burden estimate or any other aspect of this collection of information, including suggestions for reducing this burden, to Washington Headquarters Services, Directorate for Information Operations and Reports, 1215 Jefferson Davis Highway, Suite 1204, Arlington, VA 22202-4302, and to the Office of Management and Budget, Paperwork Reduction Project(0704-0188), Washington, DC 20503.				
1. AGENCY USE ONLY (Leave blank)		2. REPORT DATE December 1997	3. REPORT TYPE AND DATES COVERED Final, May 88 - Mar 93	
4. TITLE AND SUBTITLE Materials Science Studies of High-Temperature Superconducting Ceramic Oxides.			5. FUNDING NUMBERS 381K6	
6. AUTHOR(S) G. C. Vezzoli, M. F. Chen, F. Craver, and R. N. Katz				
7. PERFORMING ORGANIZATION NAME(S) AND ADDRESS(ES) U.S. Army Research Laboratory ATTN: AMSRL-WM-MC Aberdeen Proving Ground, MD 21005-5066			8. PERFORMING ORGANIZATION REPORT NUMBER ARL-TR-1570	
9. SPONSORING/MONITORING AGENCY NAMES(S) AND ADDRESS(ES)			10. SPONSORING/MONITORING AGENCY REPORT NUMBER	
11. SUPPLEMENTARY NOTES				
12a. DISTRIBUTION/AVAILABILITY STATEMENT Approved for public release; distribution is unlimited			12b. DISTRIBUTION CODE	
13. ABSTRACT (Maximum 200 words) Herein is presented the results of a comprehensive program of research aimed at understanding the materials science and the mechanistic physics of high-temperature superconducting oxides. This comprehensive research program has identified the materials properties that are consistently associated with high- T_c superconductors and has shown that the mechanism that gives rise to the phenomenon of high- T_c superconductivity is associated with bound holes that are due to charge-transfer excitations at high frequency. The latter are a result of the high internal electric field present in high- T_c materials, owing to the asymmetry of the crystal structure. The interaction of bound holes with free electrons and the interaction of local spin fluctuations with the spin of free electrons generate a charge density wave and a spin density wave that cause Cooper pairing.				
14. SUBJECT TERMS high- T_c superconductor, bound holes, antiferromagnetism, spin fluctuations, vortices, and flux exclusion			15. NUMBER OF PAGES 245	
			16. PRICE CODE	
17. SECURITY CLASSIFICATION OF REPORT UNCLASSIFIED	18. SECURITY CLASSIFICATION OF THIS PAGE UNCLASSIFIED	19. SECURITY CLASSIFICATION OF ABSTRACT UNCLASSIFIED	20. LIMITATION OF ABSTRACT UL	

INTENTIONALLY LEFT BLANK.

USER EVALUATION SHEET/CHANGE OF ADDRESS

This Laboratory undertakes a continuing effort to improve the quality of the reports it publishes. Your comments/answers to the items/questions below will aid us in our efforts.

1. ARL Report Number/Author ARL-TR-1570 (Vezzoli) Date of Report December 1997
2. Date Report Received _____
3. Does this report satisfy a need? (Comment on purpose, related project, or other area of interest for which the report will be used.) _____

4. Specifically, how is the report being used? (Information source, design data, procedure, source of ideas, etc.) _____

5. Has the information in this report led to any quantitative savings as far as man-hours or dollars saved, operating costs avoided, or efficiencies achieved, etc? If so, please elaborate. _____

6. General Comments. What do you think should be changed to improve future reports? (Indicate changes to organization, technical content, format, etc.) _____

CURRENT
ADDRESS

Organization

Name

E-mail Name

Street or P.O. Box No.

City, State, Zip Code

7. If indicating a Change of Address or Address Correction, please provide the Current or Correct address above and the Old or Incorrect address below.

OLD
ADDRESS

Organization

Name

Street or P.O. Box No.

City, State, Zip Code

(Remove this sheet, fold as indicated, tape closed, and mail.)
(DO NOT STAPLE)